ENHANCING THE CAPACITY OF MOLYBDENUM DISULPHIDE ELECTRODE MATERIALS USING THE IDEA OF DEFECTS

by

Patrick Vaati Mwonga

Supervisors:

Prof. S.R. Naidoo

Prof. A. Quandt

Prof. K.I. Ozoemena

A thesis submitted to the Faculty of Science

University of the Witwatersrand,

in fulfilment of the requirements for the degree of

Doctor of Philosophy.

School of Physics,

University of the Witwatersrand,

Johannesburg, South Africa.

May 16, 2019

DECLARATION

I declare that this thesis is my own, unaided work. It is being submitted for the degree of Doctor of Philosophy in Physics at the University of the Witwatersrand, Johannesburg. It has not been submitted before for any degree or examination in any other University.

Mwonga Patrick Vaati 1325805

Signature: 

Date: May 16, 2019

This study is dedicated to my family:

Jane, Melody and Raymond;

my parents,

mentors, relatives,

and

friends.

ABSTRACT

Transition metal chalcogenides have attracted a lot of attention due to their potential application in the semiconductor industry. Crystalline pristine molybdenum disulphide (MoS_2), is also the basis of this study. The influence of defects in MoS_2 due to ion implantation on the material's electrical and optical properties are reported, the main aim being to enhance the capacity of electrode materials for use in energy storage devices; such as supercapacitors or supercapacitor batteries.

Both simulations and experimental studies were done. Simulations were formed using the Stopping and Range of Ions in Matter (SRIM) software, which was used to predict the depth of penetration of ions in the material. Density Functional Theory (DFT) and Boltzmann transport properties (BoltzTraP) codes were employed to study effects of defects on properties, including: electrical conductivity; thermal conductivity; magnetic susceptibility and band gaps.

Optical characterisation was done using Raman spectroscopy and photoluminescence spectroscopy (PL), using a green laser wavelength of 514.2 nm. Reported here are the Raman peaks shifts, due to damaged MoS_2 surfaces and PL showing quenching of photoluminescence peaks after ion implantation. Current-voltage (I-V) characterisation was done using silver paste contacts, which formed Ohmic contacts with both pristine and implanted MoS_2. Galvanostatic measurements were also performed and capacities for various electrode samples for both unimplanted and ion implanted MoS_2 were calculated. The constant current charge-discharge (CCCD) technique was used to evaluate specific capacities. Stability and retention tests were performed for 1000 cycles of charge and discharge with ion implanted electrode samples reporting higher than 98% retention capabilities. Electrochemical Impendance Spectroscopy (EIS) showing that after recycling, the electrodes were more stable. The electrode kinetics were evaluated using the standard rate constant (k_s) and it showed significant increase in all ion implanted electrodes compared to the unimplanted one, implying that faster equilibrium was attained with implanted electrodes.

The electrodes prepared from the synthesised and annealed MoS_2 powder gave the highest specific capacitance of 15.63 $F{\cdot}g^{-1}$ while the as-synthesised MoS_2 powder had specific capacitance of 10.43 $F{\cdot}g^{-1}$. These values were one order magnitude higher than what was measured from the electrodes made from the cyrstalline bulk MoS_2. However, electrodes made from the same powders and ion-implanted with either Mo or W ions shown suppressed capacitances, attributed to blockage of the pores as a result of ion irradiation.

ACKNOWLEDGEMENTS

First and foremost, I would like is to thank The Almighty God for giving me good health and strength to do this research. My sincere appreciation and gratitude go to my supervisors Professor S. R. Naidoo, Professor A. Quandt and Professor K. I. Ozoemena, who encouraged and guided me throughout this study.

I take this opportunity too to thank the Materials for Energy Research Group (MERG), for financing my studies and upkeep. I acknowledge the Center for High Performance Computing (CHPC), for granting me the access to their computational resources, where DFT simulations were done.

Special thanks to Dr. Robert Warmbier, who tirelessly sharpened my computational skills that were required in the course of this research work. My gratitude goes to Professor Alexander Ziegler and his great team, at Microscopy and Microanalysis Unit (MMU) at the University of the Witwatersrand in Johannesburg, South Africa, for their wonderful support. Further, I wish to thank the *i*Themba LABS team, where I did the ion implantation. Thanks to Dr. Rudolph Erasmus for this assistance with the Raman and Photoluminescence measurements. To Prof. Daniel Wamwangi; I say thank you for your support, sound advice and for granting me the permission and guidance to use the Thin Film Laboratory, where I did current-voltage characterization at the initial stages of my study. To Dr. Caren Billing, I say thank you for granting me unlimited access to your Electrochemistry Lab, where all the Electrochemical Analysis related to this work was done. I wish to recognise Professor Daniel Joubert for his support, that made this research succeed. My acknowledgement will not be complete without thanking my colleagues in the office; Francis Otieno, Maxwell Vhareta, Jonah Kuria and all the other fellow postgraduate students from the Schools of Physics and Chemistry for their support. Thank you Dr. P. M. Gangatharan for your support during the homestretch of this study.

Finally, I wish to express my heartfelt gratitude to my family, for allowing me to study away from home. Your prayers and encouragement, to mention but a few, gave me the strength to soldier on.

To all, mentioned and not mentioned, I say thank you and God bless your efforts.

TABLE OF CONTENTS

DECLARATION ii

DEDICATION iii

ABSTRACT iv

ACKNOWLEDGEMENTS v

TABLE OF CONTENTS vi

LIST OF TABLES x

LIST OF FIGURES xii

LIST OF SYMBOLS AND ABBREVIATIONS OF ACRONYMS xvii

1 INTRODUCTION 1

1.1 Background 1

1.1.1 Potential Window of the Electrolytes 4

1.1.2 Performance of Supercapacitors 4

1.1.3 Choice of Electrode Material for ES 4

1.2 Defects 5

1.3 Objectives 7

2 LITERATURE REVIEW 9

2.1 Introduction 9

2.2 General Properties of Molybdenum Disulphide 9

2.3 Extraction and Purification Procedure of MoS_2 10

2.4 Research Review 10

2.4.1 Mechanical Properties 10

2.4.2 Electronic Transport Properties 11

2.4.3 Optical Properties 13

2.5 MoS_2 Modern Applications 16

3 THEORY **18**

3.1 Density Functional Theory (DFT) . . . 18

3.2 Boltzmann Transport Theory (BoltzTrap) . . . 20

3.3 Summary . . . 22

4 METHODOLOGY **23**

4.1 Introduction . . . 23

4.2 DFT and BoltzTrap Simulations . . . 23

4.3 SRIM Simulations . . . 24

4.4 Current-Voltage (I-V) Measurements . . . 26

4.5 Raman Spectroscopy . . . 27

4.6 Ion Implantation . . . 27

4.7 Electrochemical Measurements and Analysis Software . . . 28

5 RESULTS **30**

5.1 Computational Results . . . 30

5.1.1 Electronic Properties . . . 31

5.1.1.1 Structure of Pristine Crystal and Band Structure with the PDOS of MoS_2 31

5.1.1.2 Band Structure of MoS_2 with Mo Vacancy . . . 31

5.1.1.3 Band Structure of MoS_2 with Mo Interstitial . . . 32

5.1.1.4 Band Structure of MoS_2 with Mo Intercalation . . . 32

5.1.1.5 Band Structure of MoS_2 with S Vacancy . . . 33

5.1.1.6 Band Structure of MoS_2 with S Intercalation . . . 34

5.1.1.7 Band Structure of MoS_2 with W Interstitial . . . 34

5.1.2 Electronic and Thermal Conductivity . . . 37

5.2 Experimental Results . . . 41

5.2.1 Current-Voltage (I-V) Characteristics . . . 41

5.2.2 Raman Spectroscopy (RS) . . . 42

5.2.3 Photoluminescence . . . 45

5.3 Electrochemical Analysis . . . 47

5.3.1 Cyclic Voltammetry . . . 47

5.3.2 Constant Current Charge-Discharge (CCCD) . . . 51

5.3.3 Determination of the Predominant Charge Storage Mechanism in Bulk MoS_2 . . 53
5.3.4 Diffusion Coefficients . . . 62
5.3.5 Standard Rate Constant . . . 64
5.3.6 Types of Electrochemical Mechanisms . . . 69
5.3.7 Specific Capacities . . . 70
5.3.8 Stability Tests . . . 72
5.3.9 Electrode Performance . . . 75
5.3.10 Electrodes Kinetics . . . 77
5.3.11 Conclusion . . . 80

6 POWDERED MOS_2 81

6.1 MoS_2 Material Synthesis Procedure . . . 81
6.2 Characterisation Techniques . . . 81
6.3 Characterisation Results . . . 82
6.3.1 Raman Spectroscopy . . . 82
6.3.2 Powder X-ray Diffraction . . . 82
6.3.3 XPS Measurements . . . 83
6.3.4 EDS and SEM Measurements . . . 89
6.3.5 TEM Measurements . . . 91
6.3.6 BET Measurements . . . 91
6.3.7 TGA Measurements . . . 94
6.4 Electrochemistry Measurements . . . 95
6.4.1 Electrode Preparation . . . 95
6.4.2 Cyclic Voltammetry (CV) and Charge-Discharge (CD) Measurements . . . 96
6.4.3 Electrodes' Stability . . . 99
6.4.4 Conclusion . . . 100

7 CONCLUSIONS AND RECOMMENDATIONS 101

7.1 Computational Analysis . . . 101
7.2 Experimental Perspective . . . 101

Appendix 102

REFERENCES **102**

APPENDIX A SUPPORTING INFORMATION **118**

A.1 DFT Structural Optimizations 118

A.2 Cyclic Voltammograms 119

APPENDIX B CONFERENCES AND PUBLICATIONS **124**

B.1 Publications 124

B.2 Conferences 124

LIST OF TABLES

Table 1.1 Table of electrolytes and their ESPWs. 4

Table 2.1 Properties of molybdenum disulphide and remarks. 9

Table 2.2 Performance summary of different metal/2D MoS_2 contacts. 12

Table 2.3 Recent reports on the DSSCs and LiBs with MoS_2-based counter electrodes. 17

Table 4.1 Ion-implantation parameters and abbreviations. 28

Table 5.1 Comparison of bandgaps of pristine and defective MoS_2 (error ± 5%). 36

Table 5.2 Summary of resistances of pristine and ion implanted MoS_2 (error ± 5%). 42

Table 5.3 Summary of Raman vibrational modes (cm^{-1}) (error ± 5%). 44

Table 5.4 A summary of b, D and K_s values for the seven electrodes (error ± 5%). 69

Table 5.5 Specific capacities of pristine, Mo and W implanted MoS_2 at 1 $mA{\cdot}cm^{-2}$ and 10 $mA{\cdot}cm^{-2}$ (error ± 5%). 72

Table 5.6 Specific capacities of pristine, Mo and W implanted MoS_2 at 1 $mA{\cdot}g^{-1}$ and 10 $mA{\cdot}g^{-1}$ (error ± 5%). 73

Table 5.7 Specific capacities of pristine, Mo and W implanted MoS_2 at various cycles (error ± 5%). 75

Table 5.8 Percentage Coulombic efficiency and retention of pristine, Mo and W implanted MoS_2 at various cycles (error ± 5%). 75

Table 5.9 Performance evaluation of pristine, Mo and W ions implanted MoS_2 at 1 $mA{\cdot}g^{-1}$ (error ± 5%). 77

Table 5.10 Fitted values for; resistors (R_s, R_{ct1}, R_{ct2}), $CPEs$ (Q_1, Q_2) and n values (n_1, n_2) in pristine and ions implanted MoS_2 before cycling (error ± 5%). 79

Table 5.11 Fitted values for resistors (R_s, R_{ct1}, R_{ct2}), $CPEs$ (Q_1, Q_2) and n values (n_1, n_2) in pristine and ions implanted MoS_2 after 1000 cycles (error ± 5%). 79

Table 5.12 Knee frequencies before and after cycling for pristine and ions implanted MoS_2 (error ± 5%). 80

Table 6.1 Binding energies, the associated oxidation states and the atomic % concentrations for both AS and 450 samples (error ± 5%). 88

Table 6.2 BET results for MoS_2-AS and MoS_2-450 obtained using 5 probe points (error ± 5%). 92

Table 6.3 BET results for MoS_2-AS and MoS_2-AS-W_{imp} obtained using 5 probe points (error ± 5%). 97

Table 6.4 Performance evaluation for MoS_2-AS, MoS_2-450, MoS_2-AS-Mo-16, MoS_2-AS-W-12, MoS_2-450-Mo-16 and MoS_2-450-W-12 samples at current density of 0.2 $A{\cdot}g^{-1}$ (error ± 5%). 98

LIST OF FIGURES

Figure 1.1 Pie chart showing factors affecting ES performance 3

Figure 1.2 Pictorial representation of point defects 6

Figure 1.3 Pictorial representation of various defects in solids 6

Figure 2.1 Flow chart of molybdenite processing. 10

Figure 2.2 I-V characteristics for different metal/MoS_2 contacts under identical bias conditions. 12

Figure 2.3 Raman spectra of single-layer 1L, double-layer 2L, and triple-layer 3L MoS_2 . . . 13

Figure 2.4 Raman spectra of MoS_2 monolayer at 300 K and 400 K 14

Figure 2.5 Photoluminescence intensity with respect to number of layers 15

Figure 4.1 Schematic diagram of high symmetry points of hexagonal (2H) MoS_2. 24

Figure 4.2 SRIM simulations for Mo ions. 25

Figure 4.3 SRIM simulations for W ions. 26

Figure 4.4 A schematic diagram showing Ag contacts on pristine MoS_2 sample. 27

Figure 4.5 A picture of the electrochemistry studies for bulk MoS_2 setup. 29

Figure 4.6 (a) A schematic diagram of the swagelok setup, (b)-(j) pictorial procedure used to set up the swagelok. 29

Figure 5.1 (a) Structure of pristine MoS_2, (b) bands and PDOS of pristine MoS_2. 31

Figure 5.2 (a) Structure of MoS_2 with Mo vacancy, (b) bands and DOS of pristine MoS_2 (black) and MoS_2 with Mo vacancy (red). 32

Figure 5.3 (a) Structure of MoS_2 with Mo interstitial, (b) bands and DOS of pristine MoS_2 (black) and MoS_2 with Mo interstitial (red). 33

Figure 5.4 (a) Structure of MoS_2 with Mo intercalation, (b) bands and DOS structure of pristine MoS_2 (black) and MoS_2 with Mo intercalation (red). 33

Figure 5.5 (a) Structure of MoS_2 with S vacancy, (b) bands and DOS of pristine MoS_2 (black) and MoS_2 with S vacancy (red). 34

Figure 5.6 (a) Structure of MoS_2 with S interstitial, (b) bands and DOS for pristine MoS_2 (black) and MoS_2 with S interstitial (red). 35

Figure 5.7 (a) Structure of MoS_2 with W interstitial, (b) bands structure of MoS_2 (black) and MoS_2 with W interstitial (red). 35

Figure 5.8 Electronic conductivity tensor in x-direction σ_{xx} for the three systems. 37
Figure 5.9 Thermal conductivity tensor in x-direction κ_{xx} for the three model systems. 38
Figure 5.10 Thermal conductivity tensor σ_{xx}, σ_{yy} and σ_{zz} showing the anisotropic nature of MoS_2. 38
Figure 5.11 Effects of doping on MoS_2 at 300k, on the magnetic susceptibility. 39
Figure 5.12 Seebeck coefficient vs chemical potential for pristine MoS_2 and MoS_2 with Mo and W interstitials. 40
Figure 5.13 Graphs of current against voltage of pristine MoS_2 at different contact configurations. 41
Figure 5.14 Graphs of current against voltage MoS_2 pristine and MoS_2 implanted with Mo and W ions. 42
Figure 5.15 Raman shift in pristine MoS_2. 43
Figure 5.16 Raman shift in MoS_2 implanted with Mo and W atoms. 43
Figure 5.17 Photoluminescence of spectra MoS_2 implanted with Mo and W ions recorded at room temperature. 45
Figure 5.18 PL peak for pristine and tungsten ion implanted MoS_2 before and after annealing. The label B_{Ann} denotes a sample before annealing, while A_{Ann} denotes the annealed sample. 47
Figure 5.19 Cyclic voltammograms of MoS_2 implanted with Mo and W ions compared with the pristine at scan rate of 5 mV/s. 48
Figure 5.20 Cyclic voltammograms of MoS_2 implanted with Mo and W ions compared with the pristine at scan rate of 10 mV/s. 49
Figure 5.21 Cyclic voltammograms of MoS_2 implanted with Mo and W ions compared with the pristine at scan rate of 20 mV/s. 49
Figure 5.22 Cyclic voltammograms of MoS_2 implanted with Mo and W ions compared with the pristine at scan rate of 30 mV/s. 50
Figure 5.23 Cyclic voltammograms of MoS_2 implanted with Mo and W ions compared with the pristine at scan rate of 50 mV/s. 50
Figure 5.24 Cyclic voltammograms of MoS_2 implanted with Mo and W ions compared with the pristine at scan rate of 100 mV/s. 51

Figure 5.25 Charge-discharge curves of pristine MoS_2 and MoS_2 implanted with Mo and W ions at current density of 1 mA/g. 52
Figure 5.26 Charge-discharge curves of pristine MoS_2 and MoS_2 implanted with Mo and W ions at current density of 10 mA/g. 53
Figure 5.27 Cyclic voltammogram peaks a for pristine MoS_2. 55
Figure 5.28 Graph of log$j$ vs logν for pristine MoS_2. 55
Figure 5.29 Cyclic voltammogram peaks for Mo implanted MoS_2 with a fluence of 10^{14} ions/cm^2. 56
Figure 5.30 Graph of log$j$ vs logν for Mo implanted MoS_2 with a fluence of 10^{14} ions/cm^2. . 56
Figure 5.31 Cyclic voltammogram peaks for Mo implanted MoS_2 with a fluence of 10^{16} ions/cm^2. 57
Figure 5.32 Graph of log$j$ vs logν for Mo implanted MoS_2 with a fluence of 10^{16} ions/cm^2. . 57
Figure 5.33 Cyclic voltammogram peaks for Mo implanted MoS_2 with a fluence of 2×10^{16} ions/cm^2. 58
Figure 5.34 Graph of log$j$ vs logν for Mo implanted MoS_2 with a fluence of 2×10^{16} ions/cm^2. 58
Figure 5.35 Cyclic voltammogram peaks for W implanted MoS_2 with a fluence of 10^{12} ions/cm^2. 59
Figure 5.36 Graph of log$j$ vs logν for W implanted MoS_2 with a fluence of 10^{12} ions/cm^2. . . 59
Figure 5.37 Cyclic voltammogram peaks for W implanted MoS_2 with a fluence of 10^{14} ions/cm^2. 60
Figure 5.38 Graph of log$j$ vs logν for W implanted MoS_2 with a fluence of 10^{14} ions/cm^2. . . 60
Figure 5.39 Cyclic voltammogram peaks for W implanted MoS_2 with a fluence of 10^{16} ions/cm^2. 61
Figure 5.40 Graph of log$j$ vs logν for W implanted MoS_2 with a fluence of 10^{16} ions/cm^2. . . 61
Figure 5.41 Graph current I vs square root of scan rate ν; for pristine MoS_2. 63
Figure 5.42 Graph current I vs square root of scan rate ν; for MoS_2 implanted with Mo ions (Mo-16). 63
Figure 5.43 Graph current I vs square root of scan rate ν; for MoS_2 implanted with W ions (W-16). 64
Figure 5.44 Schematic CV voltammogram where i_{pa}, E_{pa}, i_{pc} and E_{pc} are anodic and cathodic peaks currents and peak potentials, respectively. 65
Figure 5.45 Graph of ln i_p vs $(E_p - E_{1/2})$ for pristine MoS_2. 65
Figure 5.46 Graph of ln i_p vs $(E_p - E_{1/2})$ for Mo-14. 66
Figure 5.47 Graph of ln i_p vs $(E_p - E_{1/2})$ for Mo-16. 66

Figure 5.48 Graph of ln i_p vs $(E_p - E_{1/2})$ for Mo-2e16. 67
Figure 5.49 Graph of ln i_p vs $(E_p - E_{1/2})$ for W-12. 67
Figure 5.50 Graph of ln i_p vs $(E_p - E_{1/2})$ for W-14. 68
Figure 5.51 Graph of ln i_p vs $(E_p - E_{1/2})$ for W-16. 68
Figure 5.52 Graph of peak currents ratio against increase in scan rates. 70
Figure 5.53 Potential against specific capacities at current density of 1 $mAcm^{-2}$. 70
Figure 5.54 Potential against specific capacities at current density of 1 mAg^{-1}. 71
Figure 5.55 Potential against specific capacities at current density of 10 $mAcm^{-2}$. 71
Figure 5.56 Potential against specific capacities at current density of 10 mAg^{-1}. 72
Figure 5.57 Specific capacities against number of cycles at current density of 100 $mA{\cdot}cm^{-2}$. . 74
Figure 5.58 Coulombic efficiency against number of cycles at current density of 100 $mA{\cdot}cm^{-2}$. 74
Figure 5.59 Schematic charge-discharge curve at 1 mA/g. 76
Figure 5.60 (a) Nyquist plots before cycling for pristine MoS_2 and MoS_2 electrodes implanted with Mo and W ions, (b) Nyquist plots after 1000 cycles for pristine MoS_2 and MoS_2 electrodes implanted with Mo and W ions, and (c) equivalent circuit used for data fitting. 78
Figure 5.61 Bode plots for pristine MoS_2, MoS_2 implanted with Mo ions and MoS_2 implanted with W ions electrodes (a) before cycling and (b) after 1000 cycles. 80

Figure 6.1 Raman spectra of bulk MoS_2 crystal, MoS_2-AS and MoS_2-450. 82
Figure 6.2 XRD spectra of MoS_2-AS and MoS_2-450 powders. 83
Figure 6.3 Deconvoluted XPS spectra for MoS_2-AS S 2p. 84
Figure 6.4 Deconvoluted XPS spectra for MoS_2-AS Mo 3d. 84
Figure 6.5 Deconvoluted XPS spectra for MoS_2-450 S 2p. 85
Figure 6.6 Deconvoluted XPS spectra for MoS_2-450 Mo 3d. 85
Figure 6.7 Wide area scan XPS spectra for MoS_2-AS. 86
Figure 6.8 Wide area scan XPS spectra for MoS_2-450. 86
Figure 6.9 XPS spectra for MoS_2-AS and MoS_2-450 S 2p. 87
Figure 6.10 XPS spectra for MoS_2-AS and MoS_2-450 Mo 3d. 87
Figure 6.11 SEM morphologies (a) and (d), EDS spectra (b) and (e), % Weights (c) and (f), for MoS_2-AS and MoS_2-450, respectively. 89

Figure 6.12 SEM morphologies (a)-(c) for MoS_2-450, (d)-(f) for MoS_2-AS, at 40 µm, 20 µm and 3 µm, respectively. 90
Figure 6.13 TEM images (a) MoS_2-AS and (b) MoS_2-450 powders. 91
Figure 6.14 BET pore size distribution spectra for MoS_2-AS and MoS_2-450 samples. 93
Figure 6.15 BET spectra for MoS_2-AS and MoS_2-450 samples. 93
Figure 6.16 BET isotherm for MoS_2-AS and MoS_2-450 samples. 94
Figure 6.17 Thermogravimetric analysis of MoS_2-AS and MoS_2-450 Samples. 95
Figure 6.18 Specific capacitances against potential. 96
Figure 6.19 Charge-discharge curves at 0.2 A/g. 97
Figure 6.20 Specific capacitances against potential for ion implanted and un-implanted powder samples. 98
Figure 6.21 Coulombic efficiencies for MoS_2-AS, MoS_2-450, MoS_2-AS-Mo-16, MoS_2-AS-W-12, MoS_2-450-Mo-16 and MoS_2-450-W-12 electrodes, for 2000 cycles. 99

Figure A.1 Graph of total energy against k-points of $\mathbf{MoS_2}$. 118
Figure A.2 Graph of total energy against the lattice of $\mathbf{MoS_2}$. 118
Figure A.3 Graph of total energy against the c/a ratio of $\mathbf{MoS_2}$. 119
Figure A.4 Graph of total energy against cut-off energy of $\mathbf{MoS_2}$. 119
Figure A.5 Cyclic voltammograms for pristine $\mathbf{MoS_2}$ electode at various scan rates. 120
Figure A.6 Cyclic voltammograms for Mo-14 electrode at various scan rates. 120
Figure A.7 Cyclic voltammograms for Mo-16 electrode at various scan rates. 121
Figure A.8 Cyclic voltammograms for Mo-2e16 electrode at various scan rates. 121
Figure A.9 Cyclic voltammograms for W-12 electrode at various scan rates. 122
Figure A.10 Cyclic voltammograms for W-14 electrode at various scan rates. 122
Figure A.11 Cyclic voltammograms for W-14 electrode at various scan rates. 123

LIST OF SYMBOLS AND ABBREVIATIONS

The following are some of the symbols and acronyms that have been frequently used in this thesis.

1D	one-dimensional
1T	trigonal structure
2D	two-dimensional
2H	hexagonal structure
3R	rhombohedral structure
$\mathring{A}$	Angstrom unit
A_{ann}	after annealing
AC	activated carbon
B_{ann}	before annealing
BET	Brunauer-Emmett-Teller technique
BTE	Boltzmann transport equation
BZ	Brillouin zone
CCCD	constant current charge-discharge
CCD	cooled charge coupled gadget identifier
CHPC	Centre for High Performance Computing
CPE	constant phase elements
CV	cyclic voltammetry
DFT	density functional theory
DOS	density of states
DSSC	dye-sensitized solar cell
EDLC	electrochemical double-layer capacitors
EDS	energy-dispersive X-ray spectroscopy
E_F	Fermi energy level
E_g	energy gap
EIS	Electrochemical Impendance Spectroscopy
ES	electrochemical supercapacitor

ESPW	electrochemical stable potential window
ESR	equivalent series resistance
F	Farad
FET	field effect transistor
GGA	generalized gradient approximation
LiBs	Lithium-ion batteries
MERG	Materials for Energy Research Group
MMU	Microscopy and Microanalysis Unit
Mo-14	bulk crystalline MoS_2 sample implanted with Mo ions at a fluence of 1×10^{14} ions/cm^2
Mo-16	bulk crytalline MoS_2 sample implanted with Mo ions at a fluence of 1×10^{16} ions/cm^2
Mo-2e16	bulk crystalline MoS_2 sample implanted with Mo ions at a fluence of 2×10^{16} ions/cm^2
Mo_{-i}	molybdenum atom interstitial
MoS_2-450	synthesised powder MoS_2 annealed at 450 °C or electrode made from it
MoS_2-450-Mo-16	MoS_2-450 electrode implanted with Mo ions at a fluence of 1×10^{16} ions/cm^2
MoS_2-450-W-12	MoS_2-450 electrode implanted with W ions at a fluence of 1×10^{12} ions/cm^2
MoS_2-AS	as-synthesised powder MoS_2 or electrode made from it, without ion implantation
MoS_2-AS-Mo-16	MoS_2-AS electrode, implanted with Mo ions at a fluence of 1×10^{16} ions/cm^2
MoS_2-AS-W-12	MoS_2-AS electrode implanted with W ions at a fluence of 1×10^{12} ions/cm^2
MoS_2-AS-W_{imp}	as-synthesised powder MoS_2 implanted with W ions at a fluence of 1×10^{12} ions/cm^2
nm	nano metre
NMP	N-methyl-2-pyrrolidinone
NTs	nanotubes
PANI	polyaniline
PBE	Perdew-Burke-Ernzerhof
PDOS	projected density of states
PL	photoluminescence spectroscopy
PPy	polypyrrole

PVDF polyvinylidene fuoride

QE quantum espresso

RHE reversible hydrogen electrode

SEM scanning electron microscope

SRIM stopping and range of ions in matter

TB tight-binding

TGA thermal gravimetric analysis

TMC transition metal chalcogenides

W-12 bulk crystalline MoS_2 sample implanted with W ions at a fluence of 1×10^{12} ions/cm^2

W-14 bulk crystalline MoS_2 sample implanted with W ions at a fluence of 1×10^{14} ions/cm^2

W-16 bulk crystalline MoS_2 sample implanted with W ions at a fluence of 1×10^{16} ions/cm^2

W_{-i} tungsten atom interstitial

XPS X-ray photoelectron spectroscopy

XRD X-ray diffraction

CHAPTER ONE

INTRODUCTION

This Chapter gives the background related to this study and outlines the aims and objectives of this research.

1.1 Background

The growing demand for electrical energy storage due to intermittent nature of renewable energy technologies, has compelled researchers to search for more efficient ways of storing this form of energy. Some of the most promising technologies are capacitors and batteries. Their energy storage properties strongly depend on the type of materials used as electrodes.

Different technologies have been developed towards mitigation of this demand for energy storage; and they were improved as man has developed. Alongside storing other forms of energy, to store electrical energy has been a challenge to scientists, trying to develop various methods in their search to effectively harvest electrical power by converting solar energy into electrical energy [1]. Several forms of transducers have been developed and are being enhanced in an attempt to increase their capacities and efficiencies. Currently, some of the devices tailored to store electrical energy include; fuel cells, rechargeable batteries and supercapacitors [2].

Capacitors have a low energy density and a higher power density compared to batteries. A system with high power density, (like a capacitor) can output large amounts of energy based on its mass. For example, a tiny capacitor may have the same power output as a large battery. However, a capacitor is so much smaller, it has a higher power density. Since capacitors release their energy quickly, high power density systems can also recharge quickly. This can be illustrated by using a camera flash which works by utilising this type of energy storage, stored in small capacitors that are tiny enough to fit inside device such a camera and have a high enough power output. Although systems with a high power density are ideal, there is need to also increase their energy densities and this makes studies towards this goal worthwhile.

Ordinary (regular) capacitors store their charge by aligning molecules of the dielectric along an electric field, while in supercapacitors charge is stored across an interface between an electrode and an electrolyte in a Helmholtz double layer of ions. This is made possible by aligning the charges of an electrolyte on either side of an insulator. Unlike in batteries that provide voltage almost constant at

low discharge rates and also a solid metal electrode that is slowly consumed, supercapacitors' voltage outputs decrease linearly as current flows but their electrodes do not erode. Fuel cells on the other hand, do not store energy. They convert the chemical energy of the fuel (like hydrogen and oxygen) directly into electrical energy and heat plus water as the byproduct (in the case of hydrogen and oxygen), without combustion. It employs two electrodes; an anode and a cathode, separated by an electrolyte that only allows specific ion flows.

A number of studies on enhancing MoS_2 as an electrode material have been done. Some of the approaches included hybridization of MoS_2 layers with graphene, lithium or carbon which yield capacities of 1289 mA·h·g^{-1} and 1174.7 mA·h·g^{-1} respectively [3, 4]. Combination of MoS_2 with polyanine (PANI) and polyrrole (PPy) have shown exciting results, reporting a specific capacitance of 553.7 F·g^{-1} [5, 6]. MoS_2 hybrids of nitrogen-doped graphene [7] and defect engineered MoS_2-TiO_2 have also been tested and showed a capacity of 1600 mA·h·g^{-1} [8]. MoS_2 exfoliated nanosheets have been reported to be a highly electrocatalytic electrode [9], suggesting that MoS_2 could perform very well as an electrode for power storage devices. This high performance of MoS_2 composites was the impetus to the investigation carried out in an effort to contribute in improving the capacity/capacitance of MoS_2.

The pie chart shown in Fig. 1.1 is a summary of factors which should be considered as a pointer towards the efforts to optimise supercapacitors performance.

In Fig. 1.1, ESR is the equivalent series resistance and ES is electrochemical supercapacitor. Ion-electrode here, means the effects due to electrolyte ions and the cathode electrode. The rest of factors assume their global definitions.

Capacitors made with an electrolyte dielectric have the advantage to store and discharge higher amounts of energy than those with solid dielectric [11]. The maximum energy W stored in such a capacitor is governed by

$$W = \frac{1}{2} C U_0^2, \tag{1.1}$$

where U_0 is the cell voltage and C the total effective capacitance.

A higher electrolyte resistance also affects the equivalent distributed resistance of the porous electrodes, and consequently reduces the maximum usable power, which is calculated according to:

$$P = U_0^2 (4R)^{-1}, \tag{1.2}$$

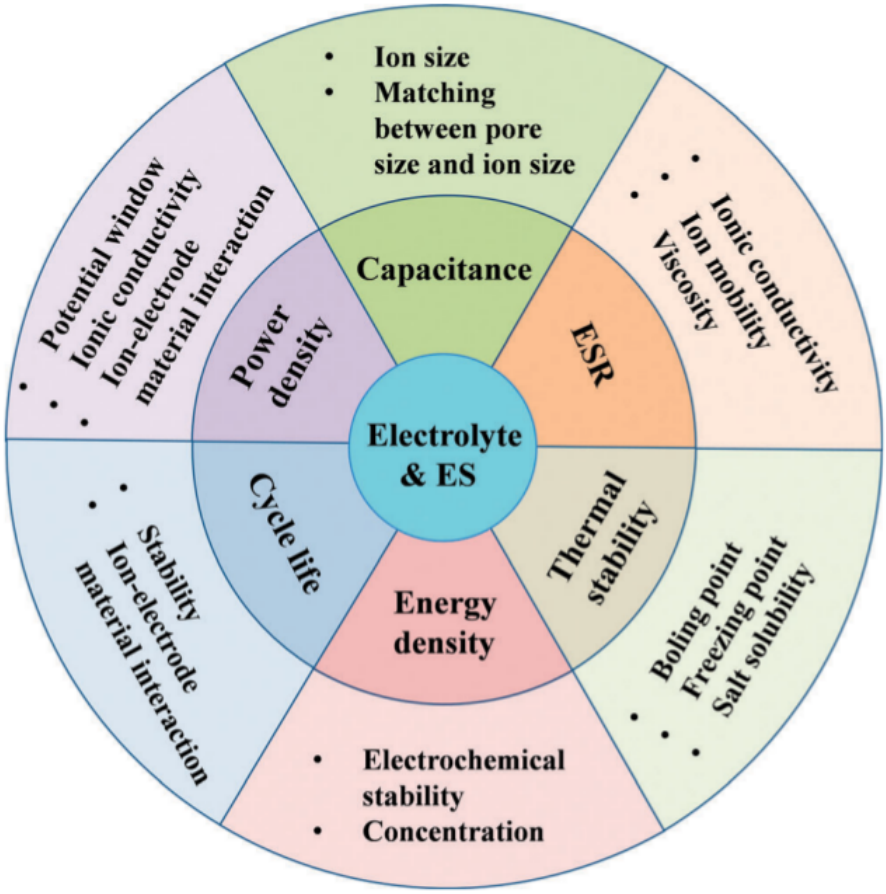

Figure 1.1: Pie chart showing factors affecting ES performance [10].

where R represents the total effective series resistance of the electrode [11]. If we factor in the device weight M_d, where M_d includes: anode, cathode, current collectors, electrolyte and any other materials that may have been used in the building of a capacitor; equation (1.2) can be re-written as,

$$P = U_0^2 (4 M_d R)^{-1}. \tag{1.3}$$

The work or energy density in equation (1.1), has a unit of W·h·kg^{-1}, while the power density in equation (1.2), has a unit of W·kg^{-1} [12]. From equations (1.1) and (1.3), its clear that U_0, C, M_d, and R are four important variables determining the performance of an electrochemical supercapacitors (ESs). In order to improve both the energy and power densities of an ES, increasing the values of both U_0 and C and simultaneously reducing the values of both M_d and R are necessary. Since both energy and power densities are proportional to the square of operating voltage (potential window), a cell voltage increase would have a greater contribution to the improvement of the ESs energy and power densities than increasing the capacitance or reducing resistance.

In general, the maximum operating voltage of an ES is strongly dependent on the electrochemical

stable potential window (ESPW) or the potential window of the electrolyte. ESPW is the voltage range within which the ESs operation is stable [13].

1.1.1 Potential Window of the Electrolytes

Table 1.1 is a short summary of some electrolytes and their ESPWs. This is necessary since any choice made has profound effects on the performance of ESs.

Table 1.1: Table of electrolytes and their ESPWs [10].

Electrolyte	**ESPW** (V)
Aqueous electrolyte-based	1.0 – 1.3
Organic electrolyte-based	2.5 – 2.7
Ionic liquid (IL) based	3.5 – 4.0

1.1.2 Performance of Supercapacitors

Electric double layer-layer capacitors (EDLC) and electrochemical capacitors (ECs), often also referred to as supercapacitors have high energy and power densities and they use electrolyte dielectrics. However, due to the demand for higher energy storage capabilities, there is need to research for more powerful and efficient supercapacitors. Currently, the energy density and maximum power of supercapacitors reach only 13 Wh/L and 70 kW/L respectively, and this need to be improved through newer technologies by at least 10% [14].

There is a great demand for high power capability supercapacitors in different fields of application today. Most of these applications need an on board electric energy storage device which can be recharged from any of the following ways: engine-driven generator, regenerative braking, or from a wall-plugin power supply. In all cases, the energy storage device can either be a battery or supercapacitor. The supercapacitors need to be resized in order to meet this energy storage requirements without sacrificing their capability to use a large fraction of their stored energy in a flash and retaining their ability to charge and discharge for a longer cycle life. Currently, most supercapacitor technologies have less than 500,000 cycle life [15].

1.1.3 Choice of Electrode Material for ES

Many materials have been studied, with the major aim to improve ES's life cycle, charge and discharge speeds among other factors. However, the search for high power capability ESs ought not sacrifice the energy density. An efficient cathode electrode is one of the ways to improve the performance of

ESs. Based on the way supercapacitors store charge, it is clear that any attempt to increase the surface area of the electrodes will lead to an increase in the charge storage and this is the basis of this study.

Different allotropes of carbon and other metal alloys have also been on focus as suitable candidates electrode material for supercapacitors. Molybdenum disulphide (MoS_2) is likely to perform better in ESs than carbon allotropes based on other successful applications it has had in motor and semiconductor industries.

This study investigated MoS_2, which belongs to metal dichalcogenides with the aim of finding out its potential as candidate material for electrodes in supercapacitors. This class of energy storage devices is used to mainly provide stable power in electrical appliances, or to give a burst of high energy required within a very short time (i.e rapid release of electrostatically stored charge). There are basically two major types of capacitors based on the type of the dielectric medium (the material between the electrodes), which may be either a solid or an electrolyte dielectric material.

1.2 Defects

Defects are known to affect transport and electronic properties of materials [16–18]. In solids, they can be classified into three broad categories namely: point defects; line defects and surface defects [19]. Point defects include vacancies and interstitials. Vacancies are characterized by missing atom(s) or ion(s) in an otherwise perfect atomic or ionic arrangements in crystal structures. Interstitials are said to occur when an atom occupies a site between atoms in the normal lattice structure. When two opposite charged ions are missing in an ionic crystal, the type of defect is referred to as a Schottky imperfection, while a cation movement into an interstitial site in ionic crystal forms a vacancy-interstitialcy pair referred to as Frenkel defect [20].

Line defects include: edge dislocation(s) which are due to intersection of extra half-plane of atoms; screw dislocation(s) which occur during upward and downward shear stresses in crystals and are separated by cutting planes. Both edge and screw dislocation can also occur simultaneously, creating a mixed dislocation. Surface defects could be external, where surface atoms are not bonded by the maximum number of nearest neighbour atoms. These atoms then possess higher energy states than those in the interior. Grain boundary and interface result where atomic packing is lower than within, due to mismatch of atoms [21–25]. Pores, cracks foreign inclusions and other phases are termed as bulk or volume defects. Twin boundary is as a result of mirror reflection of atomic arrangements. Other surface defects are due to mismatch of stacking order in the crystal. Some of the above defects could be induced

during ion implantation, especially point defects. Figure 1.2 shows a summary of defects that could be created during ion implantation. Some of the other defects that are commonly found in solids are shown in Figure 1.3.

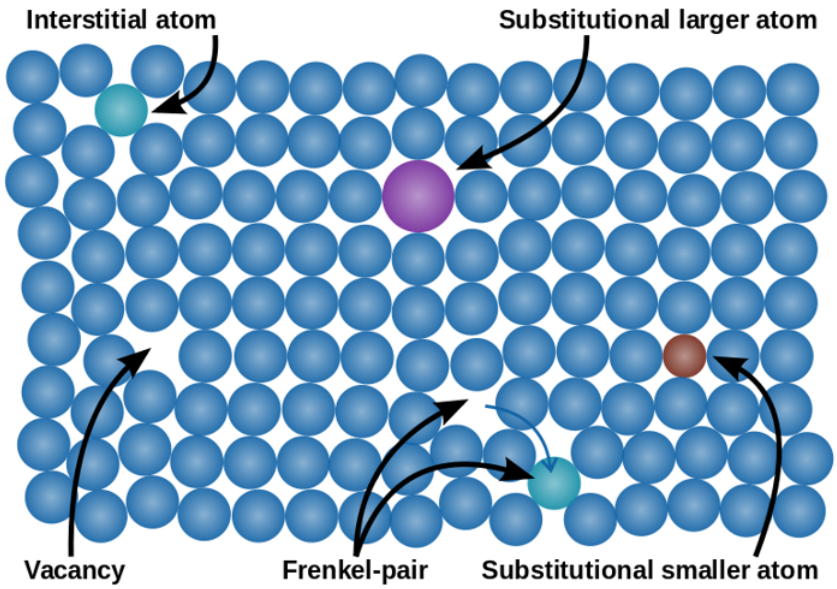

Figure 1.2: Pictorial representation of point defects [26].

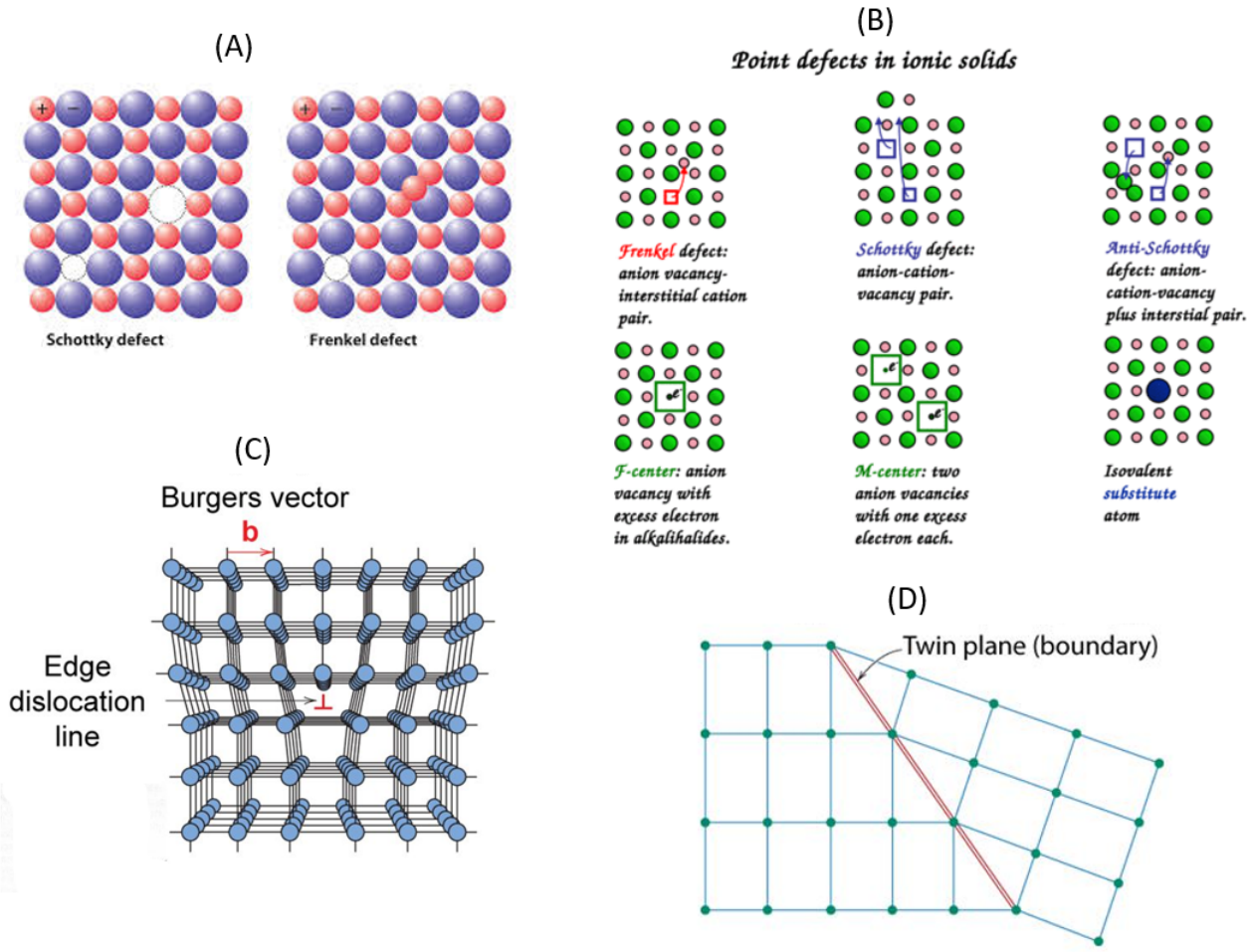

Figure 1.3: Pictorial representation of various defects in solids [26].

Previous studies on ion implanted MoS_2 focused mainly on one dimensional (1-D) or two dimensional (2-D) MoS_2, and reported transfer characteristics aimed for applications in transistors [27, 28]. Other studies where ion implantation on MoS_2 has been reported focused on their effects on mechanical properties dynamics [29].

In this study we investigated the effects of ion implantation on the near surface properties of bulk MoS_2, by the creation of defects closer to the surface (10 nm) of crystalline MoS_2 and explicitly studied the effects of these defects on charge storage, compared to the as received MoS_2 sample. By creating new active sites translates to an increase of the reactive sites in the damaged MoS_2 near the surface in contact with the electrolyte (Na_2SO_4). More Na^+ are able to interact with the electrode material, which leads to increased release of electrons during the intercalation and de-intercalation of the alkali ions. This leads to charge accumulation on the electrode materials, resulting to pseudocapacitance or capacitance behaviour.

1.3 Objectives

Molybdenum disulphide (MoS_2) has reported success stories in other Semiconductor Physics applications including 2D applications like the cases in transistors. Based on the high surface-to-volume ratio of MoS_2 and other transition metal chalcogenides (TMCs) make them especially sensitive to changes in their surroundings. Exposure to various gases has led to changes in charge transfer, doping, permittivity, and lattice vibrations [30]. Changes to the electronic properties can be detected electrically by measuring changes in the I-V characteristics of TMC-based transistor devices or optically by measuring changes in Raman spectra, photoluminescence, or absorbance [31].

It is opined that bulk MoS_2 had the potential for use as an electrode material for supercapacitors based on the multilayered structure plus the interlayer spacings. This interlayer spacings have the ability to generate/accummulate charge during the intercalation and de-intercalation of metal ions in the electrolyte. The material electrodes were enhanced by introducing defects in molybdenum disulphide (MoS_2), guided by the following specific objectives:

1. To make a supercell model of molybdenum disulphide (MoS_2) and examine it with the help of computational methods, with focus on;
    - intrinsic defects on the top layer.
    - induced defects on other layers.

2. To create defects near the top layers (about 10nm) of crystalline samples of bulk MoS_2, using ion implantation technique.

3. To study the effects of the defects on charge transfer kinematics in both pristine and ion implanted MoS_2 electrodes.

4. To study the effects of the defects on the overall performance and stability; in an attempt to improve the charge storage capacity of MoS_2 electrodes.

CHAPTER TWO

LITERATURE REVIEW

2.1 Introduction

This Chapter discusses the general properties of molybdenum disulphide and highlights on the various research works, already done by other scientists.

2.2 General Properties of Molybdenum Disulphide

Molybdenum disulphide is an inorganic compound that in nature occurs in three known polytypes namely: 1T, 2H and 3R; where T, H and R represent trigonal, hexagonal and rhombohedral structures respectively. The 2H is more stable than the 1T and 3R. Table 2.1 gives a summary of some of the properties of MoS_2 that were of concern in the study.

Table 2.1: Properties of molybdenum disulphide and remarks [32–34].

Appearance	black/lead-gray solid
Density	5.06 g/cm^3
Melting point	1,185 °C (decomposes at this temperature)
Solubility in water	insoluble
Solubility	decomposed by aqua regia, hot sulfuric acid, nitric acid insoluble in dilute acids
Band gap	1.29 eV (2H and 3R)
Crystal structure	hP6, space group $P63/mmc$, No 194 (2H): hR9, space group $R3m$, No 160 (3R)
Lattice constant	a = 3.161 Å (2H), 3.163 Å (3R), c = 12.295 Å (2H), 18.37 Å (3R)
Molar mass	160.07 g/mol

Aqua regia is a mixture of nitric acid and hydrochloric acid, optimally in a molar ratio of 1:3 [35], which disolves noble metal such as gold, is among the few acidic mixtures that MoS_2 is soluble in. This shows the robust nature of MoS_2 against corrosion in acidic environment. hP6 and hR9 represent the Pearson symbols [36] for 2H and 3R polytypes, respectively. The stacking orders are as follows: 1T - AbC; (space group $P\bar{3}m1$); 2H - AbA BaB and 3R - AbA BcB CaC. 1T is paramagnetic with no band gap (metallic), while both 2H and 3R are diamagnetic and they have almost same value of fundamental indirect band gaps. 2H polytype is the most abundant in the earth's crust, which is another advantage to it being the most stable polytype, hence, making its' study worthwhile. From Table 2.1, it's clear that MoS_2 electrode can withstand high temperatures before decomposing, as well as being able to operate properly with acid based electrolytes without the danger of corrosion.

2.3 Extraction and Purification Procedure of MoS_2

Fig. 2.1, shows typical extraction and purification procedure of MoS_2 from the molybdenite ore down to pure crystalline substance, available in the market.

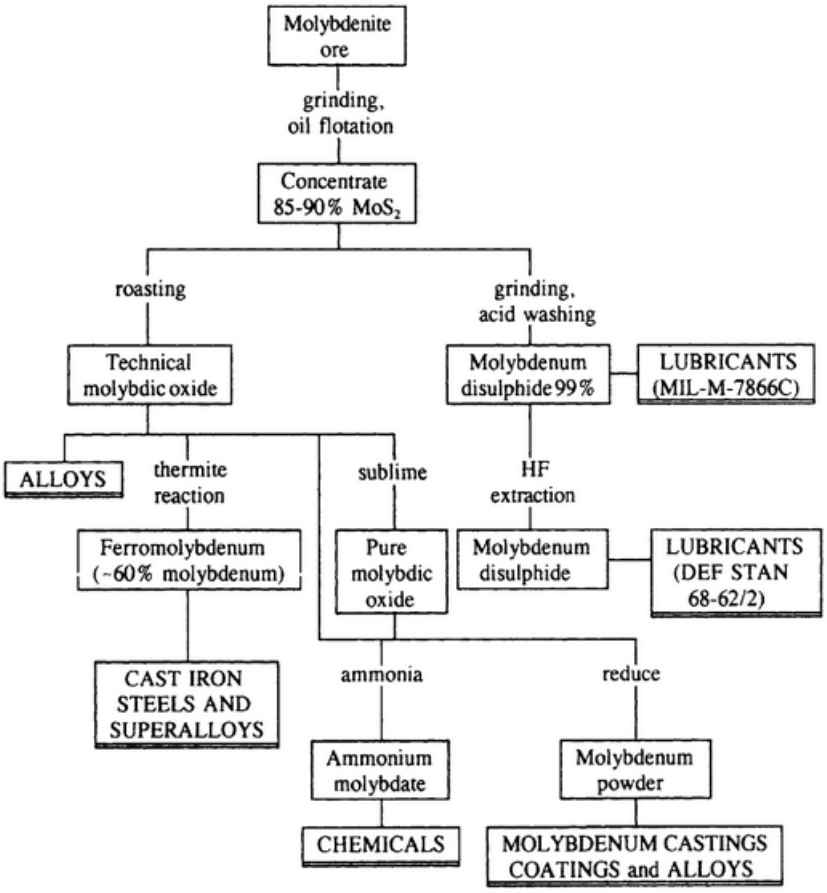

Figure 2.1: Flow chart of molybdenite processing [37].

Molybdenite is the principal ore for molybdenum disulphide [38]. HF in Fig. 2.1 is hydrogen fluoride.

2.4 Research Review

This section reviews previous research works, that are in line with the goals of this study. To this end; mechanical, electronic and optical properties that have been reported, are of major concern in the search for a robust electrode material for use in supercapacitors or/and batteries.

2.4.1 Mechanical Properties

A lot of studies have been done on MoS_2 mechanical properties, both experimental and through theoretical simulations [39–41]. Studies of mechanical properties are crucial in determining the suitability

of material applications on flexible devices. Density functional theory (DFT) calculations, reported 210 GPa Youngs modulus of MoS_2 [40], while the atomic force microscope (AFM) calculated the stiffness of about 330 GPa [42]. The computed Youngs modulus of MoS_2 for a few layers is estimated to 270 ± 100 GPa [43]. Shear modulus of MoS_2 has been determined to be around 184 GPa [43, 44]. Contact stress of ≈ 730 MPa have also been reported [45].

These prominent mechanical properties of MoS_2, including both high flexibility and strength, make it a promising candidate for elastic energy storage for clean energy. The strain energy of the unit cell is 9.52 eV, which is 1.06 eV per atom. Taking the height of 6.5 Å from the experimental value, [43] its' energy storage capacity is 8.8 $MJ{\cdot}L^{-1}$, which is about one order of magnitude larger than rechargeable Li-ion batteries. Also for specific energies, MoS_2 which is 476 $W{\cdot}h{\cdot}kg^{-1}$, is larger than that of Li-ion battery reported as 180 $W{\cdot}h{\cdot}kg^{-1}$ and carbon nanotubes quoted as 10 $W{\cdot}h{\cdot}kg^{-1}$ [46].

Since the energy storage in MoS_2 is in the form of elastic energy through strains, it is environmentally friendly as no chemical process is involved [47]. The reversible elastic deformations make it possible to be recharged many times, implying a longer lifetime. More than a million torsional and tensile impelled cycles have been demonstrated in torsional motors. This elastic energy storage could meet the demand for modern electronic devices [48].

2.4.2 Electronic Transport Properties

Charge mobility is to a great extent, influenced by morphology and chemical structure. Several methods have been used to measure charge mobility. They include; time of flight, pulse radiolysis and field effect transistor (FET) measurements. These different experimental techniques seldom give the same order of magnitude for the mobility. Pulse radiolysis measures the local mobility and thus focuses on the neighbouring pairs with the best coupling, time of flight measures the bulk mobility heavily influenced by traps and defects while FET measurements depend on the device structure and interfaces between different layers [49, 50]. However, they are all useful for computer simulated results comparison.

The experimental measurements on single-layer MoS_2 transistors showed room-temperature electron mobility of at least 200 $cm^2{\cdot}V^{-1}{\cdot}\ s^{-1}$, similar to that of graphene nanoribbons, and a room-temperature current on/off ratio up to 1×10^8. Theoretical studies have reported an electronic mobility of about 320 $cm^2{\cdot}V^{-1}{\cdot}\ s^{-1}$, with the longitudinal acoustic phonon showing the highest scattering rates at room temperature, for electron-phonon coupling effects [51]. MoS_2 nanotubes (NTs) are also semiconduc-

tors, as predicted by tight-binding (TB) method and density function theory (DFT), with more complex electronic structures and a band gap smaller than that of monolayer MoS_2 [52, 53]. Due to their many unique properties, some nano-materials and electronic devices based on transition metal chalcogenides (TMC) NTs, have been generating great interest to scientists [54–56]. However there are few reports on the mobility in TMC NTs; which is the core for microelectronic semi-conducting materials.

In order to investigate the mobility in MoS_2 NTs, a study of the effect of phonon with first principles calculations using a density-function-based approach, showed a hole mobility of 740 $cm^2 \cdot V^{-1} \cdot s^{-1}$. This was higher than that of electron mobility. This suggests that the MoS_2 NTs stands a good chance to be considered for electronic devices.

MoS_2 is an n-type semiconductor and in any attempt to study its current-voltage (I-V) characteristics, the metal contacts need to be chosen guided by the Schottkey barrer (Φ_B). The work-function (Φ_M) of the material plays an important role in determining the metal to use for the contacts. MoS_2 with an electron affinity χ of 4.0 e V [57, 58], studies done on the best choice of metal contact, revealed a metal whose Φ_M is higher than the χ of MoS_2, conducts more current compared that with a lower one. This can be summarized as shown in Table 2.2 and Fig. 2.2.

Table 2.2: Performance summary of different metal/2D MoS_2 contacts [59, 60].

Metal	Work function, Φ_M (eV)	Schottky barrier height, $\Phi_B = \Phi_M - \chi$ (eV)	Current at +2 V bias (μA)
Al	4.5	0.5	91.9
W	5.1	1.1	38.7
Au	5.4	1.4	22.5
Pt	5.7	1.7	17.3

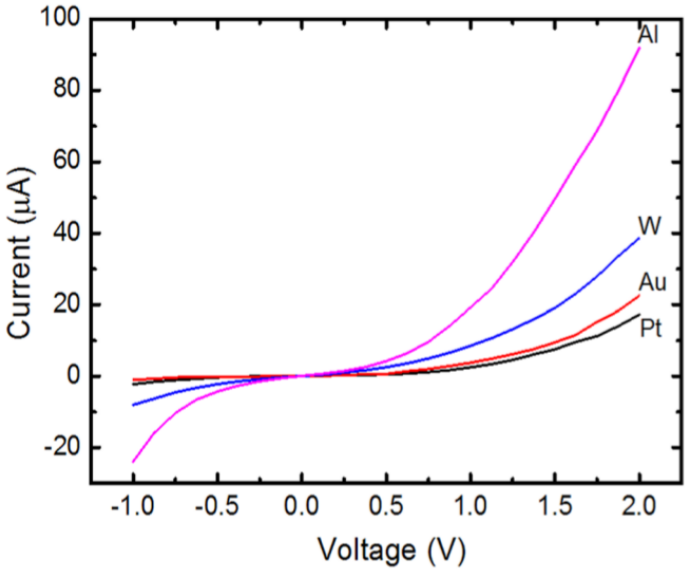

Figure 2.2: I-V characteristics for different metal/MoS_2 contacts under identical bias conditions [60].

2.4.3 Optical Properties

Other studies have reported that a monolayer (~6.5 Å) of MoS_2 is transparent in the visible wavelength range, and has a direct band gap of about 1.8 eV, while bulk MoS_2 has an indirect band gap of around 1.2 eV. The direct band gap increases the efficiency needed for photogeneration and recombination, which makes single-layered MoS_2 a preferred material for future optoelectronic devices such as solar cells among others [61–63].

MoS_2 Raman peak spacing of ~19.6 cm^{-1} from the out-of-plane A_g^1 (404.8 cm^{-1}) and in-plane E_{2g}^1 (385.2 cm^{-1}) peaks have been reported [64, 65]. Other weak vibrational modes, E_{2g}^1 (33 cm^{-1}) and E_g^1 (287 cm^{-1}) were reported [66]. The effect of laser lines used in the Raman spectroscope, to identify peak positions, as reported in references [64, 67]; have differences within 0.01% cm^{-1}. A peak at 440 cm^{-1}, has been reported and it is attributed to oxygen attacking Mo-S-Mo bonds and attaching itself at the edges of ultra-thin MoS_2 due to presence of the dangling bonds. These Raman peaks have shown to be affected by the number of layers, as shown in Fig. 2.3. E_{2g}^1 shifts to the left while A_g^1 moves to the right as the number layers increase. This leads to widening in the Raman peaks' separation distances.

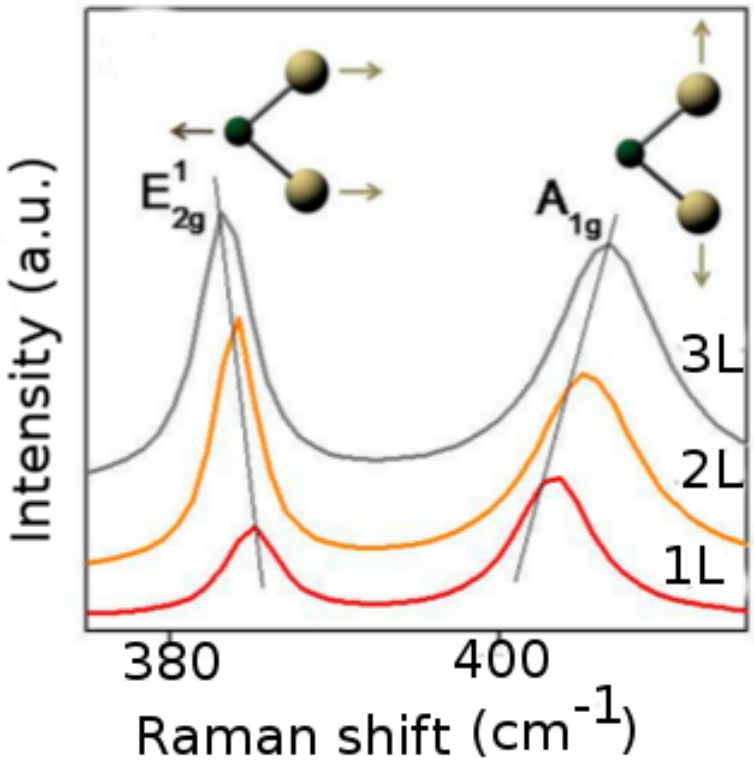

Figure 2.3: Raman spectra of single-layer 1L, double-layer 2L, and triple-layer 3L MoS_2 [68].

Temperature increase has shown to have similar Raman peak shifts that are dependent on number of layers. This is illustrated in Fig. 2.4. This was achieved using a focused laser beam of $\lambda = 514$ nm, with

power input of 0.17 mW. Unlike in Fig. 2.3, the Raman shifts show a decrease at both E^1_{2g} and A^1_g modes in Fig. 2.4.

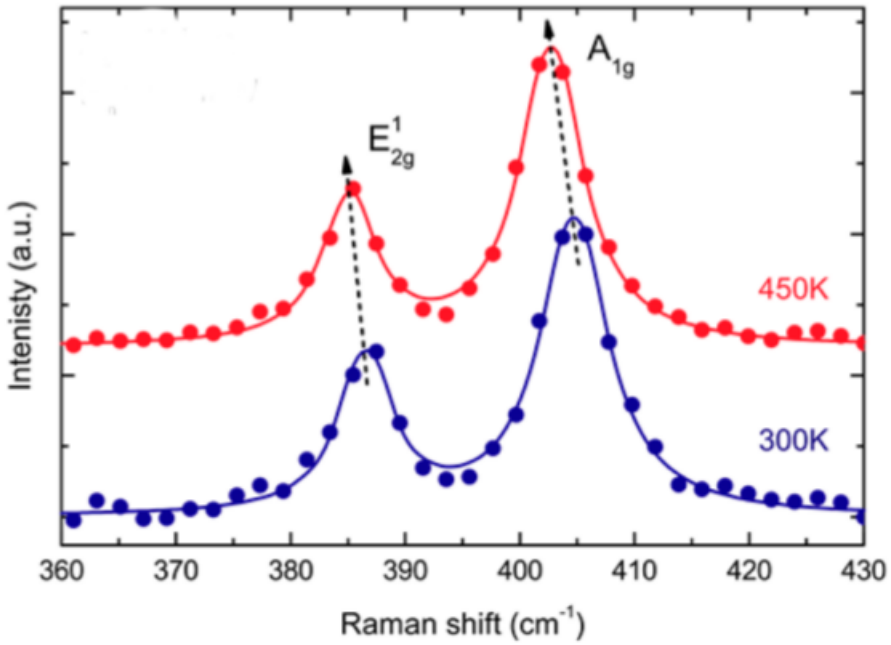

Figure 2.4: Raman spectra of MoS_2 monolayer at 300 K and 400 K [69].

Optical reflectivity peaks of 2H-MoS_2 and 3R-MoS_2 bulk, were reported to occur between 1.8 eV and 2.0 eV and they correspond to lower and higher energy excitonic transitions [68]. In bulk MoS_2, these peaks are very small compared to those prominent absorption peaks in monolayer, at 670 nm and 627 nm corresponding to two resonances excitons A1 and B1 [70]. They are associated with the direct excitonic transitions energy. This unusual luminescence behaviour is attributed to the direct band gap shown in a monolayer of MoS_2. Also, the photoluminescence increases with decrease in layer thickness.

MoS_2 monolayer photoluminescence is an intrinsic material property and not as a result of external perturbations such as defect states, since the luminescence resonances match perfectly the direct excitonic transitions [71]. Luminescence quantum efficiency η_l from such direct excitonic state in MoS_2 can be approximated as;

$$\eta_l \approx k_{rad}/(k_{rad} + k_{defect} + k_{relax}), \tag{2.1}$$

where k_{rad}, k_{defect}, and k_{relax} are; rates of radiative recombination, defect trapping, and electron relaxation within the conduction and valence bands, respectively. Since the rate of intraband relaxation to band minimum is extremely high, photoluminescence from direct excitonic transitions is normally not observable in indirect bandgap semiconductors [72, 73]. In monolayer MoS_2, k_{rad} is not likely to change appreciably with respect to bulk value, because the direct excitonic transitions remain at the same energy. Therefore, the enhanced photoluminescence in monolayer is attributed to the slower elec-

tronic relaxation k_{relax} unlike in the bulk MoS_2. The decrease of interband relaxation rate suggests a substantial change in MoS_2 electronic structure when moving from the bulk to monolayer [74].

The Fig. 2.5 is a clear illustration of how the number of layers affect photoluminescence peaks in MoS_2.

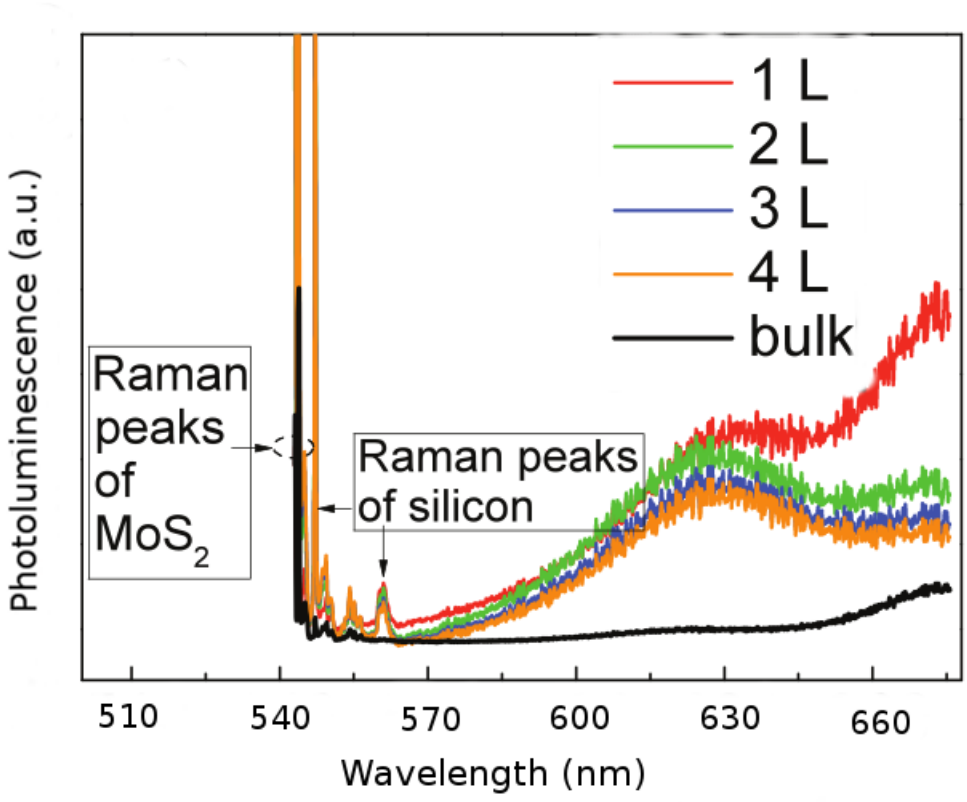

Figure 2.5: Photoluminescence intensity with respect to number of layers [67].

MoS_2 Raman intensity I_{Raman} and luminescence intensity I_l are affected in the same manner by effects such as laser excitation intensity, quantity of material, and local electric field factors; therefore such external effects are canceled out in the ratio I_l / I_{Raman}, which is the Raman efficiency η_{Raman} and it provides a measure of intrinsic luminescence quantum efficiency through the material. Hence;

$$\eta_l \approx \eta_{Raman}. \tag{2.2}$$

In equation (2.2), the small energy difference between luminescence and Raman scattered photons are neglected. Since Raman scattering efficiency η_{Raman} has minimal dependence on layer thickness, the photoluminescence spectra normalized by Raman intensity, directly reflects the luminescence efficiency η_l. This leads to the high luminescence quantum efficiency observed in MoS_2 monolayer [72].

2.5 MoS_2 Modern Applications

This section reviews some of the frontier researches on new applications of MoS_2. Since the discovery of MoS_2, it has been used as a solid state lubricant. However, this is fast changing and it is being introduced in semiconductor Physics.

Electronic and optoelectronic devices like; field-effect transistors (FET), sensors and photodetectors have been made using a few-layers of MoS_2. Their performance showing promising potential to replace conventional silicon based electronics. Multi-stage integrated circuits and logic using MoS_2 have also been reported, and they exhibit efficacy for complex digital logic and high-frequency alternating current (ac) applications [75].

Wang H. *et al.* [75], reported having made a seamless integration circuit that uses both depletion mode (D-mode) and enhancement-mode (E-mode) to fabricate MoS_2 transistors, with current saturation on/off ratio $> 10^7$ and a current density of $> 23\mu A/\mu m$. This suggests that MoS_2 logic gates, a ring oscillator operating at 1.6 MHz, and memory elements perform better than silicon-base ones. However, it is opined that defects and interface engineering is the way to go in the quest to improving MoS_2-based device output, since defect concentration increases charge (electron) transportation. Temperature increase has also been reported to greatly reduce phonon mobility and thus should be factored in, in this endeavour [76, 77].

Platinum (Pt) has been in use as a counter electrode material due to its good electrical conductivity which facilitate electrons transportfrom an external circuit with ease. However, the use of Pt is inhibited by its high cost and also the availability. In an attempt to address this Pt challenge, studies to make an electrocatalytic counter electrode using nanosheets of MoS_2 in dye-sensitized solar cells (DSSC), have been carried out and the reports are tabulated in Table 2.3. The performance efficiency of conventional Pt is shown alongside that MoS_2 or composite of MoS_2 with carbon-based materials, as per study. An additional study on lithium-ion batteries (LiBs) with MoS_2 counter electrode has also been included in Table 2.3.

From Table 2.3, its clear that MoS_2 is carving a niche in this field of application and what needs to be done is to enhance the reported counter (auxiliary) electrode efficiencies.

Research on the possibility of MoS_2 being used as an electrode material in lithium ion batteries have been done, with Liu *et al.* [90], reporting restacked MoS_2 electrodes exhibiting high reversible lithium storage capacity and superior rate capability, which were attributed to MoS_2 four-electron transfer capability of 669 $mA{\cdot}h{\cdot}g^{-1}$.

Table 2.3: Recent reports on the DSSCs and LiBs with MoS_2-based counter electrodes.

Material	Efficiency $\eta\%$
MoS_2 powder	7.59 (Pt:7.64) [78]
MoS_2/graphene flake	5.98 (Pt:6.23) [79]
MoS_2/reduced graphene oxide	6.04 (Pt:6.38) [80]
MoS_2/multi-walled carbon nanoutbes	6.45 (Pt:6.41) [81]
MoS_2/graphene nanosheet	5.81 (Pt:6.24) [82]
MoS_2/carbon	7.69 (Pt:6.74) [83]
MoS_2/carbon nanotubes	7.92 (Pt:7.11) [84]
MoS_2 nanoparticles	5.41 (Pt:6.58) [85]
Porous MoS_2 sheets	6.35 (Pt:6.19) [86]
MoS_2 film	7.01 (Pt:7.31) [87]
MoS_2/single-walled carbon nanoutbes	8.14 (Pt: 7.78) [88]
MoS_2/Li for lithium-ion batteries	98 (Coulombic efficiency) [89]

Synthesised mesoporous (pores of diameter between 2nm and 50 nm) MoS_2 electrode materials have been reported, with the following attributes: allowing liquid electrolyte easy diffusion, which leads to reduced diffusion length in the bulk of an electrode material. The large surface area increases the interface contact area between electrode and electrolyte, resulting to a faster transport channels for lithium ions and enhanced space for volume change during the discharge and charge processes. These mesoporous MoS_2 electrode in lithium ion battery showed great improvement in reversible capacity 630 $mA{\cdot}h{\cdot}g^{-1}$, with great cycling performance achieved at working voltages of between 0.01 V to 3.0 V, at a current rate of 0.05 C [91].

CHAPTER THREE

THEORY

This chapter gives some insight into computational tools that were employed in this study, in an effort to simulate defects in MoS_2. The chapter demonstrates the complementary nature of density functional and Boltzmann transport theories, as used here.

3.1 Density Functional Theory (DFT)

The Schrödinger equation that describes the evolution of a system of electrons and ions given by Equation 3.1[92, 93], which is also the basis of DFT.

$$i\hbar\frac{\partial\Phi(\mathbf{x},\mathbf{R},t)}{\partial t} = -\frac{\hbar^2}{2m}\nabla^2\Phi(\mathbf{x},\mathbf{R},t) + V\Phi(\mathbf{x},\mathbf{R},t), \tag{3.1}$$

where m is the mass of the electron, $\mathbf{x}$ is the set of all electronic positions relative to protons, $\mathbf{R}$ is the centre of mass, $\Phi(\mathbf{x},\mathbf{R})$ is the all-ion all-electronic wave function, and V is the potential. The energy states important for band structures, are stationary waves, hence, time independent. This situation is best described by the introduction of a time-independent Schrödinger equation. To achieve this, Equation 3.1 is split into temporal and spatial wave functions as follows: $\Phi(\mathbf{x},\mathbf{R},t) = \Phi(\mathbf{x},\mathbf{R})\varphi(t)$; which is leads to separation variables [94]. The resulting time-independent Schrödinger equation can then be written as shown by Equation 3.2 [92];

$$[T_N + T_e + V_{ee}(r) + V_{NN}(\mathbf{R}) + V_{Ne}(\mathbf{r},\mathbf{R})]\Phi(\mathbf{x},\mathbf{R}) = E\Phi(\mathbf{x},\mathbf{R}), \tag{3.2}$$

where $\mathbf{r}$ is the electrons coordinates, $\mathbf{R}$ is the nuclei coordinates and E is the total energy. The left side of Equation 3.2 forms the energy operator (Hamiltonian), since T_N is the kinetic energy of nuclei, T_e is kinetic energy of electrons, $V_{ee}(\mathbf{r})$ is the electron-electron potential, $V_{NN}(\mathbf{R})$ being nucleus-nucleus potential and V_{Ne} is nucleus-electron potential. Using the Hamiltonian operator H, Equation 3.2 can then be re-written as [92, 93];

$$H\Phi(\mathbf{x},\mathbf{R}) = E\Phi(\mathbf{x},\mathbf{R}) \tag{3.3}$$

where,

$$H = \sum_{I=1}^{N}\frac{\mathbf{PI}^2}{2M_I} + \sum_{i=1}^{N_e}\frac{\mathbf{Pi}^2}{2m_i} + \sum_{i>j}\frac{e^2}{|\mathbf{r_i}-\mathbf{r_j}|} + \sum_{I>J}\frac{Z_I Z_J e^2}{|\mathbf{R_I}-\mathbf{R_J}|} - \sum_{i,I}\frac{Z_I e^2}{|\mathbf{R_I}-\mathbf{r_i}|} \tag{3.4}$$

and

$$\mathbf{P} = -i\hbar\nabla \tag{3.5}$$

$\mathbf{P}$ is the electron momentum operator, M_I and m_i are ion and electron masses respectively, e is the electron charge and Z is the charge of an ion in terms of electron charge.

The nuclear and electronic motions in Equation 3.2 are then decoupled by applying Born-Oppenheimer approximation due to their difference in time-scale. This leads to $H\Psi = E\Psi$, whose general solution are eigenvectors $\Psi_0, \Psi_1, \Psi_2, ...\Psi_2$ and eigenvalues (energy states) $E_0, E_1, E2, ...E_N$. The eigenvector with the lowest energy is the ground state wave function [92].

Using the special Ansatz of a Slater determinant for all-electron ground state wave function $\Psi_0(\mathbf{r})$, corresponding to a mapping on a non-interacting reference systems shown in Equation 3.6, the Slater determinant consists of Ne one-electron wave functions (one-electron orbitals). This Ansatz is only justified if the corresponding one-particle equations are corrected by exchange and correlation potentials, which correct for the fact that the proper ground state of a many-electron system is linear combination of Slater determinants.

$$\Psi(\mathbf{r}) = \frac{1}{\sqrt{N!}} \begin{bmatrix} \psi_1(\mathbf{r_1}) & \psi_1(\mathbf{r_2}) & \dots & \psi_1(\mathbf{r_{N_e}}) \\ \psi_2(\mathbf{r_1}) & \psi_2(\mathbf{r_2}) & \dots & \psi_2(\mathbf{r_{N_e}}) \\ \vdots & \vdots & \ddots & \vdots \\ \psi_{Ne}(\mathbf{r_1}) & \psi_{Ne}(\mathbf{r_2}) & \dots & \psi_{Ne}(\mathbf{r_{N_e}}) \end{bmatrix}. \tag{3.6}$$

The above approach is computationally demanding and expensive; which led to Kohn and Sham to formulate Equation 3.7, which is the bases of DFT. It follows from a variation principle, which supposes the existence of a universal ground state functional depending on the charge density, which is expanded into the one-particle states of the Slater determinant [95].

$$\left[-\frac{\hbar^2}{2m}\nabla^2 + V(\mathbf{r}) + V_H(\mathbf{r}) + V_{XC}(\mathbf{r})\right]\psi_i(\mathbf{r}) = \varepsilon_i\psi_i(\mathbf{r}, \tag{3.7}$$

where V_H is the Hartree potential that involves the electron-electron potential, V_{ee} and is given by Equation 3.8.

$$V_H(\mathbf{r}) = e^2 \int \frac{n(\mathbf{r}')}{|\mathbf{r} - \mathbf{r}'|} d^3r', \tag{3.8}$$

V_{XC} is the exchange-correlation potential, calculated from the first derivative of exchange correlation energy, E_{XC}, with respect to density as shown in Equation 3.9.

$$V_{XC}(\mathbf{r}) = \frac{\delta E_{XC}(\mathbf{r})}{\delta n(\mathbf{r})} \tag{3.9}$$

Since Equation 3.7 gives only an approximation to the actual solution of the Schrödinger equation, advanced functionals, that factor in local density and local gradient in the electron density are employed. They are commonly referred to as generalized gradient approximation (GGA) [96]. Different types of GGA have been developed, but in this study Perdew-Burke-Ernzerhof (PBE) [96] functionals were used since they are suitable for solids.

In DFT, the ground state density of the electrons is a function of the orbitals, which leads to Equation 3.7 be solved iteratively until the solution is self-consistent for all orbitals. The resulting electronic density is then calculated through Equation 3.10 and the whole scheme is repeated until a self-consistent solution is obtained [92].

$$n_{KS}(\mathbf{r}) = n(\mathbf{r}) = 2\sum_{i} \psi_i^*(\mathbf{r})\psi_i(\mathbf{r}) \tag{3.10}$$

For solids, this leads to self-consistent orbitals and energies, for k-points in the 1^{st} Brillouin zone, which together form the band structures $\epsilon_{n(\mathbf{k})}$. Here $\mathbf{k}$ is the pseudo-momentum of the Bloch state, defined by the electrons in a crystalline solid occupying certain states corresponding to the eigenvalue $\epsilon_{n(\mathbf{k})}$. Each k-point is expanded in terms of a discrete plane-wave basis set and plane waves with small kinetic energies are the only ones considered by applying a cut-off energy relevant to a given system.

The k-points (high symmetry points in the Brillouin zone) for a DFT simulation of lattice are increased until a convergency of the total energies is achieved as shown in Figs. A.1, A.2 and A.4 in Appendix A.

3.2 Boltzmann Transport Theory (BoltzTrap)

Boltzmann transport theory is based on a microscopic model for macroscopic quantities such as mobility, electronic conductivity, thermal conductivity, Seebeck coefficient, diffusion coefficient [97], to list but a few. It was used in this study to obtain electronic and transport properties of MoS_2. In this section, a reviewed of the theory and the derivation of Boltzmann transport equation (BTE) is discussed based on Rodes iteration method for solving BTE for perturbation and carrier distribution [98].

The BTE takes into account three main mechanisms through which the distribution may be changed. These are: carriers' diffusion, external forces and inelastic scattering processes. These are represented in the general BTE in Equation 3.11 [93, 99];

$$\frac{df(\mathbf{k},T,t)}{dt} = (\frac{\partial f(\mathbf{k},T,t)}{\partial t})_s - \frac{d\mathbf{k}}{dt}\cdot\nabla_k f(\mathbf{k},T,t) - \nu(\mathbf{k})\cdot\nabla_r f(\mathbf{k},T,t), \tag{3.11}$$

where $f(\mathbf{k},T,t)$ is the distribution function at $\mathbf{k}$, temperature T, and time t. $(\frac{\partial f(\mathbf{k},T)}{\partial t})_s$ is the temporal rate of change of f due to all scattering processes. $\frac{d\mathbf{k}}{dt}\cdot\nabla_k f(\mathbf{k},T,t)$ is caused by external forces $\mathbf{k}$ and $\nu(\mathbf{k})\cdot\nabla_r f(\mathbf{k},T,t)$ is the diffusion term from carrier density gradient. $\nu(\mathbf{k})$ is the group velocity of electrons, given by Equation 3.12;

$$\nu(\mathbf{k}) = \frac{\nabla_k \varepsilon(\mathbf{k})}{\hbar}. \tag{3.12}$$

In the presence of a weak electric field and under steady state conditions, $f(\mathbf{k},T,t)$ becomes $f(\mathbf{k},T)$, $\frac{df(\mathbf{k},T,t)}{dt} = 0$ and $\frac{d\mathbf{k}}{dt}$ can be substituted by $\frac{e\mathbf{E}}{\hbar}$ [93]; reducing Equation 3.11 to Equation 3.13 [100];

$$\nu(\mathbf{k})\cdot\nabla_r f(\mathbf{k},T) + \frac{e\mathbf{E}}{\hbar}\cdot\nabla_k f(\mathbf{k},T) = \int [s(\mathbf{k}',\mathbf{k})f(\mathbf{k}',T)(1-f(\mathbf{k},T)) - s(\mathbf{k},\mathbf{k}')f(\mathbf{k},T)(1-f(\mathbf{k}',T))]d\mathbf{k}', \tag{3.13}$$

where $s(\mathbf{k},\mathbf{k}')$ is the differential scattering rate from the state k' to the state characterized by $\mathbf{k}$ and $\mathbf{E}$ is the electric field.

Equation 3.13 is then iteratively solved after which $f(\mathbf{k},T)$ and $f(\varepsilon,T)$ are converted to each other by solving the Kohn-Sham equation for $\varepsilon(\mathbf{k})$. This is achieved through setting a fixed potential or by applying a non-self consistent calculation approach. The transport properties are obtained from the conductivity tensor and the distributions functions given by Equations 3.14, 3.15 and 3.16 [101].

$$\sigma_{\alpha\beta}(T;\mu) = \frac{1}{\Omega}\int \sigma_{\alpha\beta}(\varepsilon)\left[-\frac{\partial f_\mu(T;\mu)}{\partial\varepsilon}\right]d\varepsilon, \tag{3.14}$$

$$\kappa\alpha\beta(T;\mu) = \frac{1}{e^2T\Omega}\int \sigma_{\alpha\beta}(\varepsilon)(\varepsilon-\mu)^2\left[-\frac{\partial f_\mu(T;\mu)}{\partial\varepsilon}\right]d\varepsilon, \tag{3.15}$$

$$S\alpha\beta(T;\mu) = \frac{(\sigma^{-1})\gamma\alpha}{eT\Omega}\int \sigma_{\gamma\beta}(\varepsilon)(\varepsilon-\mu)\left[-\frac{\partial f_\mu(T;\mu)}{\partial\varepsilon}\right]d\varepsilon, \tag{3.16}$$

where $\sigma_{\alpha\beta}$, $\kappa\alpha\beta$ and $S\alpha\beta$ are the electrical conductivity, electronic thermal conductivity and ther-

mopower, respectively. μ is the chemical potential. The projected energy conductivity $\sigma_{\alpha\beta}(\varepsilon)$ is defined as [101];

$$\sigma_{\alpha\beta}(\varepsilon) = \frac{1}{N}\sum_{i,k}\sigma_{\alpha\beta}(i,k)\frac{\sigma(\varepsilon-\varepsilon_{i,k})}{d\varepsilon}, \tag{3.17}$$

with

$$\sigma_{\alpha\beta}(i,k) = e^2\tau_{i,k}\nu_\alpha(i,k)\nu_\beta(i,k), \quad \nu_\alpha(i,k) = \frac{1}{\hbar}\frac{\partial\varepsilon_{i,k}}{\partial k_\alpha}, \tag{3.18}$$

where τ is the electronic relaxation time and ν_α is the group velocity; which is calculated from the band structure $\varepsilon_{i,k}$. It is obviously proportional to velocity-velocity autocorrelation function. Since the electronic scattering is taken to be independent of energy, the transport properties may easily be integrated within the BoltzTraP code [101].

The electronic specific heat c and Pauli magnetic susceptibility χ are computed as shown in Equation 3.19 and Equation 3.20 [102];

$$c(T;\mu) = \int n(\varepsilon)(\varepsilon-\mu)\left[\frac{\partial f_\mu(T;\varepsilon)}{\partial T}\right]d\varepsilon. \tag{3.19}$$

$$\chi(T;\mu) = \mu_0\mu^2 B\int n(\varepsilon)\left[-\frac{\partial f_\mu(T;\varepsilon)}{\partial\varepsilon}\right]d\varepsilon, \tag{3.20}$$

where B is the magnetic field tensor and $n(\epsilon)$ is the density of states.

3.3 Summary

The above theories were employed in this study for the computational analysis of the band structure MoS_2 and the results obtained using this approach are reported in Chapter 5. The DFT output, with a dense k-point set, was used as the input for the BoltzTrap programme.

CHAPTER FOUR

METHODOLOGY

This Chapter outlines various techniques used to study and characterise molybdenum disulphide used in this study.

4.1 Introduction

To study a given material, knowledge of its crystalline structure is prerequisite. In this study simulations were done first using the following softwares; Density functional theory (DFT), Boltzman transport properties (BoltzTraP) and stopping and range of ion in matter (SRIM). How these simulation technigues were used is discussed in Sections 4.2 and 4.3, and the theory behind them has been discussed in Chapter 3. After the simulations, the study switches to experimental work, and explores bulk crystalline MoS_2 and powder MoS_2. The MoS_2 crystalline sample had been purchased from HQ Graphene, G.Meirstraat 1, 9278TB - Netherlands while the powder MoS_2 was synthesised in the School of Chemistry at the University of the Witwatersrand, Johannesburg-South Africa. MoS_2 powder was synthesised as described in Chapter 6 which was used to compare the effects of ion implantation on crystalline MoS_2 and powder MoS_2, in terms of enhancement of energy storage capability upon ion irradiation.

Current-voltage (I-V) measurements, Raman spectroscopy (RS), photoluminescence spectroscopy (PL) and electrochemical analysis techniques were used to study the bulk crystalline MoS_2, as discussed in Sections 4.4, 4.5 and 4.7. The chacterisation of powder MoS_2 was performed using the following techniques; RS, Powder X-ray Diffraction (XRD), X-ray photoelectron spectroscopy (XPS), energy-dispersive X-ray spectroscopy (EDS), Scanning electron microscope (SEM), transmission electron microscopy (TEM), Brunauer-Emmett-Teller (BET), thermal gravimetric analysis (TGA) and electrochemical analysis and their details are discussed in Chapter 6. RS, XRD, XPS, EDS, SEM and TEM techniques were carried out to ensure that the synthesised powder was truly MoS_2.

4.2 DFT and BoltzTrap Simulations

In the DFT simulations, MoS_2-(2H) was used, which is a hexagonal structure. Its high symmetry points for the Brillouin zone are critical for computational purposes. Generally, the MoS_2 hexagonal structure has the following high symmetry points Γ, centre of the Brillouin zone; A, centre of a hexagonal face; H, corner point; K, middle of an edge joining two rectangular faces; L, the middle of an edge

joining a hexagonal and a rectangular face; and M, the centre of a rectangular face [103]. These are shown in Fig. 4.1.

The DFT modeling method was performed using quantum espresso (QE) [104] code. A supercell of 2 × 2 × 2 unit cells was modelled based on the six atoms unit cell for the hexagonal polytype (2H) of MoS_2. Defects were then introduced by either adding or removing atoms in the lattice. Mainly, either Mo or S atoms were added or removed except one case whereby a W atom was introduced in the MoS_2 lattice. Perdew-Burke-Ernzerhof (PBE) functionals [105], which are one of the generalised gradient approximation (GGA) functionals for exchange correlation energy (E_{XC}), were employed in the form of pseudopotentials, and plane wave basis set used. The system relaxation was first done with a convergence threshold set at 10^{-6} Ry (this is when the remaining interatomic forces were supposed to be zero). Thereafter, self consistent field (scf) were performed. Non-self consistent field (nscf) calculations followed, where the density of states (DOS) and projected density of states (PDOS) were calculated.

Boltzman transport properties (BoltzTraP) code [102], which depends on scf and nscf outputs from QE, was used to determine the thermal, conductivity and also electronic properties reported in Chapter 5.

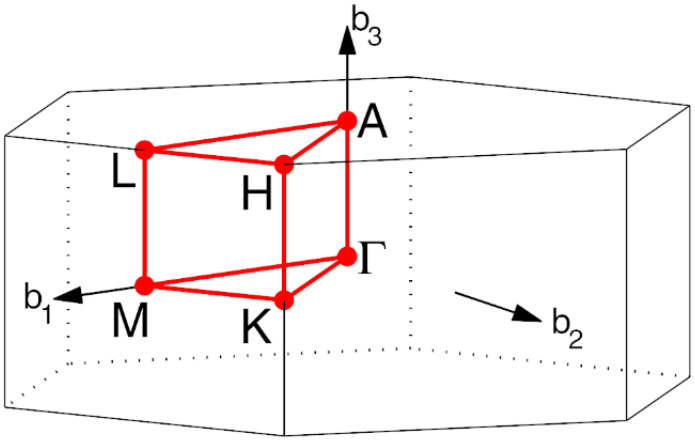

Figure 4.1: Schematic diagram of high symmetry points of hexagonal (2H) MoS_2.

As indicated in the band structure diagrams in Chapter 5, the path used is Γ-M-K-Γ-A-L-H-A|L-M|K-H.

4.3 SRIM Simulations

The experimental ion implantation was done at *i*Themba LABS (Gauteng, South Africa). However, prior to the actual implantantion, a simulation code that gives an idea of the ion distribution and approximates the penetration depth of implanted ion, referred to as the stopping and range of ion in matter

(SRIM) [106], was used.

Fig. 4.2 shows the damages and penetration range caused by Mo ions on MoS_2. The simulated defect(s) was an attempt to estimate the depth Mo ions are likely to penetrate a MoS_2 sample with the aim of creating most of the damages near the surface of the material. These ions were implanted by applying an implantation energy of 10 keV, with the target tilted at an angle of 7°. Similarly, W ions were also implanted and the simulation results are shown in Fig. 4.3. In both cases, a detailed calculation with full damage cascades were employed. Most of the damage is predicted to be from the surface to a depth of about 10 nm and the peak of the damage distribution at ≈ 4 nm. The two SRIM calculated damage and range distribution are comparable and hence adopted for the actual ion implantation in the study.

The deeper penetration of Mo ions as shown in Fig. 4.2 is attributed to its lower atomic size compared to that of W ions. This enables it to maneuver through MoS_2 easier than W atoms. However, due to W ions atomic mass and size, it causes higher degree damage in MoS_2 than Mo ions as shown in Fig. 4.3, in terms of vacancy/(Angstrom-ion).

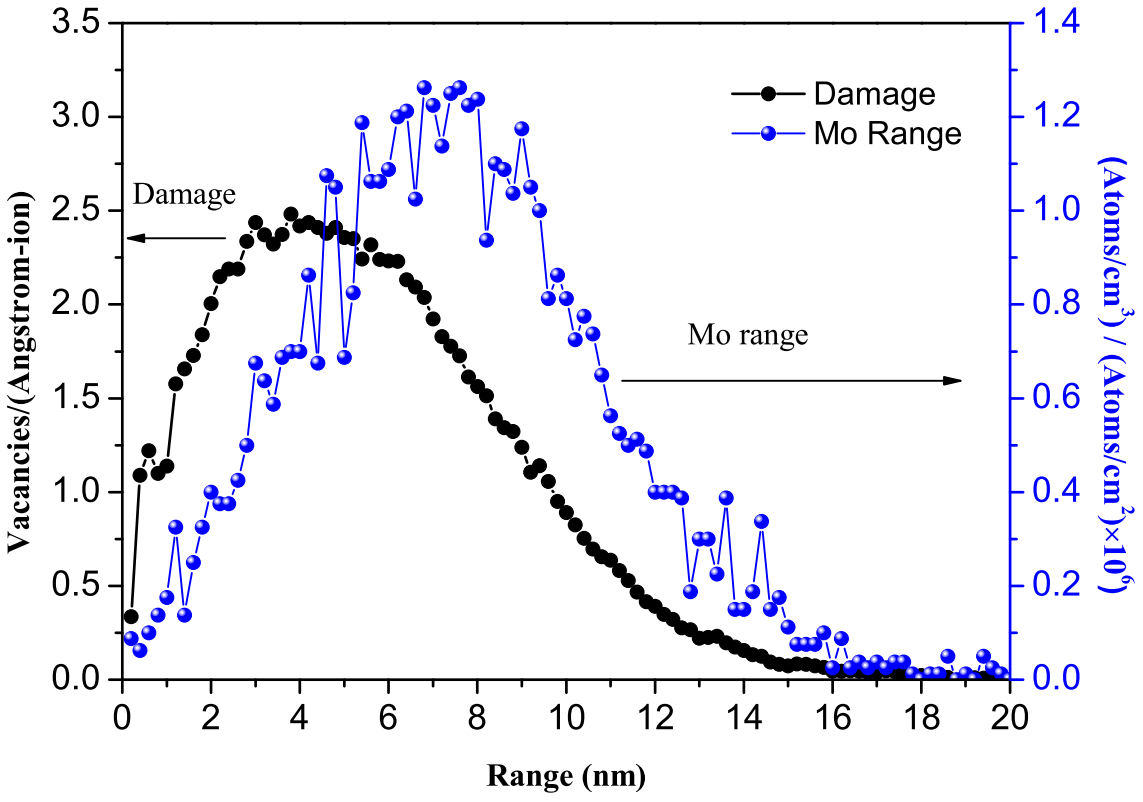

Figure 4.2: SRIM simulations for Mo ions.

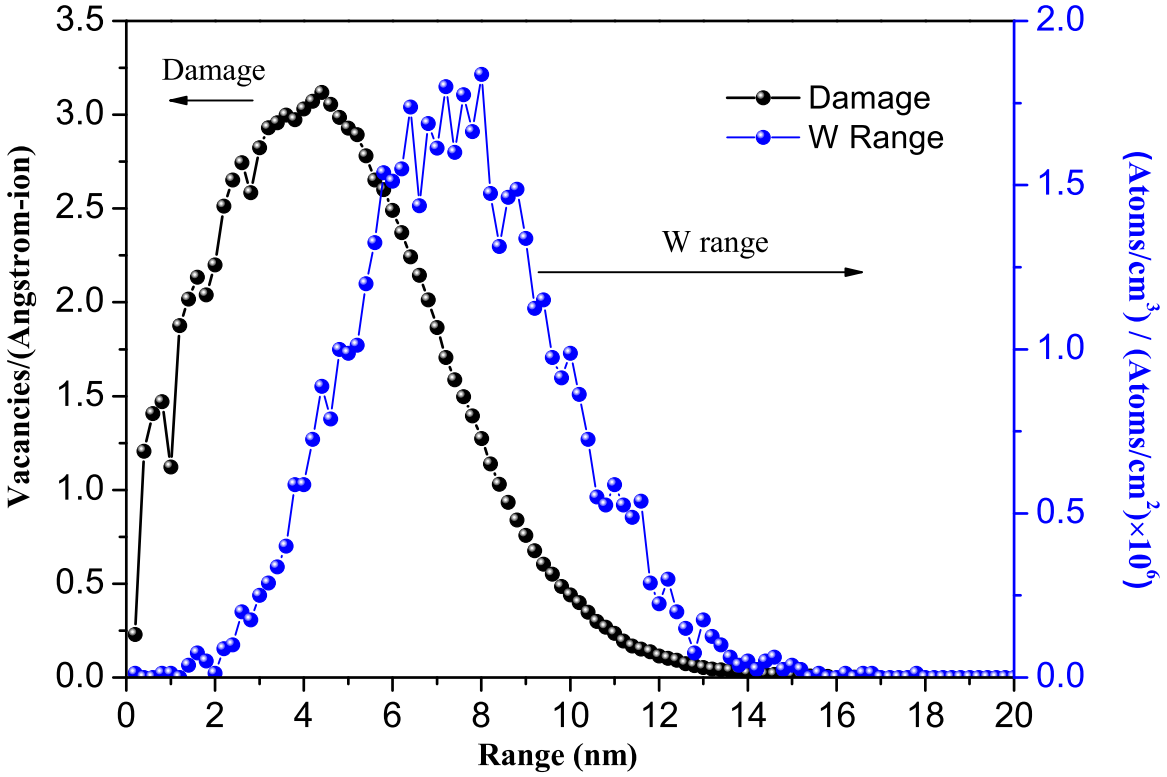

Figure 4.3: SRIM simulations for W ions.

4.4 Current-Voltage (I-V) Measurements

The I-V measurements were performed in the Thin Film Labs- Physics building using HP Model 4140B pA Meter/DC Voltage Source. The pico-Ampere meter has a basic accuracy of 0.5% over wide range (± 0.00110^{-12} - 1.999 10^{-2} A) which allows stable current measurement of 10^{-15} A per a count. This fast and stable (less than 35 ms at 1 nA) measurement technique is very useful for the measurement of the small outflow currents of semiconductor devices. The voltage sweeps were perform from +1V to -1V in steps of 0.01 V and they were analysed using LabVIEW-2010 software.

Prior to I-V measurements, the samples were cut into squares of approximately 3 mm sides. Contacts on MoS_2, were made by applying silver paste onto each of the four corners. Silver (Ag) proved to make Ohmic contacts with MoS_2 as reported in Chapter 5. Sheet resistance measurements were also performed in the Thin Film Labs. These measurements were done for both pristine MoS_2 and ion implanted samples of MoS_2. Fig. 4.4 shows how the four probe Ag contacts on MoS_2 samples were set. The measurements were then carried out by attaching the probing terminal diagonally onto the silver contacts. For instance when one probing pin was on silver contact labeled 1 while the other was connected to silver contact

labeled 4, and subsequently contacts 3 and 2 were probed.

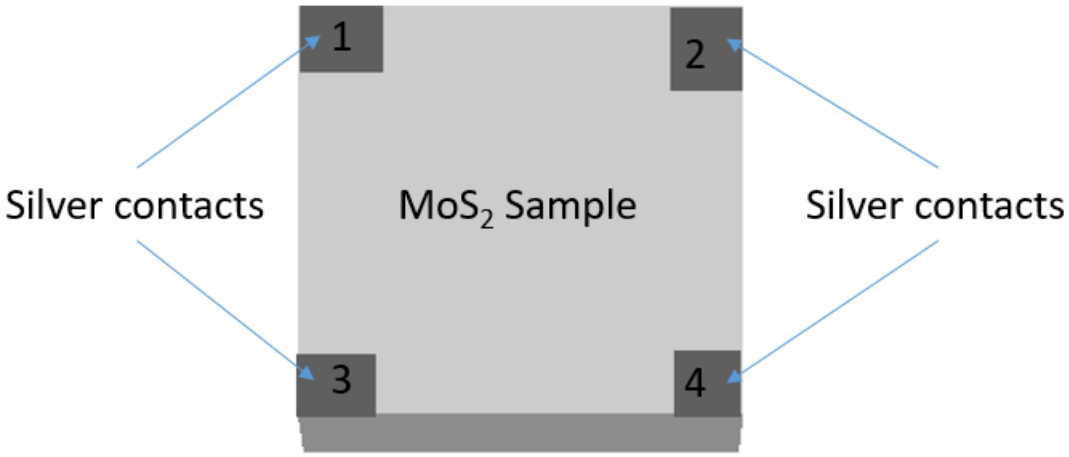

Figure 4.4: A schematic diagram showing Ag contacts on pristine MoS_2 sample.

4.5 Raman Spectroscopy

Raman spectroscopy (RS) and photoluminescence spectroscopy (PL) estimations were done before and after particle implantation in every one of the samples. Raman spectra were obtained utilizing the 514.5 nm line of a Lexel Model 95 SHG argon particle laser and a Horiba LabRAM HR Raman spectrometer outfitted with an Olympus BX41 magnifying lens joinment. The incident beam was engaged onto the sample with a 100× objective (N.A. = 0.90) and the backscattered light was scattered through a 600 lines for every mm grating onto a fluid nitrogen cooled charge coupled gadget (CCD) identifier. The information was captured utilizing LabSpec v5 software. Photoluminescence spectra were acquired at room temperature utilizing the same instrumentation, except that the grating was scanned over the range of 516 nm to 900 nm with the end goal to record the conceivable PL crests at longer wavelengths.

4.6 Ion Implantation

Ion implantation on MoS_2 was performed using the 200-20A2F ion implanter, based at *i*Themba LABS, Gauteng Province, South Africa. Square samples of sides ≈ 3 mm were cut using a scalpel, cleaned using acetone and later rinsed using ethanol. Each sample was then placed onto a teflon holder, whose aperture cross-sectional area was ≈ 6 mm^2, implying that the accessable implantation area for each sample was ≈ 6 mm^2. The implantation energy of 10 keV and a beam current of 0.02 µA, for all the samples were used. However, the fluences were varied for different sets of samples. Three MoS_2 samples were implanted with molybdenum ions, at fluences of 1×10^{14}, 1×10^{16} and 2×10^{16} ions/cm^2.

The other three samples were implanted with tungsten ions, at fluences of 1×10^{12}, 1×10^{14} and 1×10^{16} ions/cm^2. Table 4.1 is tabulated sample coding used throughout the experimental studies in Chapter 5.

Table 4.1: Ion-implantation parameters and abbreviations.

Sample label	Implanted Ions	Fluence (ions/cm^2)	Implantation Energy (keV)
Pristine	none	none	none
Mo-14	Mo	1×10^{14}	10
Mo-16	Mo	1×10^{16}	10
Mo-2e16	Mo	2×10^{16}	10
W-12	W	1×10^{12}	10
W-14	W	1×10^{14}	10
W-16	W	1×10^{16}	10

The elemental composition of each sample were that of MoS_2 plus the ion implanted.

4.7 Electrochemical Measurements and Analysis Software

Electrochemical measurements and analysis were performed at the Electrochemistry Unit, using the VMP 300 potentiostat, driven by EC-Lab-v11.01 software. It is housed in Gate House- Chemistry Department, at The University of the Witwatersrand. The assembly was done as shown in Fig 4.5. Figure 4.5a shows the screen-printed electrode (DS 110) used and it comprises of silver/silverchloride (Ag/AgCl) reference electrode labeled R, a carbon working electrode labeled W (where the samples were attached using silver paste) and a carbon counter electrodes labeled C. Figure 4.5b shows the screen-printed electrode plus the sample immersed in 1M of sodium sulphate (Na_2SO_4), which was the electrolyte used in this study. The other component with three pin (blue, red and yellow) is the screen-printed electrode holder, the blue pin as R, red pin is W and the yellow pin as C. These were then connected to the potentiostat as shown in Fig. 4.5c. Figure 4.5d shows the data storage facility and the monitoring screen, in that respect.

Figure 4.6 show the setup of the swagelok electrochemical cell used to test the MoS_2 powder-based electrodes, discussed in Chapter 6. This replaced the screen printed electrode that was used to test electrochemical performance for bulk MoS_2 electrodes, as shown in Fig. 4.5 (b). The rest the setup remained intact (i.e. Fig. 4.5 (c) and (d)).

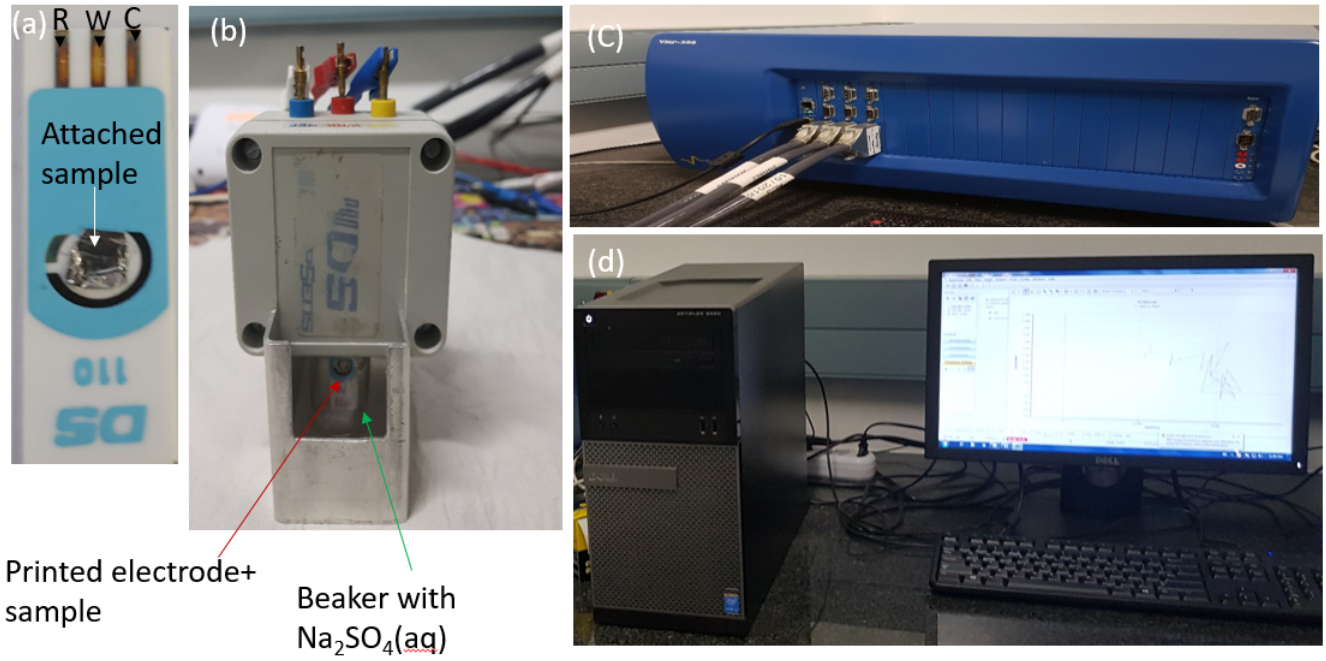

Figure 4.5: A picture of the electrochemistry studies for bulk MoS_2 setup.

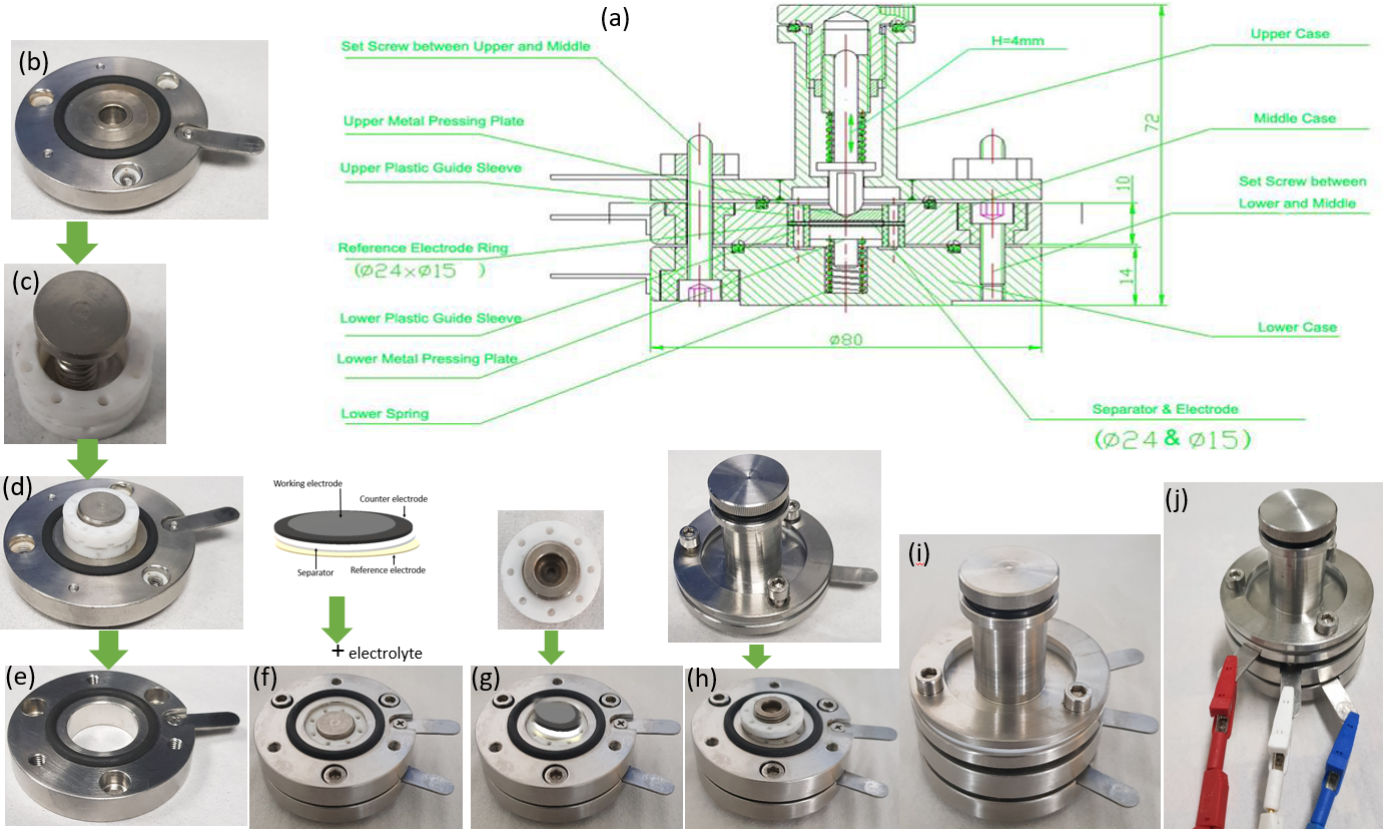

Figure 4.6: (a) A schematic diagram of the swagelok setup, (b)-(j) pictorial procedure used to set up the swagelok.

CHAPTER FIVE

RESULTS

In this chapter, both computational and experimental results for the crystalline MoS_2 are shown and discussed.

5.1 Computational Results

This section is a presentation and a discussion of the results that were obtained through DFT and BoltzTraP simulations. Considered here are some model defects that could arise from ion implantation. Pristine MoS_2 is the first system to be studied, and subsequently MoS_2 with a Mo atom vacancy, MoS_2 with a Mo atom interstitial, MoS_2 with a Mo atom intercalation, MoS_2 with a S atom vacancy and MoS_2 with a S atom intercalation are reported. Subsection 5.1.2 reports the results on electronic and thermal conductivity which were obtained using the BoltzTrap code.

Relaxation of the system under consideration was then performed. First to be discussed is the effects on bandgap upon the introduction or removal of atoms. These created vacancies or interstitial defects. Thermal conductivity as well as anisotropic behaviour of pristine and defective MoS_2 are also shown for these model systems.

5.1.1 Electronic Properties

This section describes the electronic properties related to the various defects and how they compare to the MoS_2 pristine crystal.

5.1.1.1 Structure of Pristine Crystal and Band Structure with the PDOS of MoS_2

Figure 5.1a shows the structure of optimized bulk MoS_2 while Fig. 5.1b shows the band structure and the corresponding projected density of states (PDOS), of pristine MoS_2. We obtained a indirect band gap of 1.29 eV, along Γ and K, as indicated in Fig. 5.1. From the PDOS, Mo 3d orbitals and S 2p

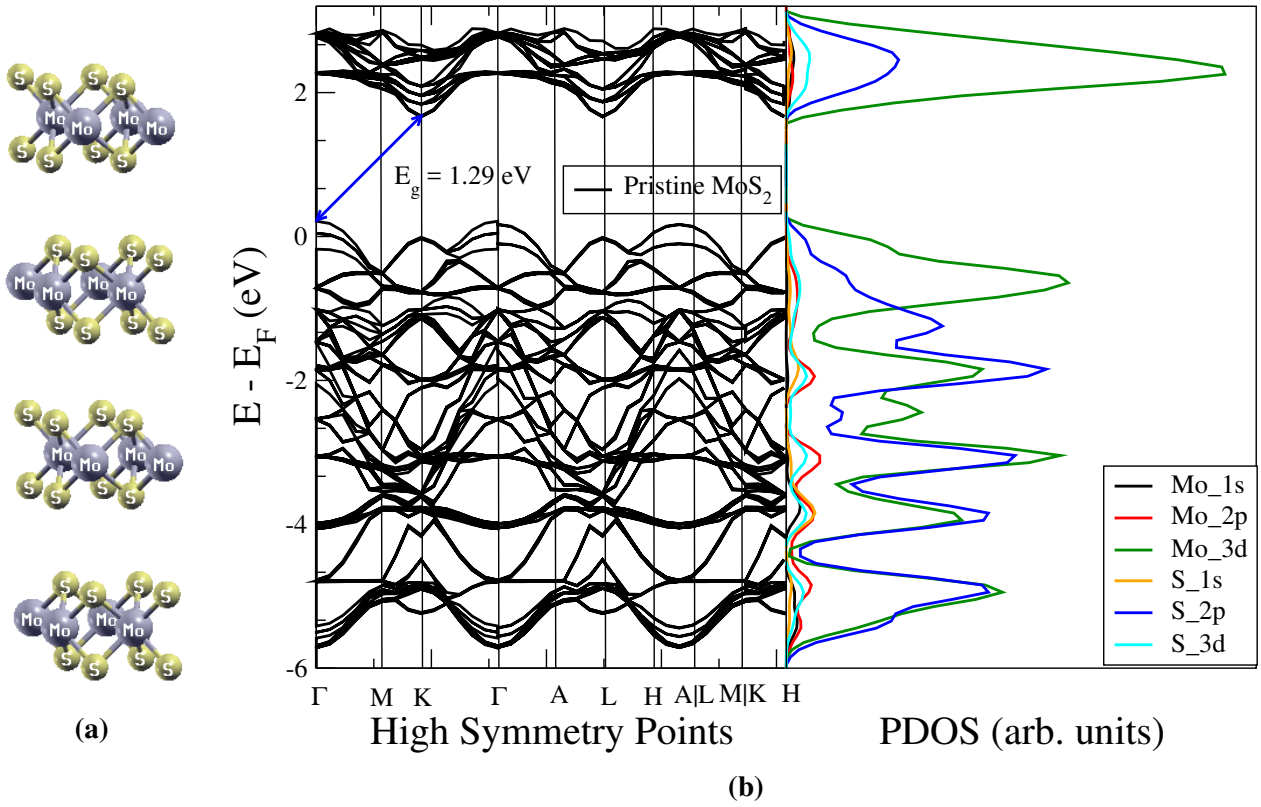

Figure 5.1: (a) Structure of pristine MoS_2, (b) bands and PDOS of pristine MoS_2.

and 3d orbitals are dominant in the conduction band of MoS_2.

5.1.1.2 Band Structure of MoS_2 with Mo Vacancy

Figure 5.2a shows the structure of optimized bulk MoS_2 with a molybdenum (Mo) atom vacancy while Fig. 5.2b shows the band structure and the corresponding density of states of bulk MoS_2 with Mo atom vacancy. The black coloured bands and DOS (almost superimposed by red coloured bands and DOS) represents the pristine crystal while the red coloured bands and density of states (DOS) represent the defective crystal. This resulted to a reduced indirect band gap of 0.5514 eV, from Γ to between L

and H, points of symmetry of the Brillouin zone (BZ).

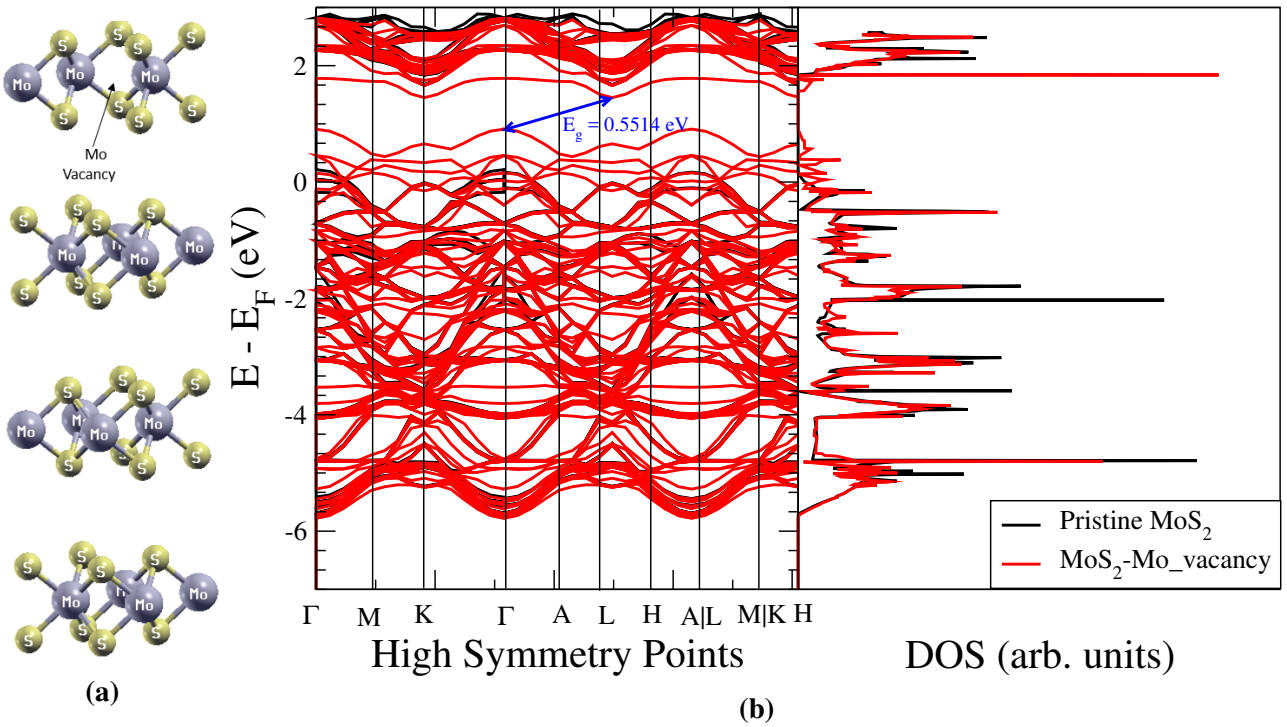

Figure 5.2: (a) Structure of MoS_2 with Mo vacancy, (b) bands and DOS of pristine MoS_2 (black) and MoS_2 with Mo vacancy (red).

5.1.1.3 Band Structure of MoS_2 with Mo Interstitial

Figure 5.3a shows the structure of optimized bulk MoS_2 with Mo atom interstitial, while Fig. 5.3b shows the band structure and the corresponding density of states of bulk MoS_2 with molybdenum (Mo) atom interstitial. The black coloured bands and DOS are for the pristine crystal while the red coloured bands and DOS are for the crystal with Mo atom interstitial. The band gap vanished after the introduction of Mo atom in the interstitial site, making this bulk MoS_2 to have metallic behaviour, a shift from its semiconductor nature.

5.1.1.4 Band Structure of MoS_2 with Mo Intercalation

Figure 5.4a shows the structure of optimized bulk MoS_2 with Mo atom intercalation, while Fig. 5.4b shows the band structure and the corresponding density of states of bulk MoS_2 with molybdenum (Mo) atom intercalation. The black coloured bands and DOS are for the pristine crystal while the red coloured bands and DOS belong to the crystal with intercalated Mo atom. A direct band gap of 0.651 eV was obtained at M as shown in Fig. 5.4b.

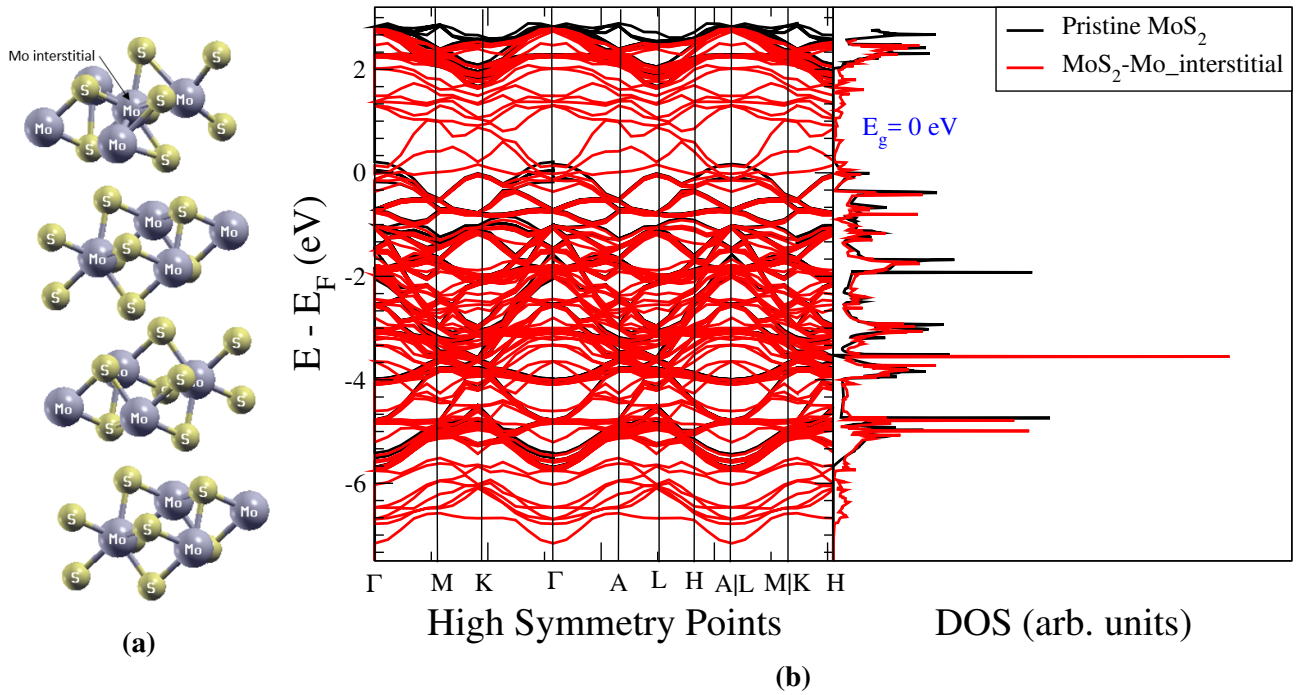

Figure 5.3: (a) Structure of MoS_2 with Mo interstitial, (b) bands and DOS of pristine MoS_2 (black) and MoS_2 with Mo interstitial (red).

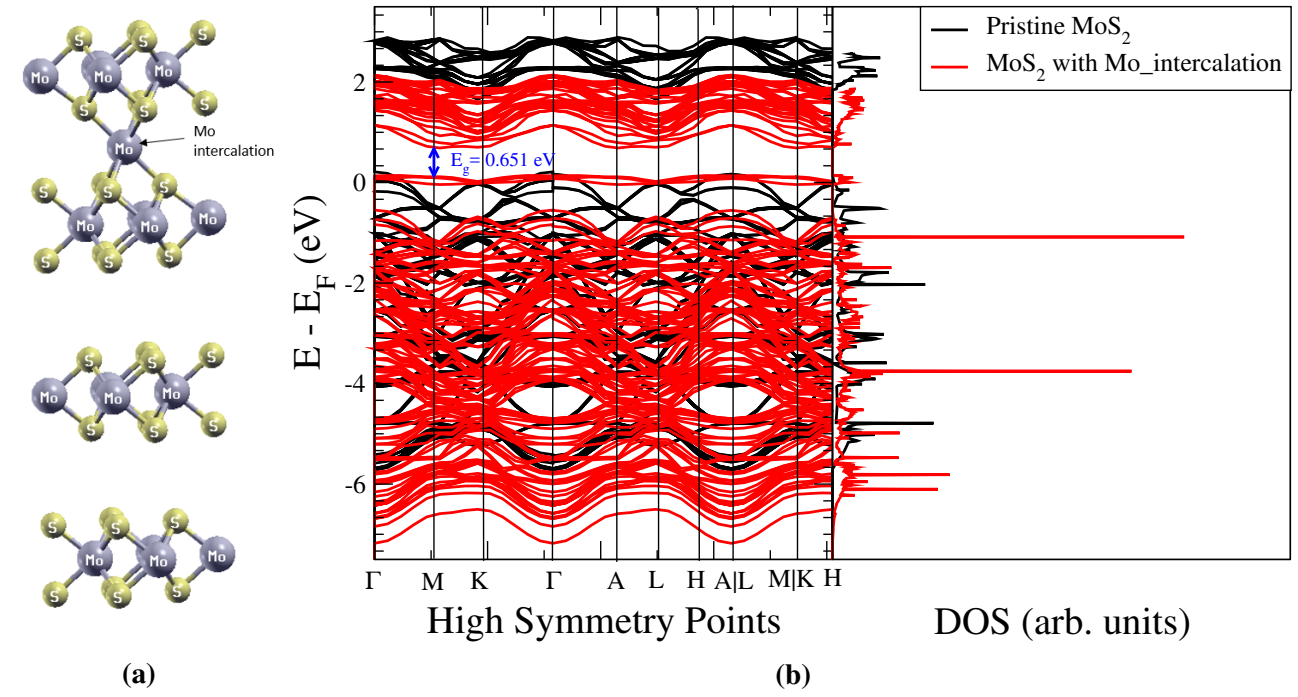

Figure 5.4: (a) Structure of MoS_2 with Mo intercalation, (b) bands and DOS structure of pristine MoS_2 (black) and MoS_2 with Mo intercalation (red).

5.1.1.5 Band Structure of MoS_2 with S Vacancy

Figure 5.5a shows the structure of optimized bulk MoS_2 with sulphur (S) atom vacancy while Fig. 5.5b shows the band structure and the corresponding density of states of bulk MoS_2 with S atom vacancy. The black coloured bands and DOS are for the pristine crystal MoS_2 while the red coloured bands and

DOS are for the MoS_2 crystal with S atom vacancy. The indirect band gap reduced to 0.438 eV and it was located at Γ and between A and L, high symmetry points of BZ.

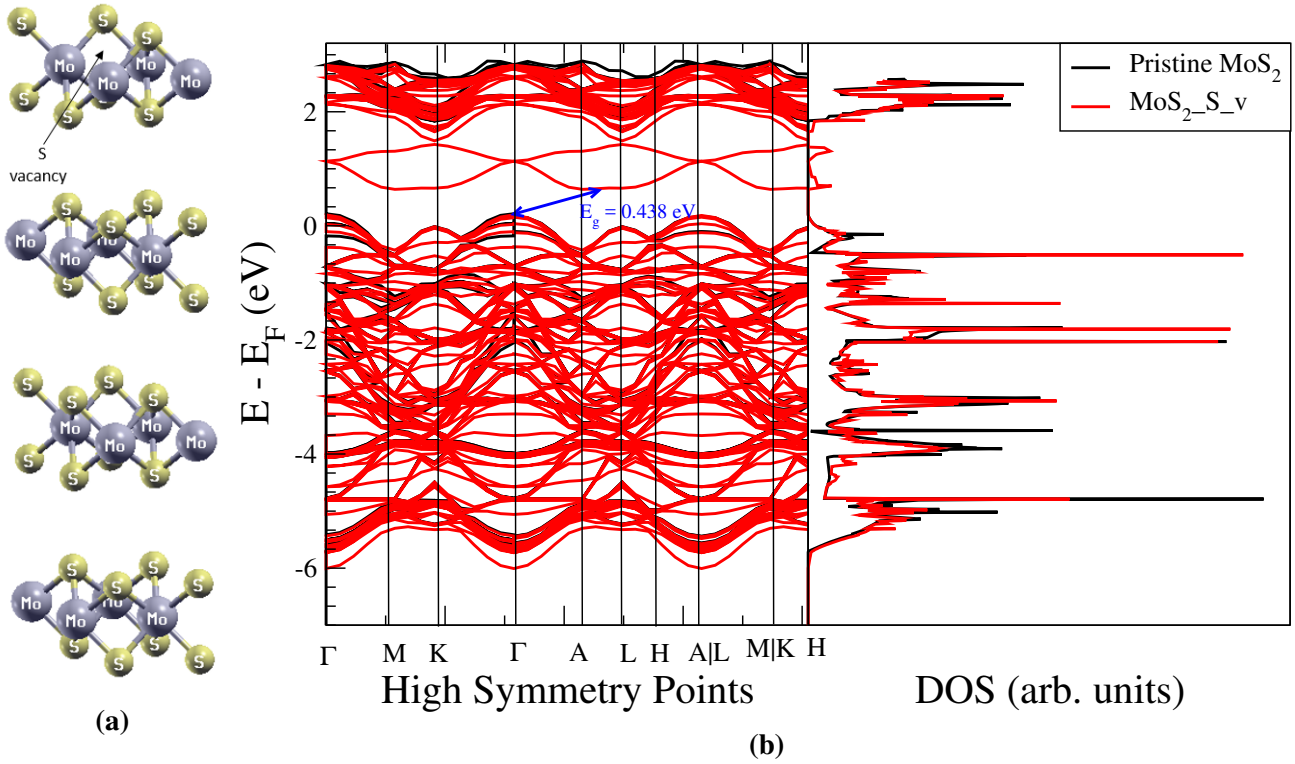

Figure 5.5: (a) Structure of MoS_2 with S vacancy, (b) bands and DOS of pristine MoS_2 (black) and MoS_2 with S vacancy (red).

5.1.1.6 Band Structure of MoS_2 with S Intercalation

Figure 5.6a shows the structure of optimized bulk MoS_2 with S atom intercalation while Fig. 5.6b shows the band structure and the corresponding density of states of bulk MoS_2 with S atom intercalation. The black coloured bands and DOS belong to the pristine MoS_2 crystal while the red coloured bands and DOS are for the crystal with S atom intercalation. The indirect band gap reduced minimally to 1.176 eV. Another notable change was observed in the Fermi level that shifted up by 1.36 eV.

5.1.1.7 Band Structure of MoS_2 with W Interstitial

Figure 5.7a shows the structure of optimized bulk MoS_2 with W atom interstitial while Fig. 5.7b shows the band structure and the corresponding density of states of bulk MoS_2 with S atom intercalation. The black coloured bands are for the pristine crystal while the red coloured bands are for the MoS_2 crystal with W atom interstitial. A direct band gap of 0.336 eV was observed at A.

All the defect-enhanced band structures show a decrease in energy band gap (E_g) compared to the E_g for pristine MoS_2. This is summarized in Table 5.1, whereby metal interstitials (Mo-interstitial and

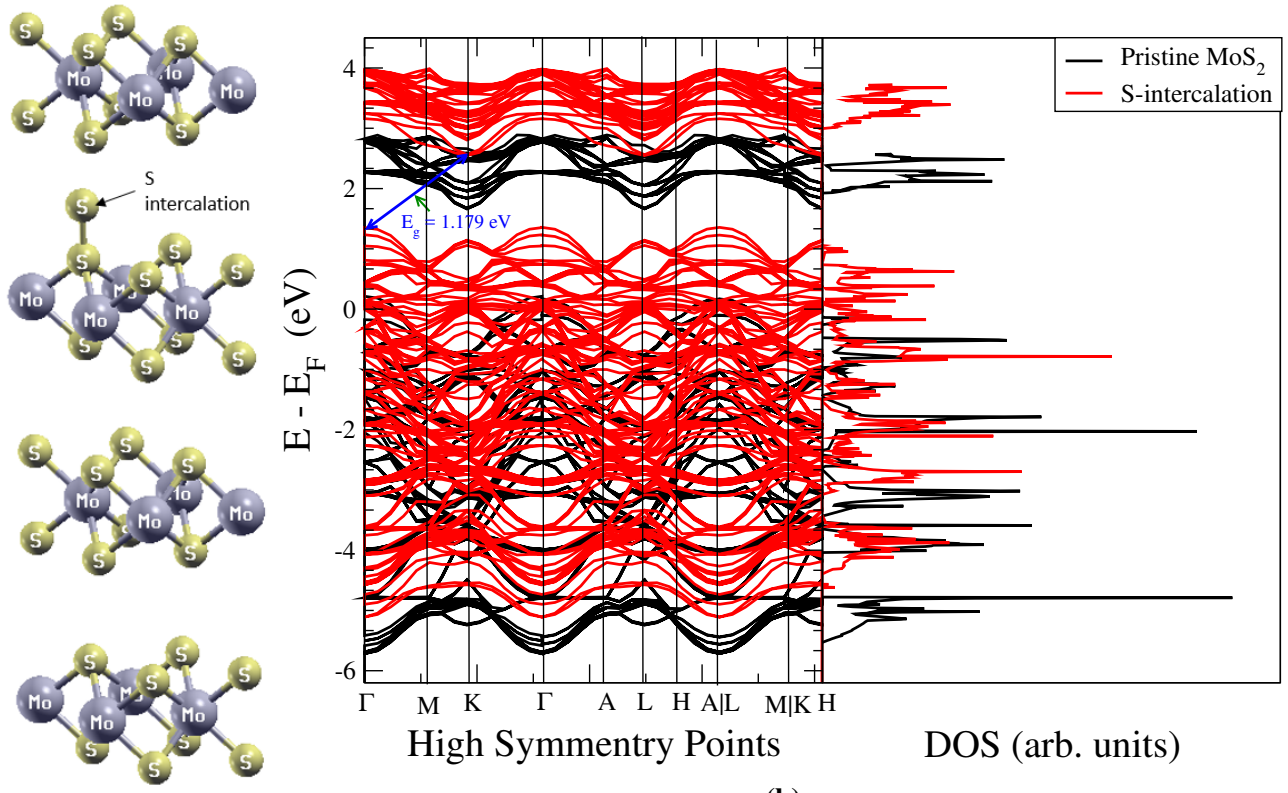

Figure 5.6: (a) Structure of MoS_2 with S interstitial, (b) bands and DOS for pristine MoS_2 (black) and MoS_2 with S interstitial (red).

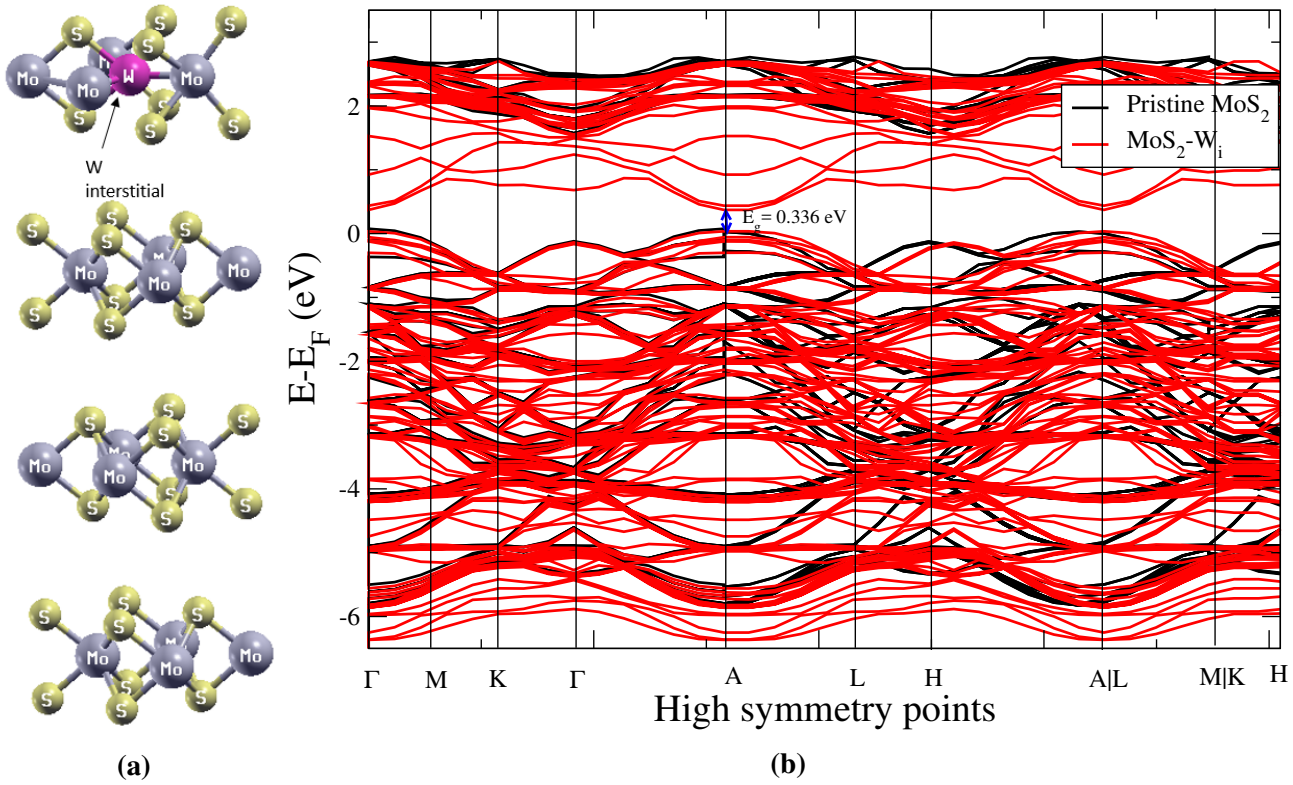

Figure 5.7: (a) Structure of MoS_2 with W interstitial, (b) bands structure of MoS_2 (black) and MoS_2 with W interstitial (red).

W-interstitial) lead to the highest energy bandgap reduction. The Mo-interstitials actually turned the semiconductor MoS_2 into a conductor.

Table 5.1: Comparison of bandgaps of pristine and defective MoS_2 (error ± 5%).

Structure defect	Bandgap E_g (eV)	% Reduction
Pristine	1.290	
Mo-vacancy	0.551	57.1
Mo-intercalation	0.651	49.6
Mo-interstitial	0	100
S-vacancy	0.438	65.9
S-intercalation	1.179	8.5
W-interstitial	0.336	73.6

As shown in Table 5.1, the MoS_2 energy bandgap is tunable through doping and this technique has already be used in expanding MoS_2 applications especially in bandgap engineering [107, 108]. A reduction of the bandgap between 8.5 % and 100 % has been achieved in this study, where metal interstitials (Mo and W) show the highest reductions of 73.6 % and 100 % for tungsten and molybdenum atoms, respectively.

5.1.2 Electronic and Thermal Conductivity

Electronic and thermal conductivities play a vital role in the design of any electrical device. Three configurations have been considered here: pristine MoS_2; MoS_2 with Mo atom interstitial and MoS_2 with W atom interstitial. Fig. 5.8 shows electronic conductivity at 300K along x-direction for pristine MoS_2, MoS_2 with Mo atom interstitial and MoS_2 with W atom interstitial. Based on Fig. 5.8, the electronic

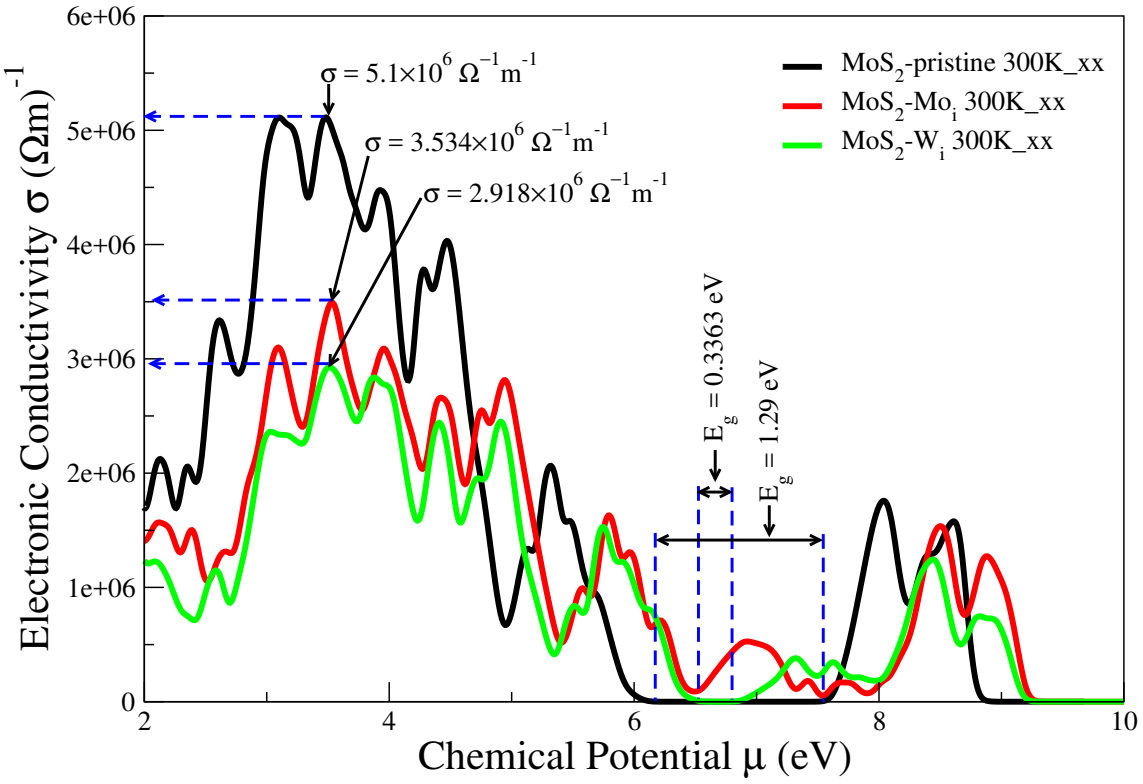

Figure 5.8: Electronic conductivity tensor in x-direction σ_{xx} for the three systems.

conductivity tensor was reduced over a wide range depending on the mass of the atom introduced. Also noticeable is the closing of the energy bandgap E_g (in the case of Mo atom interstitial) and huge reduction of the bandgap in the case of W atom interstitial. Pristine MoS_2 shows E_g of 1.29 eV, while MoS_2 with W atom interstitial reports E_g of 0.3363 eV. This observation of an electronic conductivity here, is typical of a semiconductor. On the other hand, MoS_2 with Mo atom interstitial shows a zero E_g, a conductivity that is typical of a metal. This is in agreement with Fig. 5.3b, obtained from band structure calculations (using DFT).

Fig. 5.9 shows the thermal conductivity at 300K in the x-direction, defined as $(1, \infty, \infty)$ plane, for pristine MoS_2, MoS_2 with Mo interstitial and MoS_2 with W interstitial. A gain a reduction in thermal conductivity was noted, with pristine MoS_2 recording the highest κ of 36.8 $W{\cdot}m^{-1}{\cdot}\ K^{-1}$. The energy bandgaps remained the same as those in Fig. 5.8.

Due to the anisotropic nature of MoS_2, shown in Fig. 5.10, σ and κ in the y-direction maps onto the

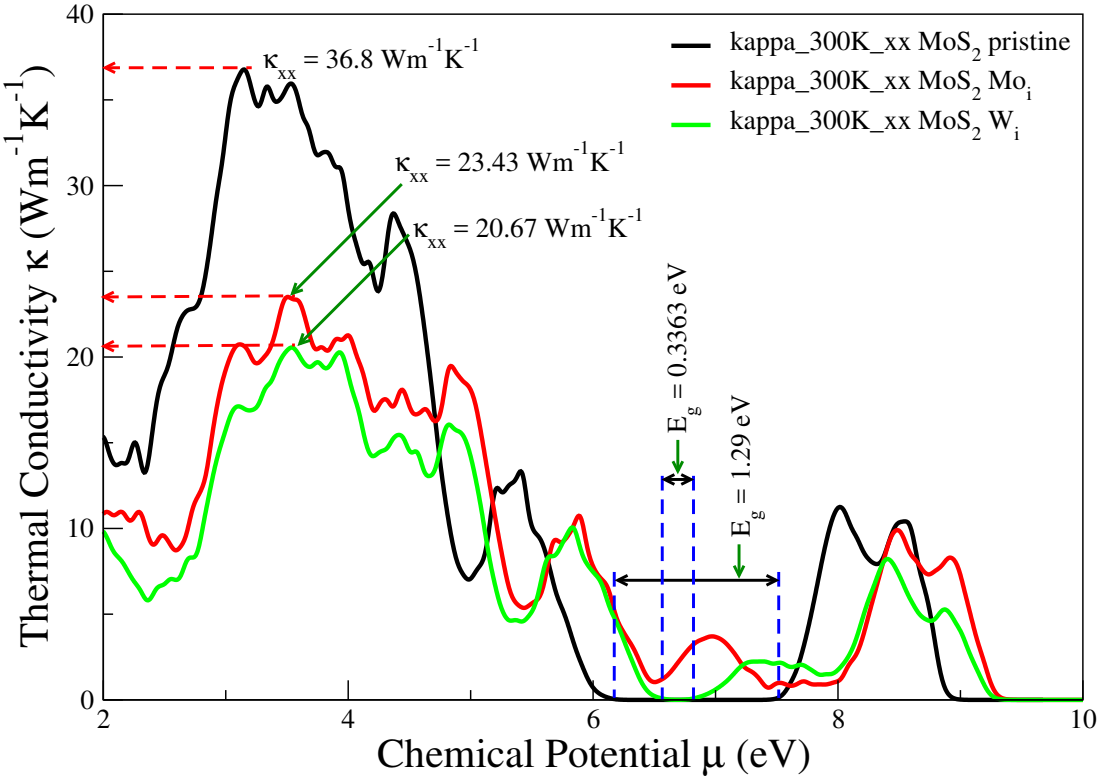

Figure 5.9: Thermal conductivity tensor in x-direction κ_{xx} for the three model systems.

x-direction, while the same σ and κ contribution along the z-direction are significantly reduced.

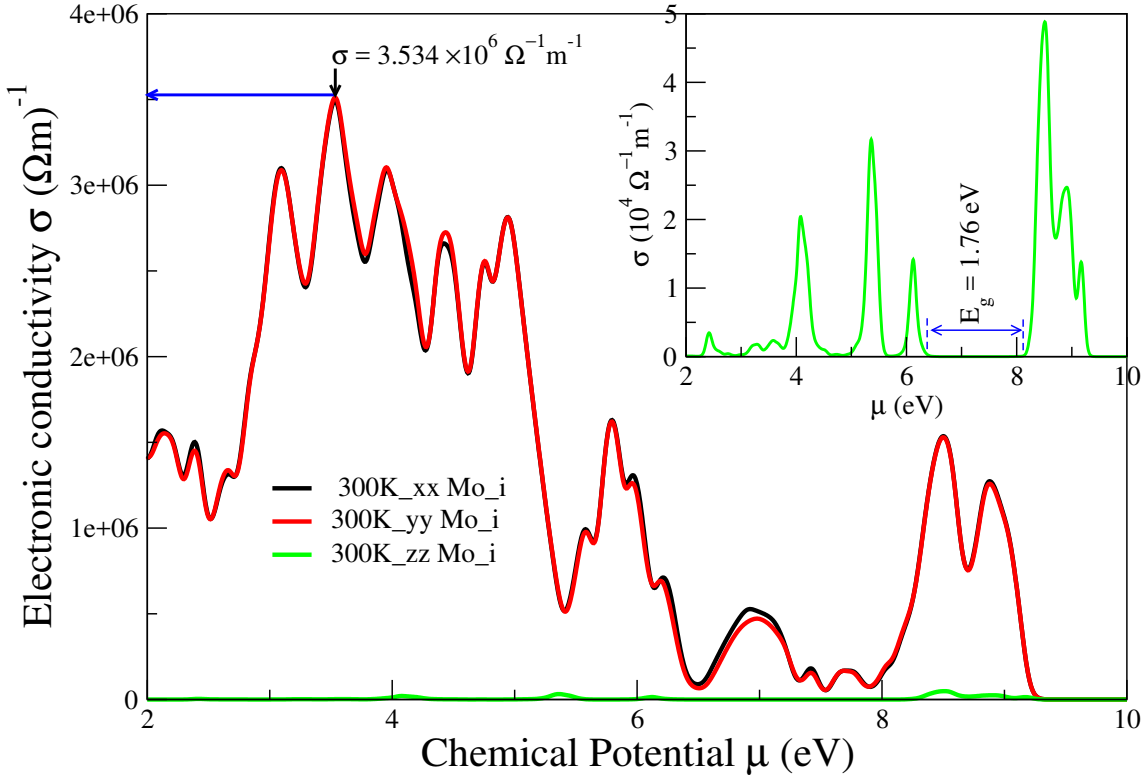

Figure 5.10: Thermal conductivity tensor σ_{xx}, σ_{yy} and σ_{zz} showing the anisotropic nature of MoS_2.

Fig. 5.11 shows the Pauli magnetic susceptibility at 300 K, for pristine MoS_2; MoS_2 implanted with Mo atoms and MoS_2 implanted with W atoms at a concentration of 2 %. Susceptibility is an indicator as

to whether a material will be attracted or repelled in a magnetic field. This has implications on practical applications like magnetic resonance imaging (MRI) scanners.

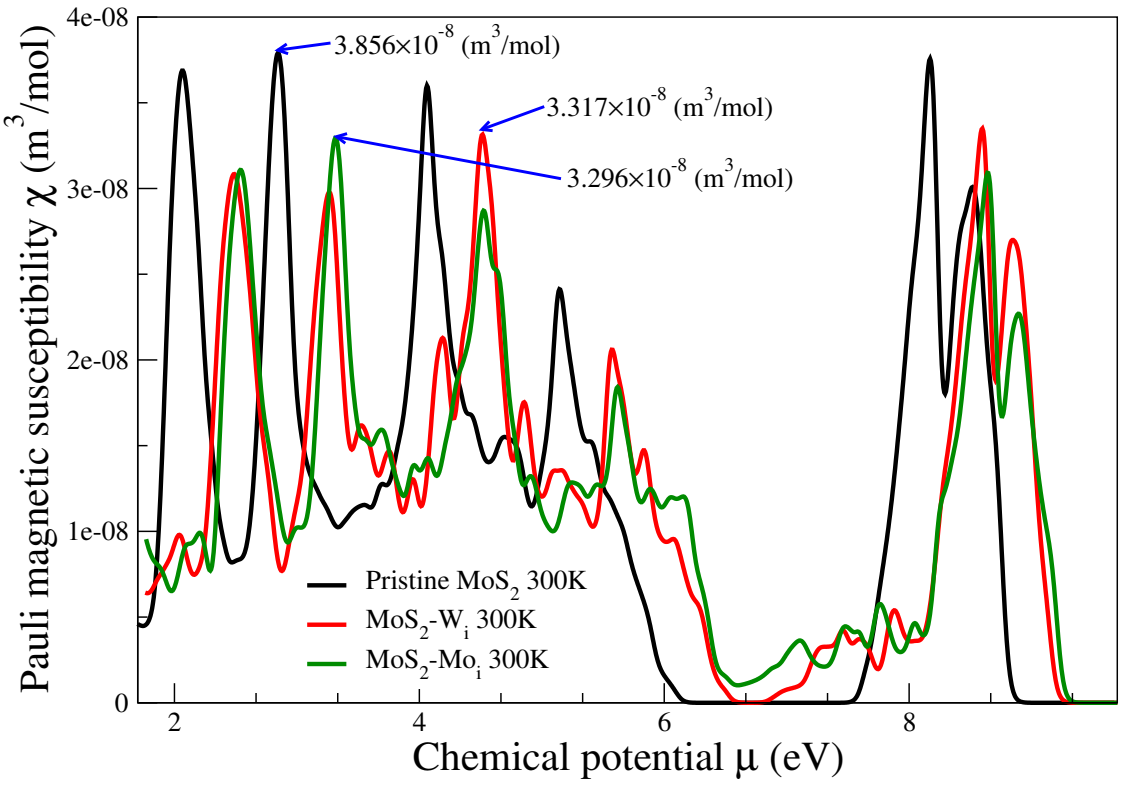

Figure 5.11: Effects of doping on MoS_2 at 300k, on the magnetic susceptibility.

Another characteristic noted upon defect creation, was the ability to change a p-type semiconductor to an n-type one. When the Seebeck coefficient (S) is greater than zero at chemical potential μ =0, then we have a p-type semiconductor; and S<0 at μ =0 implies an n-type semiconductor [109]. Fig. 5.12 shows the types of semiconductor each type of defect produced at 300 K.

MoS_2 with Mo interstitial change from a p-type to an n-type as shown in the Fig. 5.12 inset. However, MoS_2 with W interstitial remained a p-type just like the pristine MoS_2. At 300 K and $\mu \approx \pm$ 0.35 eV, this study obtained S values of 2379 μV/K, 109 μV/K, and 544 μV/K for pristine MoS_2, MoS_2 with Mo interstitial and MoS_2 with W interstitial, respectively. Our S values can not possibly be compared to the 1400 μV/K reported by Lee *et al.* at 300 K and using $\mu \approx \pm$ 0.1 eV [110]. This variation is attributed to the difference in μ used. Since S is directly related to thermopower, our defect modified MoS_2 is still a good candidate for thermoelectric applications, if the differences (0.25 eV) in μ applied is overlooked. High efficiency of a thermoelectric material is determined by the figure of merit (ZT) given by;

$$ZT = S^2\sigma T/\kappa, \tag{5.1}$$

where S is the Seebeck coefficient, σ is the electrical conductivity, and κ is the thermal conductivity at

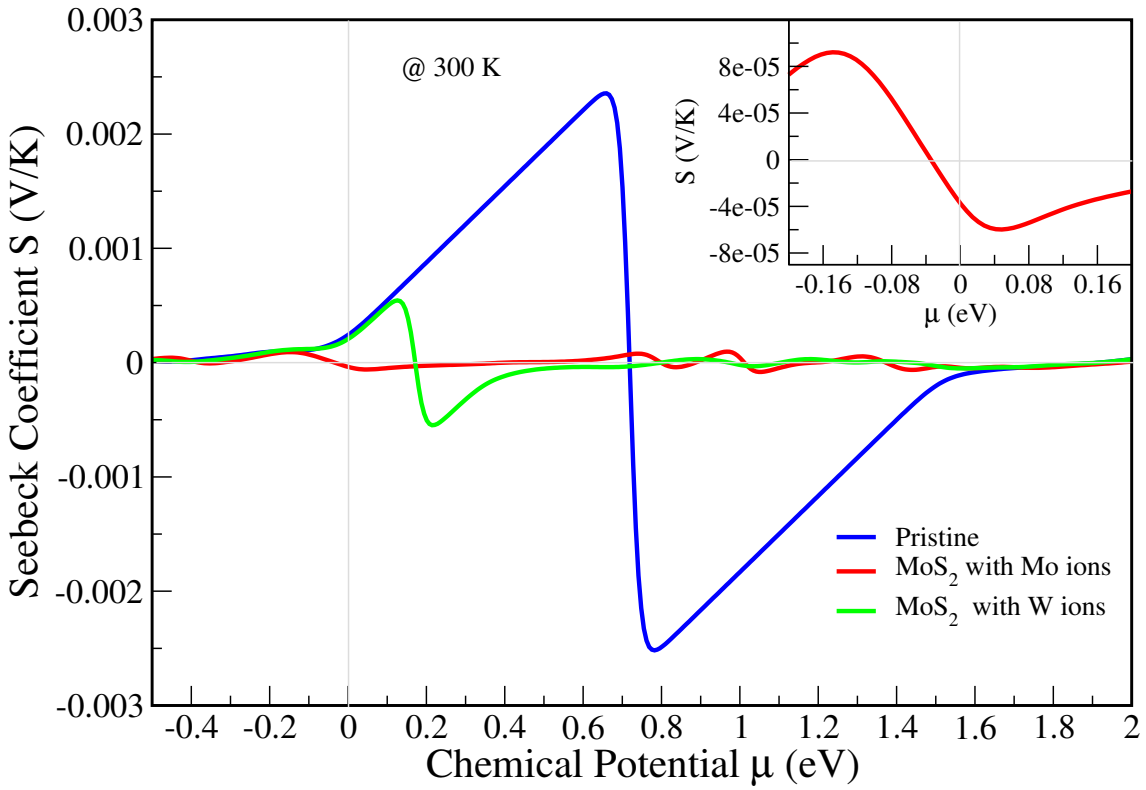

Figure 5.12: Seebeck coefficient vs chemical potential for pristine MoS_2 and MoS_2 with Mo and W interstitials.

a given temperature T. $\kappa = \kappa_e + \kappa_p$, where κ_e and κ_p are electronic and phonon contributions to thermal conductivity, respectively.

5.2 Experimental Results

This section reports the experimental results obtained for pristine MoS_2 and the implanted one, with different atoms (Mo and W). The energy used for all the implantations was 10 keV, as earlier indicated in Table 4.1. The choice of this implantation energy was to ensure that the damage occurred near the surface of all the samples.

5.2.1 Current-Voltage (I-V) Characteristics

In this subsection, studies to establish whether silver paste would make Ohmic contacts with MoS_2 were carried out. Using the four probes technique, silver contacts were made on MoS_2 samples, the following I-V characteristics graphs were obtained as shown in Figs. 5.13 and 5.14:

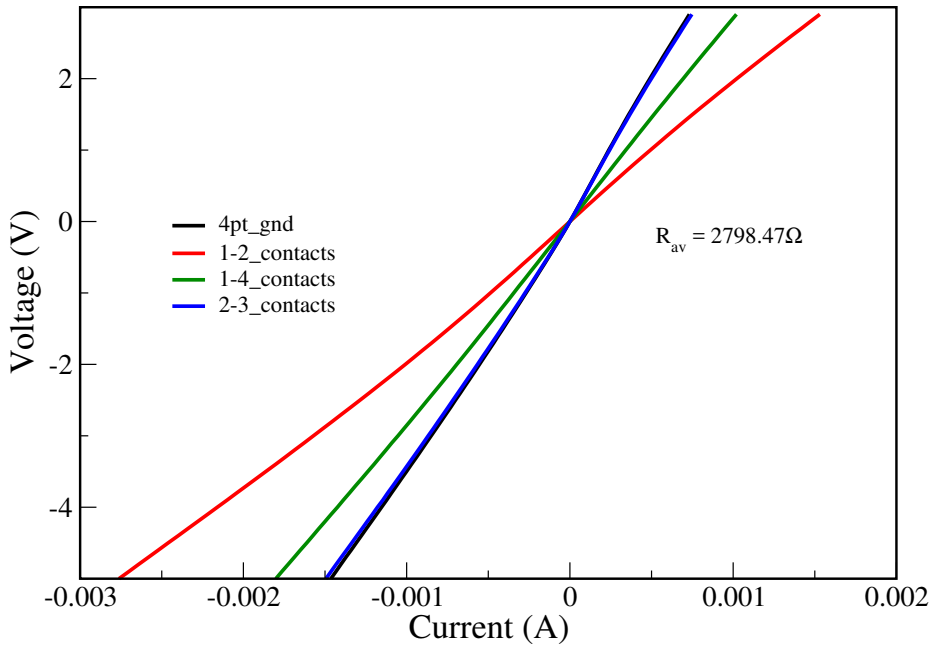

Figure 5.13: Graphs of current against voltage of pristine MoS_2 at different contact configurations.

The average sheet resistance R_{av}, shown here differs from the one reported in Table 5.2 because the section under consideration was the linear part a semiconductor I-V characteristic curves. The I-V graphs shown in 5.14 acquired through measuring the current accross pts 1-4 and 2-3 (shown in 4.4), and the average plotted against voltage, for all the samples shown.

The linear I-V characteristic graphs is an evidence that silver paste formed/forms Ohmic contacts with MoS_2. It is on this basis that silver paste was used to attach the sample electrodes onto the working electrode of the screen-printed electrode, during the electrochemistry analysis procedures reported in this study. Fig. 5.14 shows decrease in resistance upon ion implantation on pristine MoS_2.

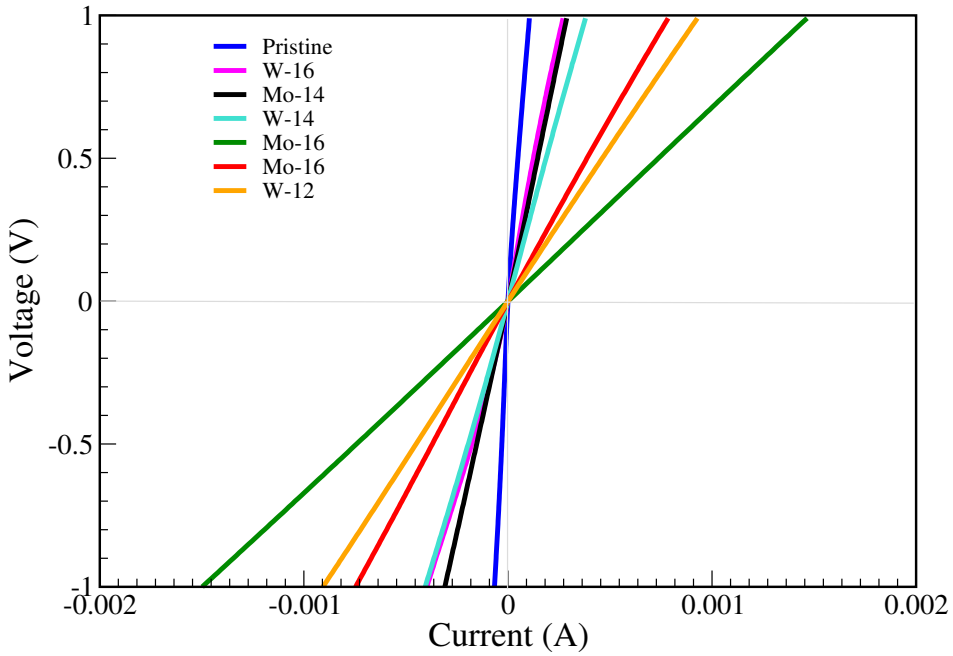

Figure 5.14: Graphs of current against voltage MoS_2 pristine and MoS_2 implanted with Mo and W ions.

This is in agreement with the data obtained using Electrochemistry impedance Spectroscopy (EIS) from the Nyquist plots fittings, tabulated in Table 5.2. The equivalent circuit used here was a series resistor R_1, connected to R_2, which is connected in parallel to capacitor C_2.

Table 5.2: Summary of resistances of pristine and ion implanted MoS_2 (error ± 5%).

Implanted atoms	R_1 (Ω)	R_2 (Ω)	$R_1 + R_2$ (Ω)	C_2 (10^{-12} F)
Pristine	4405	10674	15079	7.654
Mo-14	1836	2523	4359	19.52
W-14	1248	1428	2676	42.34
W-16	834.1	3825	4659.1	62.66
Mo-16	750.8	715.5	1466.3	83.61

Based on Table 5.2, it is clear that ion implantation generally reduces resistance in MoS_2; with the highest reduction reported in the case of implantation with Mo atoms at fluence of 10^{16} ions/cm^2. With reduced resistance, ion implanted MoS_2 as a material for electrodes enhance electron conductivity, leading to improvement in the performance of a device (like supercapacitors). From the Nyquist plots fitting, the capacitance of pristine MoS_2 was found to be 7.654 pF, while that of MoS_2 implanted with Mo atoms using a dose of 10^{16} ions/cm^2, recorded more than tenfold in capacitance (83.61 pF).

5.2.2 Raman Spectroscopy (RS)

Raman spectroscopy measurements done on both pure and ion-implanted samples are shown in Figs. 5.15 and 5.16.

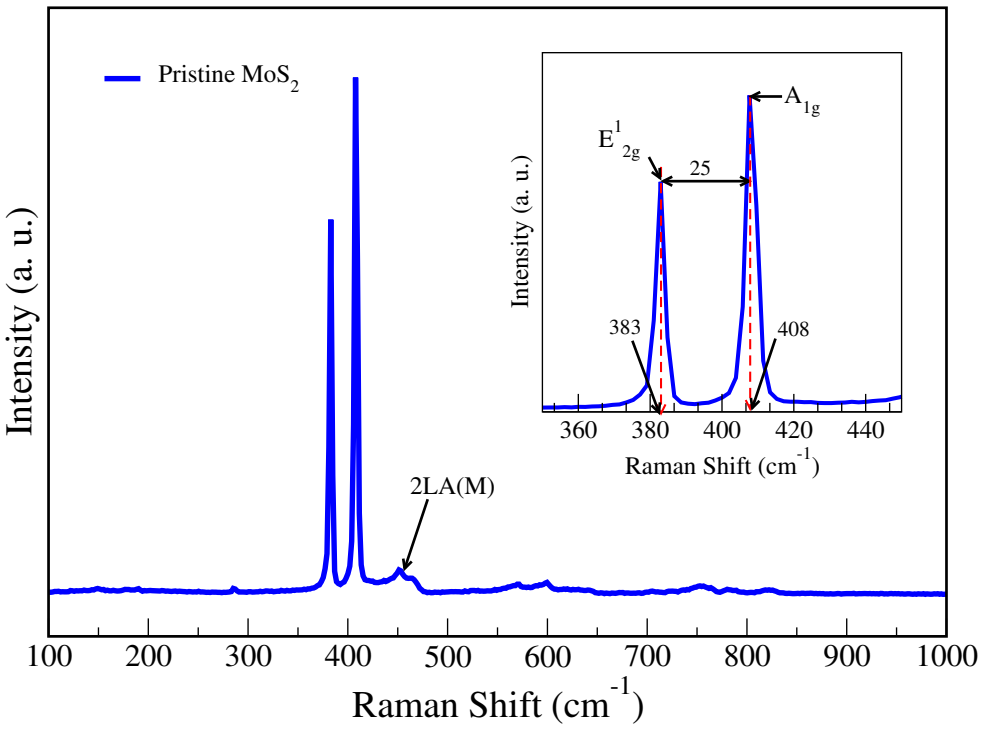

Figure 5.15: Raman shift in pristine MoS_2.

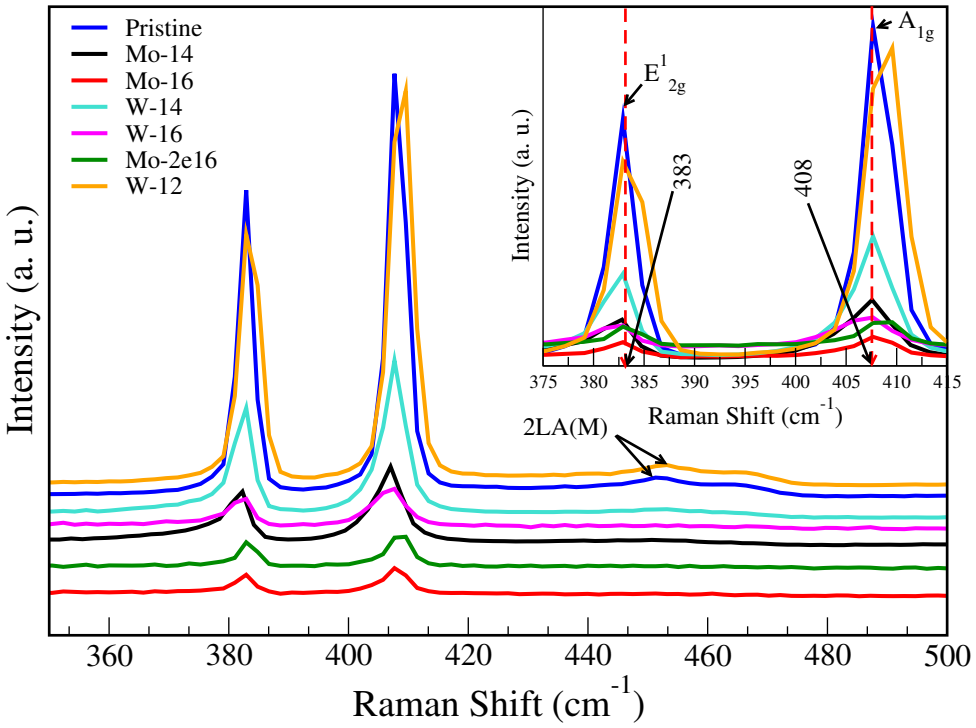

Figure 5.16: Raman shift in MoS_2 implanted with Mo and W atoms.

RS was performed on the unimplanted and implanted MoS_2 samples, using green laser beam of wavelength 514.2 nm. The in-plane E^1_{2g} and out-of-plane A_{1g} vibrational peaks were observed at about 383 and 408, respectively, for the unimplanted MoS_2 sample. The broad peak 2LA(M) observed at about 452 cm^{-1} (shown in Figs. 5.15 and 5.16) is due to the second order of LA(M) phonon resonance,[111] where M is the point in the hexagonal MoS_2 Brillouin zone (BZ) as suggested by Stacy *et al.*[112] who

estimated the frequencies of the M-point optical modes. After ion implantation the intensity of these peaks reduced significantly, as illustrated in Fig. 5.16. The intensity reduction can be attributed to damage done on specific samples by ion implantation. A noticeable shift in frequency of the A_{1g} mode was observed in the W-12 sample. The positions of the vibrational peaks of the virgin material are in good agreement with other studies [113].

Also shown in Fig. 5.16 inset is the in-plane (E^1_{2g}) and slight displacements in the Mo-14 sample, in which E^1_{2g} and A_{1g} shifted to 385 nm and 410 nm, respectively. The range between these peaks was measured as 25 units, which is the same as that of pristine MoS_2 and the other samples of MoS_2 implanted with Mo and W ions irrespective of the fluences.

Table 5.3: Summary of Raman vibrational modes (cm^{-1}) (error ± 5%).

E^1_{2g}	A_{1g}	
383.0	408.0	This study
385.2	404.8	[64, 65]
383.7	402.9	[114]
382.5	402.9	[114]
376.9	407.8	[114]
357.7	403.2	[115, 116]

The cited Raman vibrational modes shown in Table 5.3, were done using either a mono layer or a few layers of MoS_2, while in this study used bulk MoS_2. After ion implantation, shown in Fig. 5.16, the positions of the major modes (E^1_{2g} and A_{1g}) remained unchanged. However, their intensities reduced. The other small vibrational signatures (observed in pristine bulk MoS_2), changed. This indicates that the near surface of pristine MoS_2 was damaged by ion implantation and the resulting radiation damage translates into additional active sites where charge transfer of Na ions from the electrolyte (Na_2SO_4) into the active MoS_2 can take place. This effectively 'increases' the surface area, an important quality for electrodes to be used in capacitors. Equation (5.2), illustrates how area increase would enhance capacitance.

$$C = \epsilon \frac{A}{d}; \tag{5.2}$$

where C is the capacitance, ϵ is the absolute permittivity of the dielectric, A is the cross-sectional area of the electrodes and d is the distance separating the plate-electrodes. $\epsilon = \epsilon_r \epsilon_o$, where ϵ_r is the relative static permittivity of the dielectric and $\epsilon_o = 8.854 \times 10^{-12}$ Fm^{-1}, which is the electric constant.

The energy stored (W) in a (flat-plate) capacitor is:

$$W = \frac{1}{2}\epsilon_r \epsilon_o \frac{A}{d} V^2; \tag{5.3}$$

where V is the potential difference. Equation (5.3) further shows how increase in A increases the energy storage capacity.

5.2.3 Photoluminescence

Photoluminescence (PL) is defined as the light emission from any form of matter as a result of photons absorption. It is triggered by photoexcitation, that occurs when the photon energy is not sufficient to cause photoionisation. In this study, a green laser beam of wavelength 514.2 nm was used for PL measurements. Fig. 5.17 shows PL peaks of pristine MoS_2 as well as MoS_2 implanted with Mo and W ions. Pristine bulk MoS_2 shows a characteristic photoluminescence peak at 1.85 eV. However, after ion

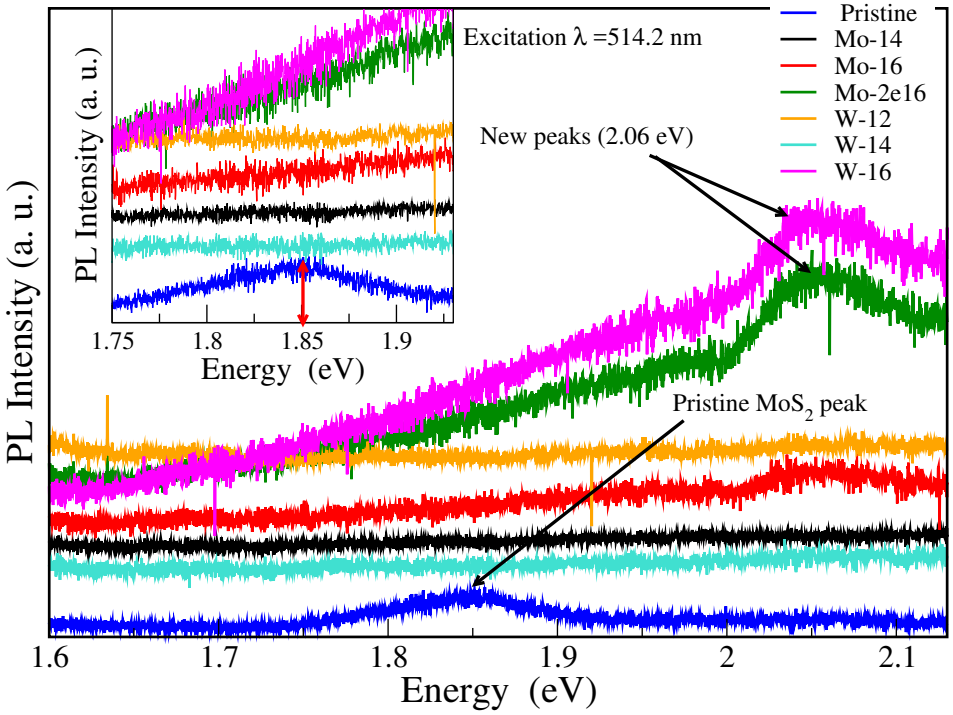

Figure 5.17: Photoluminescence of spectra MoS_2 implanted with Mo and W ions recorded at room temperature.

implantation, this peak in pristine bulk MoS_2 is quenched. New PL peaks emerged in all the samples implanted at fluences of 10^{16} ions/cm^2. These new peaks were located around 2.06 eV and are attributed to defect formations induced in the samples. It is also interesting to note that a study on monolayer MoS_2 observed a peak at 1.98 eV (which is very close to the new peaks observed in our study), associated to the A1 and B1 direct excitonic transitions [72] . This phenom suggests that MoS_2 implanted with W

ions at fluence of 10^{16} ions/cm^2 and MoS_2 implanted with Mo ions at fluence of 2×10^{16} ions/cm^2 could be used in photovoltaic diodes [117], based on the higher emission of the excitation beam as shown in Fig. 5.17, compared to implanted lower fluences.

The PL peak quenching was used as an indicator of induced defect presence and also surface damage, which was in line with the objectives of this study. Damaged surfaces increase the surface area for the samples, desired for energy storage capability of electrode materials. The absorption coefficient (α) of MoS_2 computed as $\approx 3 \times 10^5$ cm^{-1} for excitation wavelength of 514.2 nm, using the refractive index data base for 2H-MoS_2 [118]. This value was then used to calculate the scattering depth (d) of the laser beam from MoS_2 that was found to be 33.3 nm, calculated from Lambert-Beer law for penetration depth given by equation 5.4;

$$d = \frac{1}{\alpha}. \tag{5.4}$$

Fig. 5.18 shows the PL spectra before and after annealing in argon gas at 600 °C, which documents the re-emerging of the characteristic MoS_2 peaks after annealing and this explains why the samples used for energy storage capability studies here, were not annealed. The annealing obviously allows for the reconstruction of the MoS_2 lattice, such that most of the ions fall back to their normal positions as they were before bombardment of ions. However, in the iiradiated samples, the Mo and W ions could be trapped in between the layers. This could assist in widening the interlayers distance and also help holding the layers in place, and prevent them from collapsing when Na^+ ions from the electrolyte intercalate and de-intercalate between layers of MoS_2. This also leads to an increase in active surface area. A wider interlayer spacing translates to a faster movement of the electrolyte ions. Therefore the modified nanocomposite architecture of the irradiated MoS_2 enhances the intercalation and de-intercalation of the Na^+ and effectively enhances the solid-state charge storage [119].

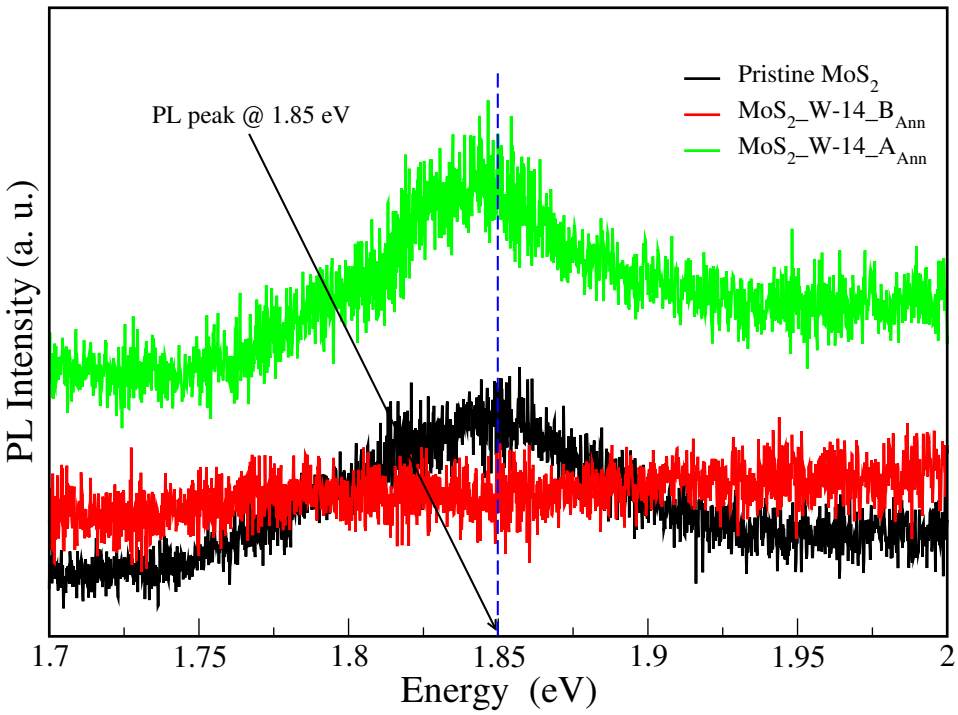

Figure 5.18: PL peak for pristine and tungsten ion implanted MoS_2 before and after annealing. The label B_{Ann} denotes a sample before annealing, while A_{Ann} denotes the annealed sample.

5.3 Electrochemical Analysis

This section presents the electrochemical analysis of the pristine MoS_2 and the MoS_2 implanted with Mo and W ions, at different fluences and using an implantation energy of 10 keV. A three-electrode system (screen-printed) was used, which comprised of silver/silver-chloride (Ag/AgCl) as the reference electrode; carbon as counter electrode and carbon also as the working electrode. It is on the working electrode where our samples were attached using silver paste. The three-electrode system with the sample(s) were then put in 1 molar of sodium sulphate (Na_2SO_4) electrolyte.

5.3.1 Cyclic Voltammetry

The cyclic voltammograms in Figs. 5.19, 5.20, 5.21, 5.22, 5.23 and 5.24, are the scan rates between 5 mVs^{-1} to 100 mVs^{-1}. The areas under the curves represent the total charge stored produced from both faradaic and non-faradaic processes [120]. The upper peaks are due to anodic reaction while the lower ones are as a result of reduction processes. Both peaks differ for each sample due to the type of ions implanted and also the fluence used in each case.

The reference electrode potential was normalised to reversible hydrogen electrode (RHE) using the formula:

$$E_{RHE} = E_{Ag/AgCl} + 0.059pH + E^{o}_{Ag/AgCl}, \tag{5.5}$$

where $E^{o}_{Ag/AgCl}$ =0.2015, pH = 7.0 and $E_{Ag/AgCl}$ is the Ag/AgCl electrode potential.

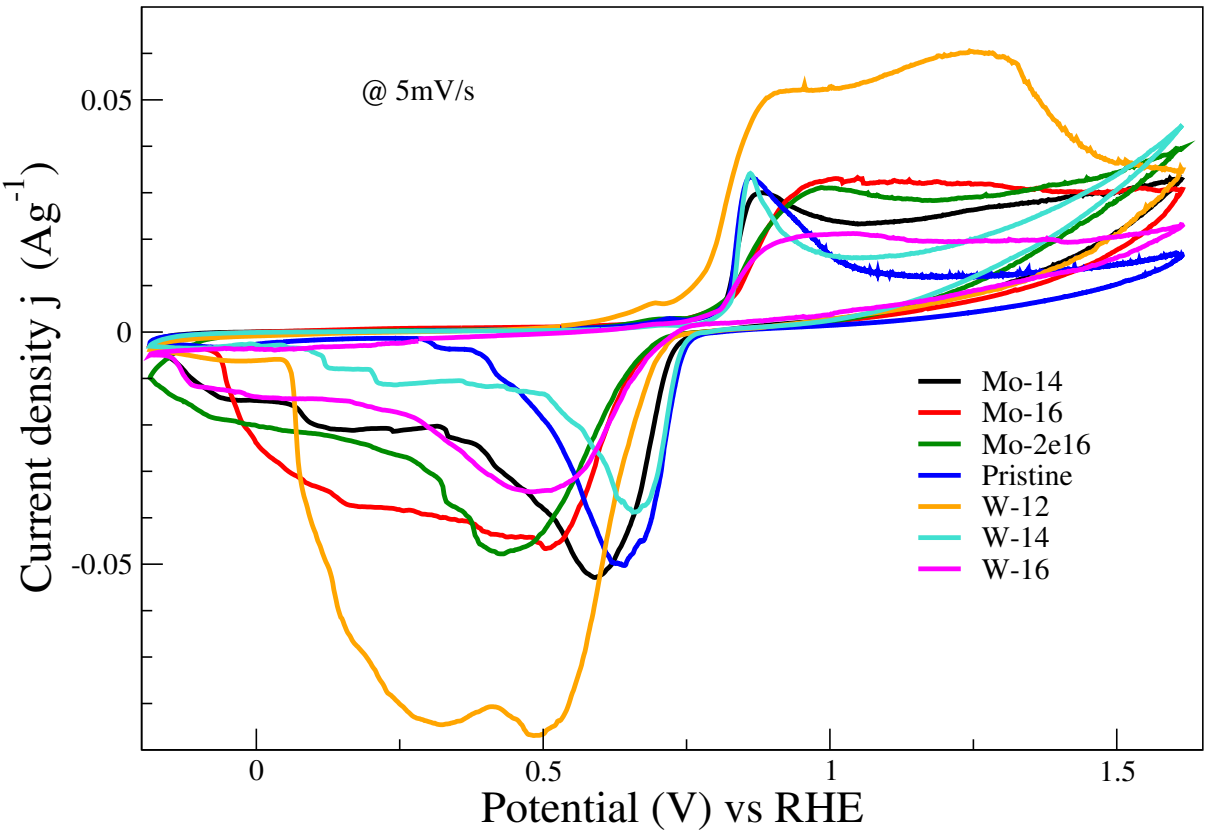

Figure 5.19: Cyclic voltammograms of MoS_2 implanted with Mo and W ions compared with the pristine at scan rate of 5 mV/s.

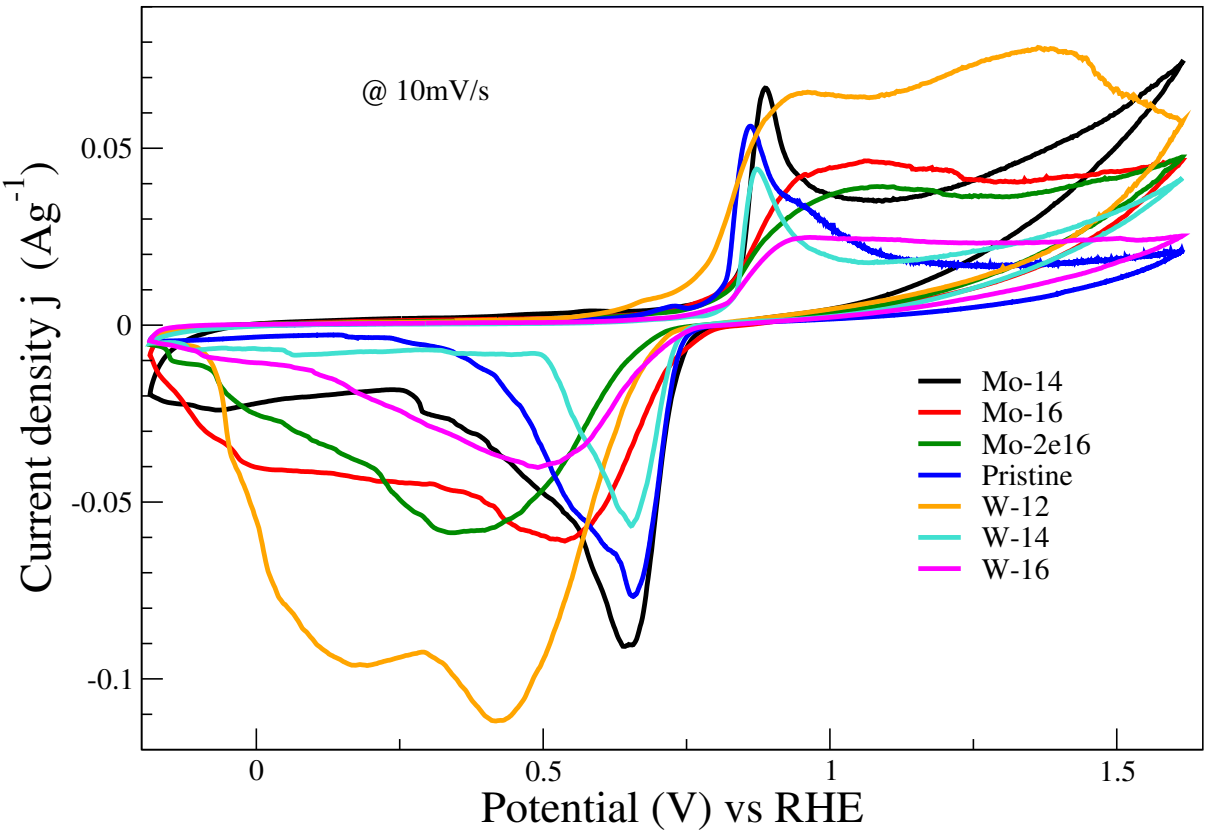

Figure 5.20: Cyclic voltammograms of MoS_2 implanted with Mo and W ions compared with the pristine at scan rate of 10 mV/s.

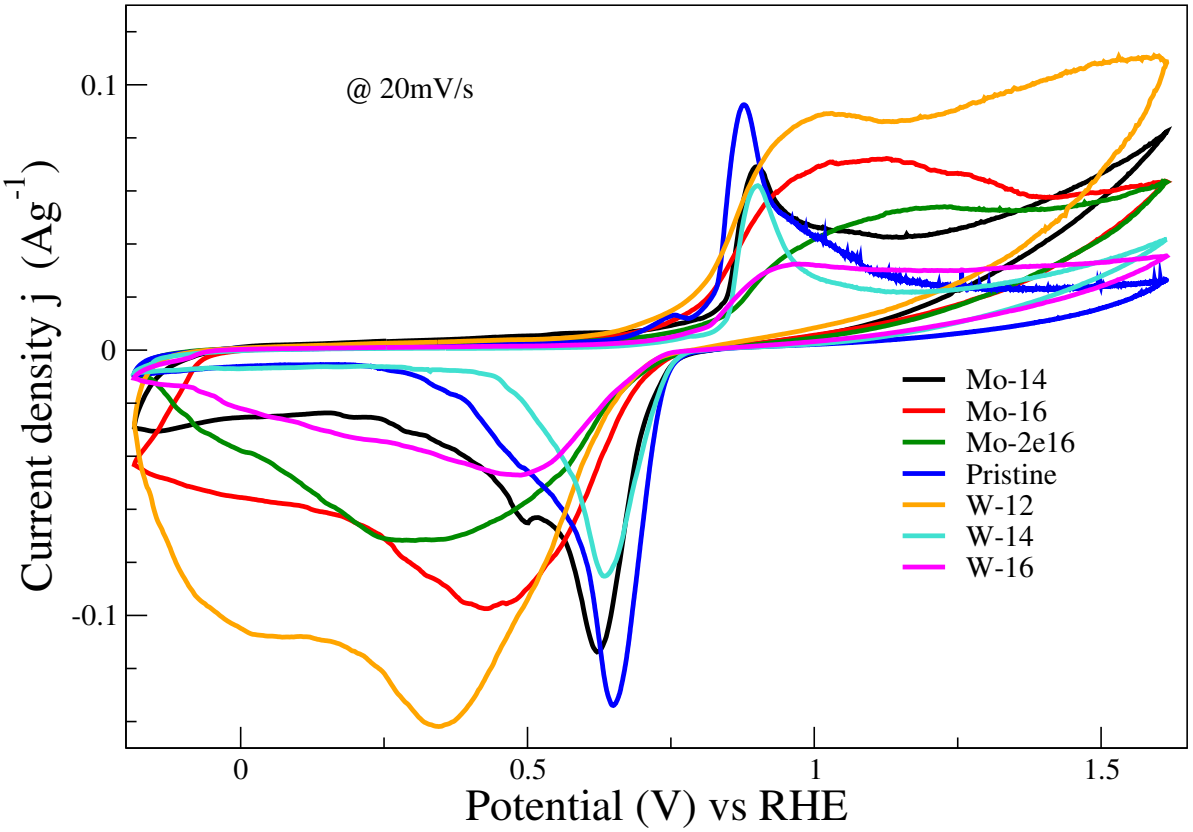

Figure 5.21: Cyclic voltammograms of MoS_2 implanted with Mo and W ions compared with the pristine at scan rate of 20 mV/s.

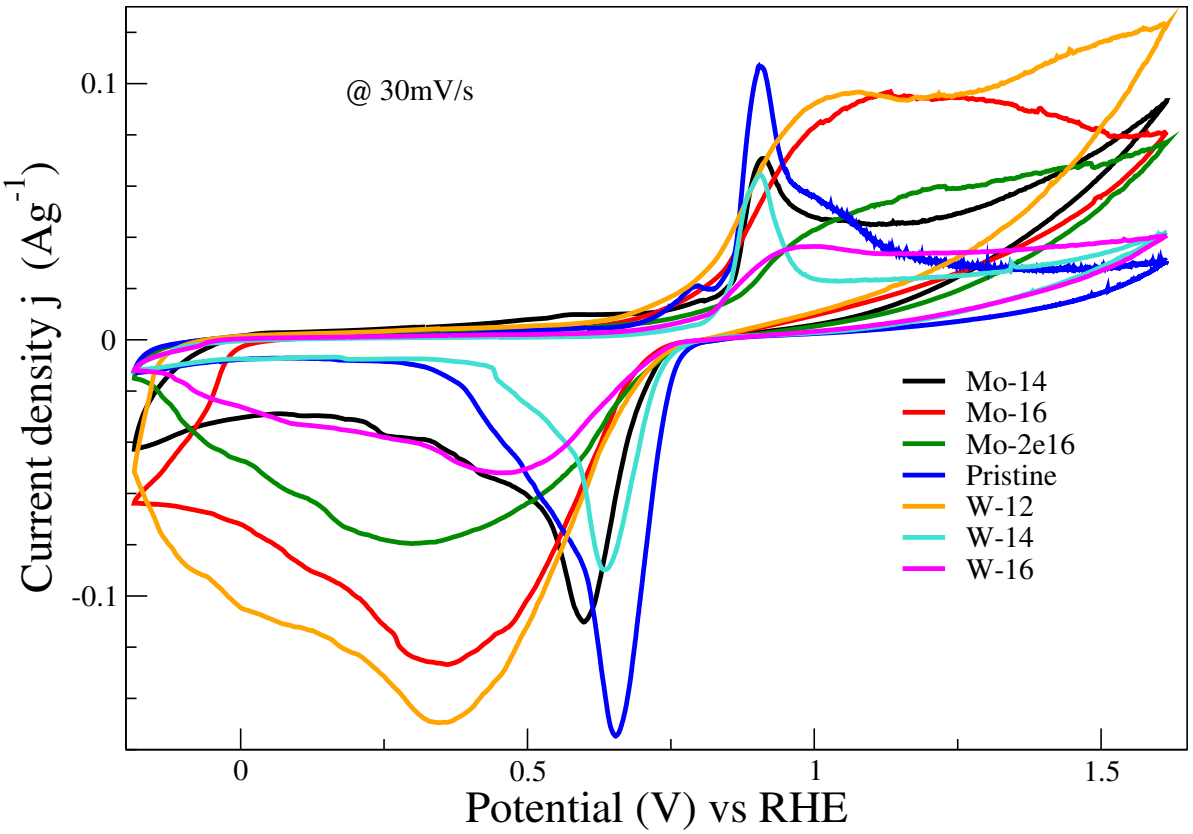

Figure 5.22: Cyclic voltammograms of MoS_2 implanted with Mo and W ions compared with the pristine at scan rate of 30 mV/s.

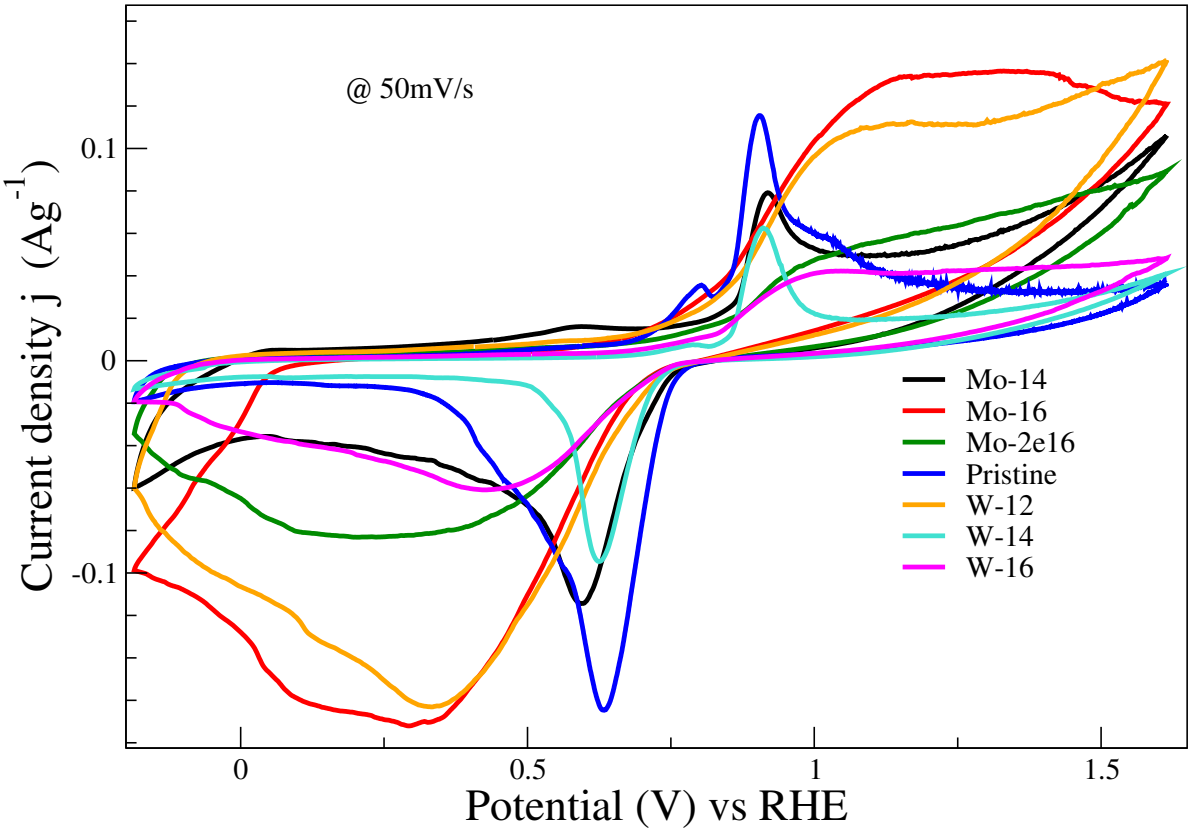

Figure 5.23: Cyclic voltammograms of MoS_2 implanted with Mo and W ions compared with the pristine at scan rate of 50 mV/s.

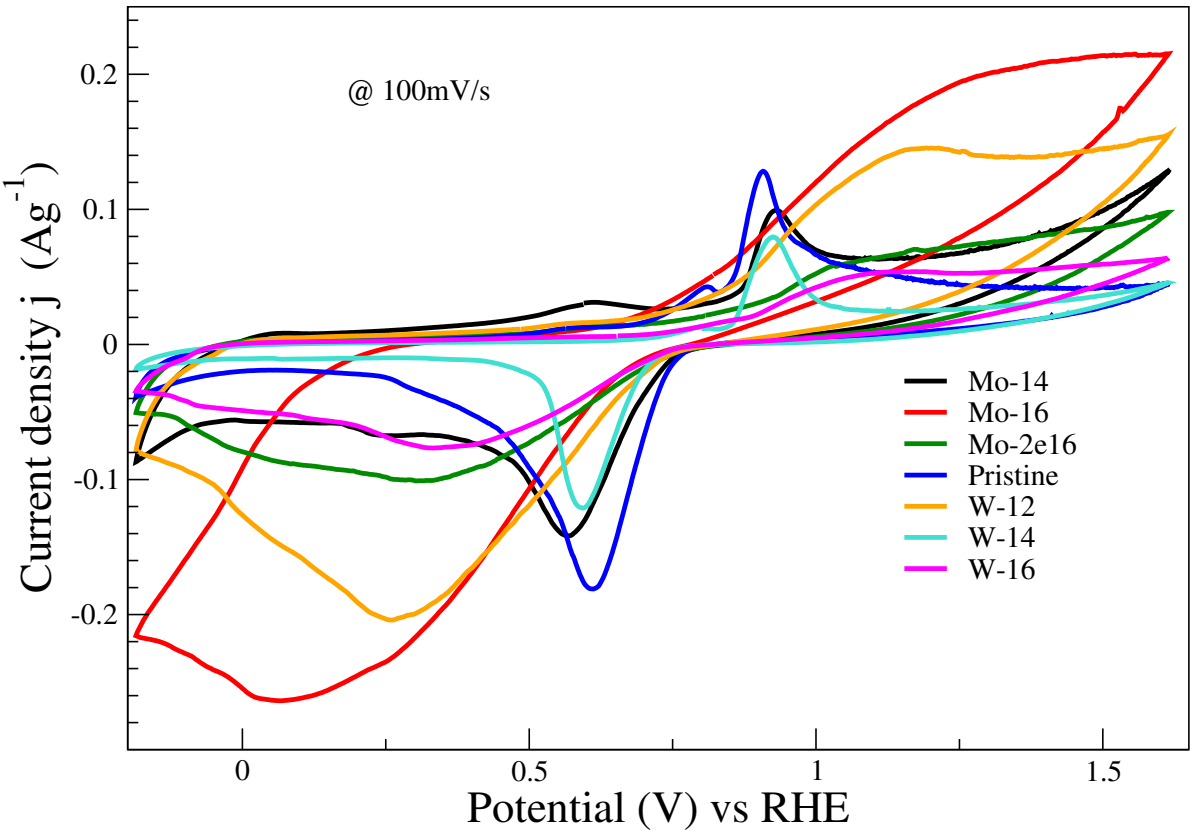

Figure 5.24: Cyclic voltammograms of MoS_2 implanted with Mo and W ions compared with the pristine at scan rate of 100 mV/s.

All the above cyclic voltammograms show evidence of charge storage. At lower scan rates (from 5 mV/s to 30 mV/s), W-12 sample shows higher charge storage capability. However, at higher scan rates (from 50 mV/s to 100 mV/s), Mo-16 sample performed better than the W-12 sample, based on the enclosed area. The CV enclosed area is not an accurate way to determine charge stored, hence a more reliable method for determining charge storage ability of an electrode is the charge-discharge technique, discussed in subsection 5.3.2.

5.3.2 Constant Current Charge-Discharge (CCCD)

CCCD technique was used to determine the abilities of each tested electrode, to charge and discharge. This is shown in Figs. 5.25 and 5.26, performed at current densities of 1 $mA{\cdot}g^{-1}$ and10 $mA{\cdot}g^{-1}$, respectively. From these CV curves alone one cannot accurately determine the pseudocapacitive performance of the samples. Constant current charge-discharge (CCCD or CD) measurements are a more reliable technique to evaluate the performance of electrode materials [121, 122], and were employed in this study. Based on these CCCD curves, W-12 leads in terms of the time it takes to charge and discharge. W-16 takes the shortest time for the same process. This implies that W-12 has a higher charge storage capability in comparison to all the other samples, with W-16 having the least.

As shown in Figs. 5.25 and 5.26, all the electrodes implanted with Mo ions show longer charge-discharge times compared to the pristine MoS_2 electrode. However, the W ions implanted electrodes depict lower charge-discharge time with reference to pristine MoS_2 electrode. The only exception is the W-12 electrode, which took 120 seconds more (shown in Fig. 5.25) to discharge after the pristine electrode had been fully discharged. This higher charge storage in W-12 can be attributed to the fact that most of the implanted ions were near the surface layers of MoS_2. This leads to an increased surface area for charge storage, either through deformation of the MoS_2 surface(s) or through widening of the interlayer gaps of the pristine material. Another scenario that could account for this high charge stored in W-12 would be a special case where W atom(s) end up lodging between the layers, which effectively results in supporting the MoS_2 layers and prevents them from caving in during the sodium ions intercalation and de-intercalation. Figs. 5.25 and 5.26 show a time difference of more than one order of magnitude in both charge and discharge, as expected.

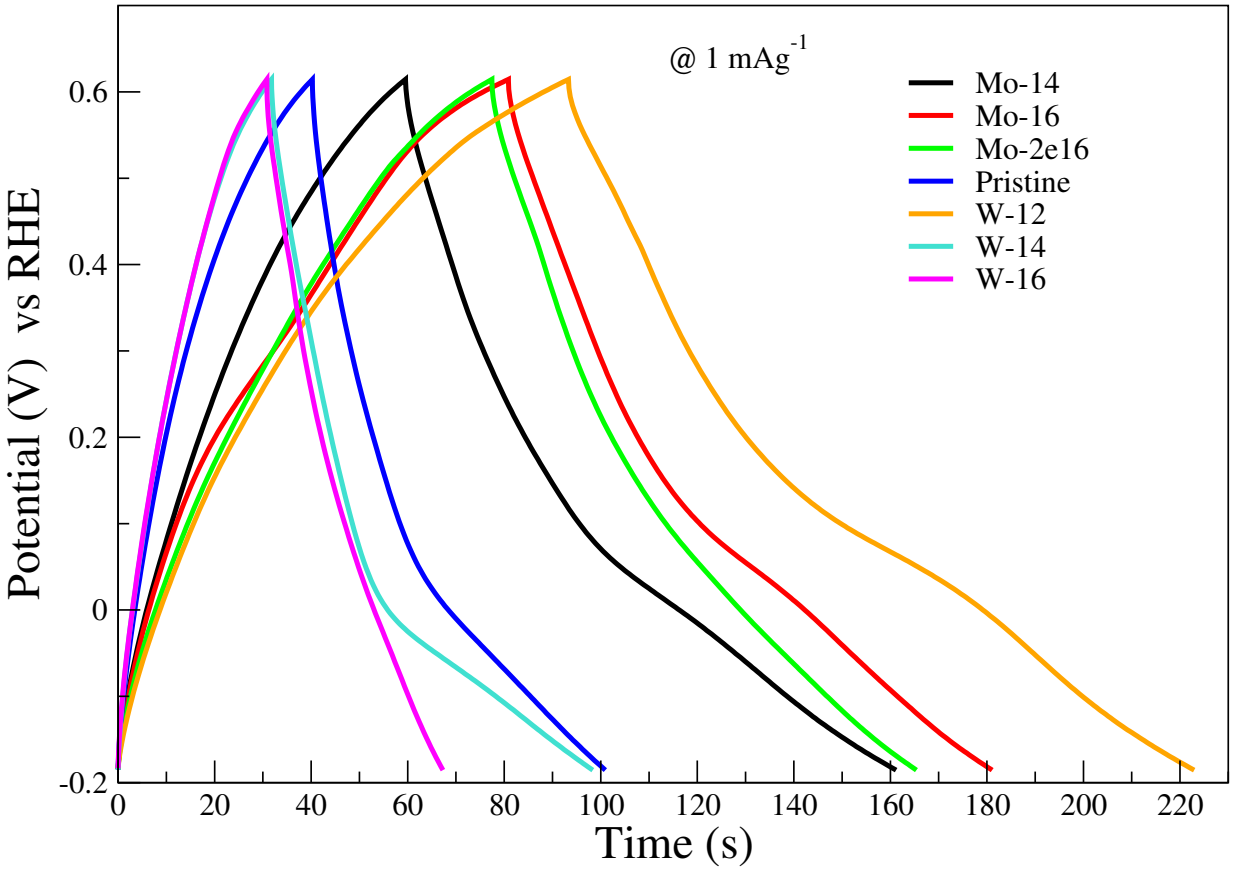

Figure 5.25: Charge-discharge curves of pristine MoS_2 and MoS_2 implanted with Mo and W ions at current density of 1 mA/g.

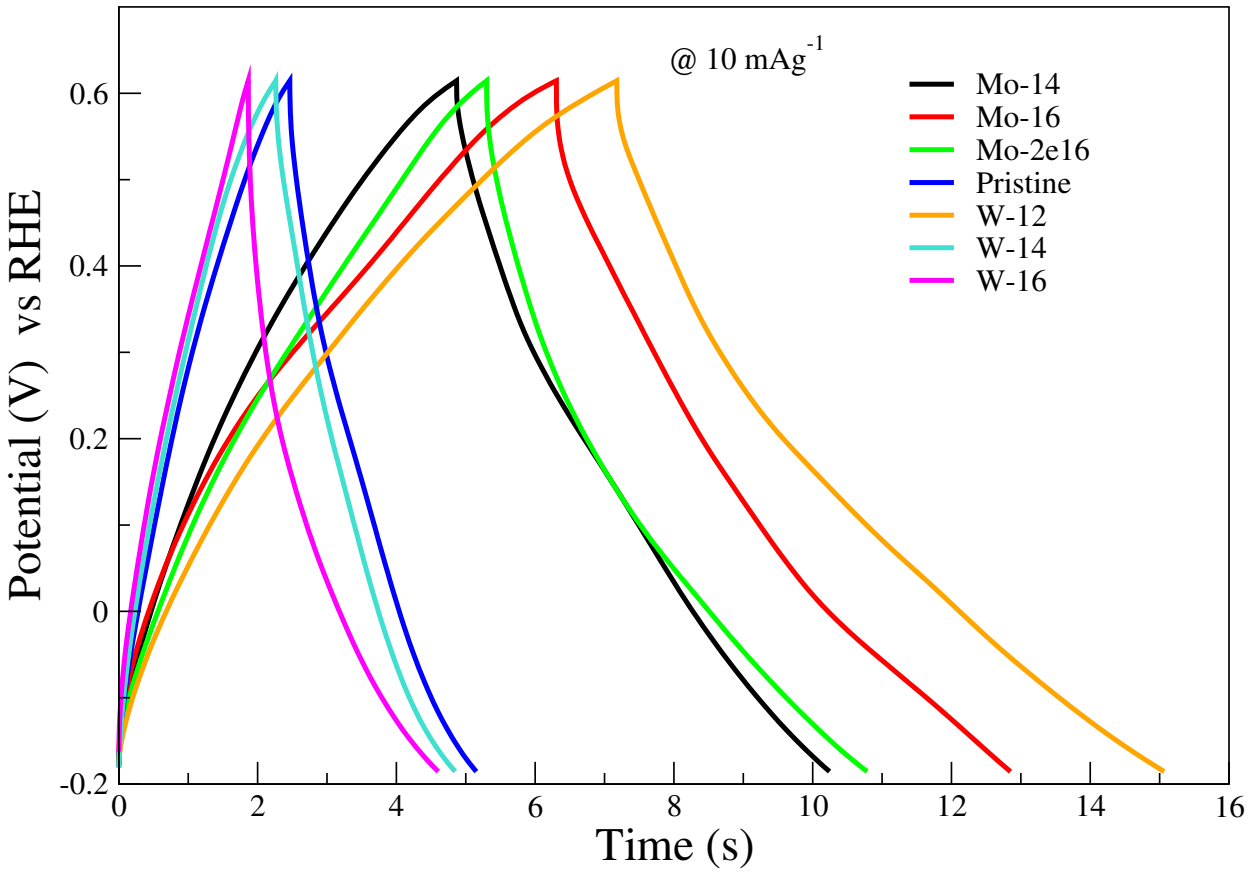

Figure 5.26: Charge-discharge curves of pristine MoS_2 and MoS_2 implanted with Mo and W ions at current density of 10 mA/g.

5.3.3 Determination of the Predominant Charge Storage Mechanism in Bulk MoS_2

Charge storage processes involve Faradaic and non-Faradaic mechanisms. In cyclic voltammetry, as described by Randles–Sevcik equation, the effect of scan rate on the peak current i_p (A) is associated with redox events which depends on the diffusional properties of the electroactive species, concentration and on the scan rate ν [123–125]. To establish the dominant processes in the electrodes used in this study, the scaling relations described by equations (5.6) and (5.7) [126] were invoked.

$$j = a\nu^b, \tag{5.6}$$

$$logj = blog\nu + loga, \tag{5.7}$$

where j is the current density, ν is the scan rate, while a and b are variable parameters.

A graph of $logj$ against $log\nu$ is used to evaluate the two adjustable parameters. However, b is what determines the predominant process. If the b value approaches 1, then the dominate charge storage mechanism is non-Faradaic (electrochemical double-layer capacitors (EDLC)), which is what happens in supercapacitors; whereas when the b value approaches 0.5, it is controlled by Faradaic processes such

as found in a battery system or a pseudocapacitor setup [126].

Using equation 5.7, Figs. 5.27, 5.28, 5.29, 5.30, 5.31, 5.32,5.33, 5.34, 5.35, 5.36, 5.37, 5.38, 5.39 and 5.40; were plotted to establish the predominate processess in our electrode material samples. To determine the peak current density values, both magnitudes of each cyclic voltammogram oxidation (peak1) and reduction (peak2), were evaluated. Logarithms of the current densities were then plotted against logarithms of each scan rate.

The b values were taken as the peak1 data best-fit straight line gradients. As shown in Figs. 5.28, 5.30, 5.32, 5.34, 5.36, 5.38 and 5.40; b value for pristine MoS_2 was found to be approximately 0.5, that of Mo implanted samples was an average of about 0.37, while that of W implanted samples averaged close to 0.31. These b values implied that the electrode material samples were mainly controlled by sodium ions (Na^+) intercalations and de-intercalations; with the Na^+ coming from the 1M Na_2SO_4 electrolyte used.

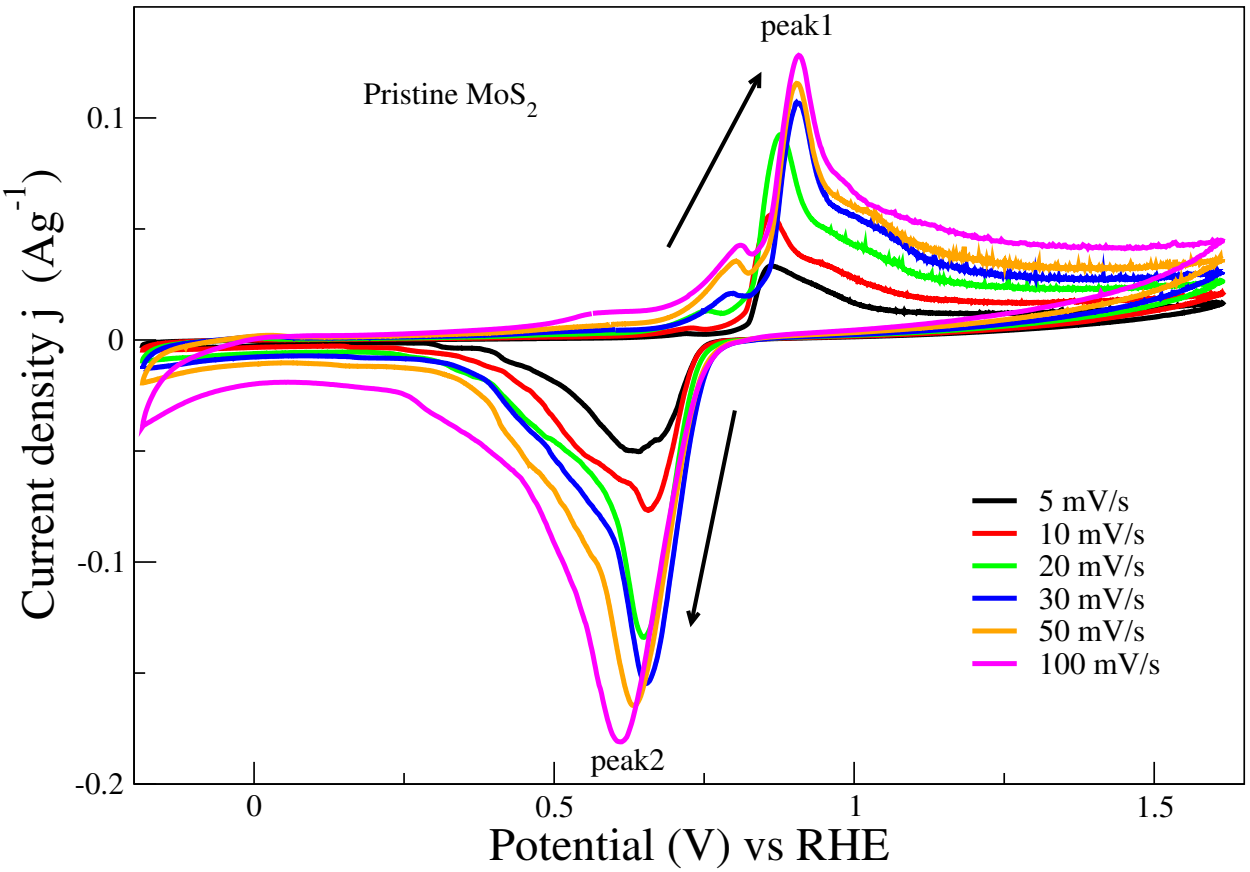

Figure 5.27: Cyclic voltammogram peaks a for pristine MoS_2.

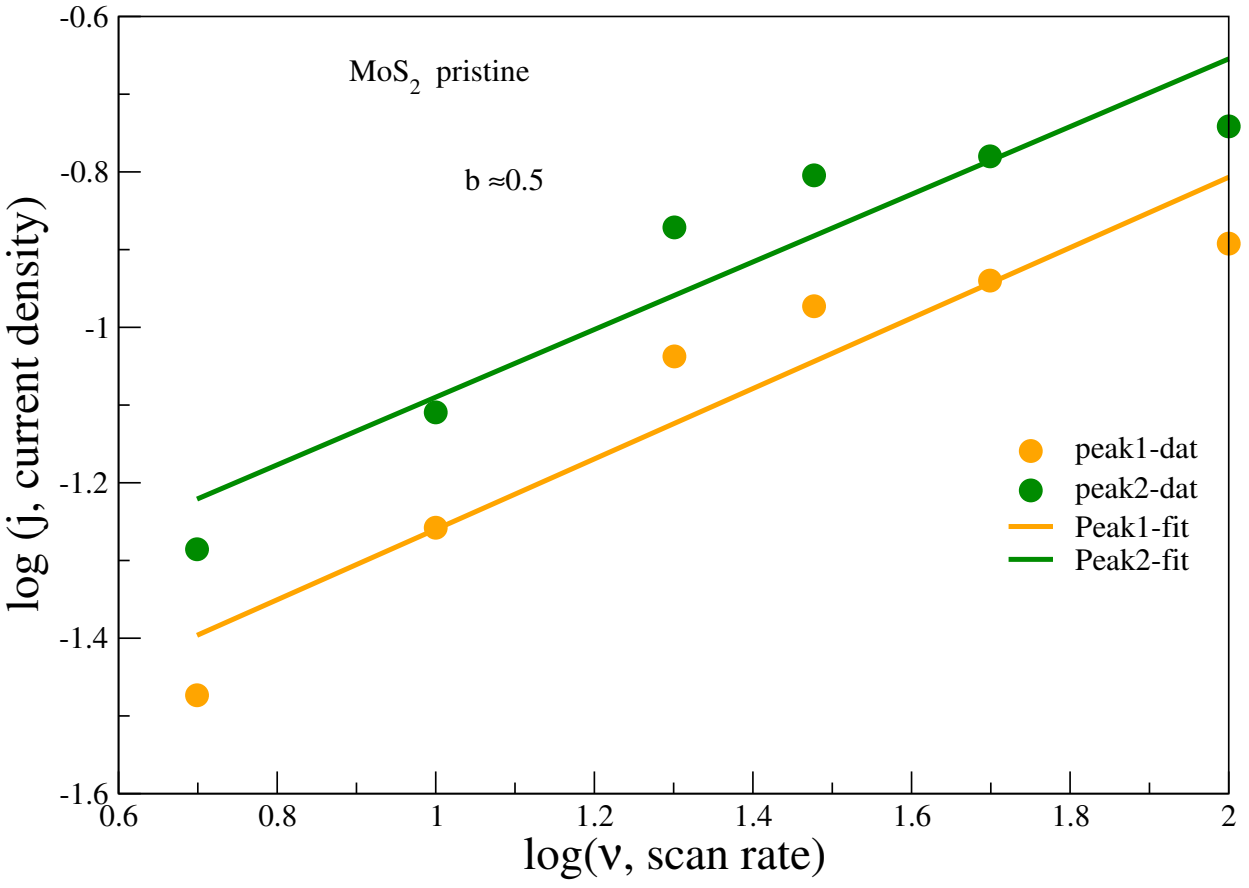

Figure 5.28: Graph of log$j$ vs logν for pristine MoS_2.

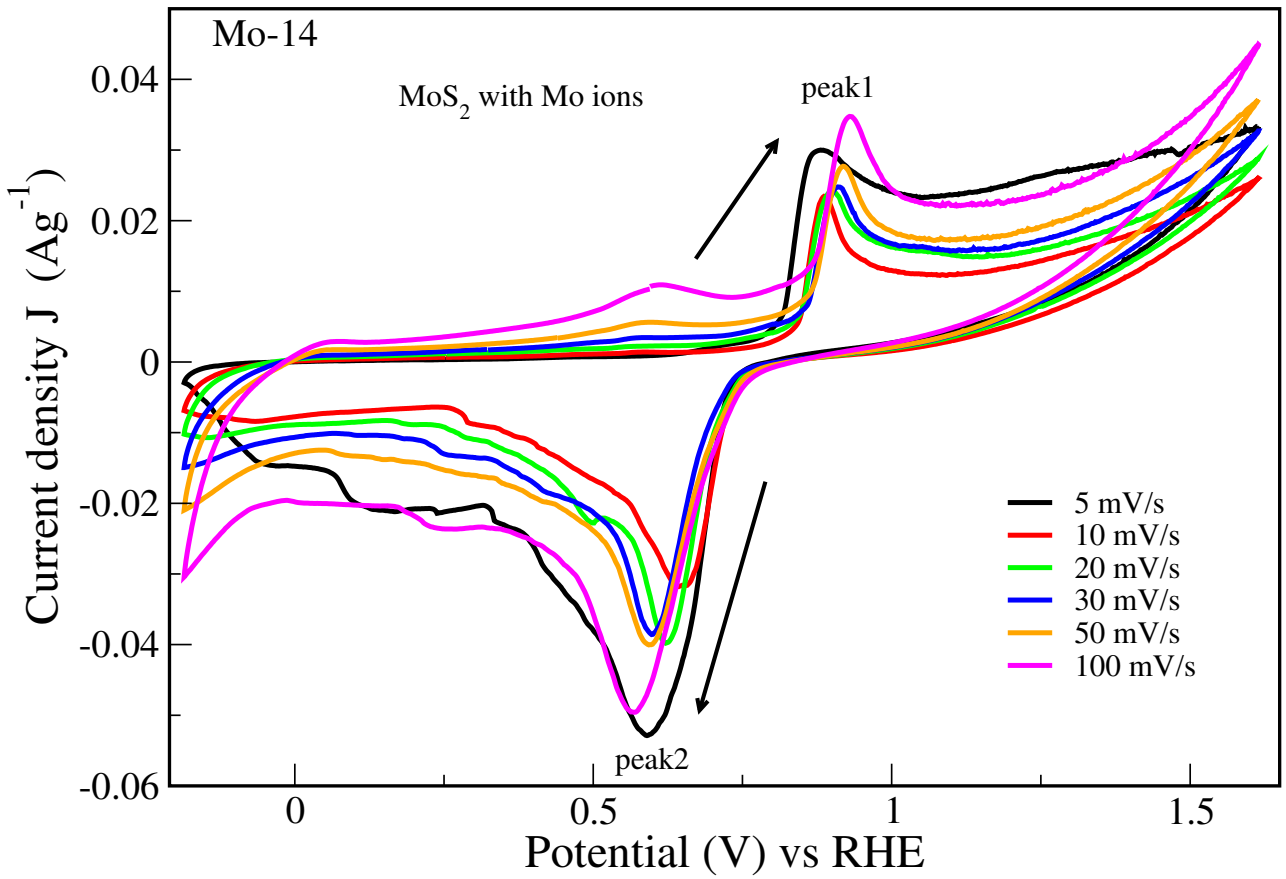

Figure 5.29: Cyclic voltammogram peaks for Mo implanted MoS_2 with a fluence of 10^{14} ions/cm^2.

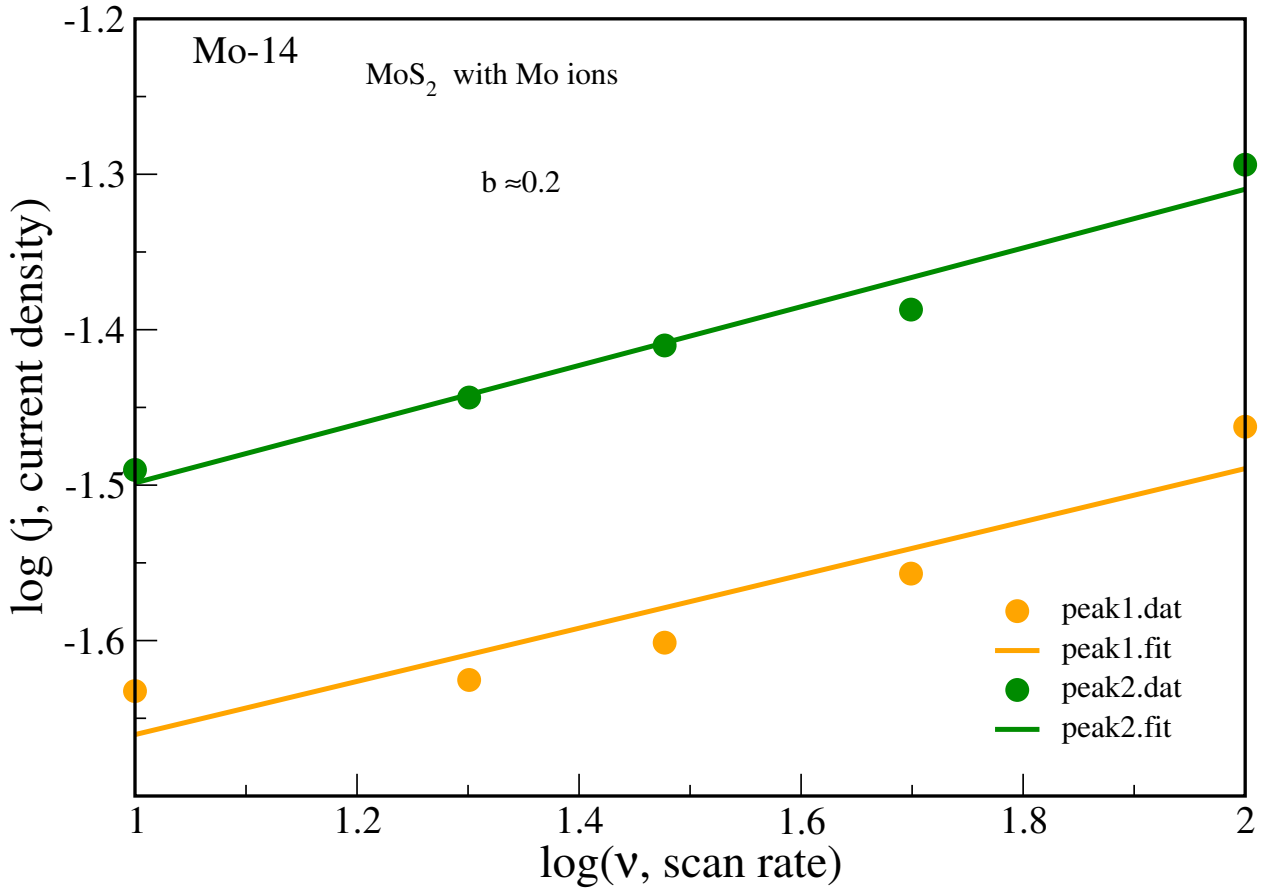

Figure 5.30: Graph of log$j$ vs logν for Mo implanted MoS_2 with a fluence of 10^{14} ions/cm^2.

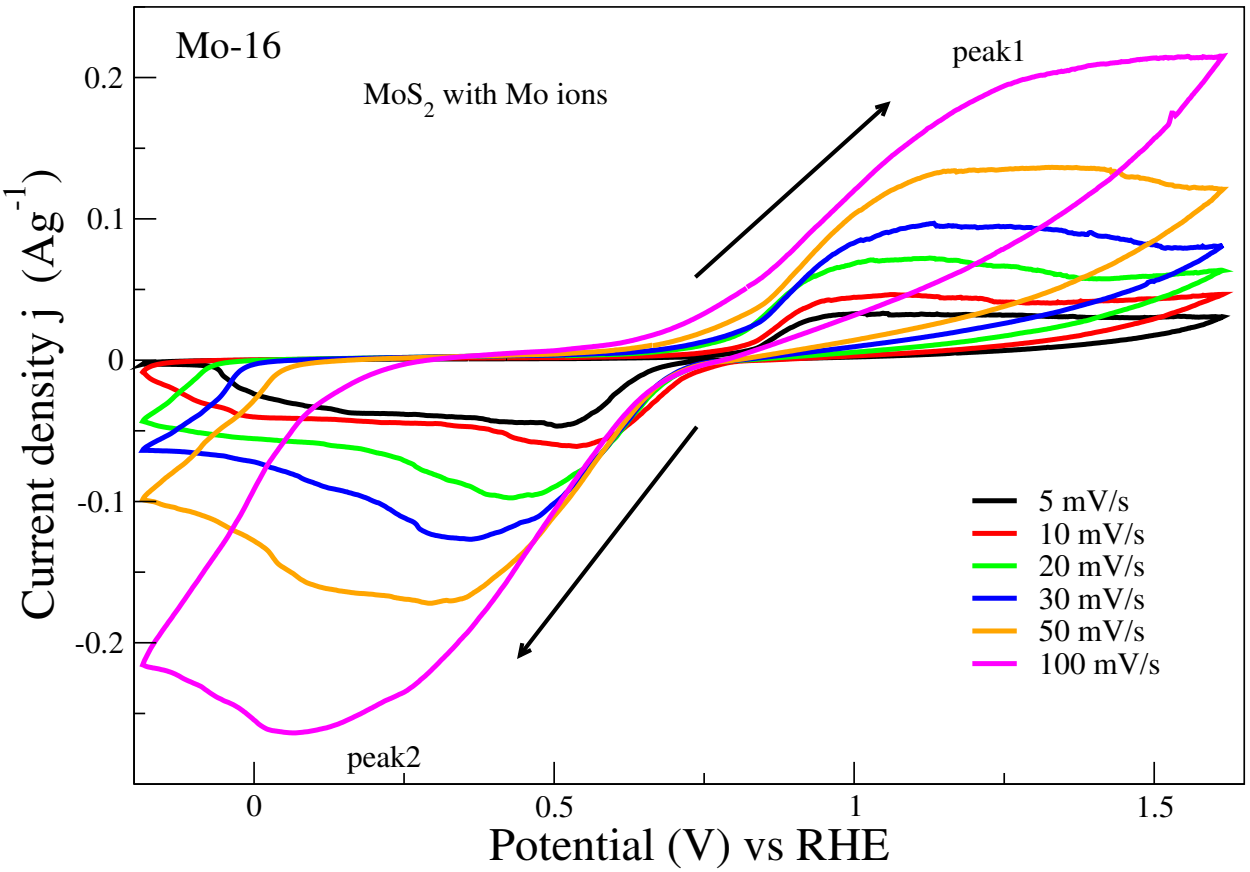

Figure 5.31: Cyclic voltammogram peaks for Mo implanted MoS_2 with a fluence of 10^{16} ions/cm^2.

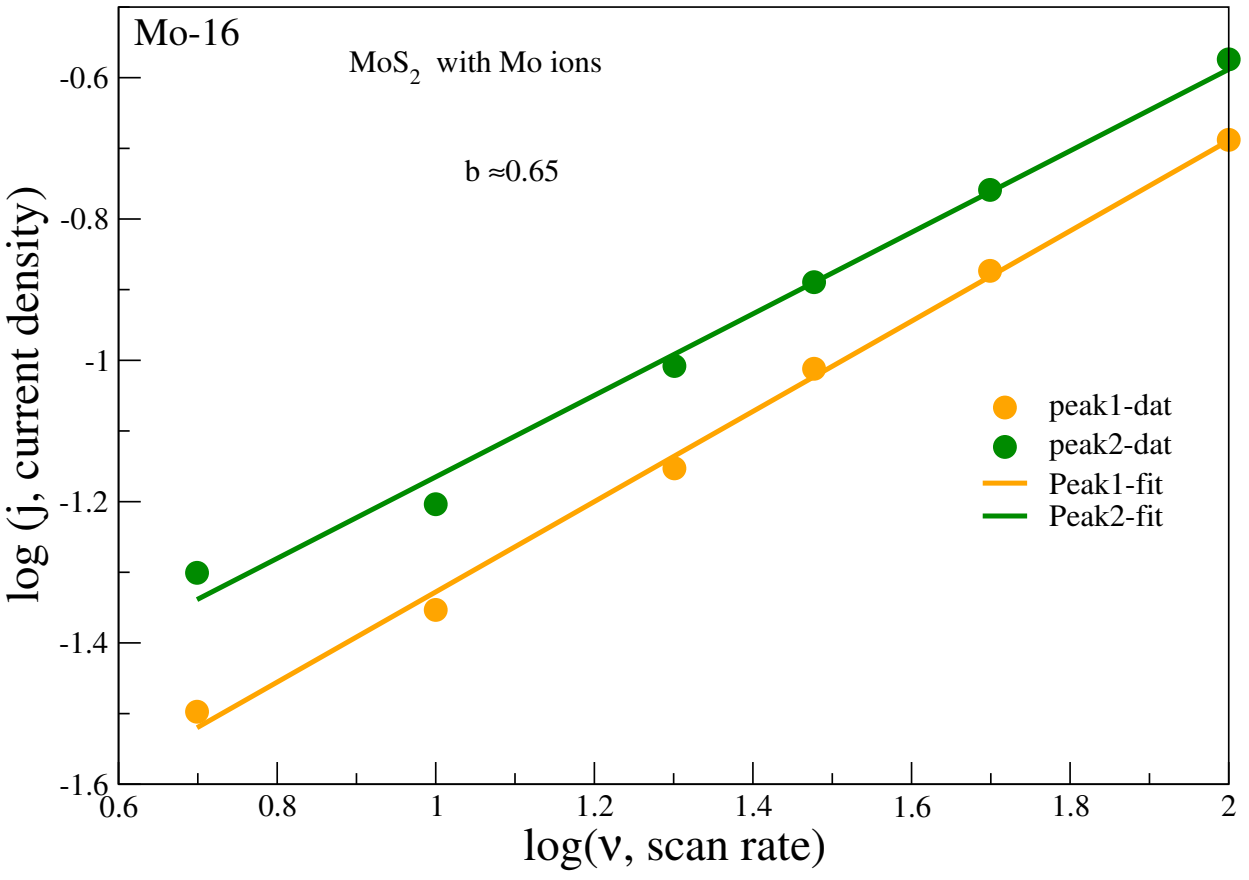

Figure 5.32: Graph of log$j$ vs logν for Mo implanted MoS_2 with a fluence of 10^{16} ions/cm^2.

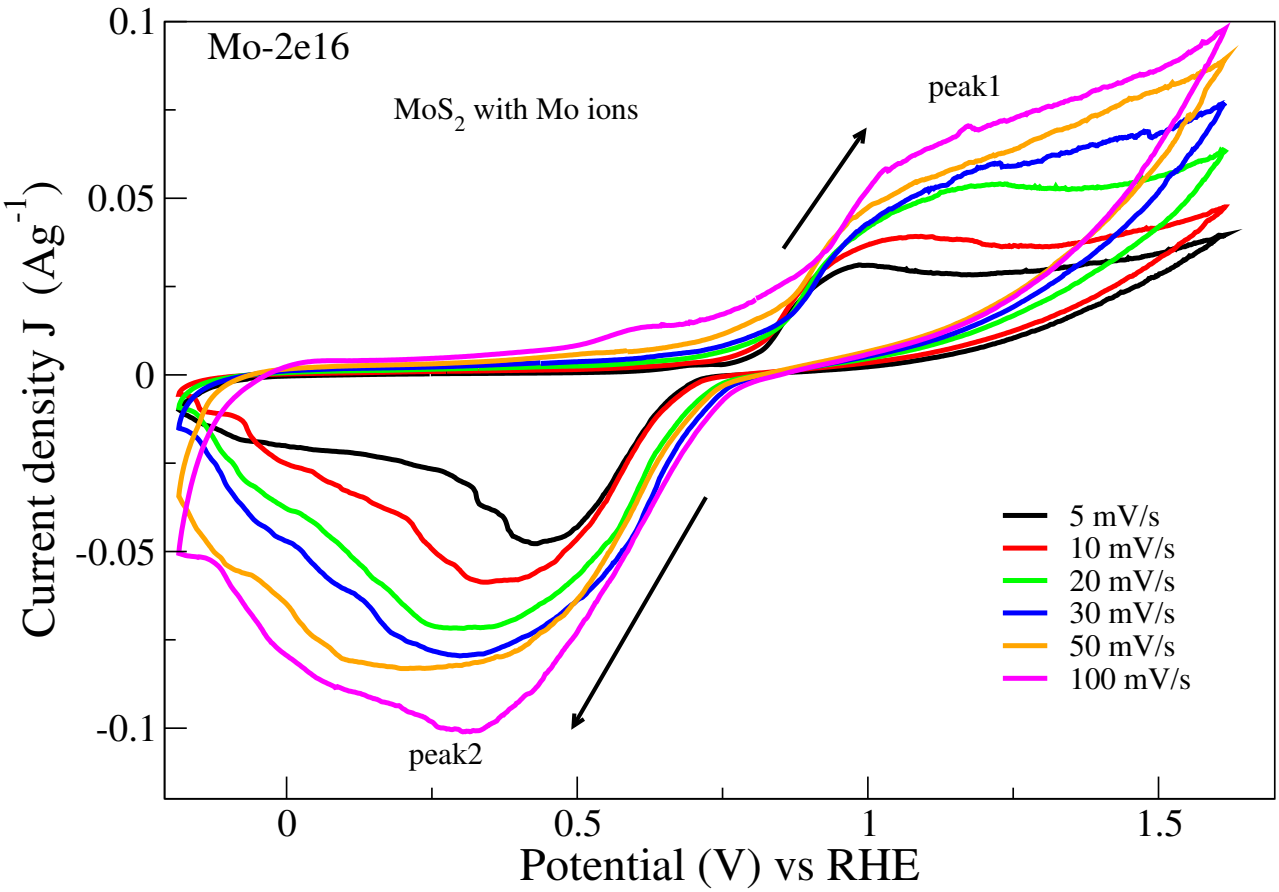

Figure 5.33: Cyclic voltammogram peaks for Mo implanted MoS_2 with a fluence of 2×10^{16} ions/cm^2.

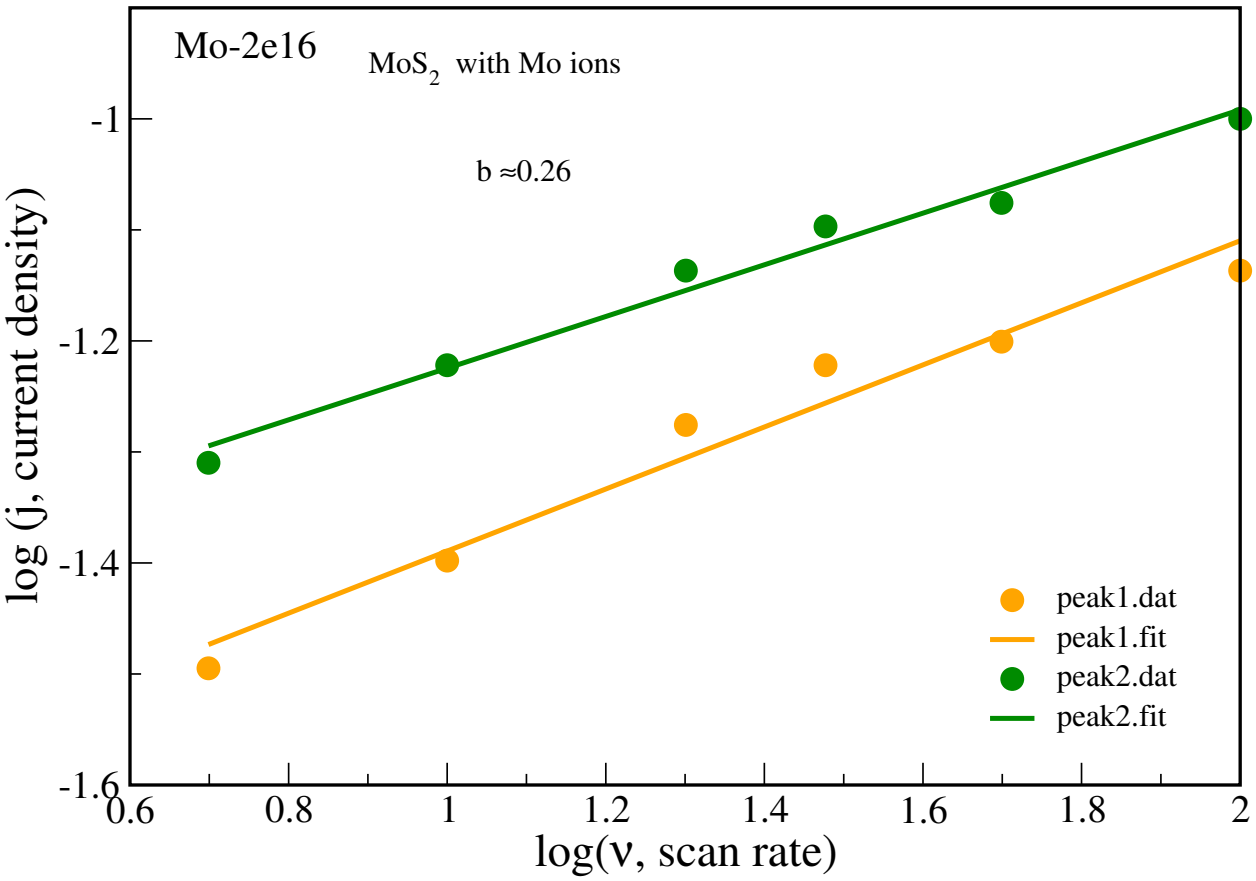

Figure 5.34: Graph of log$j$ vs logν for Mo implanted MoS_2 with a fluence of 2×10^{16} ions/cm^2.

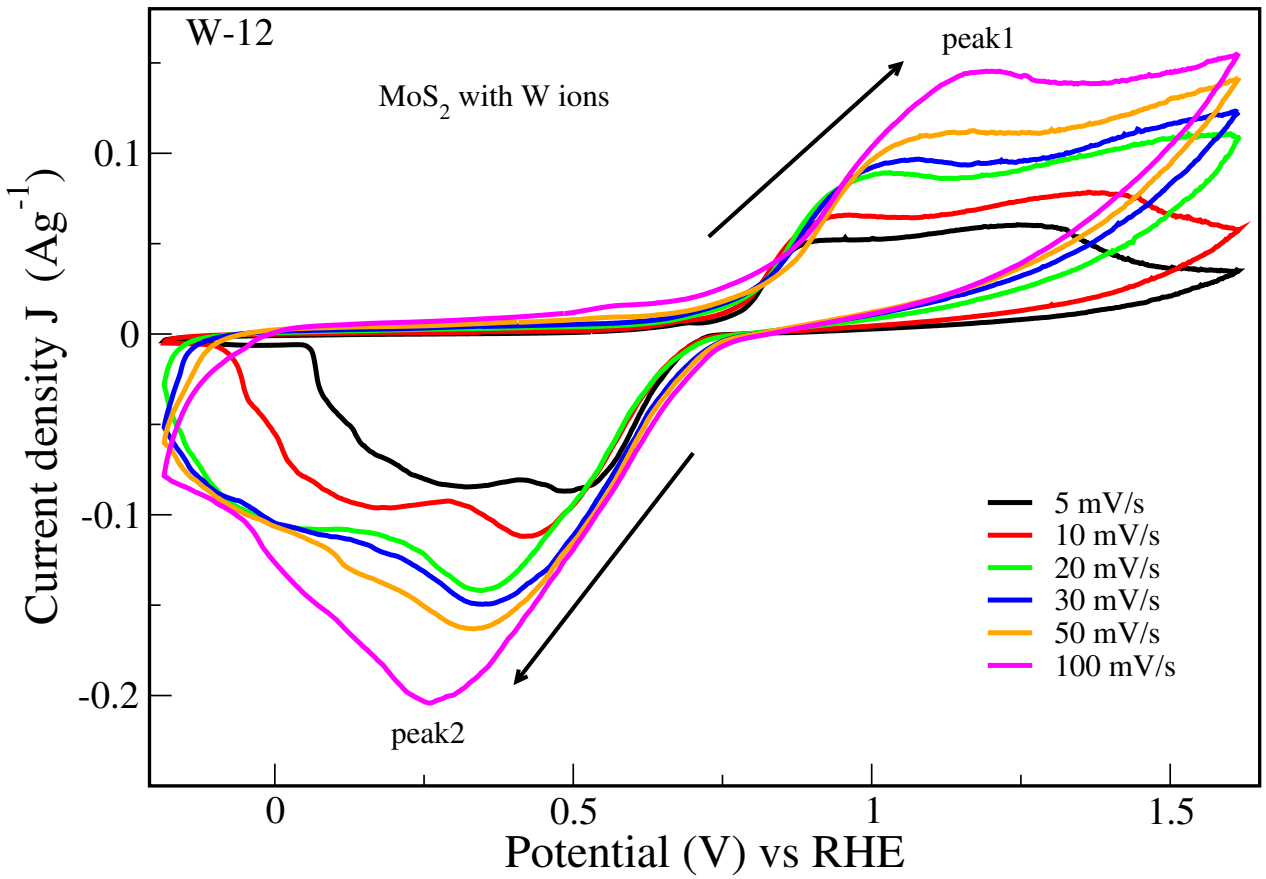

Figure 5.35: Cyclic voltammogram peaks for W implanted MoS_2 with a fluence of 10^{12} ions/cm^2.

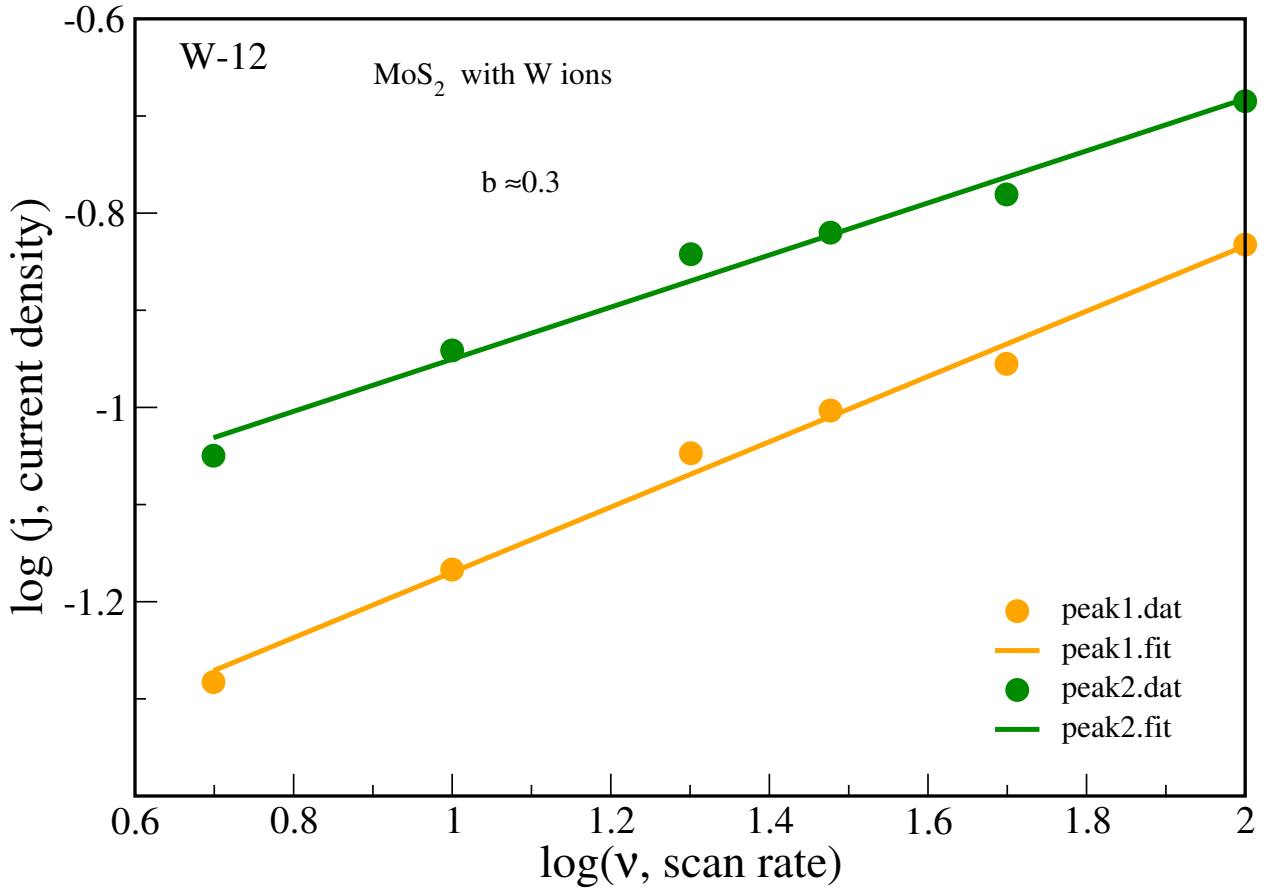

Figure 5.36: Graph of log$j$ vs logν for W implanted MoS_2 with a fluence of 10^{12} ions/cm^2.

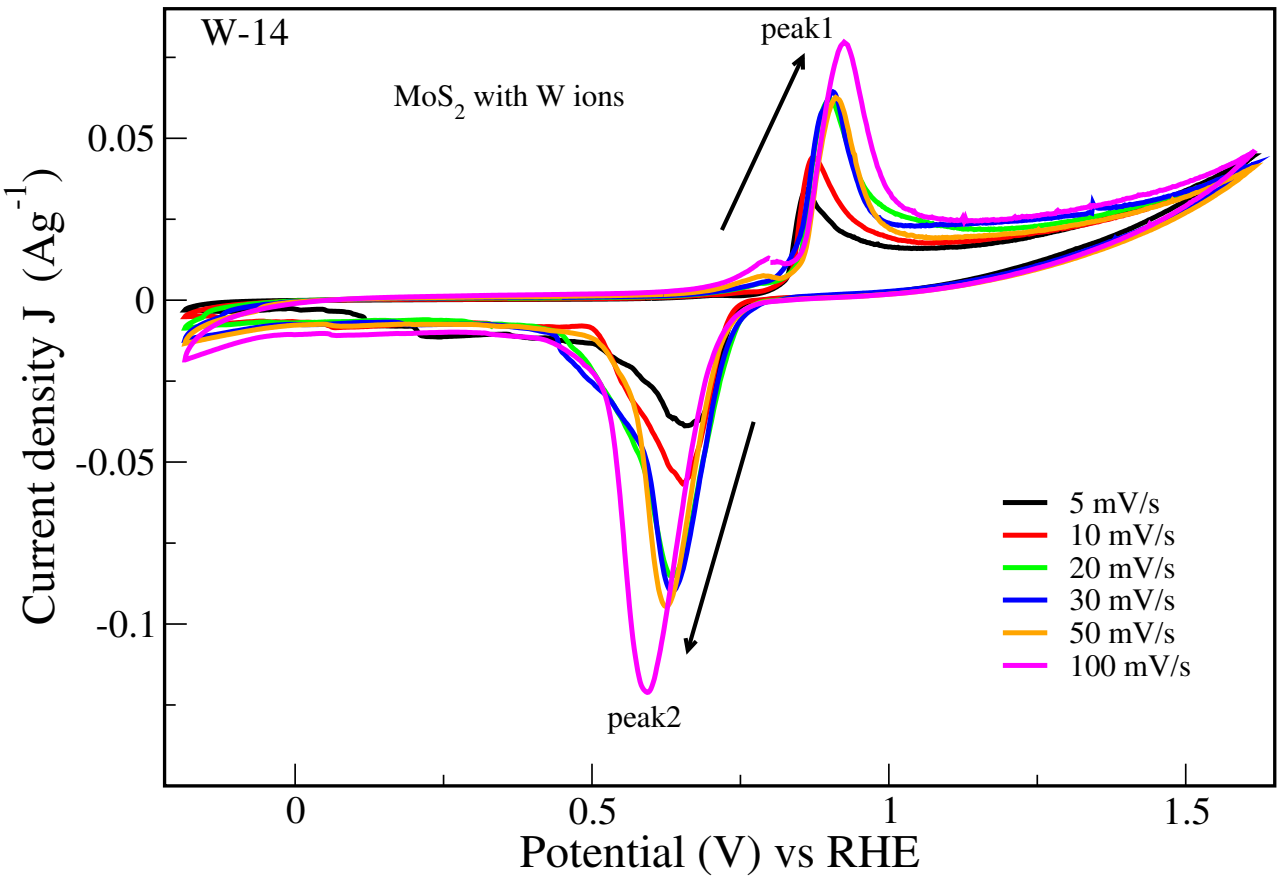

Figure 5.37: Cyclic voltammogram peaks for W implanted MoS_2 with a fluence of 10^{14} ions/cm^2.

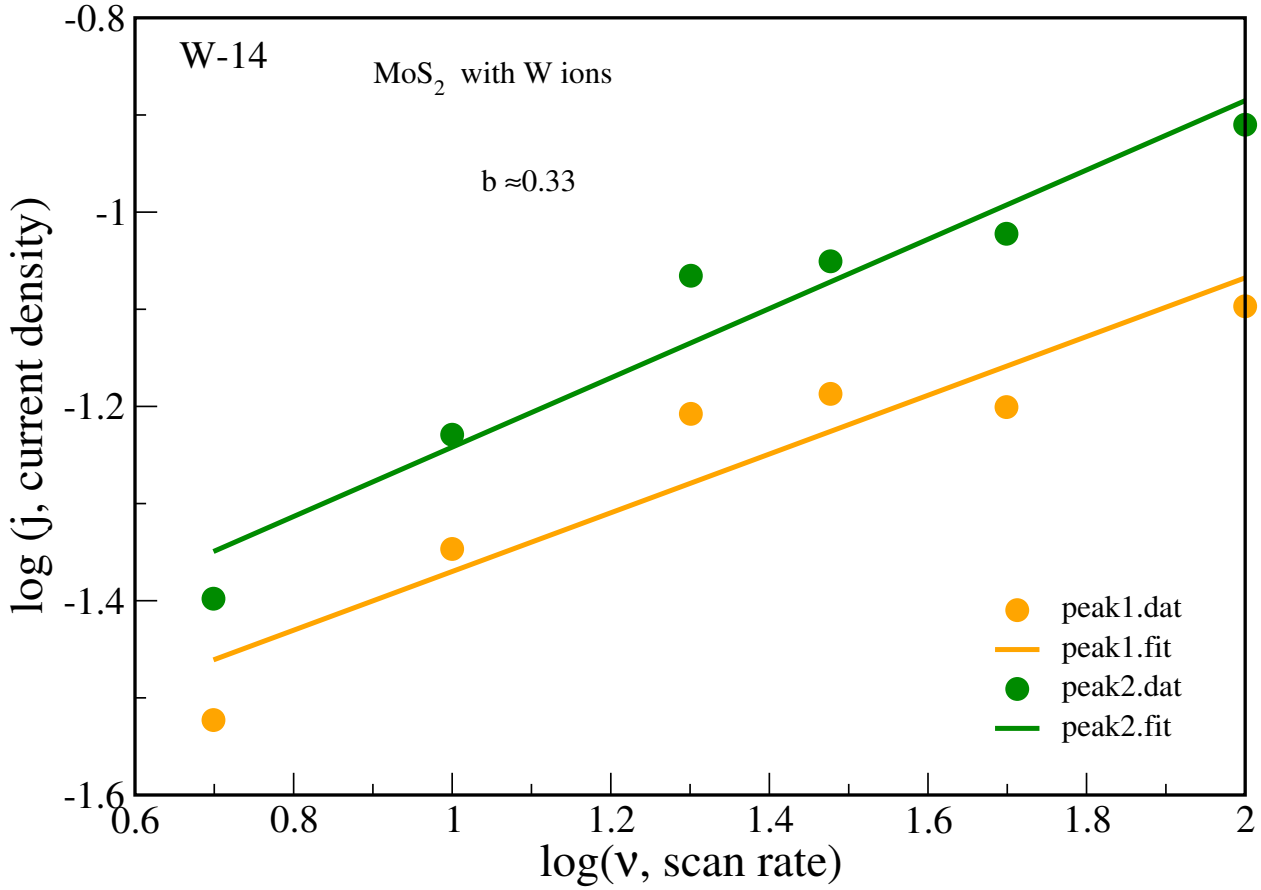

Figure 5.38: Graph of log$j$ vs logν for W implanted MoS_2 with a fluence of 10^{14} ions/cm^2.

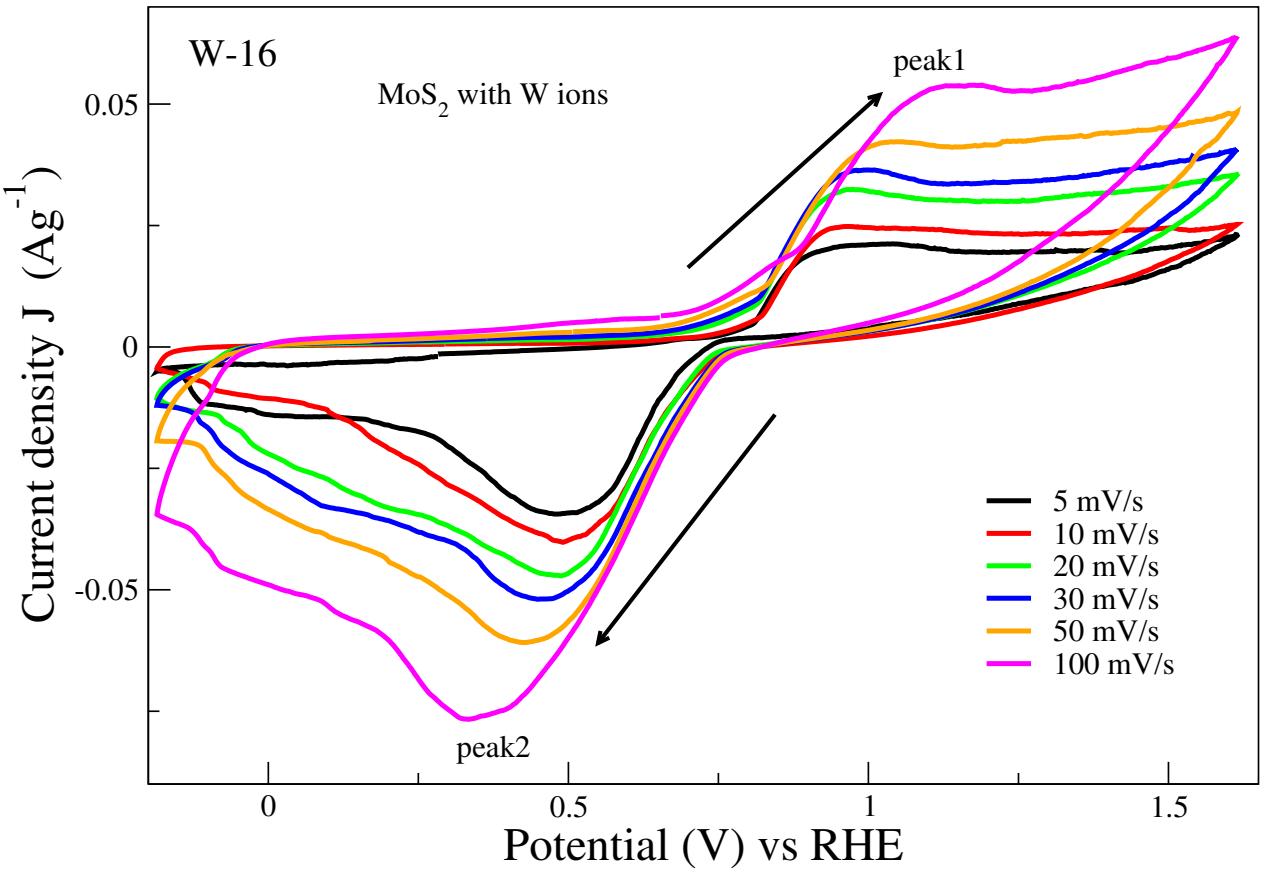

Figure 5.39: Cyclic voltammogram peaks for W implanted MoS_2 with a fluence of 10^{16} ions/cm^2.

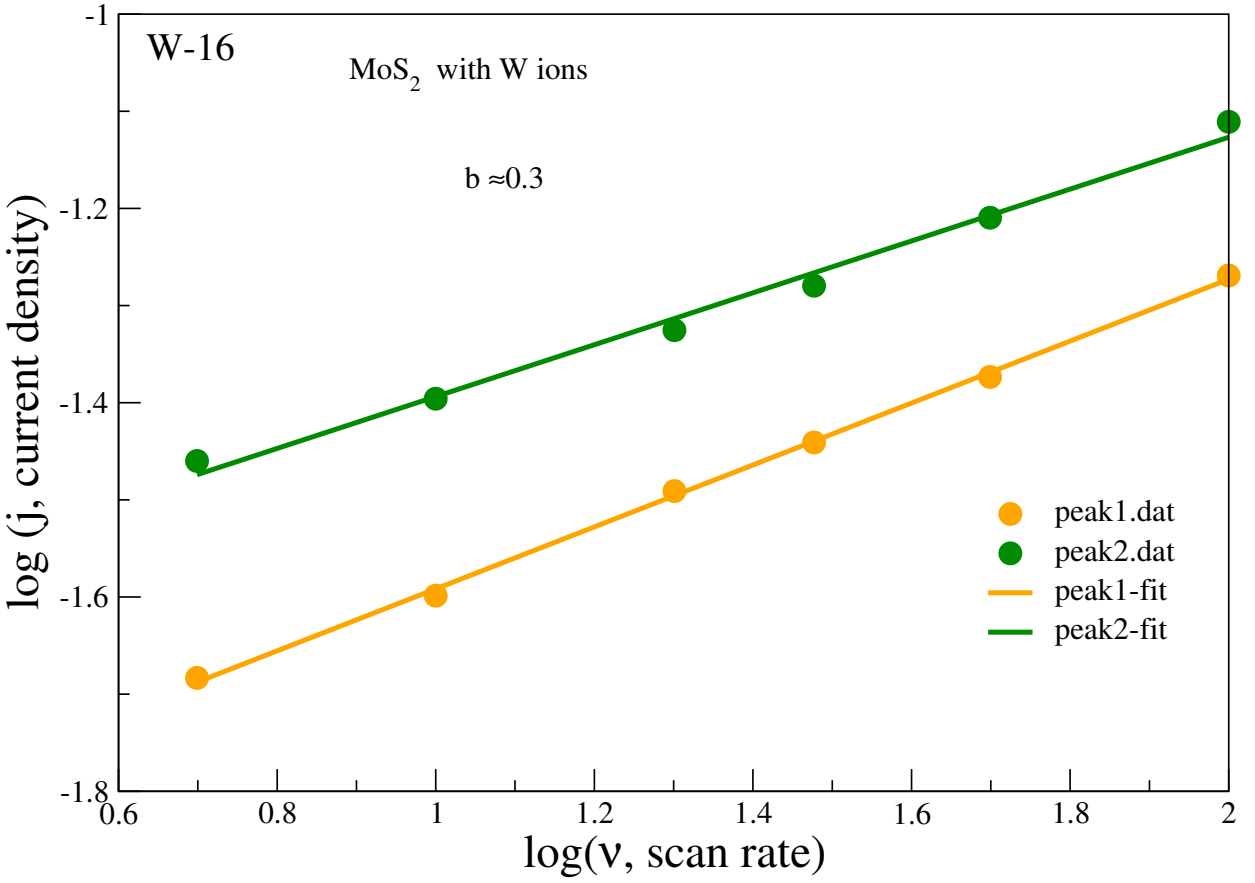

Figure 5.40: Graph of log$j$ vs logν for W implanted MoS_2 with a fluence of 10^{16} ions/cm^2.

5.3.4 Diffusion Coefficients

From Subsection 5.3.3, it is clear that there was diffusion of sodium ions into all the samples studied. This prompted this study to find out the diffusion coefficients of pristine sample and also that of the MoS_2 samples implanted with Mo ions and W ions.

To evaluate diffusion coefficient (D), Randles-Sevcik equation 5.8 was used [127].

$$i_p = 0.4463nFAC\left(\frac{nF\nu D}{RT}\right)^{\frac{1}{2}}, \tag{5.8}$$

where i_p is the current maximum in (A), n is the number of electrons transferred in the redox event (usually 1), A is the electrode area in (cm^2), F is the Faraday constant in ($C{\cdot}mol^{-1}$), D is the diffusion coefficient in ($cm^2{\cdot}s^{-1}$), C is the concentration in ($mol{\cdot}cm^{-3}$), ν is the scan rate in $V{\cdot}s^{-1}$, R is the Gas constant in ($J{\cdot}K^{-1}{\cdot}mol^{-1}$) and T is the temperature in (K). Equation 5.8 reduces to;

$$i_p = 268600AC(n^3D\nu)^{\frac{1}{2}}, \tag{5.9}$$

at 25 °C.[128]

The observed redox (battery-like or Faradaic) processes in this work likely follow the established 2-step process of intercalation followed by conversion [129]:

$$MoS_2 + xNa^+ + xe^- \rightarrow Na_xMoS_2 \tag{5.10}$$

$$Na_xMoS_2 + (4-x)Na^+ + (4-x)e^- \rightarrow 2Na_2S + Mo \tag{5.11}$$

Where equation 5.10 in for intercation reaction, while equation 5.11 is the conversion reaction.

The peak currents I_p (A) were extracted from cyclic voltammograms and the corresponding scan rates ν (V/s), shown in Figures 5.27, 5.29, 5.31, 5.33, 5.35, 5.37 and 5.39.

The D values were calculated from the slopes of Figs. 5.41, 5.42 and 5.43 and found to be as follows: pristine MoS_2 showed a diffusion coefficient of 7.1×10^{-6} cm^2/s while MoS_2 implanted with Mo ions (Mo-16) and MoS_2 implanted with W ions (W-16) showed diffusion coefficients of 8.09×10^{-6} cm^2/s and 4.21×10^{-6} cm^2/s, respectively. From these values, diffusion rate was highest when MoS_2 was implanted with W ions. The D values for all the samples are shown in Table 5.4. However, these D values are not linearly related to charge storage capabilities.

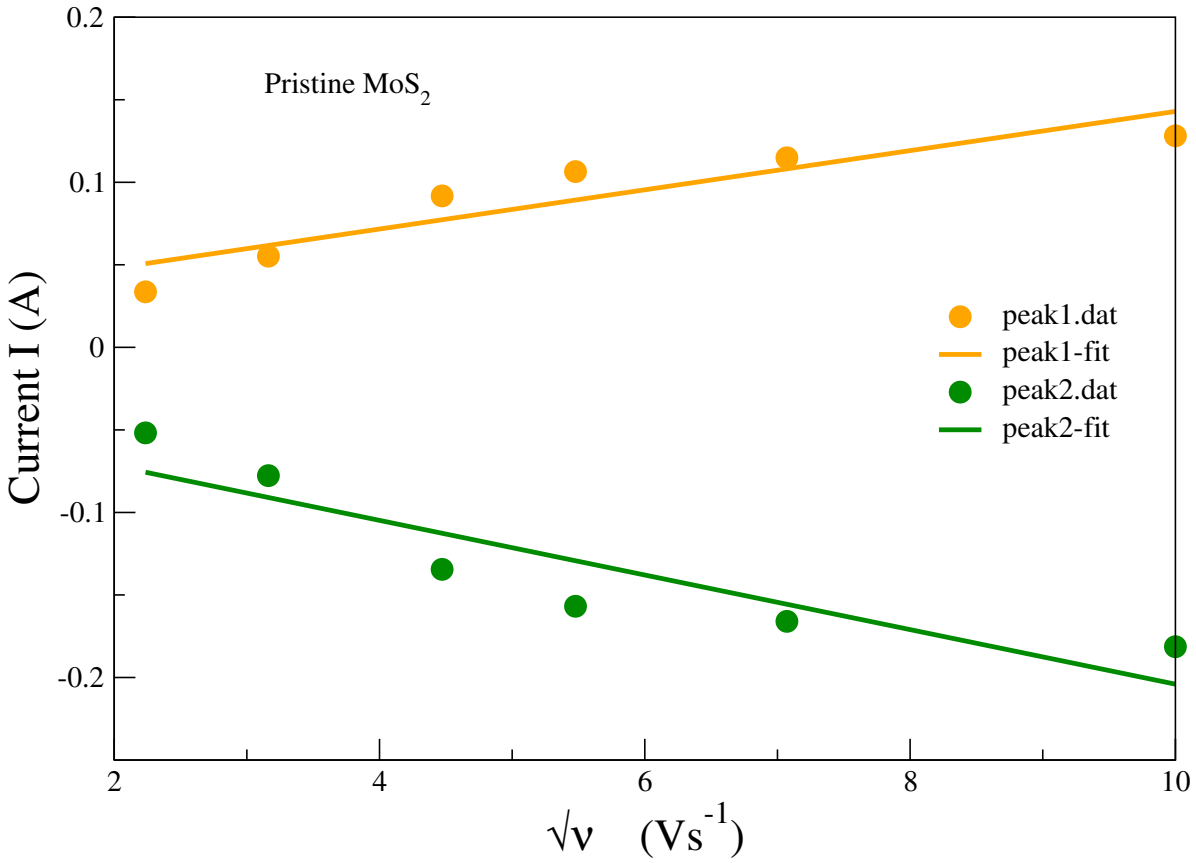

Figure 5.41: Graph current I vs square root of scan rate ν; for pristine MoS_2.

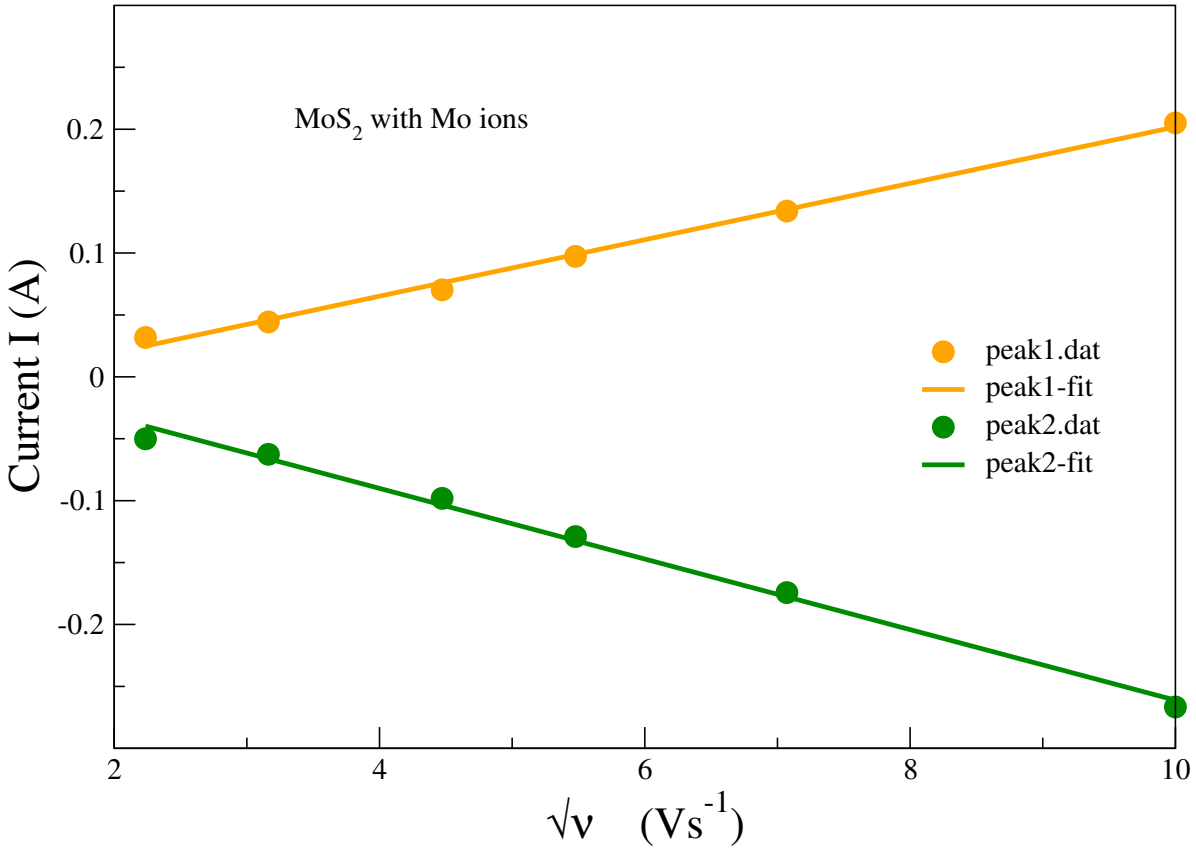

Figure 5.42: Graph current I vs square root of scan rate ν; for MoS_2 implanted with Mo ions (Mo-16).

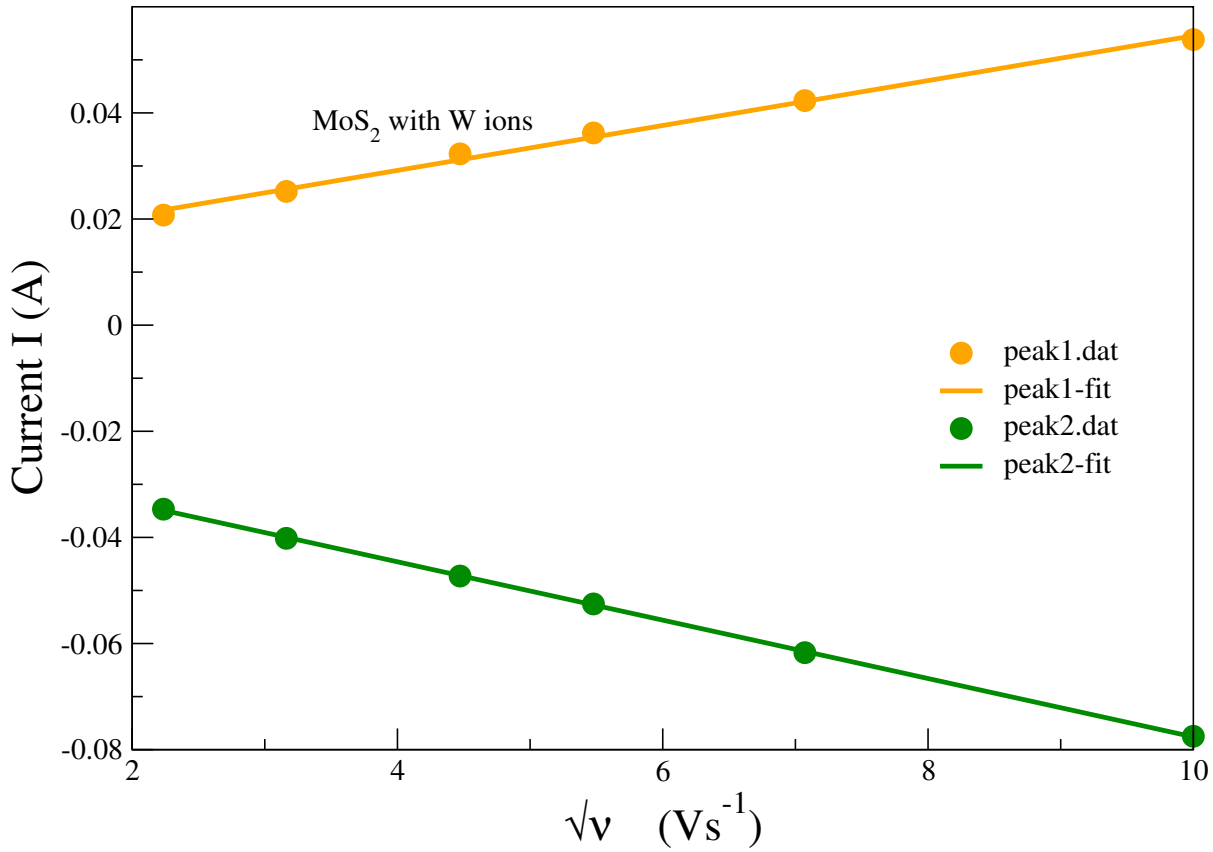

Figure 5.43: Graph current I vs square root of scan rate ν; for MoS_2 implanted with W ions (W-16).

5.3.5 Standard Rate Constant

Standard rate constant K_s is a vital parameter in electrode kinetics that measures the kinetic facility of redox couple. A large K_s value implies a faster attainment of equilibrium by a system, while smaller K_s value shows a sluggish system before it can equilibrize. The largest measured K_s values are in the order of 1-10 cm/s and can drop as low as 10^{-9} cm/s depending on the complexity of a reaction [130].

K_s for each of the electrode was obtained from Equation 5.12 by plotting ln i_p against $(E_p - E^{0'})$ at different scan rates. The other symbols have the usual meanings as stated in Equation 5.8.

$$i_p = 0.227nFACK_s \exp[-(\alpha nF/RT)(E_p - E^{0'})], \tag{5.12}$$

where i_p are the anodic and cathodic peak currents, E_p are the anodic and cathodic peak voltages and $E^{0'} = E_{1/2}$ for different scan rates, extracted as shown in Fig. 5.44.

Figures 5.45, 5.46, 5.47, 5.48, 5.49, 5.50 and 5.51, were obtained for all the electrodes and K_s calculated from the ln i_p data fit intercept.

All the b values, diffusion coefficient values and standard rate constants are summarised in Table 5.4. These are calculated averages of anodic and cathodic electrochemical processes.

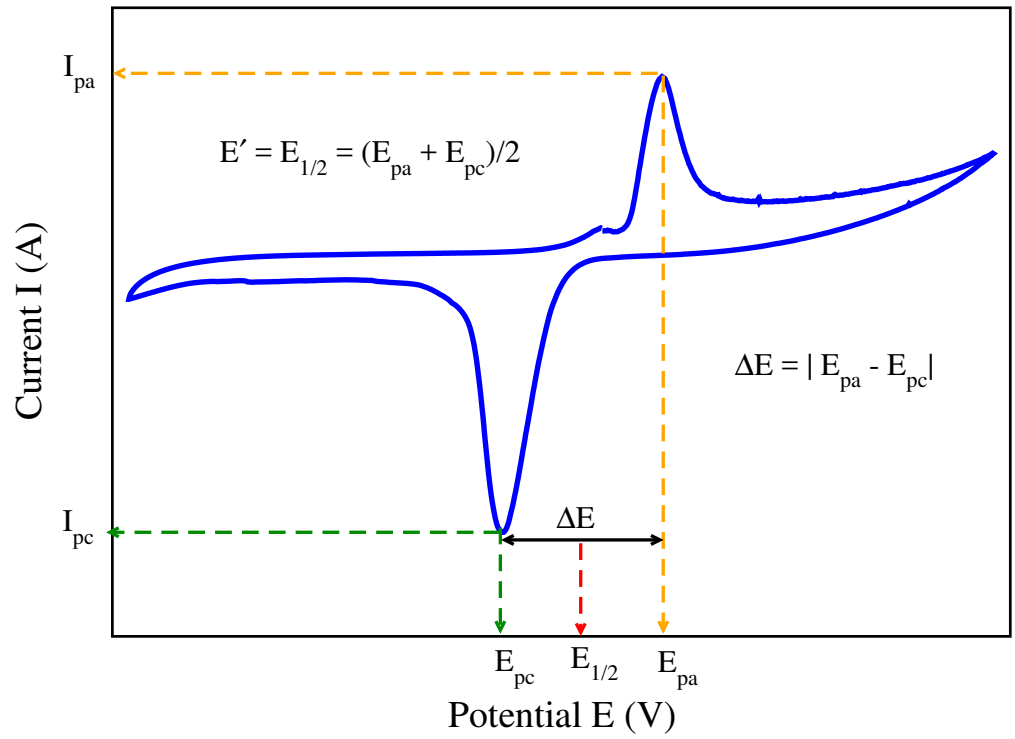

Figure 5.44: Schematic CV voltammogram where i_{pa}, E_{pa}, i_{pc} and E_{pc} are anodic and cathodic peaks currents and peak potentials, respectively.

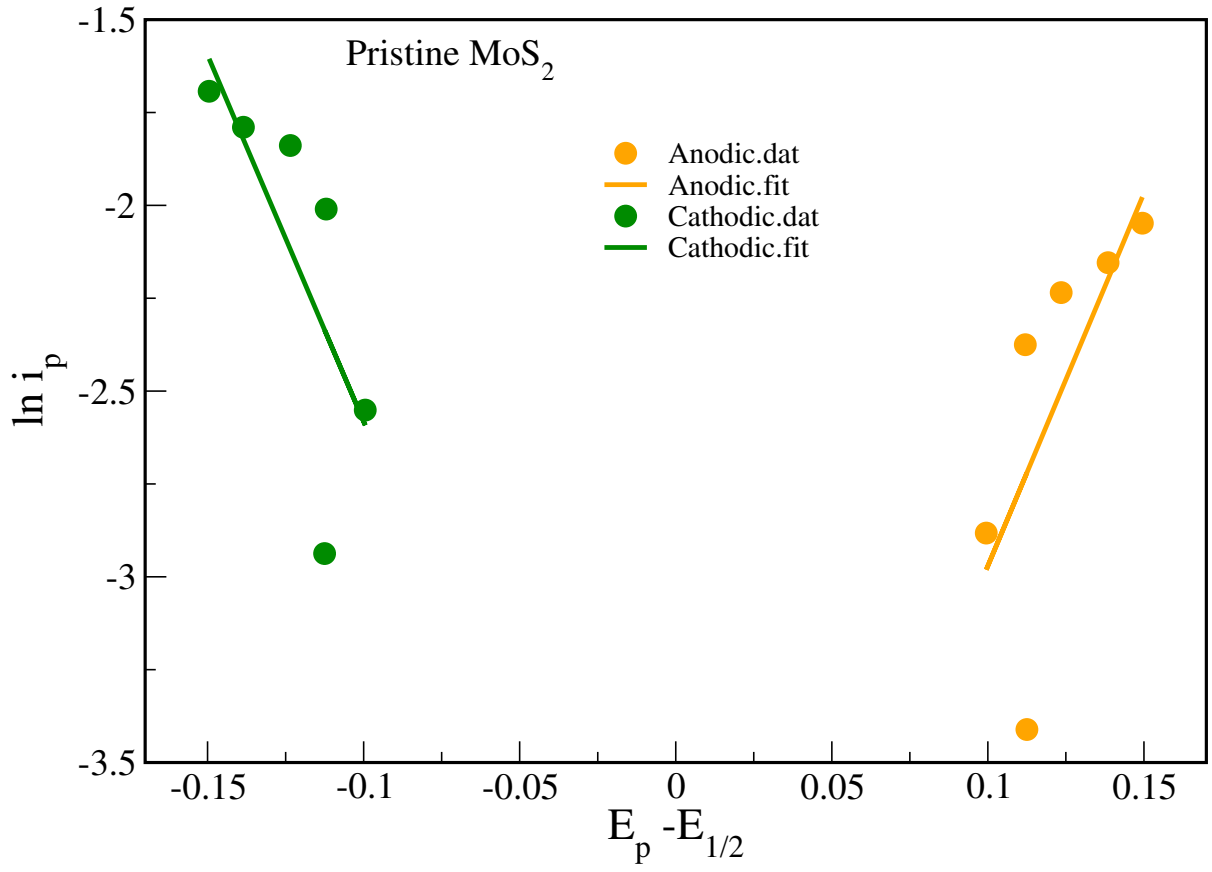

Figure 5.45: Graph of ln i_p vs $(E_p - E_{1/2})$ for pristine MoS_2.

From Table 5.4, all the ion implanted electrodes show improved electrode kinetics, implying that ion implantation reduces the equilibration time in MoS_2. W-12 reporting 18.42 $\times 10^{-6}$ cm·s^{-1} standard rate

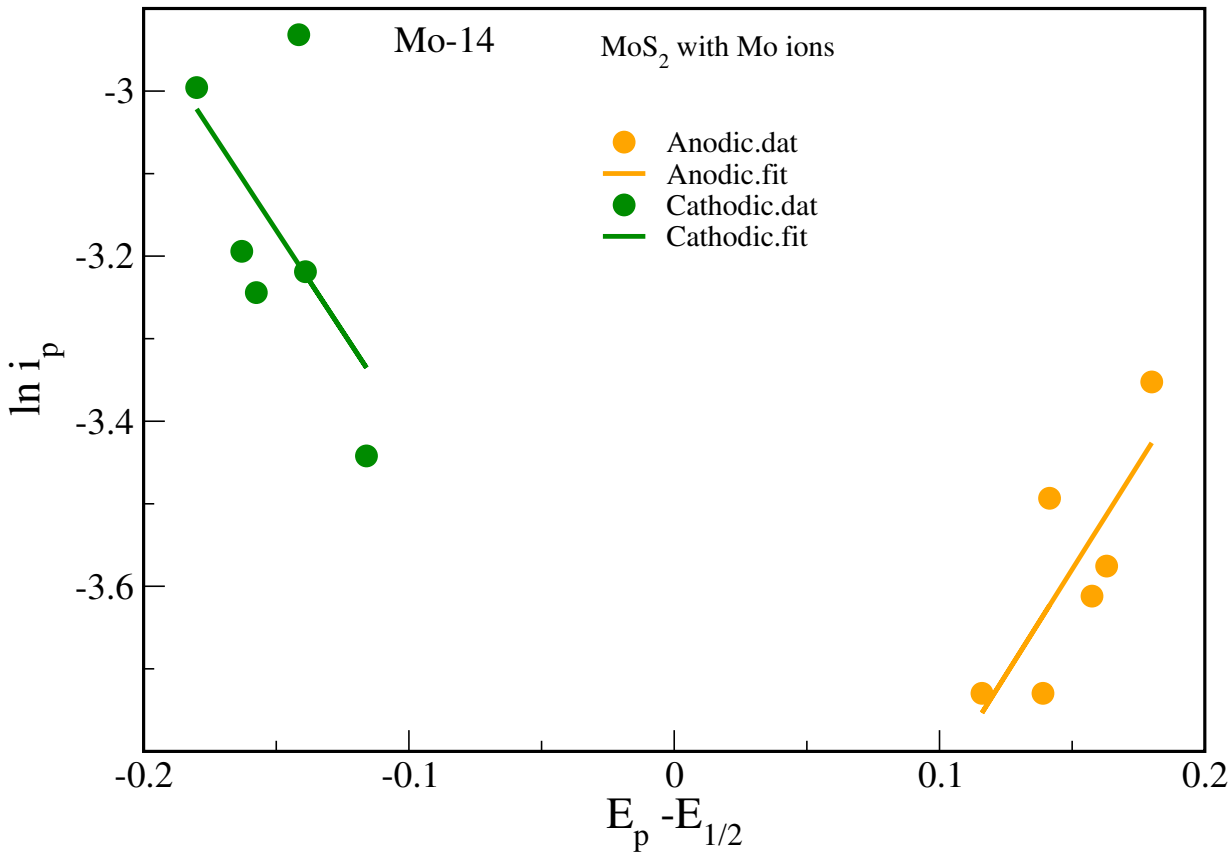

Figure 5.46: Graph of ln i_p vs $(E_p - E_{1/2})$ for Mo-14.

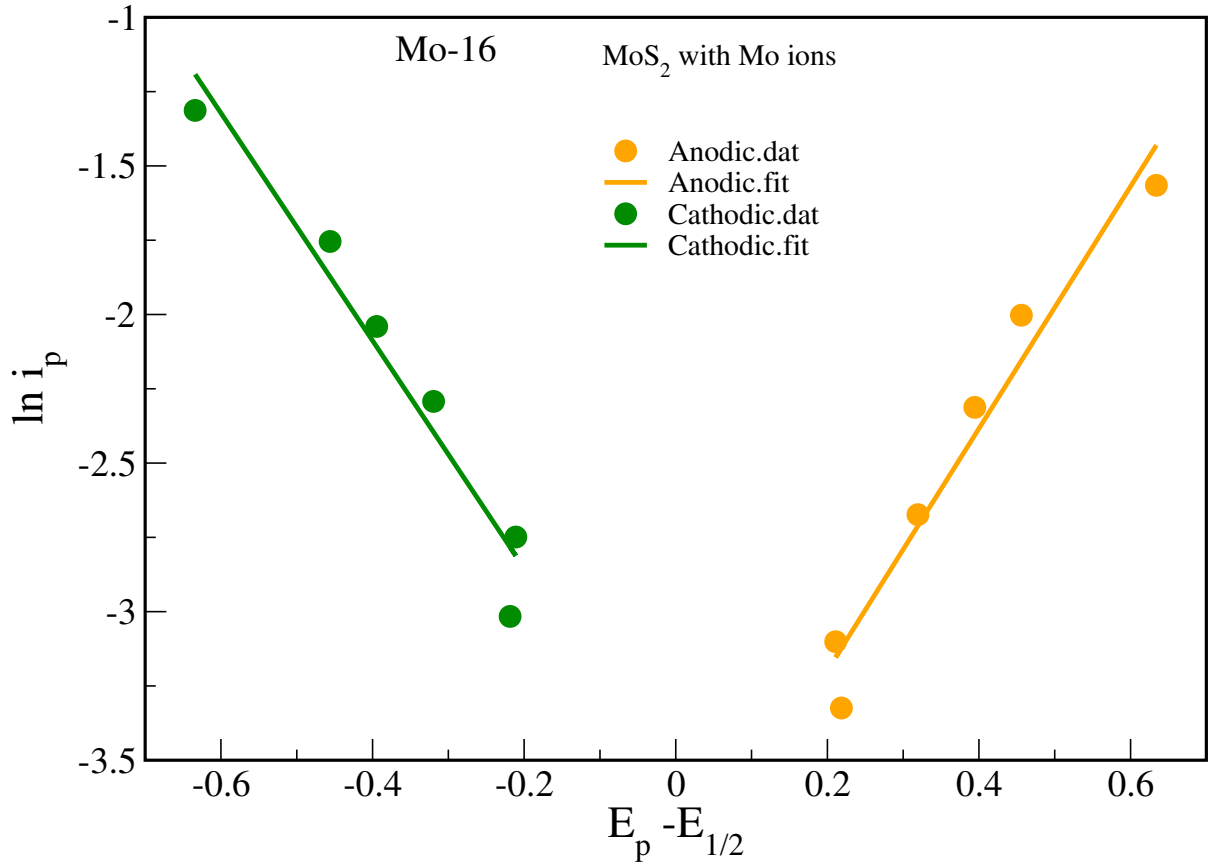

Figure 5.47: Graph of ln i_p vs $(E_p - E_{1/2})$ for Mo-16.

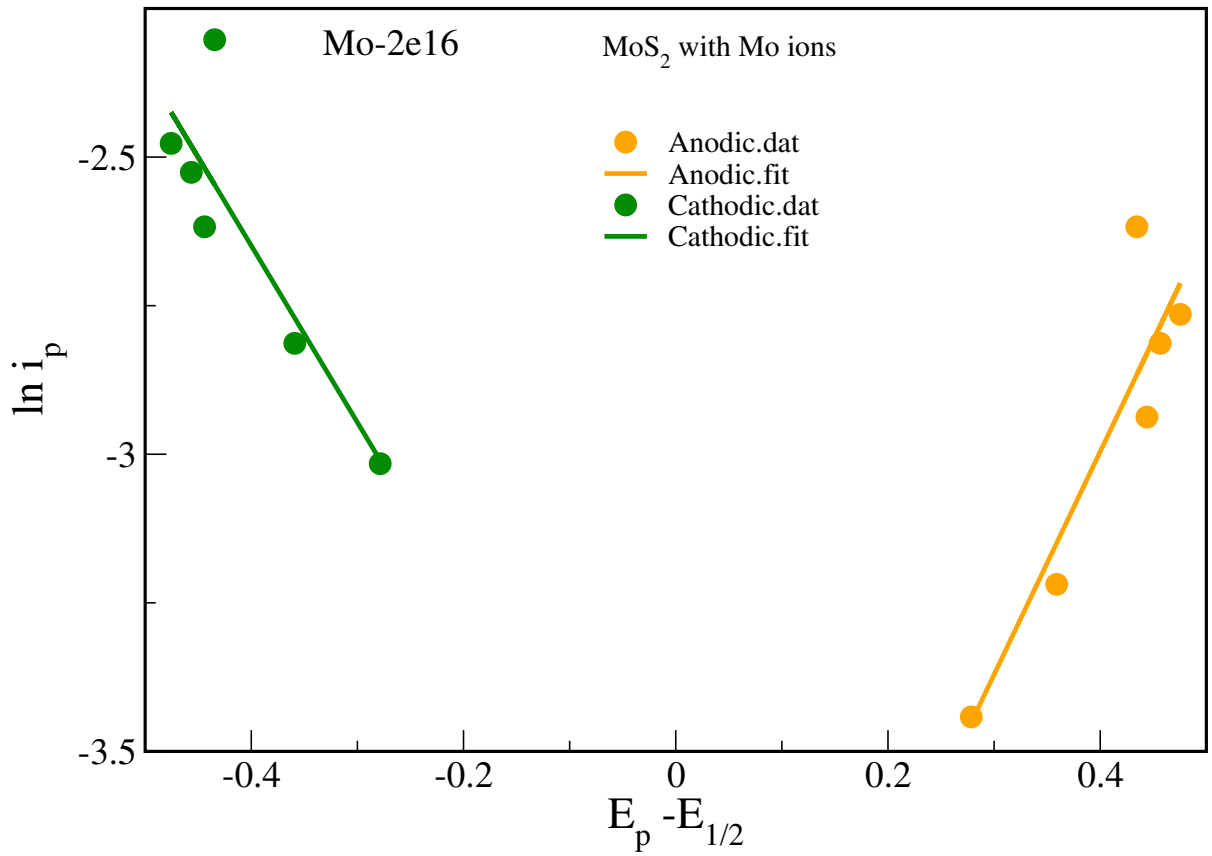

Figure 5.48: Graph of ln i_p vs $(E_p - E_{1/2})$ for Mo-2e16.

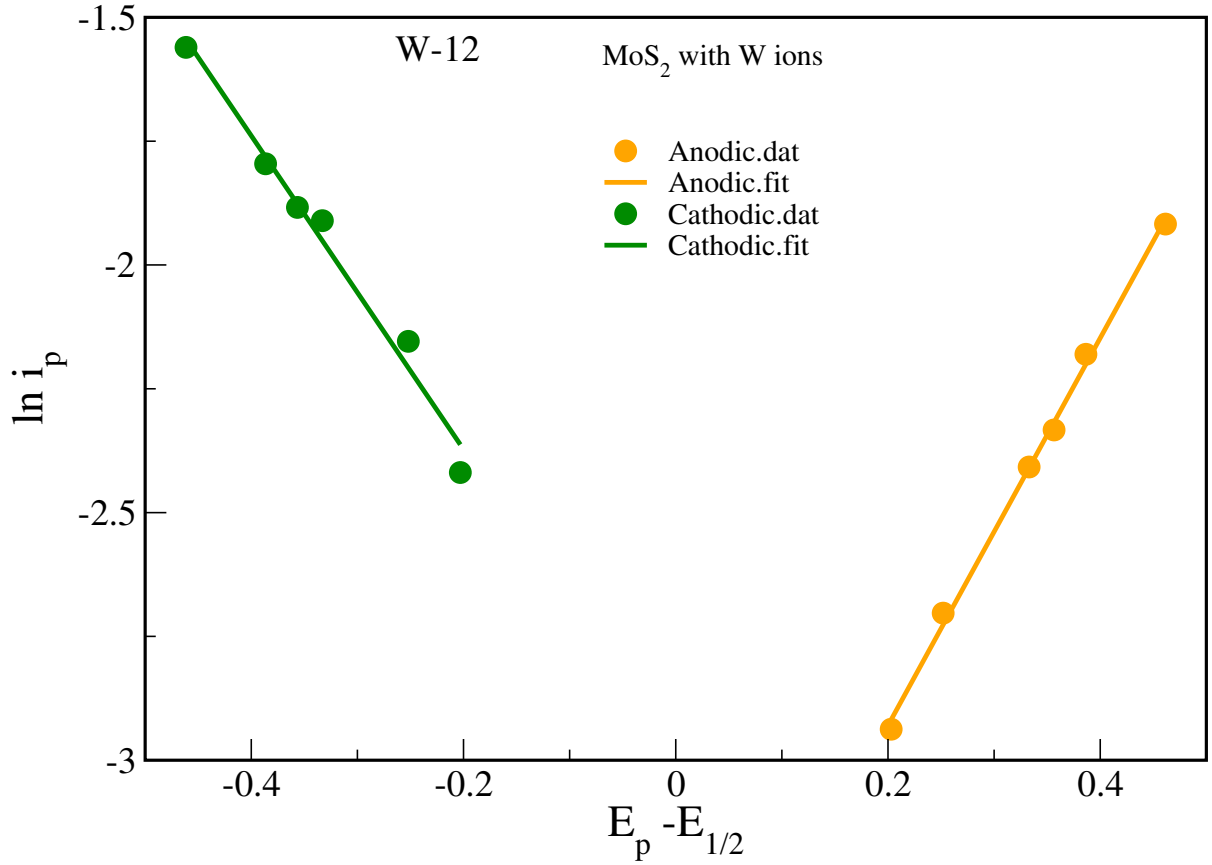

Figure 5.49: Graph of ln i_p vs $(E_p - E_{1/2})$ for W-12.

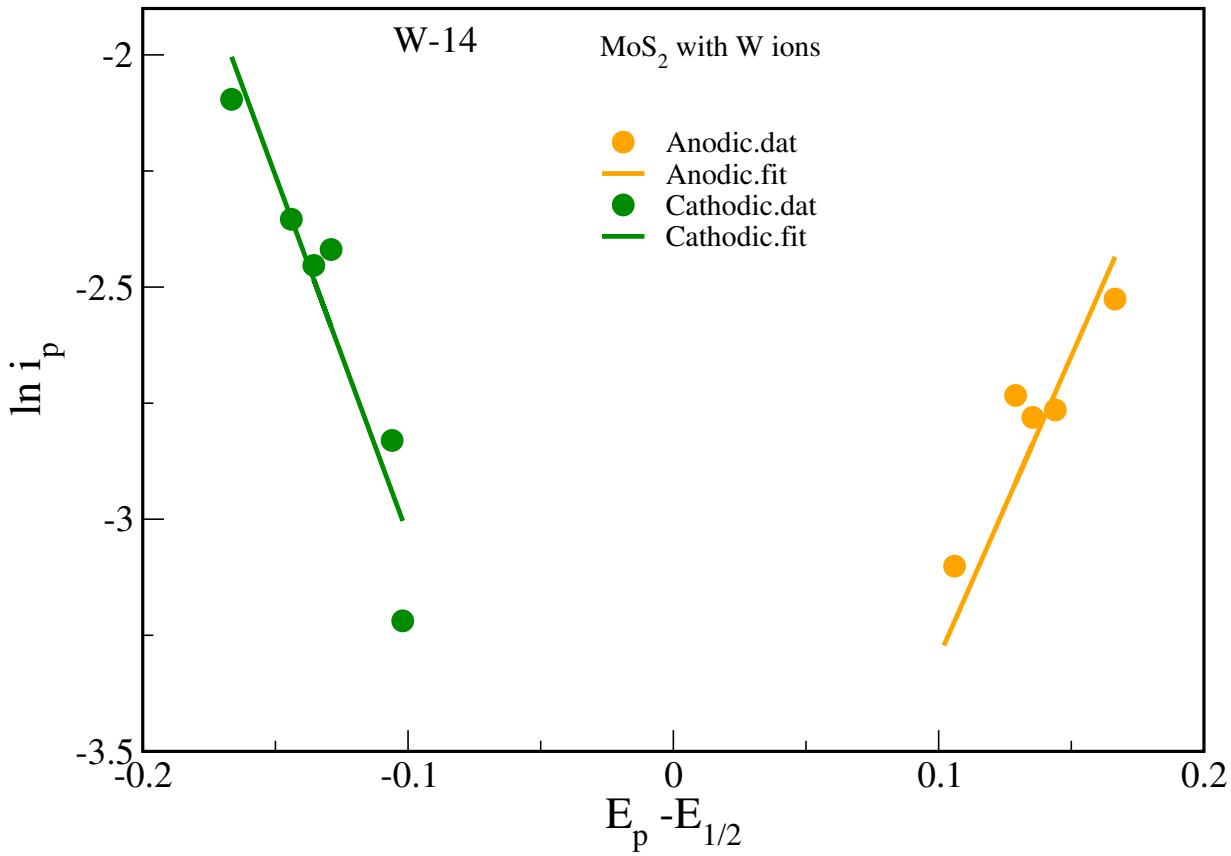

Figure 5.50: Graph of ln i_p vs $(E_p - E_{1/2})$ for W-14.

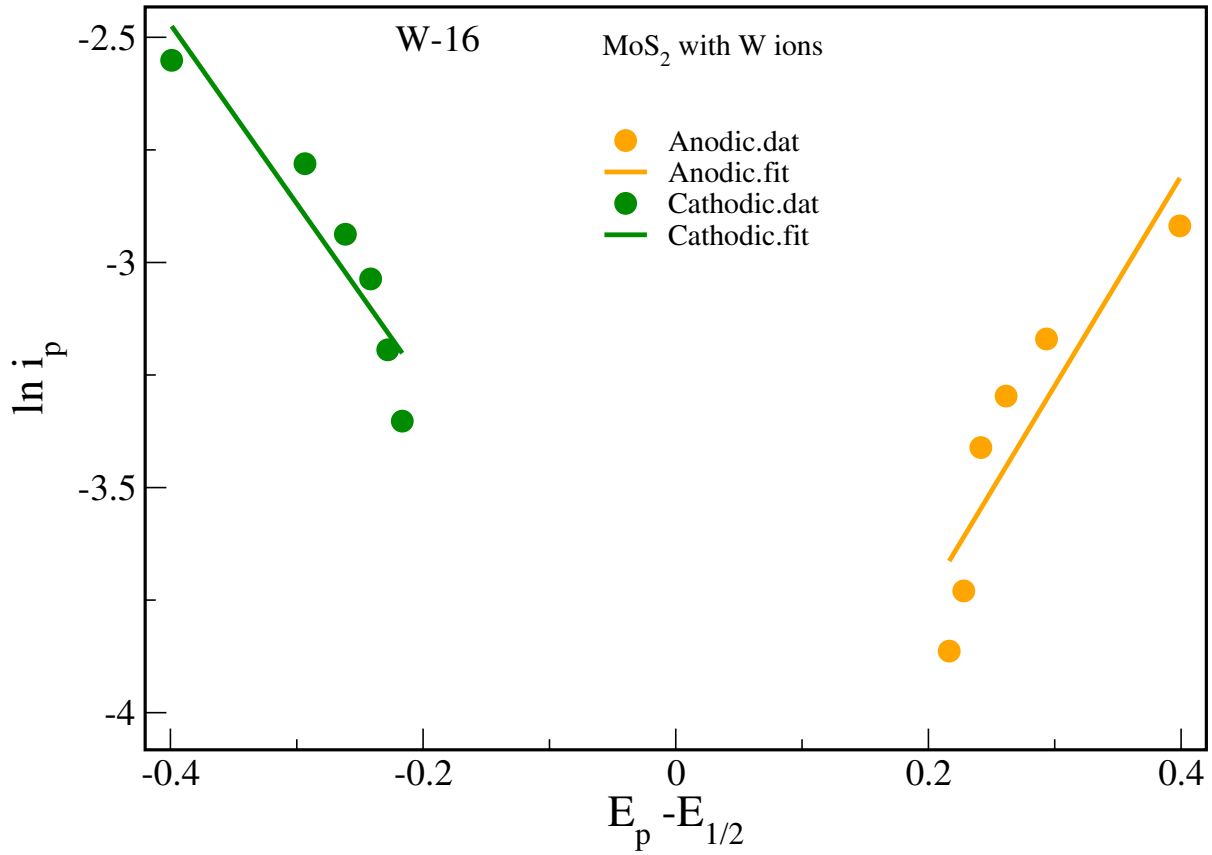

Figure 5.51: Graph of ln i_p vs $(E_p - E_{1/2})$ for W-16.

Table 5.4: A summary of b, D and K_s values for the seven electrodes (error ± 5%).

Sample	b value	D (cm^2s^{-1}) 10^{-6}	K_s (cms^{-1}) 10^{-6}
Pristine	0.50	7.10	3.66
Mo-14	0.20	2.62	6.47
Mo-16	0.65	8.09	6.80
Mo-2e16	0.26	4.99	8.20
W-12	0.30	7.53	18.42
W-14	0.33	3.21	5.85
W-16	0.30	4.21	5.88

constant translates to over 400% improvement with respect to the pristine MoS_2. The same electrode also showed the highest charge-discharge time in Fig. 5.26. Mo-16 showed the highest values b and D, of 0.61 and 8.09×10^{-4} $cm^2{\cdot}s^{-1}$, respectively. However, both the b and the D values for all the samples were an indication of Faradaic-controlled processes.

5.3.6 Types of Electrochemical Mechanisms

There are four types of electrochemical mechanisms depending on electronic transfer (E) at the electrode surface and the homogeneous chemical reaction (C). They are; E_rC_i, E_rC_r, $E_rC_r^{'}$, and $E_rC_iE_r$ [131]. An E_rC_i is where there is a reversible electronic transfer and irreversible chemical reaction. E_rC_r is where both electronic transfer and chemical reaction are reversible. $E_rC_r^{'}$ is similar to E_rC_r, however, the chemical reaction reversibility is catalyst assisted. $E_rC_iE_r$ involves both electronic transfer and chemical reaction followed further by another reversible electronic transfer.

Applying the above electrochemical mechanisms defination to Fig. 5.52, all our electrodes exhibited E_rC_i mechanism, except W-14 which showed E_rC_r mechanism behaviour, as shown in Fig. 5.52. This is achieved after plotting the anodic and cathodic peak currents ratio against the scan rates.

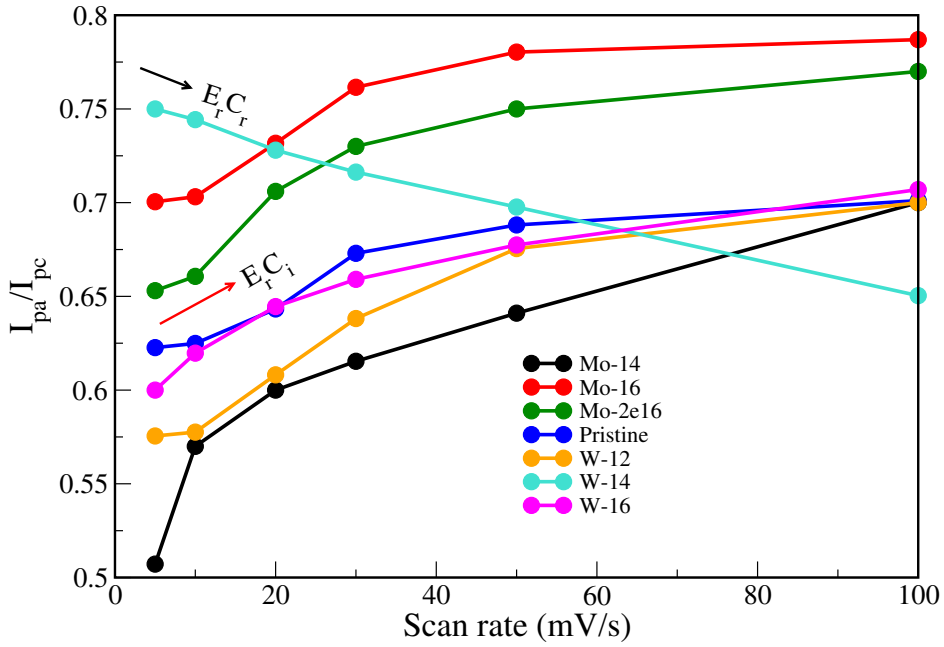

Figure 5.52: Graph of peak currents ratio against increase in scan rates.

5.3.7 Specific Capacities

Following a successful determination of the b, D and K_s values for our electrodes, the specific capacities of each sample electrode material and their performances were computed and are shown in Figs. 5.53, 5.54, 5.55 and 5.55. The values were extracted from these graphs by reading the maximum discharge specific capacities.

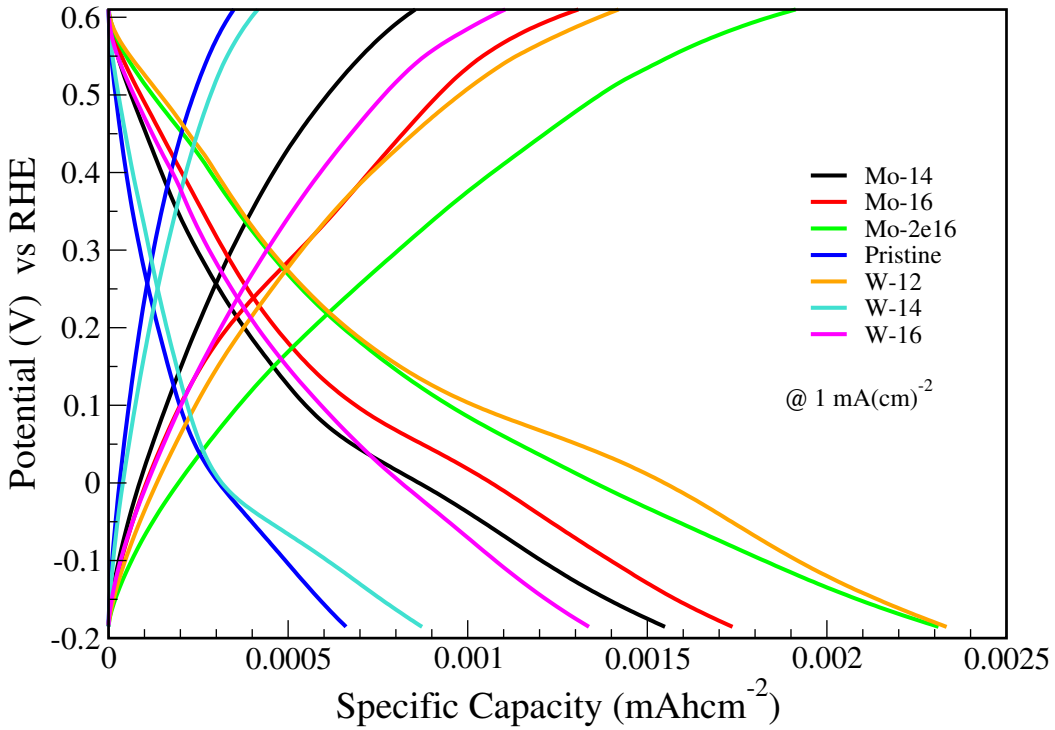

Figure 5.53: Potential against specific capacities at current density of 1 mAcm^{-2}.

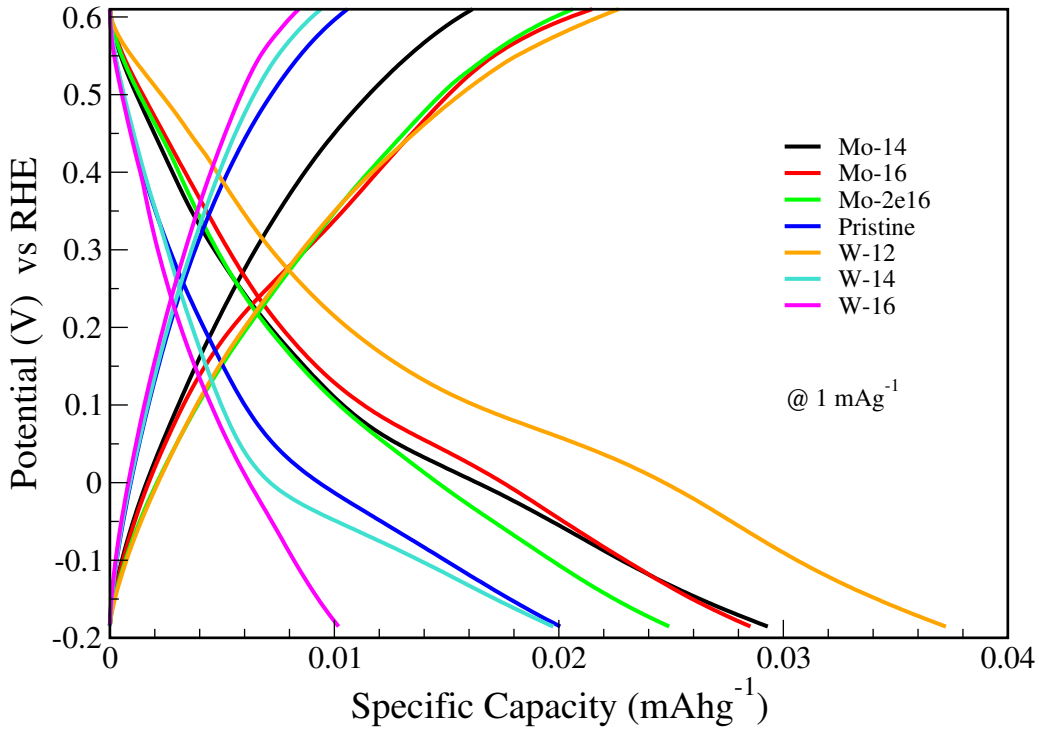

Figure 5.54: Potential against specific capacities at current density of 1 mAg^{-1}.

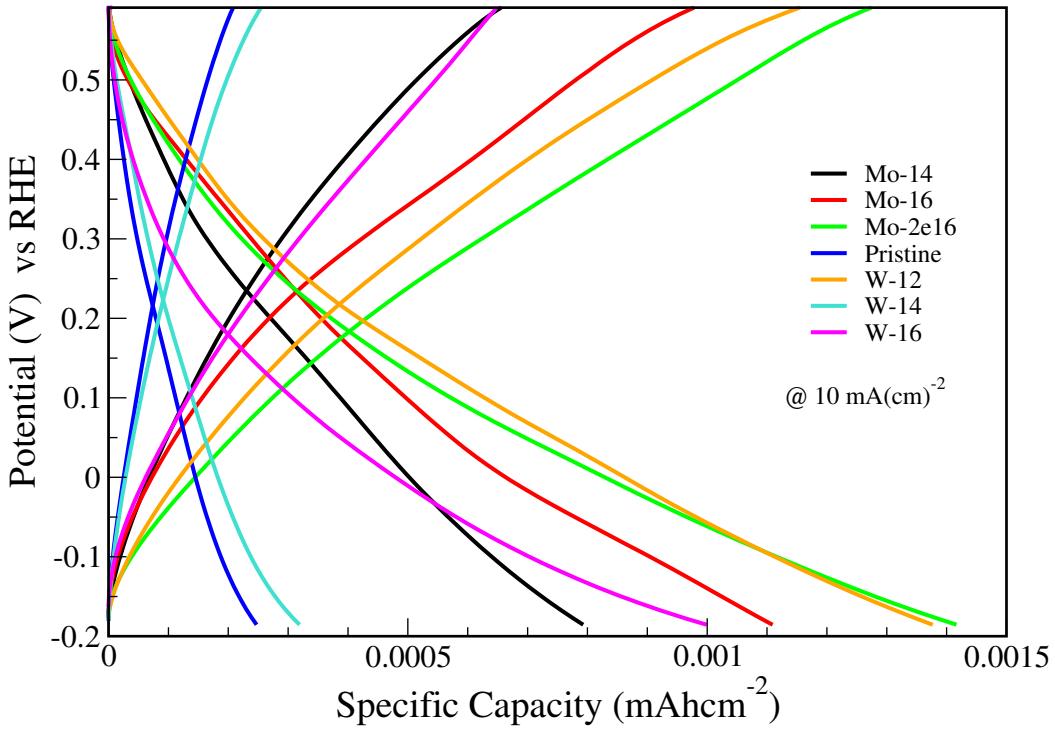

Figure 5.55: Potential against specific capacities at current density of 10 mAcm^{-2}.

The specific capacity performances, based on Figs. 5.53 and 5.55, are tabulated in Table 5.5. Compared to the pristine MoS_2, the specific capacities have been greatly enhanced in the implanted samples; with Mo-2e16 recording a 473 % increase at current density of 10 mA/cm^2. However, at 1 mA/cm^2 current density, W-12 leads at 257 % while Mo-2e16 follows with 251 %. The specific capacity performances, based on Figs. 5.54 and 5.56, are tabulated in Table 5.6. In comparison to the pristine MoS_2, the

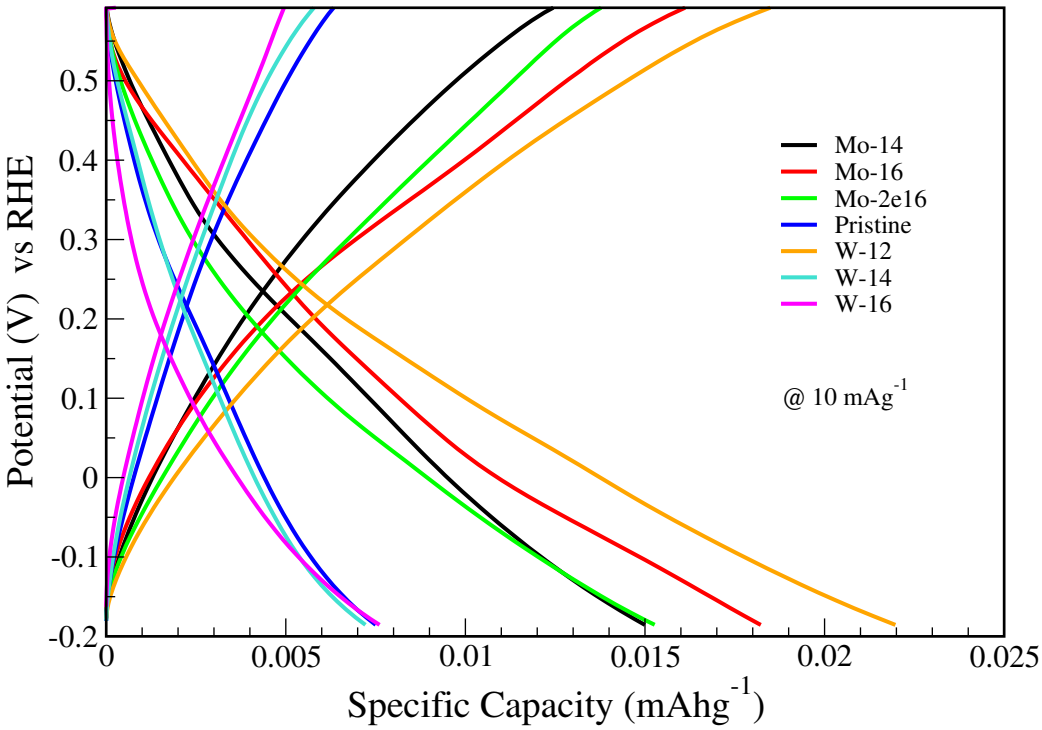

Figure 5.56: Potential against specific capacities at current density of 10 mAg^{-1}.

Table 5.5: Specific capacities of pristine, Mo and W implanted MoS_2 at 1 mA·cm^{-2} and 10 mA·cm^{-2} (error ± 5%).

Sample	@ 1 mA/cm^2 10^{-4} (mAh/cm^2)	%increase	@ 10 mA/cm^2 10^{-4} (mAh/cm^2)	%increase
Mo-2e16	23.0	251	14.2	473
Mo-16	17.4	166	11.1	348
Mo-14	15.5	136	7.9	220
Pristine	6.5		2.5	
W-12	23.4	257	13.7	455
W-14	8.7	33	3.2	27
W-16	13.3	104	10.0	304

percentage increase one order of magnitude lower for 1 mA/g current density, and even a decrease was observed. However, in the case of 10 mA/g current density, lower percentage increases were recorded but with the same order of magnitude as that at current density of 10 mA/cm^2, except for W-12 and W-16.

5.3.8 Stability Tests

The stability tests were done for specific capacity and Coulombic efficiency for a thousand cycles at current density for 100 mA/cm^2 (100mA·g^{-1}). Coulombic efficiency (η) is defined simply as:

Table 5.6: Specific capacities of pristine, Mo and W implanted MoS_2 at 1 mA·g^{-1} and 10 mA·g^{-1} (error ± 5%).

Sample	@ 1 mA/g 10^{-4} (mAh/g)	%increase	@ 10 mA/g 10^{-4} (mAh/g	%increase
Mo-2e16	249	24.5	153	106.8
Mo-16	285	42.5	182	145.9
Mo-14	292	46.0	150	102.7
Pristine	200		74	
W-12	372	86.0	220	197.3
W-14	198	-1.0	72	-2.7
W-16	101	-49.5	76	2.7

$$\eta = \frac{t_d}{t_c} \times 100\%, \tag{5.13}$$

where t_c and t_d are the charge and discharge times, respectively.

Figure 5.57 shows the specific capacities variations for 1000 charge-discharge cycles. Mo-2e16 maintained the lead right from the zeroth cycle to 1000^{th} cycle. Mo-14 followed Mo-2e16 upto about the 700^{th} cycle after which it was overtaken by W-12. The overall picture of the performance and percentage specific capacity drops are tabulated in Table 5.7.

The percentage Coulombic efficiency is reported in Fig. 5.58. Here, the pristine electrode has the highest efficiency starting from the zeroth cycle to the 1000^{th} cycle. As shown in Table 5.8, the Coulombic efficiency drop between the zeroth and 1000^{th} cycles is between 0.8 % and 3.8 %. This is an indication that MoS_2 implanted electrodes are very stable. The Mo-2e16 electrode showed the highest retention of 98.53 % after 1000 charge-discharge cycles, as tabulated in Table 5.8.

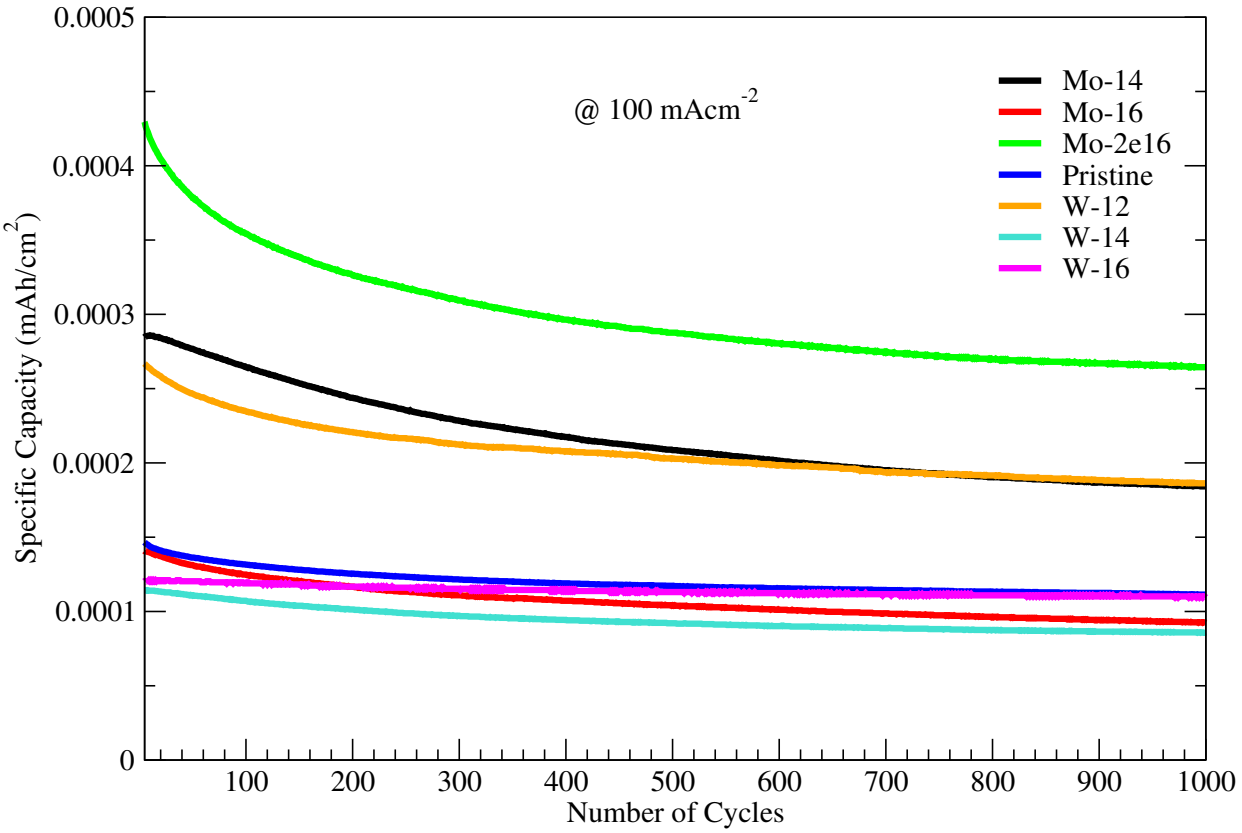

Figure 5.57: Specific capacities against number of cycles at current density of 100 mA·cm^{-2}.

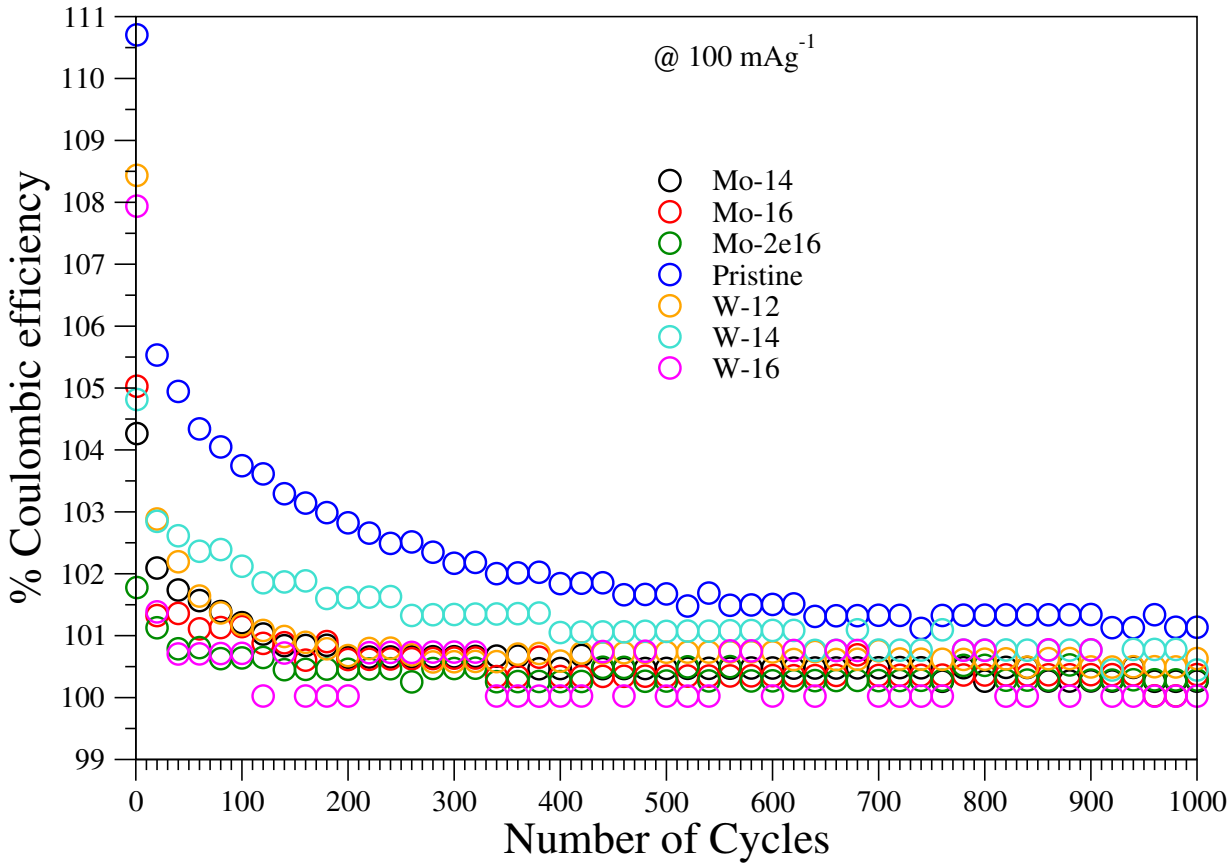

Figure 5.58: Coulombic efficiency against number of cycles at current density of 100 mA·cm^{-2}.

Table 5.7: Specific capacities of pristine, Mo and W implanted MoS_2 at various cycles (error ± 5%).

Sample	@ Zeroth cycle 10^{-4} mAhcm^{-2}	@ 200th cycle 10^{-4} mAhcm^{-2}	@ 500th cycle 10^{-4} mAhcm^{-2}	@ 1000th cycle 10^{-4} mAhcm^{-2}	%drop from zeroth to 1000^{th} cycle
Mo-2e16	4.259	3.262	2.894	2.645	38
Mo-16	1.397	1.187	1.056	0.907	35
Mo-14	2.850	2.430	2.115	1.826	36
Pristine	1.458	1.275	1.178	1.126	23
W-12	2.658	2.220	2.001	1.861	30
W-14	1.135	0.986	0.907	0.854	25
W-16	1.196	1.169	1.126	1.073	10

Table 5.8: Percentage Coulombic efficiency and retention of pristine, Mo and W implanted MoS_2 at various cycles (error ± 5%).

Sample	@ Zeroth cycle %	@ 200th cycle %	@ 500th cycle %	@ 1000th cycle %	%Retention after 1000 cycles
Mo-2e16	100.897	100.718	100.435	100.057	98.53
Mo-16	101.338	100.771	100.435	100.256	95.53
Mo-14	101.758	100.929	100.561	100.204	96.17
Pristine	105.000	102.830	101.779	100.992	91.36
W-12	102.168	101.149	100.687	100.340	92.80
W-14	102.735	101.590	101.065	100.645	96.83
W-16	101.000	100.487	100.288	100.109	92.67

5.3.9 Electrode Performance

The working electrode performance was assessed based on the following parameters: capacitance (C); specific capacitance (Cs_m or Cs_a); voltage drop (ΔV_d); equivalent series resistance (ESR); power (P); maximum power (P_{max}) and energy density (E). These were computed from the galvanostatic CD in Fig. 5.59 employing the standard equations 5.14 to 5.19 [132, 133].

$$C = I\frac{\Delta t}{\Delta V}(\text{F}), \tag{5.14}$$

$$Cs_m = \frac{C}{m}(\text{Fg}^{-1}), \tag{5.15}$$

$$Cs_a = \frac{C}{Area}(\text{Fcm}^{-2}), \tag{5.16}$$

$$ESR = \frac{\Delta V_d}{2I}(\Omega), \tag{5.17}$$

$$E = \frac{Cs_m \Delta V^2}{2} \times \frac{1000}{3600}(\text{Whkg}^{-1}), \tag{5.18}$$

$$P_{max} = \frac{1000 \Delta V^2}{4m \times ESR}(\text{Wkg}^{-1}), \tag{5.19}$$

where, I is the applied current, Δt is the discharge time and ΔV is maximum voltage after the voltage drop.

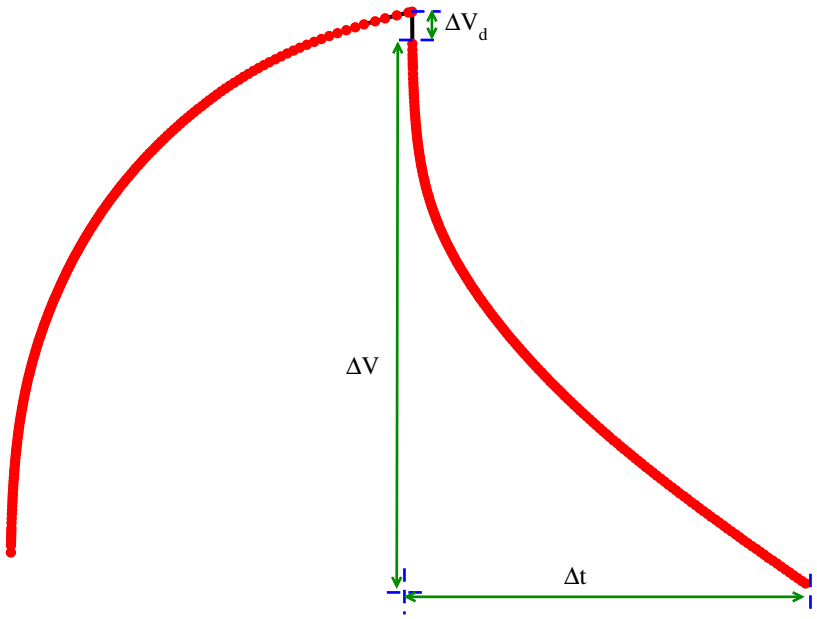

Figure 5.59: Schematic charge-discharge curve at 1 mA/g.

Based on the results shown in Table 5.9, the implanted electrodes recorded higher values of the parameters considered in the evaluation, compared to the pristine electrode. The capacitance was enhanced by as high as 327 % in Mo-16, while the geometric and gravimetric specific capacitances improved by about 211 % and 66 %,respectively. W-12 reported the highest gravimetric specific capacitance and energy of 93 % increase relative to the pristine electrode. Maximum power rise of 19 % was reported in W-14, with reference to the pristine electrode. However, in terms of equivalent series resistance, we noted 26 times higher in W-14 electrode, which is undesired for good electrode. This is due to W-14 having the lowest voltage drop (ΔV_d).

Table 5.9: Performance evaluation of pristine, Mo and W ions implanted MoS_2 at 1 mA·g^{-1} (error ± 5%).

Sample	C 10^{-4} (F)	Cs_m 10^{-2} (F·g^{-1})	Cs_a 10^{-3} (F·cm^{-2})	ESR 10^{-3} (Ω)	E 10^{-3} (W·h·kg^{-1})	P_{max} 10^{6} (W·kg^{-1})
Mo-14	7.4	12.6	6.7	2.5	10.9	10.7
Mo-16	12.8	14.3	8.7	7.8	12.3	2.3
Mo-2e16	11.2	14.0	13.0	4.8	12.1	4.2
Pristine	3.0	8.6	2.8	1.0	7.4	44.2
W-12	8.9	16.6	10.4	27.1	14.3	1.1
W-14	3.4	9.6	3.7	0.9	8.3	52.7
W-16	7.0	5.2	6.8	17.0	4.5	0.7

Key: Cs_a =geometric pseudocapacitance; Cs_m =gravimetric pseudocapacitance; ESR = equivalent series resistance; E= energy; P_{max} = maximum power.

Nevertheless, the other evidence is that ion implantation enhances charge storage capability in MoS_2, making ion implantation technique a viable method to incorporate with the already existing ways of increasing charge capacity in MoS_2. For instance, addition of active carbon has been reported to enhance capacitance in MoS_2 [134], and ion implantation could further improve this, as shown in this study.

5.3.10 Electrodes Kinetics

Nyquist plots were also used to analyze the electrode kinetics, electronic and ionic transport. These are shown in Figs. 5.60a and 5.60b. This was acquired through the use of Electrochemical impedance spectroscopy (EIS), which has the ability to determine both the resistive and capacitive (dielectric) properties of materials. The equivalent circuits used for the data fitting are shown in Fig. 5.60c (with the least number of parameters necessary for the fitting the acquired data). They consist of a series resistor R_s, charge transfer resistances R_{ct1} and R_{ct2} connected in parallel to constant phase elements (CPE) Q_1 and Q_2. R_s, R_{ct1} and Q_1 are solid-ectrolyte interface resistances and capacitance, respectively, while R_{ct2} and Q_2 are interface charge transfer resistance and double layer capacitance, respectly. Q_1 and Q_2 or simply Q relates to capacity C according to equation 5.20 [135];

$$C = R^{\frac{1-n}{n}} \cdot Q^{\frac{1}{n}}, \tag{5.20}$$

where R is the resistance and n is the phase change obtained from the fitting. n varies between 0 and 1 and when n = 1, it shows the system is a pure capacitor, as shown from the impendance of CPE in

equation 5.21 otherwise the capacity/capacitance is calculated depending on the n value. The n value is also obtained from the slope of log Z vs log f: if n= -1, it shows an inductor; n= 0, shows a pure resistor; n= 1 describes a pure capacitor and n= 0.5 shows Warburg impendance (Z_w), resulting from ion diffusion [121, 134]. A CPE is used to model the non-uniform capacitive effect along the length and over the surface of electrodes [136].

$$\frac{1}{\hat{Z}_{CPE}} = Q \cdot (i\omega)^n, \tag{5.21}$$

where i is the imaginary part, and Q is the pre-factor of CPE, with ω as the signal frequency.

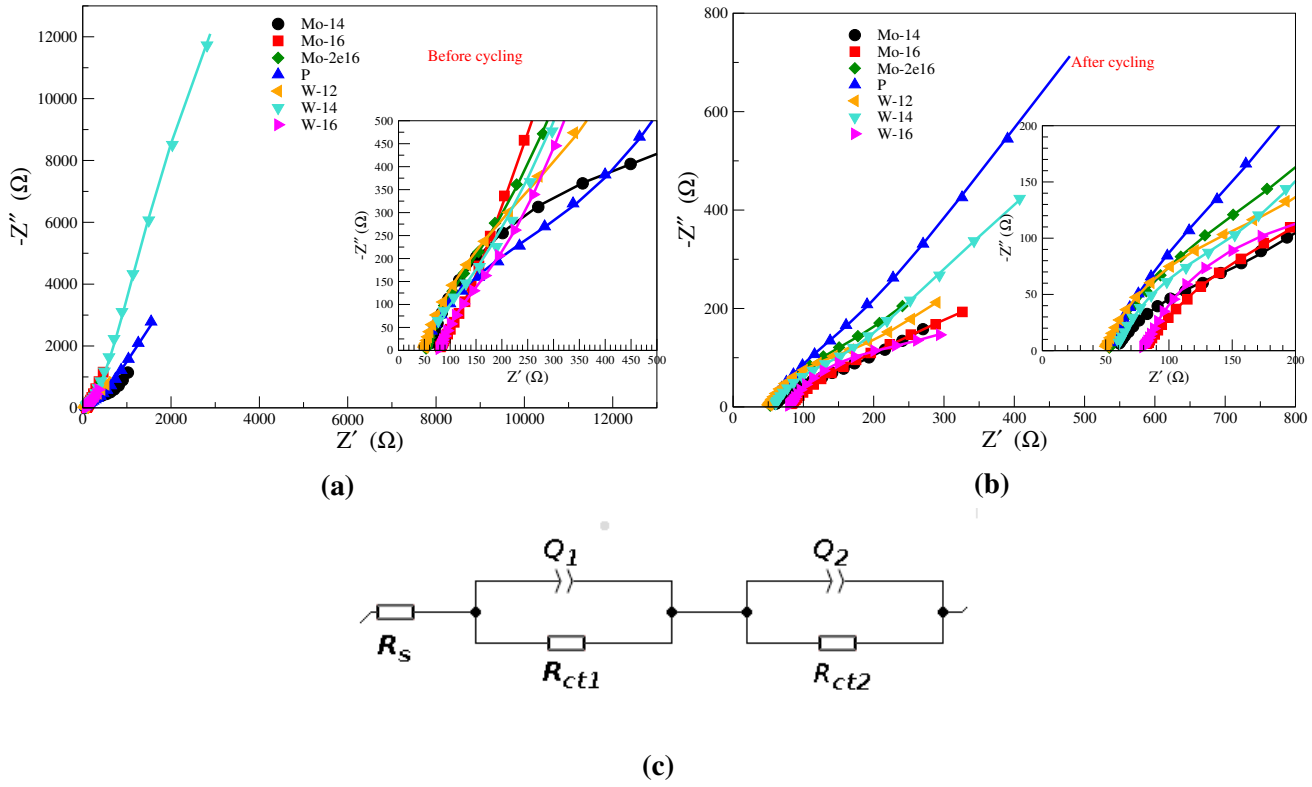

Figure 5.60: (a) Nyquist plots before cycling for pristine MoS_2 and MoS_2 electrodes implanted with Mo and W ions, (b) Nyquist plots after 1000 cycles for pristine MoS_2 and MoS_2 electrodes implanted with Mo and W ions, and (c) equivalent circuit used for data fitting.

Table 5.10 and Table 5.11 show the values of resistors R_s, R_{ct1}, R_{ct2} and constant phase elements Q_1, Q_2 and n values n_1 and n_2, before and after 1000 cycles. All these values were obtained from Nyquist plot data fitting using the equivalent circuit shown in Fig. 5.60c. It is obvious that, all Q_1 and Q_2 values increased after cycling (except Q_2 for W-14). Since CPE is associated with the capacitance, (as shown in Eqs. 5.20 and 5.21) its increase implies improved charge storage capabilities. A slight increase in series resistance across all the electrodes after cycling was noted and it implies a reduction in conductivity. For some electrodes, the charge transfer resistances are quite high and are attributed to the fitting algorithm employed by EC-lab software. For the half-cells tested, the n values observed were

all greater than 0.5, which confirms pseudocapacitive properties of our MoS_2 electrodes, with most of the very high n values recorded for MoS_2 ion implanted electrodes, confirming that ion implantation enhances the pseudocapacitance in MoS_2.

Table 5.10: Fitted values for; resistors (R_s, R_{ct1}, R_{ct2}), $CPEs$ (Q_1, Q_2) and n values (n_1, n_2) in pristine and ions implanted MoS_2 before cycling (error ± 5%).

Sample	R_s (Ω)	Q_1 (μF·s$^{n_1-1}$)	n_1	R_{ct1} (Ω)	Q_2 (μF·s$^{n_2-1}$)	n_2	R_{ct2} (Ω)
Mo-14	56.2	4.14	0.91	488.7	36.6	0.74	42268
Mo-16	77.4	216.4	0.63	50.85	26.6	0.83	56123
Mo-2e16	51.7	44.71	0.78	1981000	36.2	0.96	71.39
Pristine	43.8	5.03	0.79	291.2	16.2	0.73	33115
W-12	43.5	17.54	1	4894	23.2	0.81	501.6
W-14	12.6	1.49	1	99910	59.0	0.47	49136
W-16	78.5	56.92	0.85	108.5	57.8	0.81	12419

Table 5.11: Fitted values for resistors (R_s, R_{ct1}, R_{ct2}), $CPEs$ (Q_1, Q_2) and n values (n_1, n_2) in pristine and ions implanted MoS_2 after 1000 cycles (error ± 5%).

Sample	R_s (Ω)	Q_1 (μF·s$^{n_1-1}$)	n_1	R_{ct1} (Ω)	Q_2 (μF·s$^{n_2-1}$)	n_2	R_{ct2} (Ω)
Mo-14	59.7	378.5	0.59	1426	74.78	0.74	73.64
Mo-16	78.6	288.6	0.57	1396	89.76	0.84	47.89
Mo-2e16	52.1	130.9	0.95	1086	106.00	0.75	223.00
Pristine	51.2	43.9	0.85	71.3	65.77	0.71	40361
W-12	48.8	40.3	0.88	100.8	226.10	0.68	1717
W-14	56.7	133.1	0.64	9195	16.42	0.94	57.37
W-16	78.2	331.6	0.63	714.1	53.71	0.93	92.53

Figs. 5.61a and 5.61b show the Bode plots for the samples before and after cycling. The phase angles are between -76° and -48°, which is lower than -90° expected for an ideal supercapacitor. This implies that all the electrodes exhibit pseudocapacitive behaviour. At knee frequency f_o, which is the frequency at which supercapacitors reveal their dominant properties [137], the phase angle ϕ = 45°. The higher f_o is, the faster a device will charge and discharge.

Table 5.12, clearly shows the changes in knee frequency and time constant (T=$\frac{1}{f_o}$) before and after 1000 cycles. With the exception of W-14, all of the ion implanted electrodes reported lower f_o % drop after cycling with respect to the pristine MoS_2 electrode. This supports the assumption that ion implantation improves the MoS_2 electrode performance.

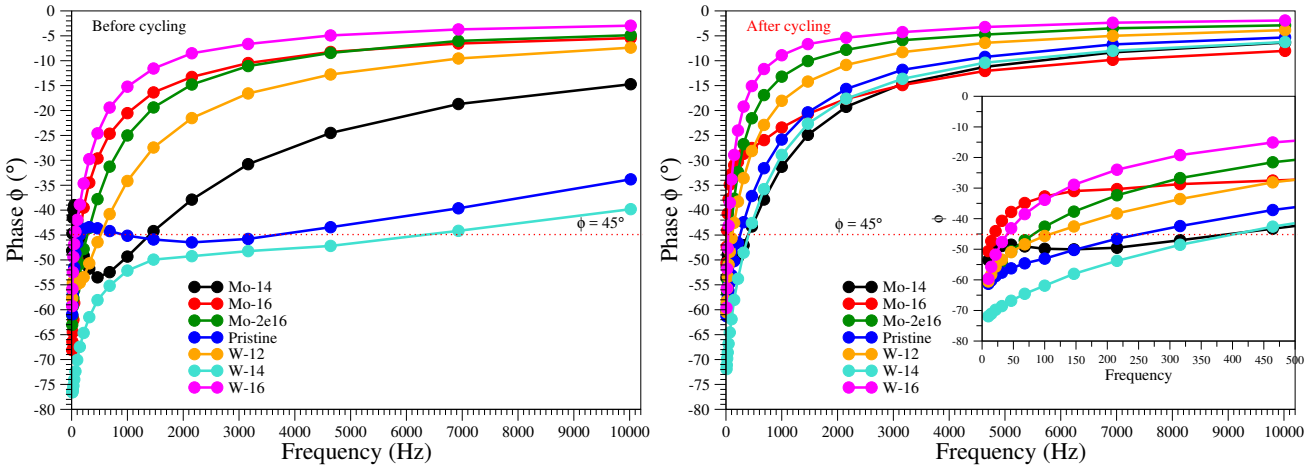

Figure 5.61: Bode plots for pristine MoS_2, MoS_2 implanted with Mo ions and MoS_2 implanted with W ions electrodes (a) before cycling and (b) after 1000 cycles.

Table 5.12: Knee frequencies before and after cycling for pristine and ions implanted MoS_2 (error ± 5%).

	Before cycling		After 1000 cycles		
Sample	f_o (Hz)	T 10^{-4}(s)	f_o (Hz)	T 10^{-4}(s)	f_o % drop
Mo-14	1400	7.14	413	24.21	71
Mo-16	150	66.67	20	500.00	87
Mo-2e16	307	32.57	80	125.00	74
Pristine	3600	2.78	247	40.04	93
W-12	557	17.95	110	90.90	80
W-14	6400	1.56	413	24.21	93.5
W-16	70	142.86	40	250.00	43

5.3.11 Conclusion

In most cases, the ion implanted electrodes showed enhanced capabilities compared to the pristine MoS_2. However, ion implanted showed increase in resistance which translates to decrease in conductivity.

CHAPTER SIX

POWDERED MOS_2

This Chapter highlights the synthesis of fower-like MoS_2 powder, characterisation techniques employed, ion implantation and the electrochemical performance testing. It is a follow up to the findings reported in Chapter 5, based on the crystalline bulk MoS_2.

6.1 MoS_2 Material Synthesis Procedure

Thiourea (N_2H_4CS) (molar mass: 79.12 g/mol) was dissolved in distilled water followed by addition of Ammonium molybdate tetrahydrate [$(NH_4)_4Mo_7O_{24}\cdot 4\,H_2O$] (molar mass: 1235.9 g/mol). All reagents were of the analytical grade and no further purification was carried out. The concentration of ammonium heptamolybdate tetrahydrate was kept constant at 0.05 mol l^{-1} while thiourea was in 12.6% excess of the stoichiometric amount, to ensure complete reaction. A similar synthesis procedure has also been reported [138].

The hydrothermal reaction was carried out in a polytetrafluoroethylene (Teflon)-lined stainless autoclave at 220 °C for 10 h. After this reaction, a clear liquid was poured out and a black, waxy, slippery material (MoS_2) had formed on the inner lining of the Teflon liner. It was then scrubbed out, collected and thoroughly washed with distilled water and ethanol by centrifugation, and dried at 80 °C. The dried powder was divided into two portions. One part was annealed at 450 °C (referred to as MoS_2-450) for 5 h in a N_2 atmosphere, while the remaining portion was used as synthesised (referred to as MoS_2-AS).

6.2 Characterisation Techniques

To ensure that the synthesised material was MoS_2, Raman spectroscopy and powder X-ray diffraction (XRD) analyses were carried. X-ray photoelectron spectroscopy (XPS), which is surface-sensitive quantitative technique was performed to confirm the elemental composition. Also done in this respect was the energy-dispersive X-ray spectroscopy (EDS) that was to determine the elementary composition of this material. Scanning electron microscope (SEM) was used to provide information about the surface topography, while transmission electron microscopy (TEM) was used to capture the finer details. Brunauer-Emmett-Teller (BET) technique was employed to characterise the porous nature of the samples, while the material's stability was tested through thermal gravimetric analysis (TGA). All the instruments required for the above characterisation techniques are within the University of the Witwa-

tersrand, except for XPS, which was done in University of South Africa (Unisa).

6.3 Characterisation Results

This section discusses the characterisation results obtained from the techniques mentioned in Section 6.2.

6.3.1 Raman Spectroscopy

Figure 6.1 shows the Raman spectroscopy measurements performed on the bulk crystalline material (discussed in Chapter 5) and compared with the synthesised powders of MoS_2. A perfect match of the peaks depict that the synthesised material is MoS_2. However, the weak intensity peaks show a low presence of crystalline material. After annealing, the MoS_2-450 peaks intensity increased, an indication of crystallisation upon annealing.

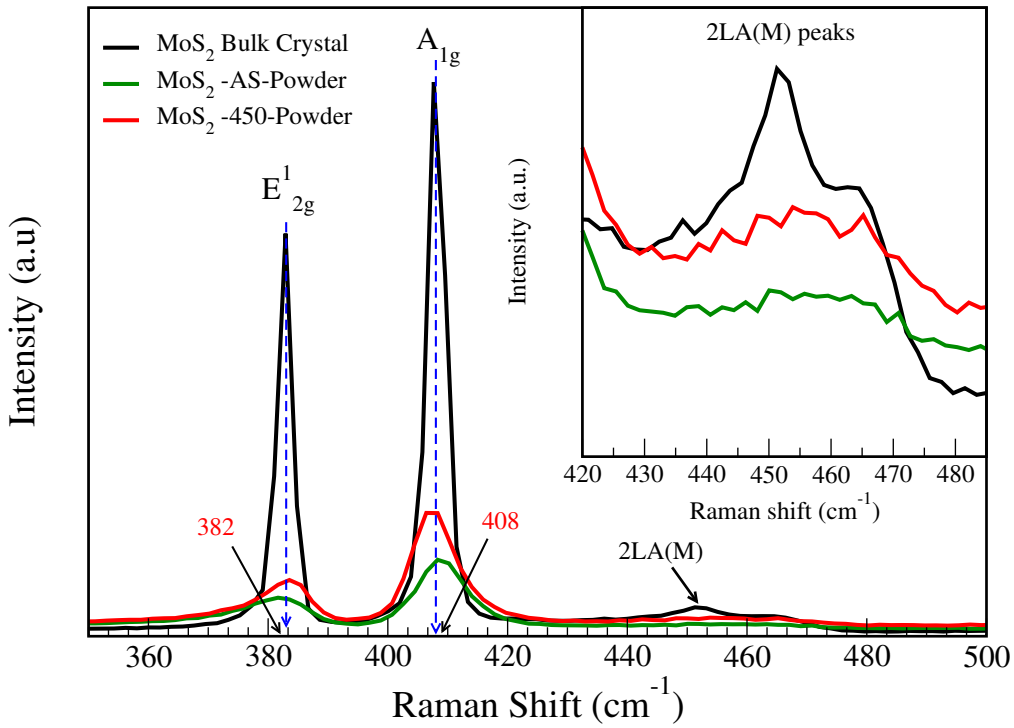

Figure 6.1: Raman spectra of bulk MoS_2 crystal, MoS_2-AS and MoS_2-450.

6.3.2 Powder X-ray Diffraction

X-ray diffraction done using a diffractometer employing a Cu-$K_{\alpha 1}$ source of wavelength 1.5406 $\mathring{A}$, produced the XRD spectra shown in Fig. 6.2. The diffraction peaks at 2θ =14, 33, 40 and 60, are assigned to (002), (100), (103) and (110) plane, in that order. In both samples, no peaks resulting from impurity phase were observed. The formation of a well-stacked layer structure is indicated by the sharp

peak (002) [138]. Moreover, no notable difference was observed between MoS_2-AS and MoS_2-450 spectra peaks.

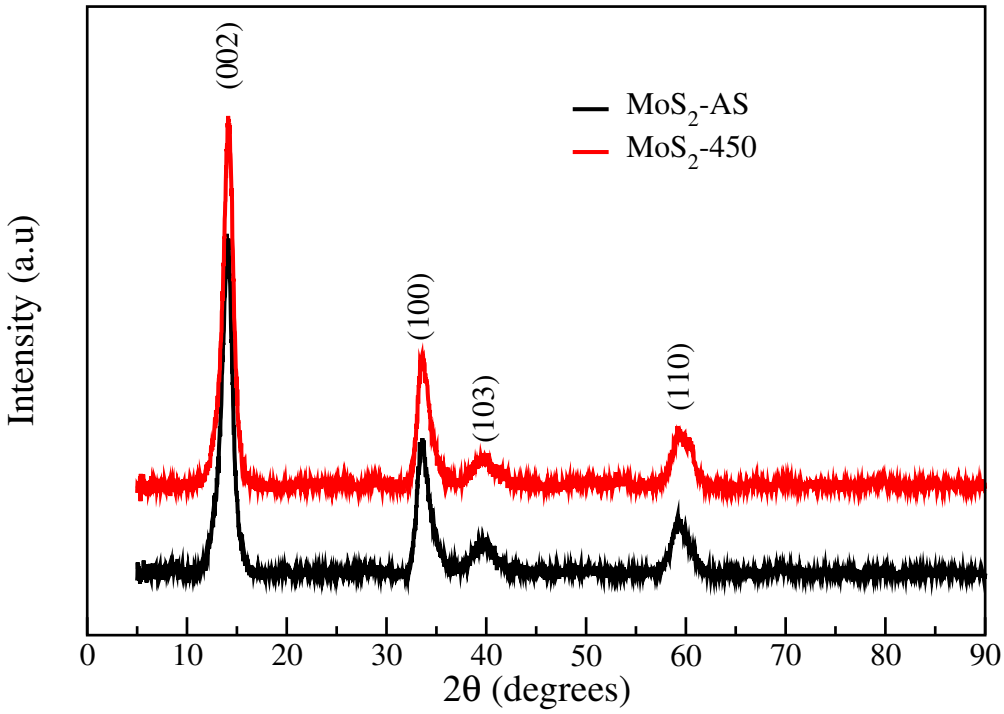

Figure 6.2: XRD spectra of MoS_2-AS and MoS_2-450 powders.

6.3.3 XPS Measurements

To establish the elements present in the synthesised powder material, X-ray photoelectron spectroscopy was performed using KRATOS-SUPRA spectrometer, operating monochromatic Al Kα ratdiation with an excitation energy of $h\nu$ = 1486.6 eV with a base pressure of 1.2×10^{-8} Torr. It is based in University of South Africa (Unisa) and it uses LabSpec v5 software to process XPS spectra, some of which are shown and discussed below. Figures 6.3 and 6.5 reveal the presence of the characteristic S 2p peaks in both MoS_2-AS and MoS_2-450 samples. Upon deconvolution of the S 2p peaks, S $2p_{1/2}$ and S $2p_{3/2}$ peaks were observed, and it is a clear indication of sulphur element present in both samples. Figs. 6.4 and 6.6 show molybdenum spectra characterised by Mo 3d peaks which splits into Mo $3d_{3/2}$ and Mo $3d_{5/2}$, a true signature of Mo atoms present in the two samples (MoS_2-AS and MoS_2-450). Based on these spectra, the only elements predominantly present in the two powder samples were Mo and S. However, the wide scan XPS spectra reveals presence of adventitious O atom(s) in MoS_2-AS sample as indicated in Fig. 6.7. This was not observed in MoS_2-450 sample as shown in Fig. 6.8.

The binding energy for MoS_2-450 sample is higher than that of MoS_2-AS as indicated in Figs. 6.9 and 6.10, for both S and Mo atoms. This could be attributed to more crystallisation occurring in MoS_2-

450 sample material due to the annealing, which led to changes in oxidation states and local chemical environment of the Mo and S elements [139].

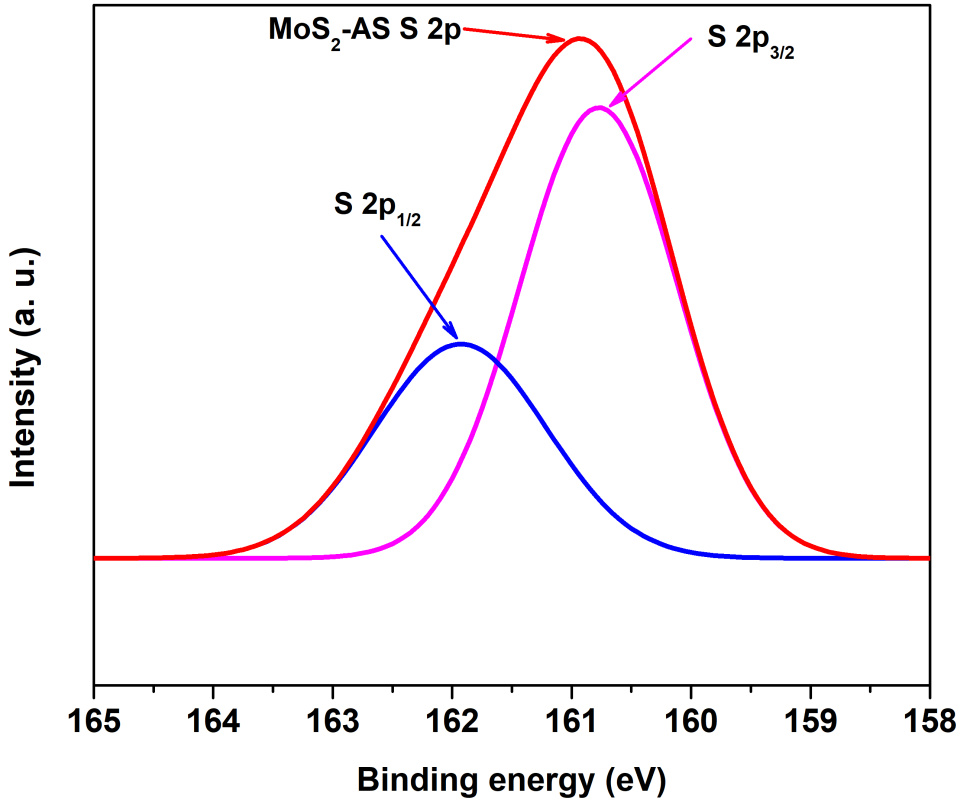

Figure 6.3: Deconvoluted XPS spectra for MoS_2-AS S 2p.

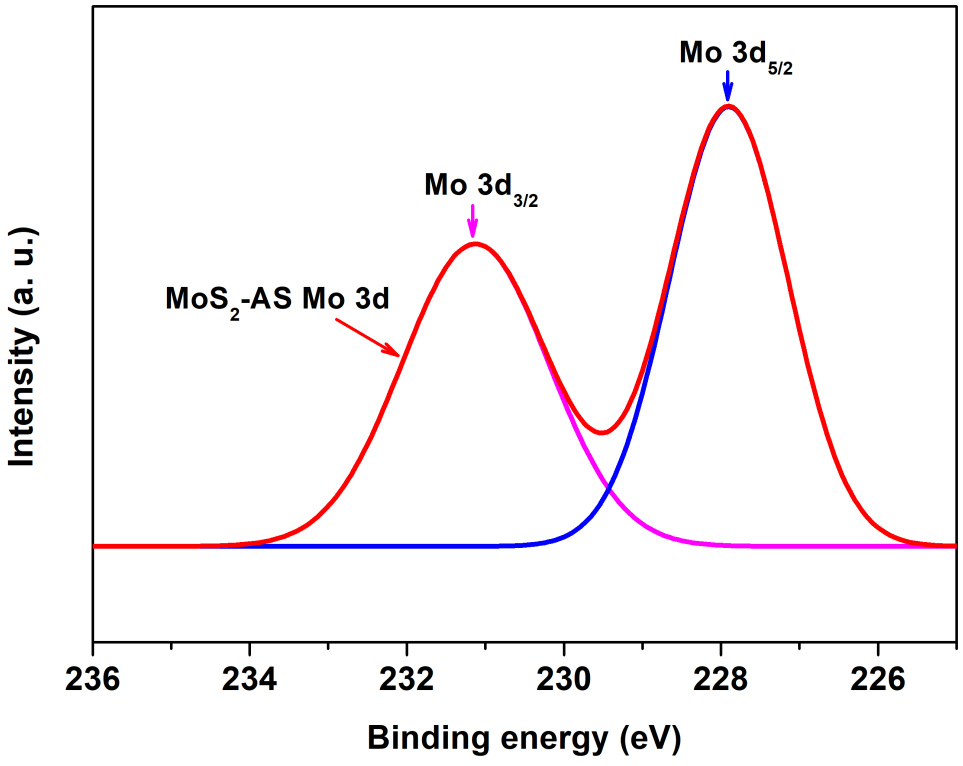

Figure 6.4: Deconvoluted XPS spectra for MoS_2-AS Mo 3d.

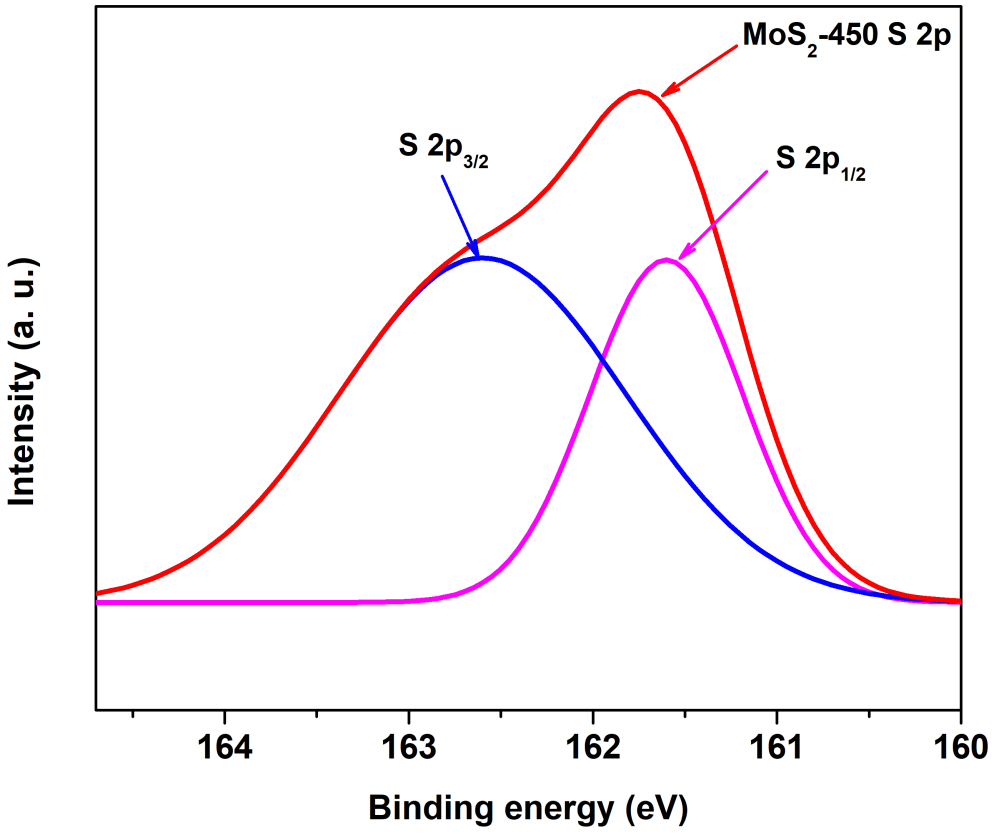

Figure 6.5: Deconvoluted XPS spectra for MoS_2-450 S 2p.

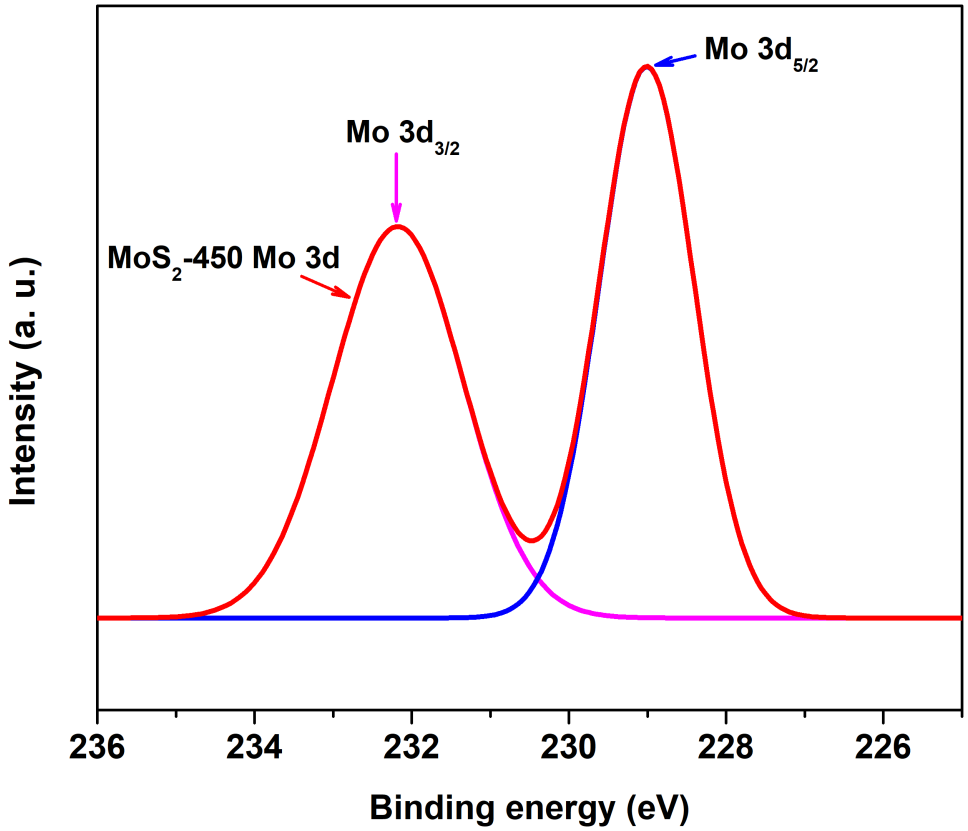

Figure 6.6: Deconvoluted XPS spectra for MoS_2-450 Mo 3d.

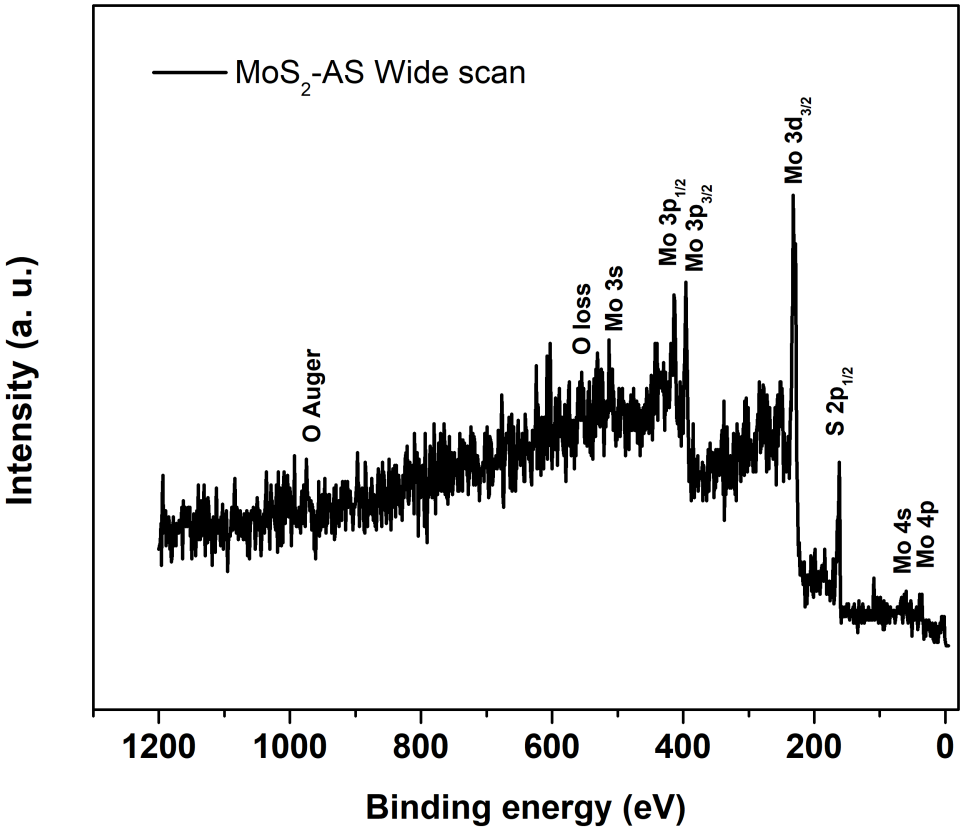

Figure 6.7: Wide area scan XPS spectra for MoS_2-AS.

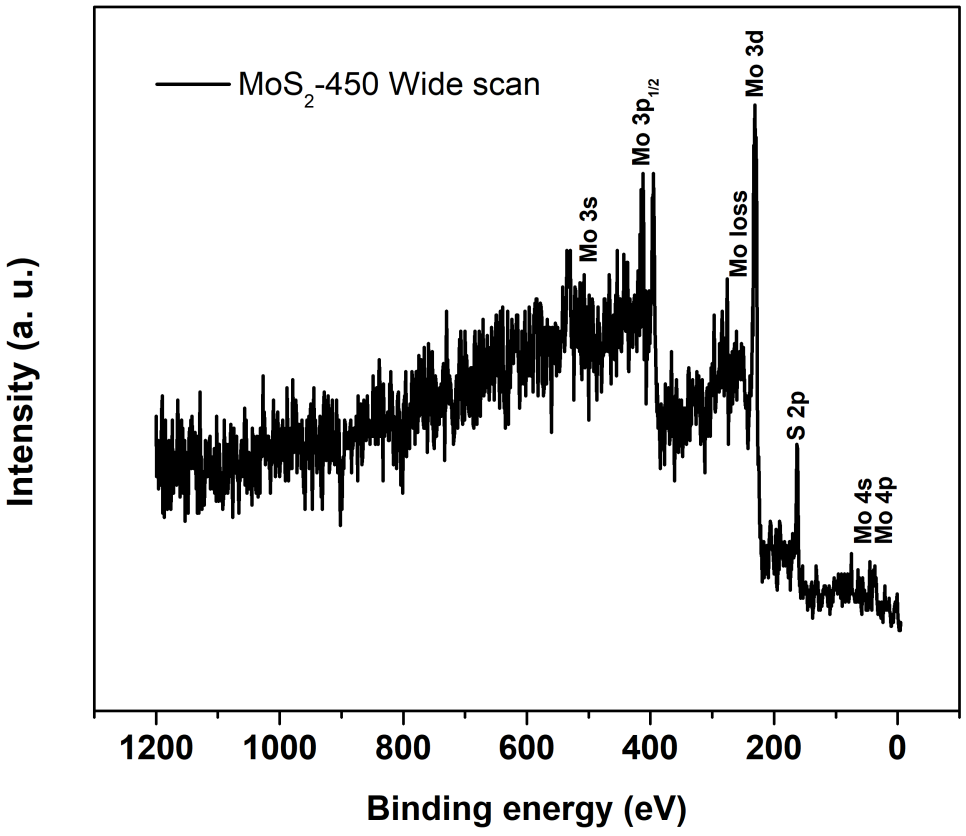

Figure 6.8: Wide area scan XPS spectra for MoS_2-450.

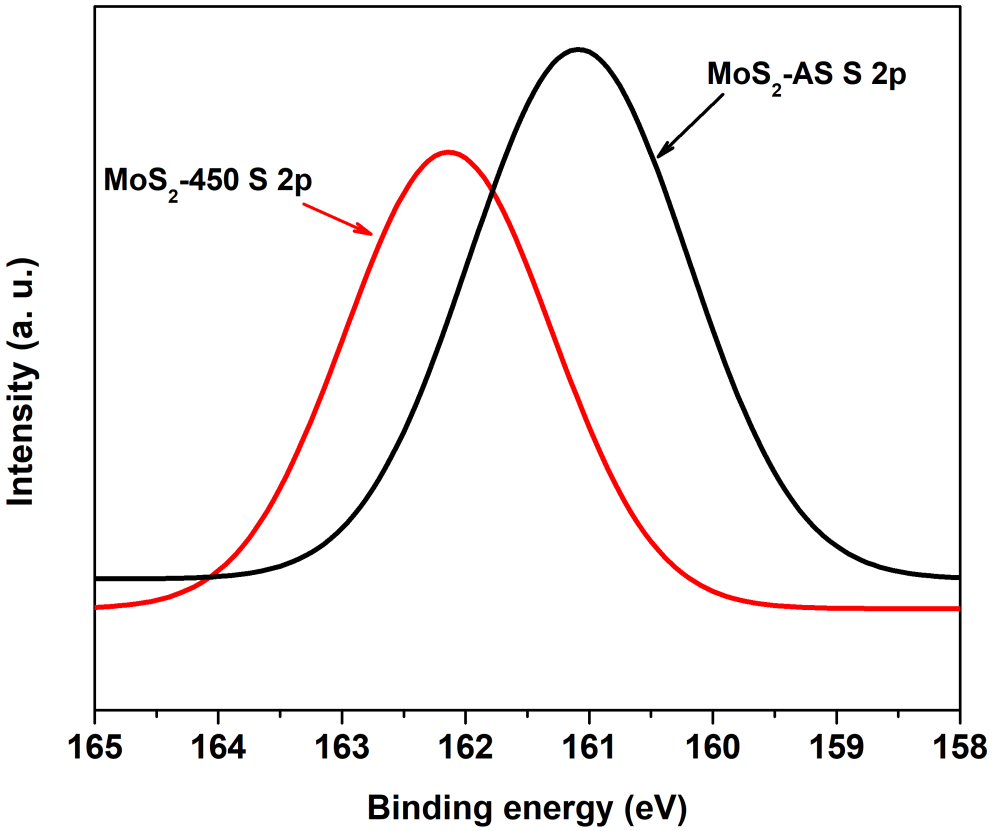

Figure 6.9: XPS spectra for MoS_2-AS and MoS_2-450 S 2p.

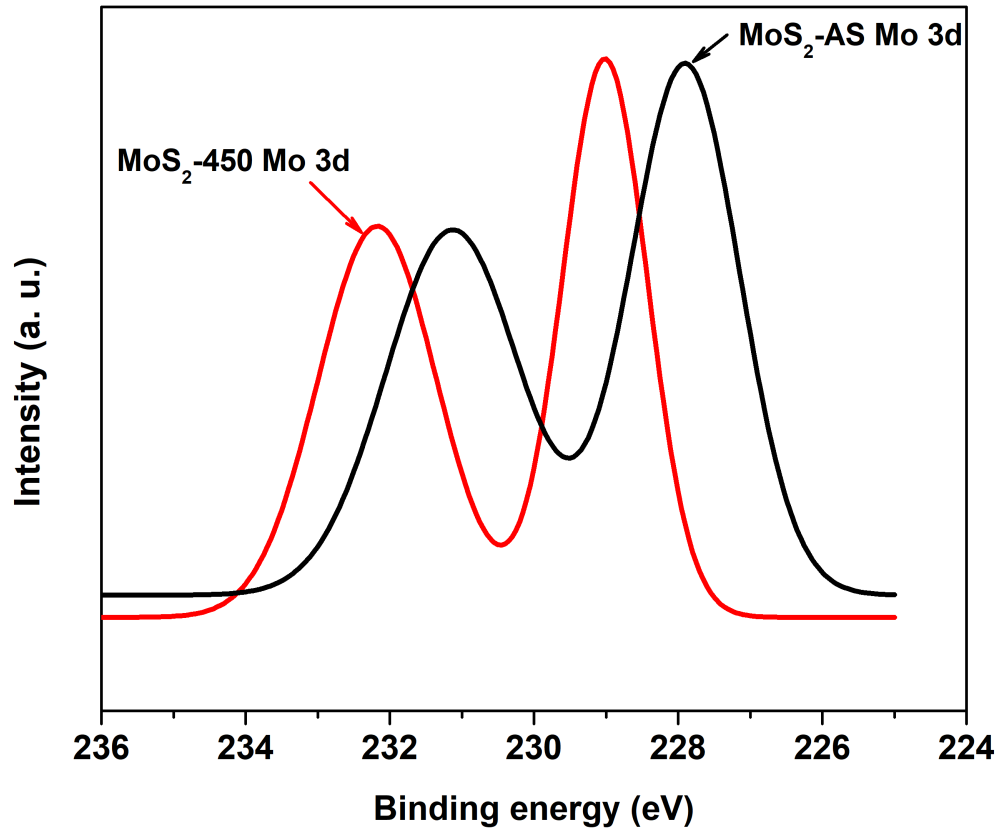

Figure 6.10: XPS spectra for MoS_2-AS and MoS_2-450 Mo 3d.

Table 6.1 gives a summary of the binding energies, the associated oxidation states and the atomic percentage concentrations for both MoS_2-AS and MoS_2-450 samples, determined by fitting the measured spectra.

Table 6.1: Binding energies, the associated oxidation states and the atomic % concentrations for both AS and 450 samples (error ± 5%).

	Binding energy (eV)				Atomic concentration (%)	
Sample	S $2p_{1/2}$ (S^{2-} or S_2^{2-})	S $2p_{3/2}$ (S^{2-} or S_2^{2-})	Mo $3d_{5/2}$	Mo $3d_{3/2}$	S	Mo
MoS_2-AS	161.92	160.76	231.1 (Mo^{5+})	227.9 (Mo^0)	62.88 ±4.18	37.1 ±4.18
MoS_2-450	162.59	161.59	229.0 (Mo^{4+})	232.2 (Mo^{3+})	38.93 ±6.38	67.07 ±6.38

The oxidation states associated with S $2p_{1/2}$ and S $2p_{3/2}$ were found to be S^{2-} or S_2^{2-}, which are in agreement with what other studies have reported [134, 140]. The associated binding energies for S 2p were at 161.92 eV and 160.76 eV for MoS_2-AS sample, while for MoS_2-450 sample they were at 162.59 eV and 161.59 eV. In the case of 3d orbitals for MoS_2-AS, Mo $3d_{5/2}$ had Mo^{5+} oxidation state, while its Mo $3d_{3/2}$ showed Mo^0 (neutral) oxidation state, with binding energies of 231.1 eV and 227.9 eV, respectively. This Mo $3d_{5/2}$ doublet is attributed to oxysulphide intermediate phases [141], due to the presence of oxgyen shown in AS wide scan in Fig. 6.7. A doublet was observed for MoS_2-450 sample Mo $3d_{5/2}$, with a binding energy of 229.0 eV and it is associated with Mo^{4+} centres in MoS_2 [141]. A binding energy of 232.2 eV in Mo $3d_{3/2}$ is attributed to Mo^{3+}. However, if the same energy is observed in Mo $3d_{5/2}$, it is associated with Mo^{4+} oxidation state [142].

The higher atomic mass percentage concentration (67.07 %) in MoS_2-450 sample material implies that an electrode composed of MoS_2-450 material has more active sites due to the presence of Mo^{3+} and Mo^{4+} ion, than an electrode whose composition has higher concentration (62.88 %) of S^{2-} or/and S_2^{2-} ion, as it is the case of an electrode material made of MoS_2-AS material composition. Furthermore, the Mo has a neutral oxidation state for MoS_2-AS material, as revealed by XPS analysis. However, this claim could only be confirmed through electrochemical analysis.

6.3.4 EDS and SEM Measurements

FEI Nova Nanolab 600 SEM was used for both EDS and SEM data acquisition. The EDS spectra showed presence of oxygen in MoS_2-AS sample while in MoS_2-450, only molybdenum and sulphur atoms were detected. This presence of oxygen in MoS_2-AS is in agreement with the XPS analysis too. SEM images revealed a better formation of flower-like MoS_2 morphology in MoS_2-450 compared to MoS_2-AS sample.

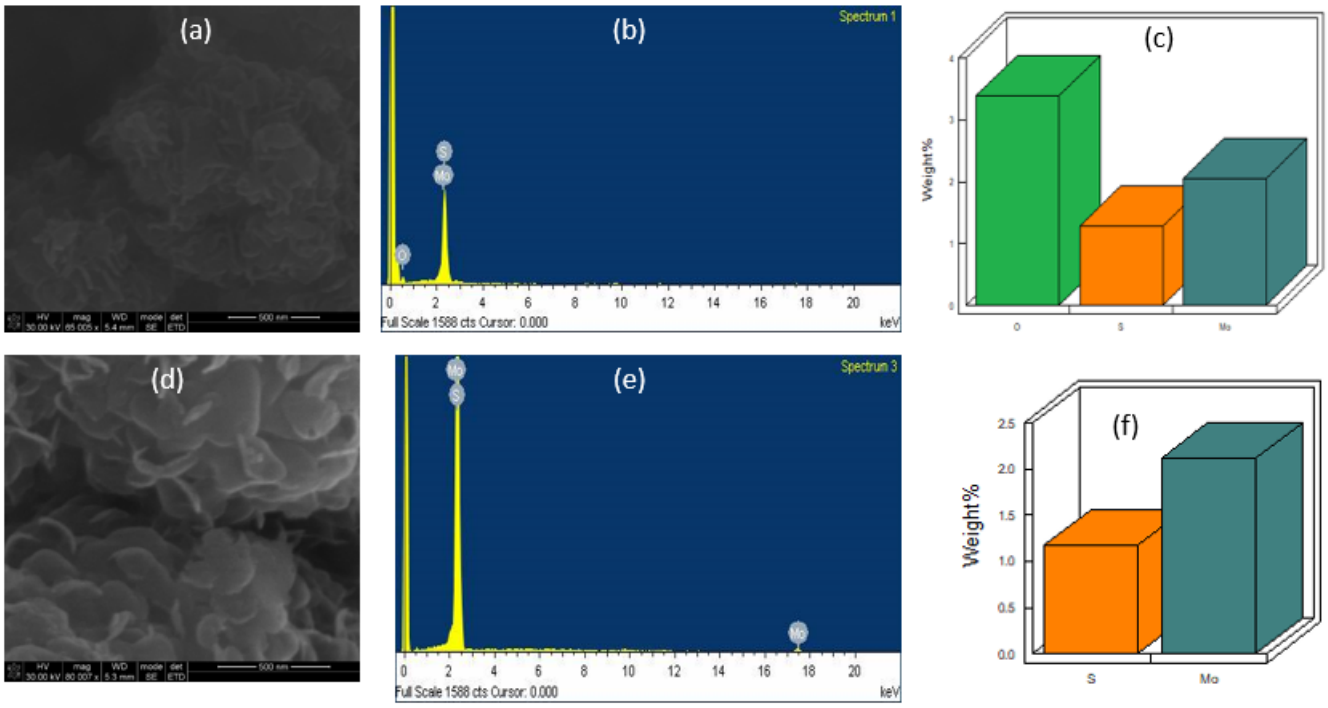

Figure 6.11: SEM morphologies (a) and (d), EDS spectra (b) and (e), % Weights (c) and (f), for MoS_2-AS and MoS_2-450, respectively.

From Fig. 6.11, the SEM morphology, at a magnification scale of 500 nm, shows a well formed flower-like structures for MoS_2-450 compared to that of MoS_2-AS at the same magnification. Fig. 6.11 (b) reveals presence of oxygen in MoS_2-AS which is absent in MoS_2-450 (Fig. 6.11 (e)). Annealing in N_2 gas removed all the oxygen, leaving MoS_2 only. This is further shown in Figs. 6.11 (c) and (f). Figure 6.12 shows a cascade of SEM images acquired at various magnifications for both MoS_2-450 and MoS_2-AS. A comparison of these images captured at same magnification scale for MoS_2-450 and MoS_2-AS clearly shows that the annealed sample has its particles closely packed to each other compared to those of the as-synthesised one.

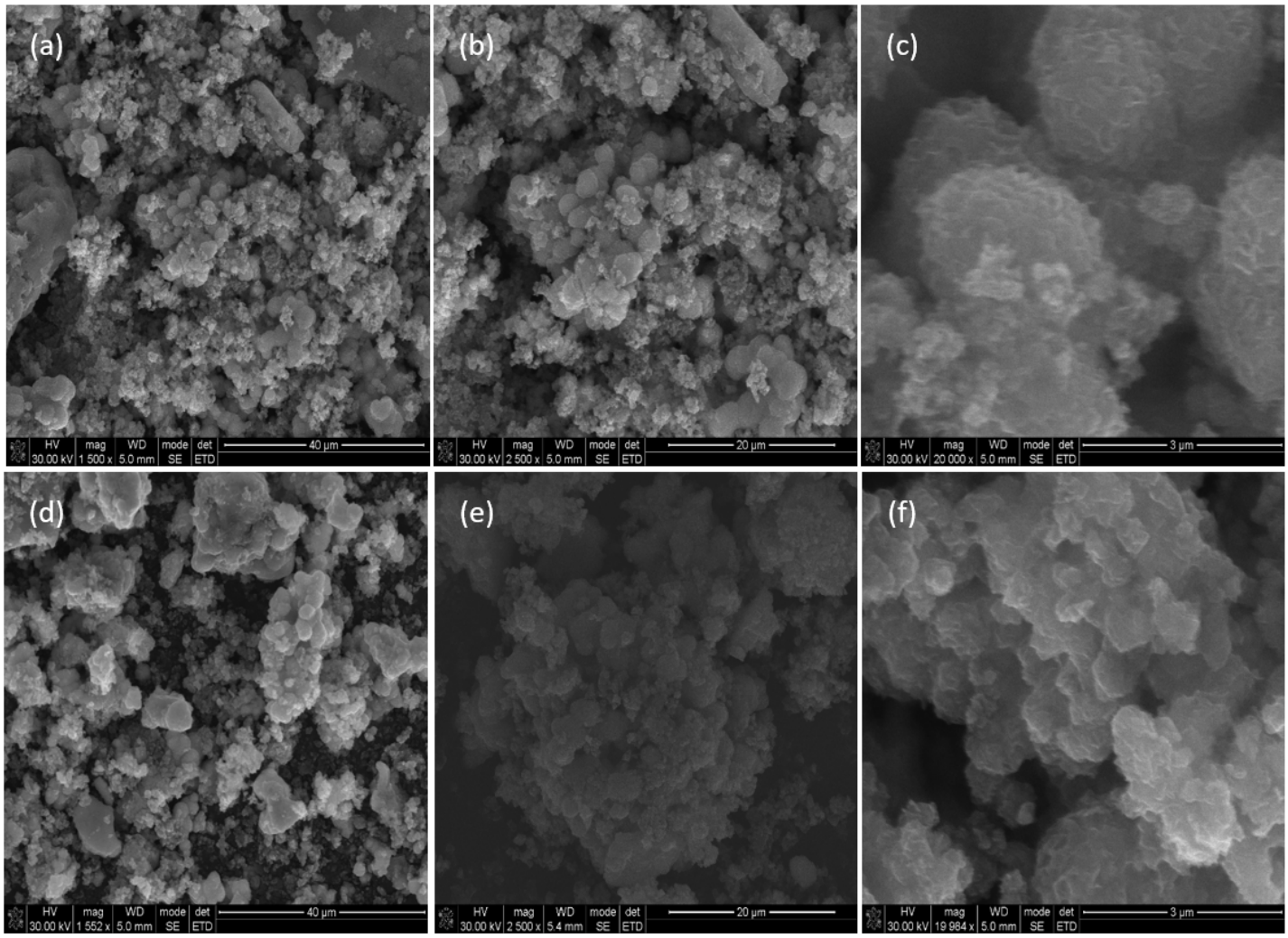

Figure 6.12: SEM morphologies (a)-(c) for MoS_2-450, (d)-(f) for MoS_2-AS, at 40 μm, 20 μm and 3 μm, respectively.

6.3.5 TEM Measurements

FEI Tecnai T12 TEM was used to acquire this data. TEM images displayed a typical interlayer structure of MoS_2, with the fringe distance (d-spacing) spacing of 6.95 Å. This was measured and averaged using ImageJ software [143]. These d-spacing are conspicuous in MoS_2-450 sample compared to MoS_2-AS as shown in Fig. 6.13, a clear indication that annealing enhanced MoS_2 crystals' formation. The fringe distance correspond to the spacing between (002) MoS_2 basal plane [138, 144].

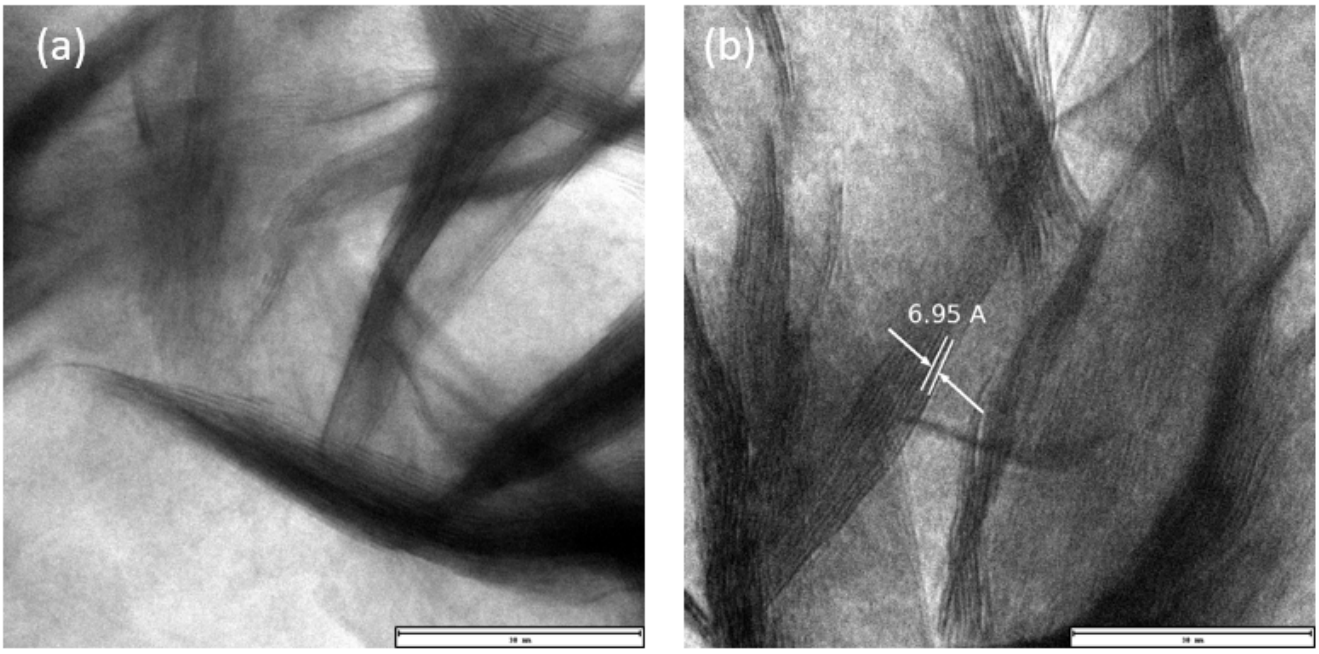

Figure 6.13: TEM images (a) MoS_2-AS and (b) MoS_2-450 powders.

All the above characterisation techniques have clearly shown that the synthesised powder material is MoS_2. From this juncture, it shall be treated as MoS_2 powdered sample(s). Brunauer-Emmett-Teller technique (BET) and thermal gravimetric analysis measurements were carried out to determine the porosity and thermal stability of the synthesised MoS_2 powder, respectively.

6.3.6 BET Measurements

A Micromeritics TriStar-Surface area and Porosity analyser, was used for these measurements. It was done by degassing samples of mass of ≈ 0.2 g in nitrogen at 150 °C for about four hours and analysis done using Micromeritcs flow Prep 060, sample degas apparatus. The Brunauer-Emmett-Teller technique has been connected for quite a few years to physisorption isotherm information to yield the estimations of the surface zone. The initial step in computing the BET surface zone includes the calculation of the

monolayer limit concurring the accompanying condition:

$$\frac{p}{n^a(p_o - p)} = \frac{1}{n^a_m C} + \frac{C-1}{n^a_m C} \cdot \frac{p}{p_o} \tag{6.1}$$

where n^a is the sum adsorbed at the relative weight $\frac{p}{p_o}$, n^a_m speaks to the monolayer limit, and C is a constant. The direct bend acquired from plotting $\frac{p}{n^a(p_o-p)}$ versus $\frac{p}{p_o}$ (as shown in Fig. 6.15), at relative weights somewhere in the range of 0.05 and 0.3, is utilized to compute the estimation of the monolayer limit, n^a_m. Based on n^a_m acquired and the normal sub-atomic cross-sectional zone (a_m) expected for the adsorptive particles, the BET surface zone can be assessed by the following condition:

$$SA_{BET} = n^a_m \cdot L \cdot a_m \tag{6.2}$$

where L is the Avogadro constant. A typical presumption for nitrogen is that the BET monolayer is close-pressed, which yields an estimation of a_m of 0.162 nm^2 (at 77 K). The surface area obtained using this technique is exclusive of the contribution from those pores that are smaller than the molecules of the probing gas (nitrogen in this study) used [145].

The BET measurements carried out were as tabulated in Table 6.2. The porosity of the as-synthesised and the annealed samples show a significant difference in BET (five point analysis) surface area as well as in pore size. The pore volume recorded minimal change after annealing. MoS_2-AS has a higher specific surface area (32.37 m^2g^{-1}) than its MoS_2-450 counterpart (23.25 m^2g^{-1}). The drastic reduction of surface area in the MoS_2-450 sample can be explained by the morphology transformation due to annealing observed from the SEM images discussed earlier. It is clearly shown from BET results that MoS_2-AS and MoS_2-450 are mesoporous (2-50 nm) materials [146], with the pore size of the former being smaller ($\approx$ 8 nm) than the latter ($\approx$ 10 nm).

Table 6.2: BET results for MoS_2-AS and MoS_2-450 obtained using 5 probe points (error ± 5%).

Sample	BET Surface area (m^2g^{-1})	Pore Volume (cm^3g^{-1})	Pore Size (nm)
MoS_2-AS	32.37	0.063	7.83
MoS_2-450	23.25	0.058	9.99

Figure 6.14 distribution for MoS_2-AS and MoS_2-450 samples. This shows in general that the MoS_2-AS had large sizes compared to MoS_2-AS sample, ranging from 1.7 nm to 70.8 nm, while those of MoS_2-450 sample range from 1.7 nm to 50.0 nm.

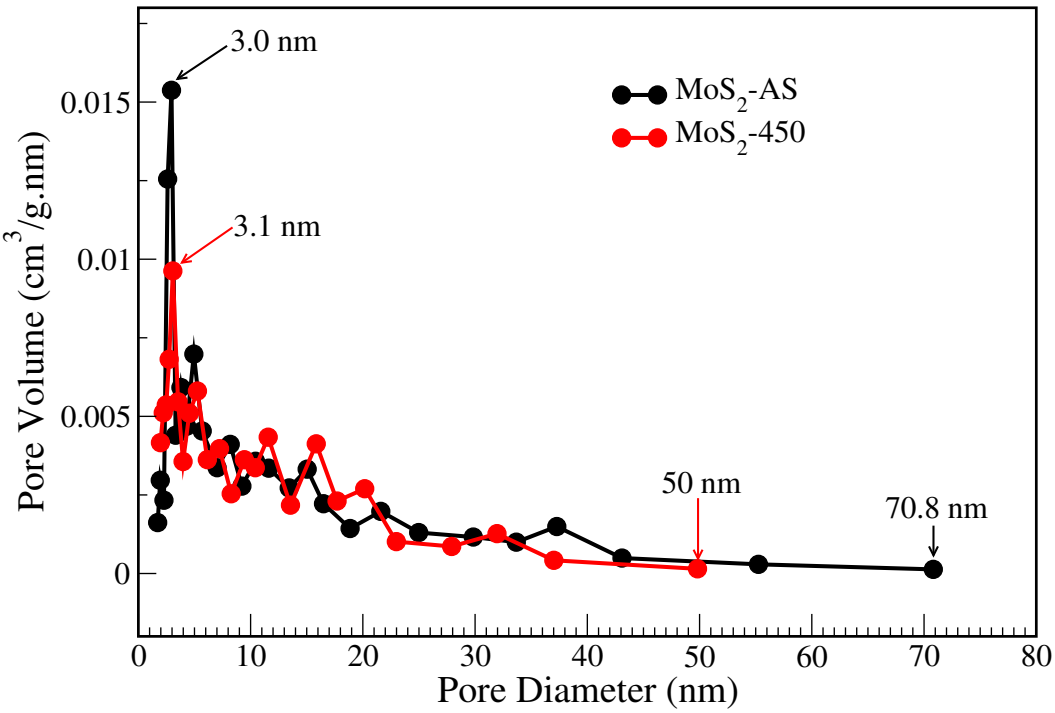

Figure 6.14: BET pore size distribution spectra for MoS_2-AS and MoS_2-450 samples.

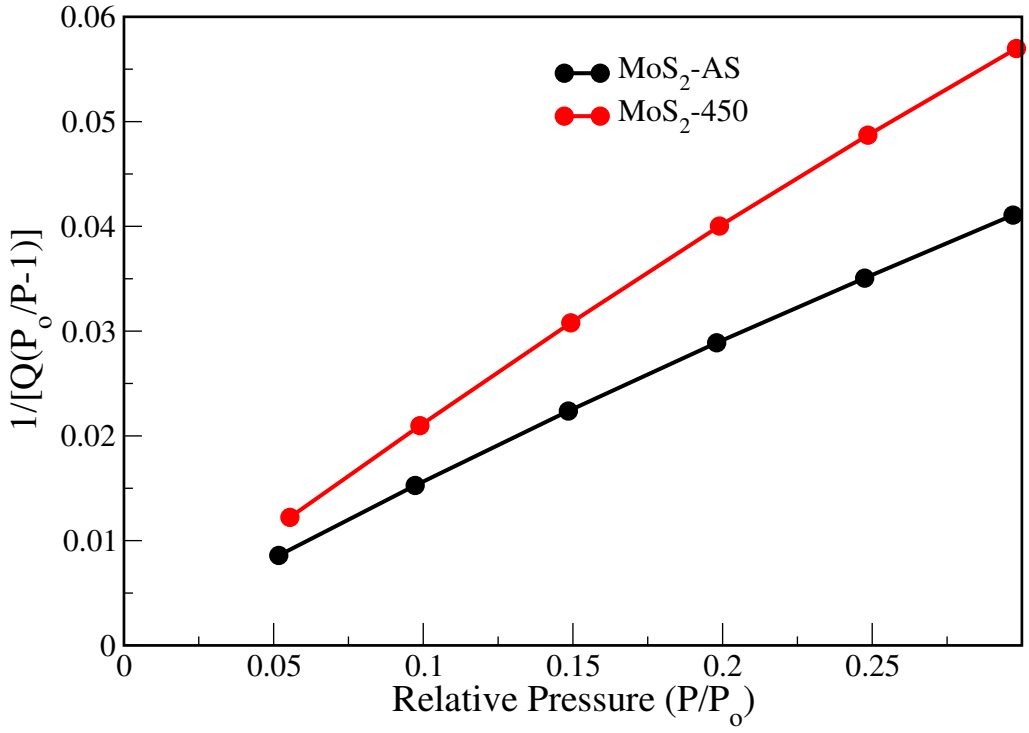

Figure 6.15: BET spectra for MoS_2-AS and MoS_2-450 samples.

Figure 6.16 shows the BET adsorption and desorption isotherms for MoS_2-AS and MoS_2-450 samples. It reveals that annealing reduced both the adsorption and desorption abilities of MoS_2-450 compared to MoS_2-AS.

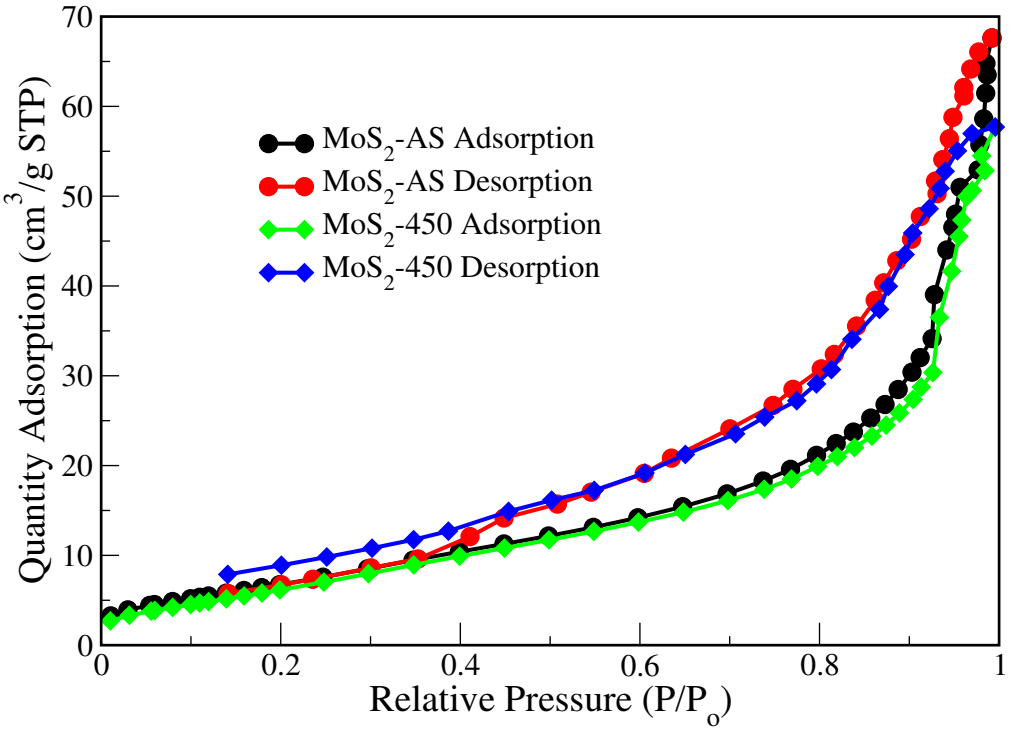

Figure 6.16: BET isotherm for MoS_2-AS and MoS_2-450 samples.

6.3.7 TGA Measurements

A Perkin Elmer TGA 4000 Thermal-gravimetric analyzer was used for this analysis. Samples of about 10 mg were constantly heated at a rate of 10 °C/min, starting from room temperature to 900 °C and the analysis done with 20 mL/min air flow rate. TGA was performed to establish the stability of MoS_2-AS and MoS_2-450 samples and the results are shown in Fig.6.17. Based on Fig.6.17 (Inset), the as-synthesis MoS_2 appears to be more stable at temperatures below 217 °C at which both samples show a percentage weight loss of 0.4. Beyond this temperature, the annealed sample (MoS_2-450) shows a lesser weight % loss in comparison to MoS_2-AS, implying that annealing assisted in enhancing the sample's thermal stability. At about 530 °C, MoS_2-450 sample had decomposed by 9 % while at the same temperature, MoS_2-AS sample showed a decomposition of 13 %. This change in the rate of mass reduction can be accounted for from the presence of oxygen reported to be present in MoS_2-AS sample.

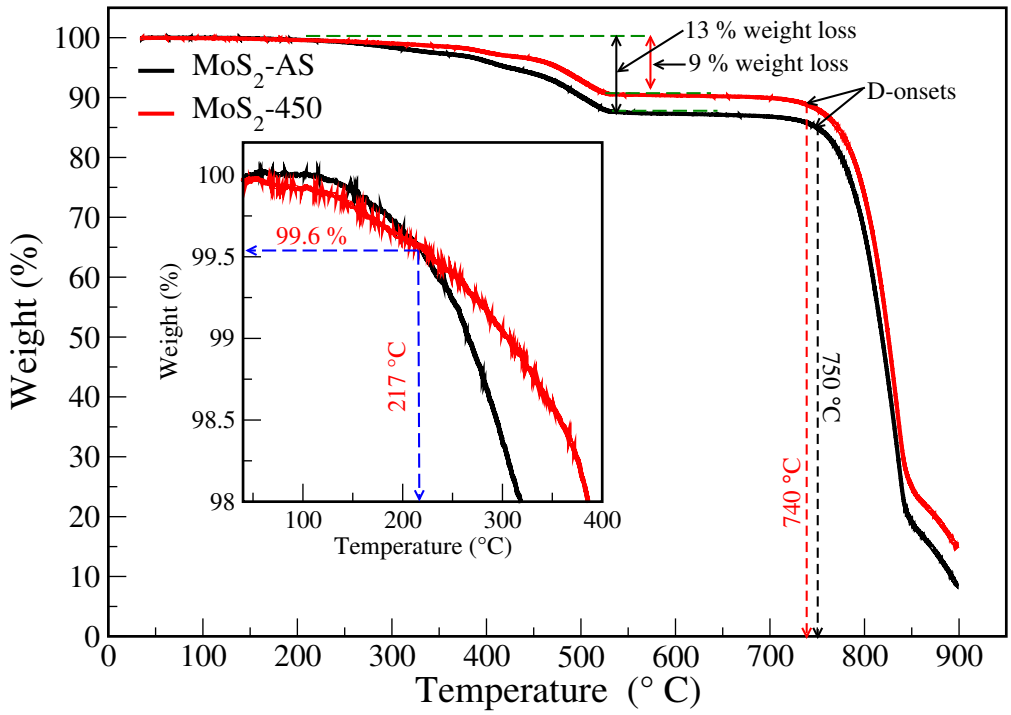

Figure 6.17: Thermogravimetric analysis of MoS_2-AS and MoS_2-450 Samples.

6.4 Electrochemistry Measurements

In order to show the energy storage or capacitance capabilities of the synthesised MoS_2, electrochemistry measurements were performed as outlined. First was the preparation of the electrodes. This was followed by W or Mo ion implantation on some of the electrodes and finally, the electrochemistry measurements.

6.4.1 Electrode Preparation

The working electrodes were prepared by a slurry tape casting procedure for both the as synthesised (AS) and the annealed (450) MoS_2 samples. The slurry consisted of 80 wt% active materials, 15 wt% carbon black and 5 wt% polyvinylidene fuoride (PVDF) dissolved in N-methyl-2-pyrrolidinone (NMP). The slurry was tape-cast on the carbon paper. The coated electrodes were dried at 80 °C, for 24 h in a vacuum. Six working electrodes of 12 mm in diameter were punched out of the coated carbon sheets; three from MoS_2-AS coated carbon paper and the other three from MoS_2-450 coated sheet. Therefore, each of these electrodes had an active area of 0.36π cm^2.

Two electrodes from each set were then ion implanted. One with Mo ions at fluences of 1×10^{16} ions/cm^2 (referred to as MoS_2-AS-Mo-16 and MoS_2-450-Mo-16) and the other with W ions 1×10^{12} ions/cm^2 (referred to as MoS_2-AS-W-12 and MoS_2-450-W-12). An implantation energy of 10 keV was used for all the four ion implantated samples.

6.4.2 Cyclic Voltammetry (CV) and Charge-Discharge (CD) Measurements

Both the CV and the CD measurements were carried out in 1 M Na_2SO_4 electrolyte at a potential window of 1 V (-0.5V to 0.5 V) using Swagelok electrochemical cell. Nickel foam was used as the counter electrode and activated carbon (AC) as the pseudo-reference electrode, while the working electrodes were the MoS_2 coated AC electrodes. The nickel foam was seperated from the working electrode by a glass-fiber filter paper (Whatman®).

Figures 6.18 and 6.19 show the gravimetric specific capacitance and charge-discharge curves, respectively. These are the curves from where maximum charge stored in the cells could be calculated from. That is from the lowest achievable scan rate (5 mV·s^{-1}) and current density (0.2 A·g^{-1}) for the synthesised powder MoS_2.

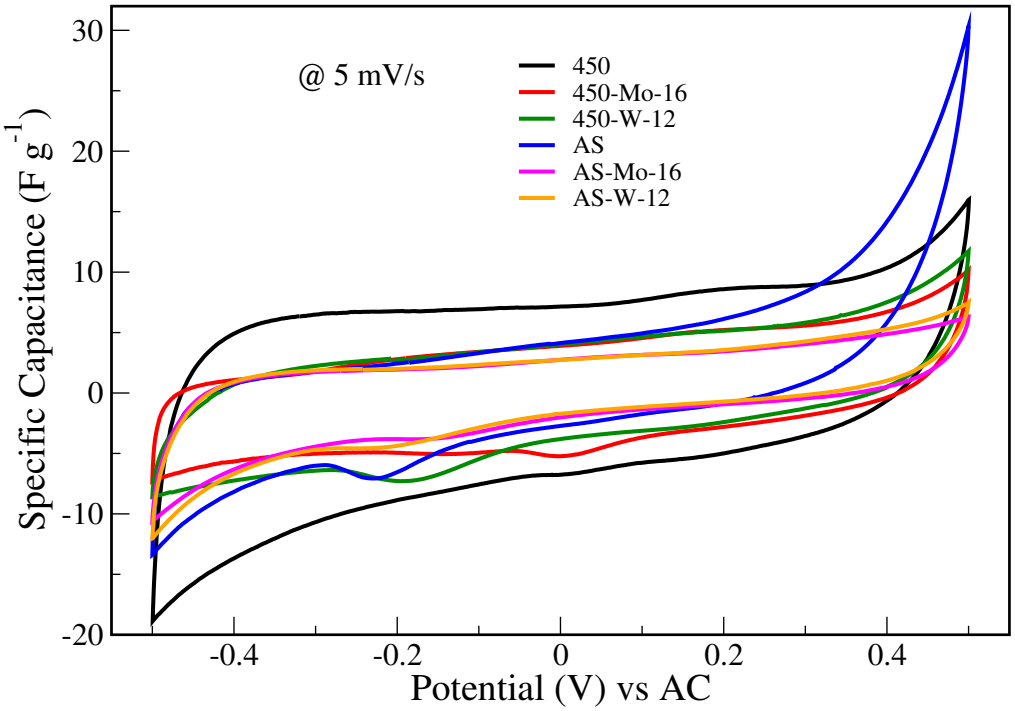

Figure 6.18: Specific capacitances against potential.

Based on both Figures (6.18 and 6.19), it is clear that annealed sample (MoS_2-450) has the highest charge storage capabilities. All the ion implanted electrodes showed suppressed capacitances and this attributed to pores size reduction due to ion implantation. The comparison of the pore sizes for un-implanted and implanted MoS_2-AS is shown in Table 6.3, where MoS_2-AS-W_{imp} denotes the as-synthesised MoS_2 powder, implanted with W ions a dose of 10 keV and a fluence of 1×10^{12} ions/cm^3. After W ion implantation into MoS_2-AS powder, a 23 % reduction in pore size was recorded. The high perfomance displayed by the MoS_2-450 sample, that was not ion implanted is accounted for by the larger pore sizes (9.99 nm) than that of MoS_2-AS (7.83 nm), based on the BET measurements. From the CV

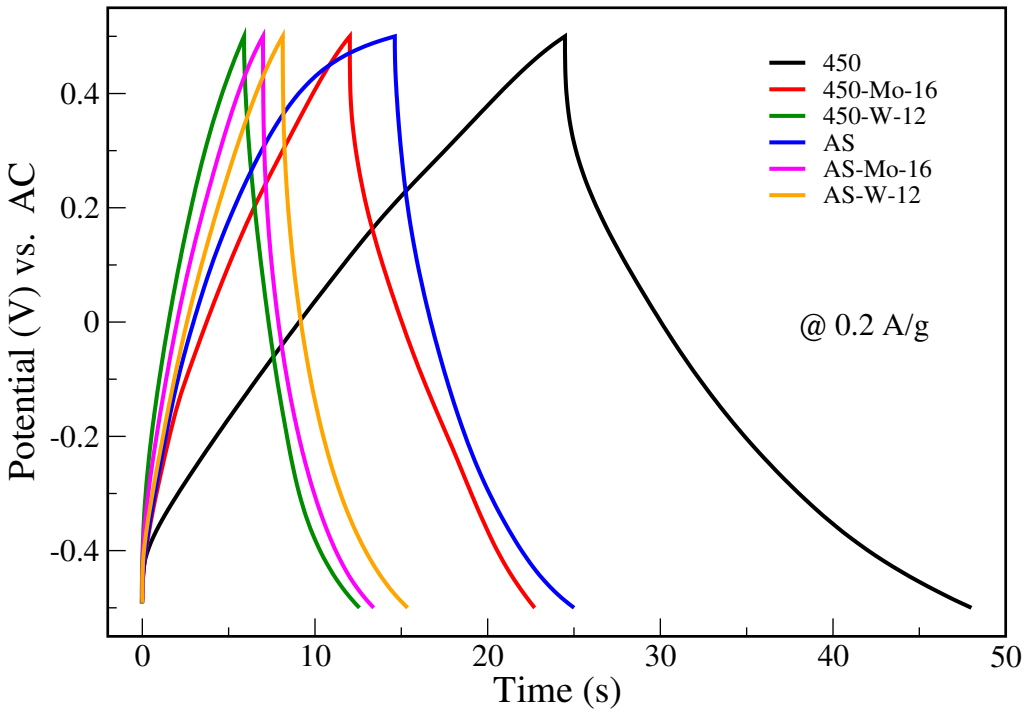

Figure 6.19: Charge-discharge curves at 0.2 A/g.

measurements, no oxidation or reduction peaks were observed. This implied that the electrochemical reaction processes were purely non-Faradaic. This is also shown from the tabulated results in Table 6.4.

Table 6.3: BET results for MoS_2-AS and MoS_2-AS-W_{imp} obtained using 5 probe points (error ± 5%).

Sample	BET Surface area (m^2g^{-1})	Pore Volume (cm^3g^{-1})	Pore Size (nm)
MoS_2-AS	32.37	0.06295	7.83
MoS_2-AS-W_{imp}	42.07	0.06336	5.98

Figure 6.20 demonstrates the comparison in the specific capacitances of electrodes made from the un-implanted and W ions implanted powder samples.The ion implantation in the powder was done at the *i*Themba LABS, Johannesburg. The powder was put in a special cup and implantation done as the powder tumbled in the rotating cup. The difference between this ion implanted electrode and the ones reported earlier is in the powder preparation, whereby, in the former ion implanted electrodes, the ion implantation was done after coating the slurries prepared from the un-implanted powders onto glassy carbon paper, while the MoS_2-AS-W_{imp} electrode was prepared using the slurry of already ion implanted powder. Based on Fig.6.20, the key finding here is that capacitance is mostly dependent on the pore size rather than area. From Table 6.3 it is also shown that W ions implantation process increases the surface area (possibly by reducing the sizes of the MoS_2 flakes while at the same time reducing the

pore size).

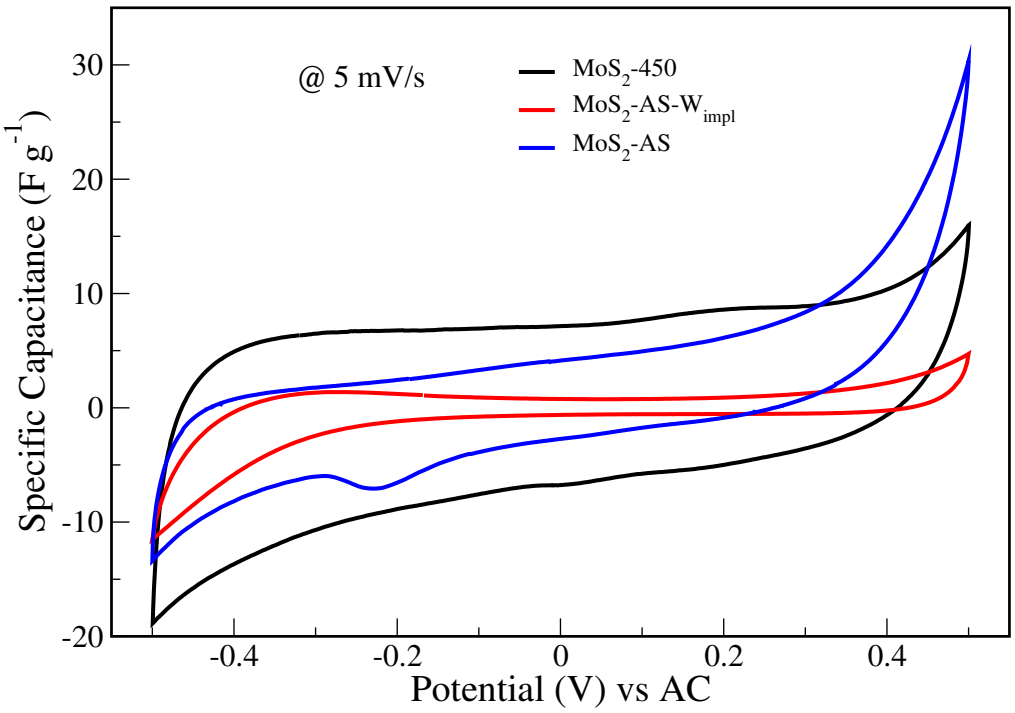

Figure 6.20: Specific capacitances against potential for ion implanted and un-implanted powder samples.

Table 6.4: Performance evaluation for MoS_2-AS, MoS_2-450, MoS_2-AS-Mo-16, MoS_2-AS-W-12, MoS_2-450-Mo-16 and MoS_2-450-W-12 samples at current density of 0.2 A·g^{-1} (error ± 5%).

Sample	C 10^{-3} (F)	Cs_m (F·g^{-1})	Cs_a 10^{-3} (F·cm^{-2})	ESR (Ω)	E 10^{-1} (W·h·kg^{-1})	P_{max} 10^{3} (W·kg^{-1})
MoS_2-AS	10.43	2.09	7.96	4.31	2.78	11.55
MoS_2-AS-Mo-16	7.44	1.31	5.68	10.01	1.70	4.31
MoS_2-AS-W-12	7.16	1.46	5.47	5.14	1.93	9.81
MoS_2-450	15.63	4.77	11.94	5.00	6.24	15.03
MoS_2-450-Mo-16	9.43	2.17	7.20	6.30	2.85	9.01
MoS_2-450-W-12	2.83	1.35	2.16	1.58	1.79	74.73

Key: Cs_a =geometric capacitance; Cs_m =gravimetric capacitance;
ESR = equivalent series resistance; E= energy; P_{max} = maximum power.

The annealed sample (MoS_2-450) shows a capacitance that is more than twice that of the as-synthesised (MoS_2-AS) sample. This is attributed to the larger size of its pores that enhances ion transport, despite its poor surface area as shown in the BET results in Table 6.2. The better formation of the d-spacings and flower-like morphology shown by TEM and SEM images could also account for this higher performance observed in MoS_2-450. The TGA results also show that MoS_2-450 sample is more thermostable

than the MoS_2-AS. However, ion implantation did not enhance the energy storage capability for all the powder samples. Diminished charge storage abilities are noted in both the MoS_2-450 and MoS_2-AS samples after introduction of either Mo or W ions.

The results tubulated in Table 6.4 are not comparable with those shown in Table 5.9, for bulk MoS_2 given that they were computed based on different current densities (0.001 $A{\cdot}g^{-1}$ and 0.2 $A{\cdot}g^{-1}$). However, irrespective of the current densities, which is two orders of magnitude difference, the powder MoS_2 yielded capacitances which were one order of magnitude higher than that of bulk MoS_2. Furthermore, the geometric capacitance for the powder MoS_2 is also two orders of magnitude higher than that of the bulk crystalline MoS_2, irrespective of the effects of its ion implantation. A notable drawback for the powder MoS_2 samples is the high equivalent series resistance (ESR), which is two orders of magnitude higher than that of the bulk MoS_2 samples.

6.4.3 Electrodes' Stability

All the electrodes made from the powdered MoS_2 were subjected to a 2000 cycles of charge and discharge stability test and the results are shown in Fig. 6.21. Based on Fig. 6.21 (inset), it is clear that the electrodes made from the annealed powder (MoS_2-450) are more stable compared to those created from the as-synthesised powder (MoS_2-AS), as revealed by the higher coulombic efficiency percentages throughout the 2000 cycles. The powder based electrodes were able to withstand 2000 cycles of charge-discharge unlike the bulk MoS_2 based electrodes, which only achieved 1000 cycles of charge-discharge, as shown in Chapter 5.

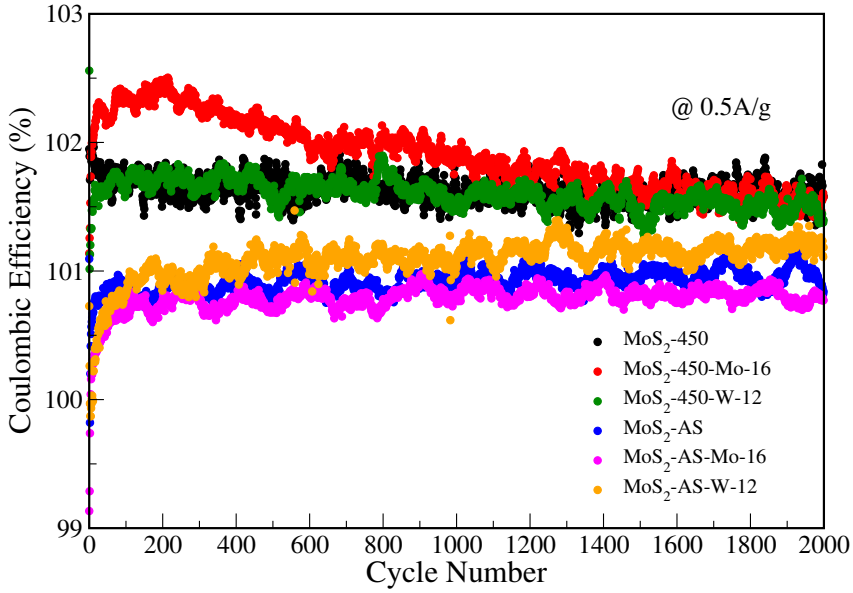

Figure 6.21: Coulombic efficiencies for MoS_2-AS, MoS_2-450, MoS_2-AS-Mo-16, MoS_2-AS-W-12, MoS_2-450-Mo-16 and MoS_2-450-W-12 electrodes, for 2000 cycles.

6.4.4 Conclusion

This Chapter has demonstrated a successful synthesis of powder MoS_2, which has flower-like morphology. Annealing the powder MoS_2 sample increases the pore size leading to enhanced ion transport. All the electrodes made from the powder MoS_2 showed capacitance behaviour unlike the ones reported in Chapter 5 for bulk crystalline MoS_2, which revealed both Faradiac and non-Faradaic processes dominance. The electrodes prepared from powder MoS_2 reported higher capacitances compared to the bulk one due to their generally higher surface area and porosity. However, ion implantation suppresses energy storage capabilities in powdered MoS_2, unlike in bulk crystalline MoS_2.

CHAPTER SEVEN

CONCLUSIONS AND RECOMMENDATIONS

This Chapter highlights the fundamental findings, discusses the shortcomings and suggests further research areas that could improve what is reported in this study.

7.1 Computational Analysis

From the computational perspective, we have clearly demonstrated how MoS_2 energy bandgap could be tuned, aiming at widening its applications. A reduction of between 8.5 % and 100 % has been achieved, with metal interstitials (Mo and W) showing the highest reductions of 73.6 % and 100 % for tungsten and molybdenum atoms, respectively. Fundamental studies on effects of introduced defects in MoS_2 could possibly open up new application areas for MoS_2. One possibility being energy conversion devices, like solar cells due to its semiconducting properties which are tunable by altering the chemical composition, hence changing the lattice structure [147, 148].

Also interesting is that MoS_2 can be changed from a p-type semiconductor into an n-type semiconductor, which further increase its potential areas for application in semiconductor industry. Based on these results, the technique used could be extended to other transition metal dichalcogenides (TMD) and metallic compounds such as Niobium disulphide (NbS_2) and Niobium diselenide ($NbSe_2$), thus opening different possibilities for band gap engineering.

7.2 Experimental Perspective

MoS_2 electrical conductivity and pseudocapacitive behaviour was enhanced by ion implantation in bulk crystalline MoS_2. This controlled enhancement of capacitance for bulk MoS_2 system could lead to a study of the fundamental effects that lead to this enhancement. The optimization of the annealing temperature for powder MoS_2 is likely to lead to more areas of application, based on the thermal stability and higher capacitance upon annealing at 450 °C, reported in this study. Other beneficiaries to improved MoS_2, include the optoelectronic and magnetic application since its semiconducting properties are tunable by altering the chemical composition, hence changing the lattice structure [149].

Studies on nanospheres of MoS_2 by Khawula *et al.* [134], exhibited better capacitance, power and energy densities (230 $F{\cdot}g^{-1}$, 6443 $W{\cdot}kg^{-1}$ and 26 $W{\cdot}h{\cdot}kg^{-1}$). This is due to the porous nature and the introduction of carbon nano-spheres into MoS_2, guaranteed improved electrochemical performance they

reported. The first set of electrodes made from ion implanted bulk MoS_2, reported in this study had their enhancement not due to porosity but due to implantation process and point defect interactions and they reported a maximum power which is three orders of magnitude higher than Khawula *et al.* [134] as shown in Table 5.9. From Table 5.9, it is not trivial to point out the optimal procedure of ion implantation since almost all the electrodes had their strong and weak points based on Cs_m, Cs_a, ESR, E and P_{max}.

The ion implantation used in this study has clearly shown great enhancement in terms of energy capacity, recycling stability as well as a very high retention after 1000 cycles -with Mo-2e16 at over 98 %. Hence, demonstrating higher potential that could be incorporated with other currently used techniques to boost MoS_2 energy storage capabilities and electrodes' stability.

Electrodes made from the synthesised powder MoS_2 reported capacitances which were one order of magnitude higher than what the bulk MoS_2 electrodes yielded, as shown in Table 6.4. Similarly, the gravimetric specific capacitances recorded for the powder based electrodes also were one order of magnitude higher. This is attributed to their high surface area and larger pore sizes, which enhance ion transport. However, ion implantation on the MoS_2 powder-based electrodes showed suppressed capacitances attributed to possible decrease in pore sizes as a result of ion irradiation.

Although ion implantantion showed enhanced energy storage for bulk crystalline MoS_2, it did not yield positive results for the electrodes prepared with powder for porous materials due to the possibility of it causing reduction in the pore sizes, which are active sites that boost energy storage ability. One of the keys to improving capacitance or capacity in MoS_2 powder electrodes lies in the annealing temperature optimization, as observed in this study. A comparison between the as-synthesised MoS_2-AS electrode and the electrode prepared from the 450 °C annealed powder MoS_2-450, showed a gravimetric capacitance of 4.77 $F{\cdot}g^{-1}$, which is more than two-folds that recorded for MoS_2-AS electrode (2.09 $F{\cdot}g^{-1}$).

Generally, Mo and W ions irradiations enhanced the energy storage capacity of bulk crystalline MoS_2, studies on other elements can also be done to find out how they influence charge storage in both crystalline and powder MoS_2. This study's choice of Mo and was based on the fact that Mo forms part of MoS_2 constituent elements while W was chosen since it also forms layered material with S, like in the case of WS_2. It is also worthy to note that the theoritical results in this study could no be compared with the experimental ones. The theoritical studies mainly focused on aspects of MoS_2 that require sophisticated instrumention to measure, thus making its comparison with the experiment results impractical.

REFERENCES

[1] Sodano H. A., Inman D. J., and Park G., "Generation and storage of electricity from power harvesting devices," *Journal of Intelligent Material Systems and Structures*, vol. 16, no. 1, pp. 67–75, (2005).

[2] Leschin S., Cass R., and Mohammadi F., "Self-powered portable electronic device," (May 7 2007). US Patent App. 11/745,222.

[3] Yu Z., Ye J., Chen W., Xu S., and Huang F., "Fabrication of few-layer molybdenum disulfide/reduced graphene oxide hybrids with enhanced lithium storage performance through a supramolecule-mediated hydrothermal route," *Carbon*, vol. 114, pp. 125–133, (2017).

[4] Feng C., Ma J., Li H., Zeng R., Guo Z., and Liu H., "Synthesis of molybdenum disulfide (MoS_2) for lithium ion battery applications," *Materials Research Bulletin*, vol. 44, no. 9, pp. 1811–1815, (2009).

[5] Zhang S., Hu R., Dai P., Yu X., Ding Z., Wu M., Li G., Ma Y., and Tu C., "Synthesis of rambutan-like MoS_2/mesoporous carbon spheres nanocomposites with excellent performance for supercapacitors," *Applied Surface Science*, vol. 396, pp. 994–999, (2017).

[6] Ma G., Peng H., Mu J., Huang H., Zhou X., and Lei Z., "In situ intercalative polymerization of pyrrole in graphene analogue of MoS_2 as advanced electrode material in supercapacitor," *Journal of Power Sources*, vol. 229, pp. 72–78, (2013).

[7] Xie D., Tang W., Xia X., Wang D., Zhou D., Shi F., Wang X., Gu C., and Tu J., "Integrated 3D porous C-MoS_2/nitrogen-doped graphene electrode for high capacity and prolonged stability lithium storage," *Journal of Power Sources*, vol. 296, pp. 392–399, (2015).

[8] Chen B., Liu E., Cao T., He F., Shi C., He C., Ma L., Li Q., Li J., and Zhao N., "Controllable graphene incorporation and defect engineering in MoS_2-$TiOS_2$ based composites: Towards high-performance lithium-ion batteries anode materials," *Nano Energy*, vol. 33, pp. 247–256, (2017).

[9] Kim S.-S., Lee J.-W., Yun J.-M., and Na S.-I., "2-dimensional MoS_2 nanosheets as transparent and highly electrocatalytic counter electrode in dye-sensitized solar cells: effect of thermal treatments," *Journal of Industrial and Engineering Chemistry*, vol. 29, pp. 71–77, (2015).

[10] Zhong C., Deng Y., Hu W., Qiao J., Zhang L., and Zhang J., "A review of electrolyte materials and compositions for electrochemical supercapacitors," *Chemical Society Reviews*, vol. 44, no. 21, pp. 7484–7539, (2015).

[11] Kötz R. and Carlen M., "Principles and applications of electrochemical capacitors," *Electrochimica Acta*, vol. 45, no. 15, pp. 2483–2498, (2000).

[12] Burke A. and Miller M., "The power capability of ultracapacitors and lithium batteries for electric and hybrid vehicle applications," *Journal of Power Sources*, vol. 196, no. 1, pp. 514–522, (2011).

[13] Wang G., Zhang L., and Zhang J., "A review of electrode materials for electrochemical supercapacitors," *Chemical Society Reviews*, vol. 41, no. 2, pp. 797–828, (2012).

[14] Saxl O., "Nanotechnology: Applications and markets, present and future," in *Ellipsometry at the Nanoscale*, pp. 705–730, Springer, (2013).

[15] Burke A., Liu Z., and Zhao H., "Present and future applications of supercapacitors in electric and hybrid vehicles," in *Electric Vehicle Conference (IEVC), 2014 IEEE International*, pp. 1–8, IEEE, (2014).

[16] Charlier J.-C., Blase X., and Roche S., "Electronic and transport properties of nanotubes," *Reviews of Modern Physics*, vol. 79, no. 2, p. 677, (2007).

[17] Knipp D., Street R., Völkel A., and Ho J., "Pentacene thin film transistors on inorganic dielectrics: Morphology, structural properties, and electronic transport," *Journal of Applied Physics*, vol. 93, no. 1, pp. 347–355, (2003).

[18] Balandin A. A., "Thermal properties of graphene and nanostructured carbon materials," *Nature materials*, vol. 10, no. 8, p. 569, (2011).

[19] Stoneham A. M., *Theory of defects in solids: electronic structure of defects in insulators and semiconductors*. Oxford University Press, (2001).

[20] Schroeder D. J., Berry G. D., and Rockett A. A., "Gallium diffusion and diffusivity in $CuInSe_2$ epitaxial layers," *Applied Physics Letters*, vol. 69, no. 26, pp. 4068–4070, (1996).

[21] Stroh A., "Dislocations and cracks in anisotropic elasticity," *Philosophical Magazine*, vol. 3, no. 30, pp. 625–646, (1958).

[22] Penn R. L. and Banfield J. F., "Imperfect oriented attachment: dislocation generation in defect-free nanocrystals," *Science*, vol. 281, no. 5379, pp. 969–971, (1998).

[23] Keller R., Maier H., and Mughrabi H., "Characterization of interfacial dislocation networks in a creep-deformed nickel-base superalloy," *Scripta Metallurgica et Materialia*, vol. 28, no. 1, pp. 23–28, (1993).

[24] Ishida Y., Ishida H., Kohra K., and Ichinose H., "Determination of the Burgers vector of a dislocation by weak-beam imaging in a HVEM," *Philosophical Magazine A*, vol. 42, no. 4, pp. 453–462, (1980).

[25] Benedictus R., Böttger A., and Mittemeijer E., "Thermodynamic model for solid-state amorphization in binary systems at interfaces and grain boundaries," *Physical Review B*, vol. 54, no. 13, p. 9109, (1996).

[26] Read W. T., *Dislocations in crystals*, vol. 53. McGraw-Hill New York, (1953).

[27] Murray R., Haynes K., Zhao X., Perry S., Hatem C., and Jones K., "The effect of low energy ion implantation on MoS_2," *ECS Journal of Solid State Science and Technology*, vol. 5, no. 11, pp. 3050–3053, (2016).

[28] Xu K., Zhao Y., Lin Z., Long Y., Wang Y., Chan M., and Chai Y., "Doping of two-dimensional MoS_2 by high energy ion implantation," *Semiconductor Science and Technology*, vol. 32, no. 12, p. 124002, (2017).

[29] Wahl K., Dunn D., and Singer I., "Effects of ion implantation on microstructure, endurance and wear behavior of IBAD MoS_2," *Wear*, vol. 237, no. 1, pp. 1–11, (2000).

[30] Shao L., Wu Z., Duan H., and Shaymurat T., "Discriminative and rapid detection of ozone realized by sensor array of Zn^{2+} doping tailored MoS_2 ultrathin nanosheets," *Sensors and Actuators B: Chemical*, (2017).

[31] Kümmell T., Quitsch W., Matthis S., Litwin T., and Bacher G., "Gate control of carrier distribution in k-space in MoS_2 monolayer and bilayer crystals," *Physical Review B*, vol. 91, no. 12, p. 125305, (2015).

[32] Kobayashi K. and Yamauchi J., "Electronic structure and scanning-tunneling-microscopy image of molybdenum dichalcogenide surfaces," *Physical Review B*, vol. 51, no. 23, p. 17085, (1995).

[33] Schönfeld B., Huang J., and Moss S., "Anisotropic mean-square displacements (MSD) in single-crystals of 2H-and 3R-MoS_2," *Acta Crystallographica Section B: Structural Science*, vol. 39, no. 4, pp. 404–407, (1983).

[34] Li H., Wu J., Yin Z., and Zhang H., "Preparation and applications of mechanically exfoliated single-layer and multilayer MoS_2 and WSe_2 nanosheets," *Accounts of chemical research*, vol. 47, no. 4, pp. 1067–1075, (2014).

[35] Tang J., *Recovery of Copper and Zinc in Ashes from Municipal Solid Waste Combustion*. PhD thesis, Chalmers University of Technology, (2015).

[36] Pearson W. B., *A handbook of lattice spacings and structures of metals and alloys*. (1967).

[37] Lansdown A. R., *Molybdenum disulphide lubrication*, vol. 35. Elsevier, (1999).

[38] Haopeng L., "Physics and Materials Science," (2014).

[39] Zhao J., Jiang J.-W., and Rabczuk T., "Temperature-dependent mechanical properties of single-layer molybdenum disulphide: molecular dynamics nanoindentation simulations," *Applied Physics Letters*, vol. 103, no. 23, p. 231913, (2013).

[40] Cooper R. C., Lee C., Marianetti C. A., Wei X., Hone J., and Kysar J. W., "Nonlinear elastic behavior of two-dimensional molybdenum disulfide," *Physical Review B*, vol. 87, no. 3, p. 035423, (2013).

[41] Ansari R., Malakpour S., Faghihnasiri M., and Ajori S., "Characterization of the mechanical properties of monolayer molybdenum disulfide nanosheets using first principles," *Journal of Nanotechnology in Engineering and Medicine*, vol. 4, no. 3, p. 034501, (2013).

[42] Castellanos-Gomez A., Poot M., Steele G. A., van der Zant H. S., Agraït N., and Rubio-Bollinger G., "Elastic properties of freely suspended MoS_2 nanosheets," *Advanced Materials*, vol. 24, no. 6, pp. 772–775, (2012).

[43] Bertolazzi S., Brivio J., and Kis A., "Stretching and breaking of ultrathin MoS_2," *ACS Nano*, vol. 5, no. 12, pp. 9703–9709, (2011).

[44] Peng Q. and De S., "Outstanding mechanical properties of monolayer MoS_2 and its application in elastic energy storage," *Physical Chemistry Chemical Physics*, vol. 15, no. 44, pp. 19427–19437, (2013).

[45] Lince J. R., "Tribology of co-sputtered nanocomposite Au/MoS_2 solid lubricant films over a wide contact stress range," *Tribology Letters*, vol. 17, no. 3, pp. 419–428, (2004).

[46] Armand M. and Tarascon J.-M., "Building better batteries," *Nature*, vol. 451, no. 7179, pp. 652–657, (2008).

[47] Zhang R., Wen Q., Qian W., Su D. S., Zhang Q., and Wei F., "Superstrong ultralong carbon nanotubes for mechanical energy storage," *Advanced Materials*, vol. 23, no. 30, pp. 3387–3391, (2011).

[48] Lima M. D., Li N., De Andrade M. J., Fang S., Oh J., Spinks G. M., Kozlov M. E., Haines C. S., Suh D., and Foroughi J., "Electrically, chemically, and photonically powered torsional and tensile actuation of hybrid carbon nanotube yarn muscles," *Science*, vol. 338, no. 6109, pp. 928–932, (2012).

[49] Laquai F., Wegner G., Im C., Bässler H., and Heun S., "Comparative study of hole transport in polyspirobifluorene polymers measured by the charge-generation layer time-of-flight technique," *Journal of Applied Physics*, vol. 99, no. 2, p. 023712, (2006).

[50] Laquai F., Wegner G., Im C., Bässler H., and Heun S., "Nondispersive hole transport in carbazole- and anthracene-containing polyspirobifluorene copolymers studied by the charge-generation layer time-of-flight technique," *Journal of Applied Physics*, vol. 99, no. 3, p. 033710, (2006).

[51] Li X., Mullen J. T., Jin Z., Borysenko K. M., Nardelli M. B., and Kim K. W., "Intrinsic electrical transport properties of monolayer silicene and MoS_2 from first principles," *Physical Review B*, vol. 87, no. 11, p. 115418, (2013).

[52] Seifert G., Terrones H., Terrones M., Jungnickel G., and Frauenheim T., "Structure and electronic properties of MoS_2 nanotubes," *Physical Review Letters*, vol. 85, no. 1, p. 146, (2000).

[53] Zibouche N., Kuc A., and Heine T., "From layers to nanotubes: transition metal disulfides TMS_2," *The European Physical Journal B*, vol. 85, no. 1, pp. 1–7, (2012).

[54] Remskar M., Mrzel A., Virsek M., Godec M., Krause M., Kolitsch A., Singh A., and Seabaugh A., "The MoS_2 nanotubes with defect-controlled electric properties," *Nanoscale Res Lett*, vol. 6, no. 1, p. 1, (2010).

[55] Zhang C., Ning Z., Liu Y., Xu T., Guo Y., Zak A., Zhang Z., Wang S., Tenne R., and Chen Q., "Electrical transport properties of individual WS_2 nanotubes and their dependence on water and oxygen absorption," *Applied Physics Letters*, vol. 101, no. 11, p. 113112, (2012).

[56] Bindumadhavan K., Srivastava S. K., and Mahanty S., "MoS_2–mwcnt hybrids as a superior anode in lithium-ion batteries," *Chemical Communications*, vol. 49, no. 18, pp. 1823–1825, (2013).

[57] Lee K., Kim H.-Y., Lotya M., Coleman J. N., Kim G.-T., and Duesberg G. S., "Electrical characteristics of molybdenum disulfide flakes produced by liquid exfoliation," *Advanced Materials*, vol. 23, no. 36, pp. 4178–4182, (2011).

[58] Das S., Chen H.-Y., Penumatcha A. V., and Appenzeller J., "High performance multilayer MoS_2 transistors with scandium contacts," *Nano Letters*, vol. 13, no. 1, pp. 100–105, (2012).

[59] Skriver H. L. and Rosengaard N., "Surface energy and work function of elemental metals," *Physical Review B*, vol. 46, no. 11, p. 7157, (1992).

[60] Walia S., Balendhran S., Wang Y., Ab Kadir R., Zoolfakar A. S., Atkin P., Ou J. Z., Sriram S., Kalantar-zadeh K., and Bhaskaran M., "Characterization of metal contacts for two-dimensional MoS_2 nanoflakes," *Applied Physics Letters*, vol. 103, no. 23, p. 232105, (2013).

[61] Wang Q. H., Kalantar-Zadeh K., Kis A., Coleman J. N., and Strano M. S., "Electronics and optoelectronics of two-dimensional transition metal dichalcogenides," *Nature Nanotechnology*, vol. 7, no. 11, pp. 699–712, (2012).

[62] Tsai M.-L., Su S.-H., Chang J.-K., Tsai D.-S., Chen C.-H., Wu C.-I., Li L.-J., Chen L.-J., and He J.-H., "Monolayer MoS_2 heterojunction solar cells," *ACS Nano*, vol. 8, no. 8, pp. 8317–8322, (2014).

[63] Li D., Cheng R., Zhou H., Wang C., Yin A., Chen Y., Weiss N. O., Huang Y., and Duan X., "Electric-field-induced strong enhancement of electroluminescence in multilayer molybdenum disulfide," *Nature Communications*, vol. 6, (2015).

[64] Lee C., Yan H., Brus L. E., Heinz T. F., Hone J., and Ryu S., "Anomalous lattice vibrations of single-and few-layer MoS_2," *ACS Nano*, vol. 4, no. 5, pp. 2695–2700, (2010).

[65] Zhan Y., Liu Z., Najmaei S., Ajayan P. M., and Lou J., "Large-area vapor-phase growth and characterization of MoS_2 atomic layers on a SiO_2 substrate," *Small*, vol. 8, no. 7, pp. 966–971, (2012).

[66] Wieting T. and Verble J., "Infrared and raman studies of long-wavelength optical phonons in hexagonal MoS_2," *Physical Review B*, vol. 3, no. 12, p. 4286, (1971).

[67] Li H., Zhang Q., Yap C. C. R., Tay B. K., Edwin T. H. T., Olivier A., and Baillargeat D., "From bulk to monolayer MoS_2: evolution of Raman scattering," *Advanced Functional Materials*, vol. 22, no. 7, pp. 1385–1390, (2012).

[68] Lee H. S., Min S.-W., Chang Y.-G., Park M. K., Nam T., Kim H., Kim J. H., Ryu S., and Im S., "MoS_2 nanosheet phototransistors with thickness-modulated optical energy gap," *Nano Letters*, vol. 12, no. 7, pp. 3695–3700, (2012).

[69] Taube A., Judek J., Łapinska A., and Zdrojek M., "Temperature-dependent thermal properties of supported MoS_2 monolayers," *ACS Applied Materials and Interfaces*, vol. 7, no. 9, pp. 5061–5065, (2015).

[70] Coehoorn R., Haas C., Dijkstra J., Flipse C., De Groot R., and Wold A., "Electronic structure of $MoSe_2$, MoS_2, and WSe_2. i. band-structure calculations and photoelectron spectroscopy," *Physical Review B*, vol. 35, no. 12, p. 6195, (1987).

[71] Lifshitz E., Glozman A., Litvin I., and Porteanu H., "Optically detected magnetic resonance studies of the surface/interface properties of II-VI semiconductor quantum dots," *The Journal of Physical Chemistry B*, vol. 104, no. 45, pp. 10449–10461, (2000).

[72] Splendiani A., Sun L., Zhang Y., Li T., Kim J., Chim C.-Y., Galli G., and Wang F., "Emerging photoluminescence in monolayer MoS_2," *Nano letters*, vol. 10, no. 4, pp. 1271–1275, (2010).

[73] Schaller R. D., Sykora M., Jeong S., and Klimov V. I., "High-efficiency carrier multiplication and ultrafast charge separation in semiconductor nanocrystals studied via time-resolved photoluminescence," *The Journal of Physical Chemistry B*, vol. 110, no. 50, pp. 25332–25338, (2006).

[74] Castellanos-Gomez A., Roldán R., Cappelluti E., Buscema M., Guinea F., van der Zant H. S., and Steele G. A., "Local strain engineering in atomically thin MoS_2," *Nano Letters*, vol. 13, no. 11, pp. 5361–5366, (2013).

[75] Wang H., Yu L., Lee Y.-H., Shi Y., Hsu A., Chin M. L., Li L.-J., Dubey M., Kong J., and Palacios T., "Integrated circuits based on bilayer MoS_2 transistors," *Nano Letters*, vol. 12, no. 9, pp. 4674–4680, (2012).

[76] Radisavljevic B. and Kis A., "Mobility engineering and a metal–insulator transition in monolayer MoS_2," *Nature Materials*, vol. 12, no. 9, pp. 815–820, (2013).

[77] Kaasbjerg K., Thygesen K. S., and Jacobsen K. W., "Phonon-limited mobility in n-type single-layer MoS_2 from first principles," *Physical Review B*, vol. 85, no. 11, p. 115317, (2012).

[78] Wu M., Wang Y., Lin X., Yu N., Wang L., Wang L., Hagfeldt A., and Ma T., "Economical and effective sulfide catalysts for dye-sensitized solar cells as counter electrodes," *Physical Chemistry Chemical Physics*, vol. 13, no. 43, pp. 19298–19301, (2011).

[79] Yue G., Lin J.-Y., Tai S.-Y., Xiao Y., and Wu J., "A catalytic composite film of MoS_2/graphene flake as a counter electrode for Pt-free dye-sensitized solar cells," *Electrochimica Acta*, vol. 85, pp. 162–168, (2012).

[80] Liu C.-J., Tai S.-Y., Chou S.-W., Yu Y.-C., Chang K.-D., Wang S., Chien F. S.-S., Lin J.-Y., and Lin T.-W., "Facile synthesis of MoS_2/graphene nanocomposite with high catalytic activity toward triiodide reduction in dye-sensitized solar cells," *Journal of Materials Chemistry*, vol. 22, no. 39, pp. 21057–21064, (2012).

[81] Tai S.-Y., Liu C.-J., Chou S.-W., Chien F. S.-S., Lin J.-Y., and Lin T.-W., "Few-layer MoS_2 nanosheets coated onto multi-walled carbon nanotubes as a low-cost and highly electrocatalytic counter electrode for dye-sensitized solar cells," *Journal of Materials Chemistry*, vol. 22, no. 47, pp. 24753–24759, (2012).

[82] Lin J.-Y., Chan C.-Y., and Chou S.-W., "Electrophoretic deposition of transparent MoS_2–graphene nanosheet composite films as counter electrodes in dye-sensitized solar cells," *Chemical Communications*, vol. 49, no. 14, pp. 1440–1442, (2013).

[83] Yue G., Wu J., Xiao Y., Huang M., Lin J., and Lin J.-Y., "High performance platinum-free counter electrode of molybdenum sulfide–carbon used in dye-sensitized solar cells," *Journal of Materials Chemistry A*, vol. 1, no. 4, pp. 1495–1501, (2013).

[84] Yue G., Zhang W., Wu J., and Jiang Q., "Glucose aided synthesis of molybdenum sulfide/carbon nanotubes composites as counter electrode for high performance dye-sensitized solar cells," *Electrochimica Acta*, vol. 112, pp. 655–662, (2013).

[85] Lei B., Li G., and Gao X., "Morphology dependence of molybdenum disulfide transparent counter electrode in dye-sensitized solar cells," *Journal of Materials Chemistry A*, vol. 2, no. 11, pp. 3919–3925, (2014).

[86] Liu W., He S., Yang T., Feng Y., Qian G., Xu J., and Miao S., "TEOS-assisted synthesis of porous MoS_2 with ultra-small exfoliated sheets and applications in dye-sensitized solar cells," *Applied Surface Science*, vol. 313, pp. 498–503, (2014).

[87] Patil S. A., Kalode P. Y., Mane R. S., Shinde D. V., Doyoung A., Keumnam C., Sung M., Ambade S. B., and Han S.-H., "Highly efficient and stableDSSCs of wet-chemically synthesized MoS_2 counter electrode," *Dalton Transactions*, vol. 43, no. 14, pp. 5256–5259, (2014).

[88] Yue G., Ma X., Jiang Q., Tan F., Wu J., Chen C., Li F., and Li Q., "PEDOT: PSS and glucose assisted preparation of molybdenum disulfide/single-wall carbon nanotubes counter electrode and served in dye-sensitized solar cells," *Electrochimica Acta*, vol. 142, pp. 68–75, (2014).

[89] Shokhen V., Miroshnikov Y., Gershinsky G., Gotlib N., Stern C., Naveh D., and Zitoun D., "On the impact of vertical alignment of MoS_2 for efficient lithium storage," *Scientific Reports*, vol. 7, no. 1, p. 3280, (2017).

[90] Du G., Guo Z., Wang S., Zeng R., Chen Z., and Liu H., "Superior stability and high capacity of restacked molybdenum disulfide as anode material for lithium ion batteries," *Chemical Communications*, vol. 46, no. 7, pp. 1106–1108, (2010).

[91] Fang X., Yu X., Liao S., Shi Y., Hu Y.-S., Wang Z., Stucky G. D., and Chen L., "Lithium storage performance in ordered mesoporous MoS_2 electrode material," *Microporous and Mesoporous Materials*, vol. 151, pp. 418–423, (2012).

[92] Faghaninia A., "Theory of carrier transport from first principles: Applications in photovoltaic and thermoelectric materials," vol. 1, no. 1, pp. 157–166, (2016).

[93] Naidu S. M., *A text book of applied Physics*, vol. 5. Pearson Education India, (2009).

[94] Hill D. E., "Activation energy of holes in Zn-doped GaAs," *Journal of Applied Physics*, vol. 41, no. 4, pp. 1815–1818, (1970).

[95] Casida M. E. and Huix-Rotllant M., "Progress in time-dependent density-functional theory," *Annual Review of Physical Chemistry*, vol. 63, pp. 287–323, (2012).

[96] Perdew J. P., Burke K., and Ernzerhof M., "Generalized gradient approximation made simple," *Physical Review Letters*, vol. 77, no. 18, p. 3865, (1996).

[97] Singh J., *Modern Physics for Engineers*. John Wiley & Sons, (2008).

[98] Rode D., "Low-field electron transport," in *Semiconductors and Semimetals*, vol. 10, pp. 1–89, Elsevier, (1975).

[99] McGaughey A. J. and Kaviany M., "Quantitative validation of the Boltzmann transport equation phonon thermal conductivity model under the single-mode relaxation time approximation," *Physical Review B*, vol. 69, no. 9, p. 94303, (2004).

[100] Sholl D. and Steckel J. A., *Density functional theory: a practical introduction*. John Wiley & Sons, (2011).

[101] Madsen G. K., Schwarz K., Blaha P., and Singh D. J., "Electronic structure and transport in type-I and type-VIII clathrates containing strontium, barium, and europium," *Physical Review B*, vol. 68, no. 12, p. 125212, (2003).

[102] Madsen G. K. and Singh D. J., "Boltztrap. a code for calculating band-structure dependent quantities," *Computer Physics Communications*, vol. 175, no. 1, pp. 67–71, (2006).

[103] Ibach H. and Lüth H., *Solid State Physics: An Introduction to Principles of Materials Science*. Advanced Texts in Physics, Springer Berlin Heidelberg, (1995).

[104] Giannozzi P., Baroni S., Bonini N., Calandra M., Car R., Cavazzoni C., Ceresoli D., Chiarotti G. L., Cococcioni M., Dabo I., and others , "Quantum espresso: a modular and open-source software project for quantum simulations of materials," *Journal of Physics: Condensed Matter*, vol. 21, no. 39, p. 395502, (2009).

[105] Wu Z. and Cohen R. E., "More accurate generalized gradient approximation for solids," *Physical Review B*, vol. 73, no. 23, p. 235116, (2006).

[106] Ziegler J. F., Ziegler M. D., and Biersack J. P., "SRIM–the stopping and range of ions in matter (2010)," *Nuclear Instruments and Methods in Physics Research Section B: Beam Interactions with Materials and Atoms*, vol. 268, no. 11, pp. 1818–1823, (2010).

[107] Qi J., Li X., Qian X., and Feng J., "Bandgap engineering of rippled MoS_2 monolayer under external electric field," *Applied Physics Letters*, vol. 102, no. 17, p. 173112, (2013).

[108] Zhang S., Yan Z., Li Y., Chen Z., and Zeng H., "Atomically thin arsenene and antimonene: semimetal–semiconductor and indirect–direct band-gap transitions," *Angewandte Chemie*, vol. 127, no. 10, pp. 3155–3158, (2015).

[109] Jayaraman A., Bhat Kademane A., and Molli M., "DFT study on the carrier concentration and temperature-dependent thermoelectric properties of antimony selenide," *Indian Journal of Materials Science*, vol. 2016, pp. 1155–1162, (2016).

[110] Lee C., Hong J., Lee W. R., Kim D. Y., and Shim J. H., "Density functional theory investigation of the electronic structure and thermoelectric properties of layered MoS_2, $MoSe_2$ and their mixed-layer compound," *Journal of Solid State Chemistry*, vol. 211, pp. 113–119, (2014).

[111] Frey G. L., Tenne R., Matthews M. J., Dresselhaus M., and Dresselhaus G., "Raman and resonance Raman investigation of MoS_2 nanoparticles," *Physical Review B*, vol. 60, no. 4, p. 2883, (1999).

[112] Stacy A. and Hodul D., "Raman spectra of IVB and VIB transition metal disulfides using laser energies near the absorption edges," *Journal of Physics and Chemistry of Solids*, vol. 46, no. 4, pp. 405–409, (1985).

[113] Song I., Park C., and Choi H. C., "Synthesis and properties of molybdenum disulphide: from bulk to atomic layers," *RSC Advances*, vol. 5, no. 10, pp. 7495–7514, (2015).

[114] Wu D., Huang H., Zhu X., He Y., Xie Q., Chen X., Zheng X., Duan H., and Gao Y., "Eraman mode in thermal strain-fractured cvd-MoS_2," *Crystals*, vol. 6, no. 11, p. 151, (2016).

[115] Sandoval S. J., Yang D., Frindt R., and Irwin J., "Raman study and lattice dynamics of single molecular layers of MoS_2," *Physical Review B*, vol. 44, no. 8, p. 3955, (1991).

[116] Dou X., Ding K., Jiang D., and Sun B., "Tuning and identification of interband transitions in monolayer and bilayer molybdenum disulfide using hydrostatic pressure," *ACS Nano*, vol. 8, no. 7, pp. 7458–7464, (2014).

[117] Deschler F., Price M., Pathak S., Klintberg L. E., Jarausch D.-D., Higler R., Huttner S., Leijtens T., Stranks S. D., Snaith H. J., and others , "High photoluminescence efficiency and optically pumped lasing in solution-processed mixed halide perovskite semiconductors," *The Journal of Physical Chemistry Letters*, vol. 5, no. 8, pp. 1421–1426, (2014).

[118] Polyanskiy M. N., "Refractive index database." https://refractiveindex.info. Accessed on 2019-03-05.

[119] Wang X., Huang J., Li J., Cao L., Hao W., and Xu Z., "Improved Na storage performance with the involvement of nitrogen-doped conductive carbon into WS_2 nanosheets," *ACS Applied Materials & Interfaces*, vol. 8, no. 36, pp. 23899–23908, (2016).

[120] Wang J., Polleux J., Lim J., and Dunn B., "Pseudocapacitive contributions to electrochemical energy storage in TiO_2 (anatase) nanoparticles," *The Journal of Physical Chemistry C*, vol. 111, no. 40, pp. 14925–14931, (2007).

[121] Chidembo A. T. and Ozoemena K. I., "Electrochemical capacitive behaviour of multiwalled carbon nanotubes modified with electropolymeric films of nickel tetraaminophthalocyanine," *Electroanalysis*, vol. 22, no. 21, pp. 2529–2535, (2010).

[122] Zhang S. and Pan N., "Supercapacitors performance evaluation," *Advanced Energy Materials*, vol. 5, no. 6, p. 175, (2015).

[123] Oldham K. B., "Analytical expressions for the reversible Randles-Sevcik function," *Journal of Electroanalytical Chemistry and Interfacial Electrochemistry*, vol. 105, no. 2, pp. 373–375, (1979).

[124] Ngamchuea K., Eloul S., Tschulik K., and Compton R. G., "Planar diffusion to macro disc electrodeswhat electrode size is required for the Cottrell and Randles-Sevcik equations to apply quantitatively?," *Journal of Solid State Electrochemistry*, vol. 18, no. 12, pp. 3251–3257, (2014).

[125] Strømme M., Niklasson G. A., and Granqvist C. G., "Voltammetry on fractals," *Solid State Communications*, vol. 96, no. 3, pp. 151–154, (1995).

[126] Hu Z., Wang L., Zhang K., Wang J., Cheng F., Tao Z., and Chen J., "MoS_2 nanoflowers with expanded interlayers as high-performance anodes for sodium-ion batteries," *Angewandte Chemie*, vol. 126, no. 47, pp. 13008–13012, (2014).

[127] Zanello P., *Inorganic Electrochemistry: theory, practice and application*. Royal Society of Chemistry, (2007).

[128] Skoog D., Holler F., and Crouch S., "Principles of instrumental analysis Cengage learning," *Brooks Cole, CT*, vol. 32, pp. 3143–3145, (2007).

[129] Zhang S., Chowdari B., Wen Z., Jin J., and Yang J., "Constructing highly oriented configuration by few-layer MoS_2: toward high-performance lithium-ion batteries and hydrogen evolution reactions," *ACS Nano*, vol. 9, no. 12, pp. 12464–12472, (2015).

[130] Nath R., Yue N., Shahnazi K., and Bongiorni P. J., "Measurement of dose-rate constant for 103Pd seeds with air kerma strength calibration based upon a primary national standard," *Medical Physics*, vol. 27, no. 4, pp. 655–658, (2000).

[131] Ward K. R., Lawrence N. S., Hartshorne R. S., and Compton R. G., "Cyclic voltammetry of the EC mechanism at hemispherical particles and their arrays: the split wave," *The Journal of Physical Chemistry C*, vol. 115, no. 22, pp. 11204–11215, (2011).

[132] Béguin F., Presser V., Balducci A., and Frackowiak E., "Carbons and electrolytes for advanced supercapacitors," *Advanced Materials*, vol. 26, no. 14, pp. 2219–2251, (2014).

[133] Makgopa K., Ejikeme P., Jafta C., Raju K., Zeiger M., Presser V., and Ozoemena K. *J. Mater. Chem. A*, vol. 3, pp. 3480–3490, (2015).

[134] Khawula T. N., Raju K., Franklyn P. J., Sigalas I., and Ozoemena K. I., "Symmetric pseudocapacitors based on molybdenum disulfide (MoS_2)-modified carbon nanospheres: correlating physicochemistry and synergistic interaction on energy storage," *Journal of Materials Chemistry A*, vol. 4, no. 17, pp. 6411–6425, (2016).

[135] Abouzari M. S., Berkemeier F., Schmitz G., and Wilmer D., "On the physical interpretation of constant phase elements," *Solid State Ionics*, vol. 180, no. 14-16, pp. 922–927, (2009).

[136] Dhirde A. M., Dale N. V., Salehfar H., Mann M. D., and Han T.-H., "Equivalent electric circuit modeling and performance analysis of a PEM fuel cell stack using impedance spectroscopy," *IEEE transactions on energy conversion*, vol. 25, no. 3, pp. 778–786, (2010).

[137] Enterría M., Gonçalves A., Pereira M. F. R., Martins J. I., and Figueiredo J. L., "Electrochemical storage mechanisms in non-stoichiometric cerium oxide/multiwalled carbon nanotube composites," *Electrochimica Acta*, vol. 209, pp. 25–35, (2016).

[138] Sun P., Zhang W., Hu X., Yuan L., and Huang Y., "Synthesis of hierarchical MoS_2 and its electrochemical performance as an anode material for lithium-ion batteries," *Journal of Materials Chemistry A*, vol. 2, no. 10, pp. 3498–3504, (2014).

[139] Corneille J. S., He J.-W., and Goodman D. W., "XPS characterization of ultra-thin MgO films on a Mo (100) surface," *Surface Science*, vol. 306, no. 3, pp. 269–278, (1994).

[140] Smart R. S. C., Skinner W. M., and Gerson A. R., "XPS of sulphide mineral surfaces: metal-deficient, polysulphides, defects and elemental sulphur," *Surface and Interface Analysis: An International Journal devoted to the development and application of techniques for the analysis of surfaces, interfaces and thin films*, vol. 28, no. 1, pp. 101–105, (1999).

[141] Weber T., Muijsers J., Van Wolput J., Verhagen C., and Niemantsverdriet J., "Basic reaction steps in the sulfidation of crystalline MoO_3 to MoS_2, as studied by x-ray photoelectron and infrared emission spectroscopy," *The Journal of Physical Chemistry*, vol. 100, no. 33, pp. 14144–14150, (1996).

[142] Castillo C., Buono-Core G., Manzur C., Yutronic N., Sierpe R., Cabello G., and Chornik B., "Molybdenum trioxide thin films doped with gold nanoparticles grown by a sequential methodology: photochemical metal-organic deposition (pmod) and dc-magnetron sputtering," *Journal of the Chilean Chemical Society*, vol. 61, no. 1, pp. 2816–2820, (2016).

[143] Rasband W., "Imagej software," *National Institutes of Health: Bethesda, MD, USA*, vol. 2012, (1997).

[144] Joensen P., Crozier E., Alberding N., and Frindt R., "A study of single-layer and restacked MoS_2 by X-ray diffraction and X-ray absorption spectroscopy," *Journal of Physics C: Solid State Physics*, vol. 20, no. 26, p. 4043, (1987).

[145] Klobes P. and Munro R. G., "Porosity and specific surface area measurements for solid materials," tech. rep., (2006).

[146] Ciesla U. and Schüth F., "Ordered mesoporous materials," *Microporous and Mesoporous Materials*, vol. 27, no. 2-3, pp. 131–149, (1999).

[147] Choi M. S., Qu D., Lee D., Liu X., Watanabe K., Taniguchi T., and Yoo W. J., "Lateral MoS_2 p–n junction formed by chemical doping for use in high-performance optoelectronics," *ACS Nano*, vol. 8, no. 9, pp. 9332–9340, (2014).

[148] Mouri S., Miyauchi Y., and Matsuda K., "Tunable photoluminescence of monolayer MoS_2 via chemical doping," *Nano Letters*, vol. 13, no. 12, pp. 5944–5948, (2013).

[149] Wang G., Robert C., Suslu A., Chen B., Yang S., Alamdari S., Gerber I. C., Amand T., Marie X., and Tongay S., "Spin-orbit engineering in transition metal dichalcogenide alloy monolayers," *Nature Communications*, vol. 6, p. 10110, (2015).

APPENDIX A

SUPPORTING INFORMATION

A.1 DFT Structural Optimizations

The Figures A.1, A.2 and A.4 show information on how the k points, the lattice parameters (celldm 1) and cut-off energies (E-cut) were optimized in the case of pristine MoS_2.

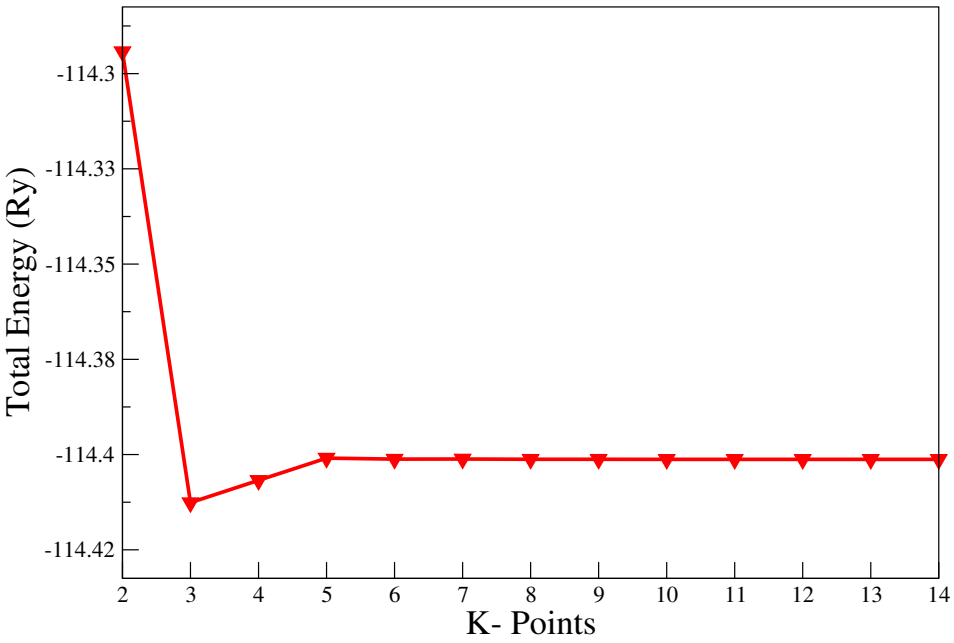

Figure A.1: Graph of total energy against k-points of MoS_2.

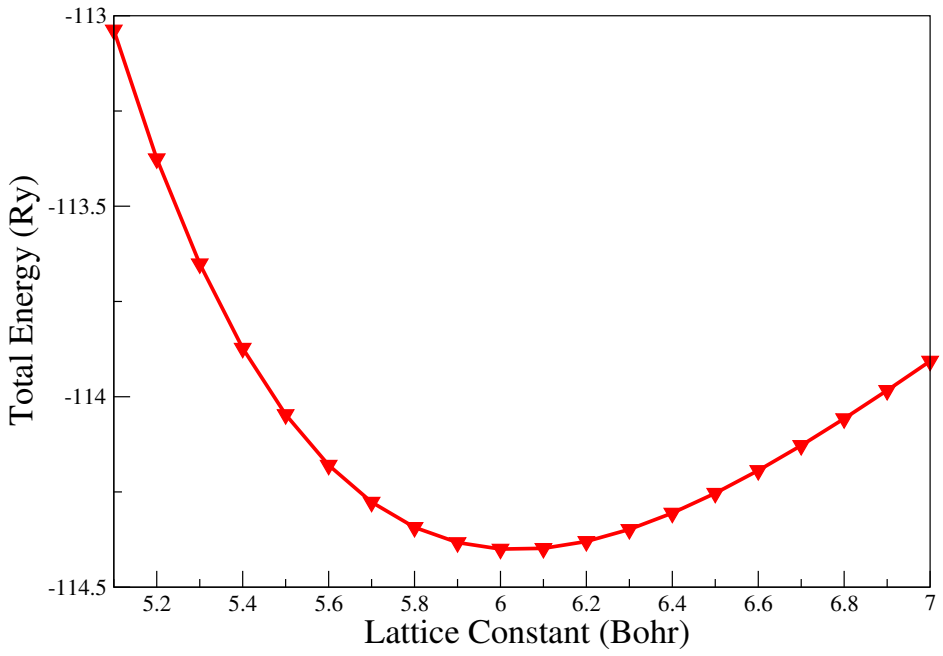

Figure A.2: Graph of total energy against the lattice of MoS_2.

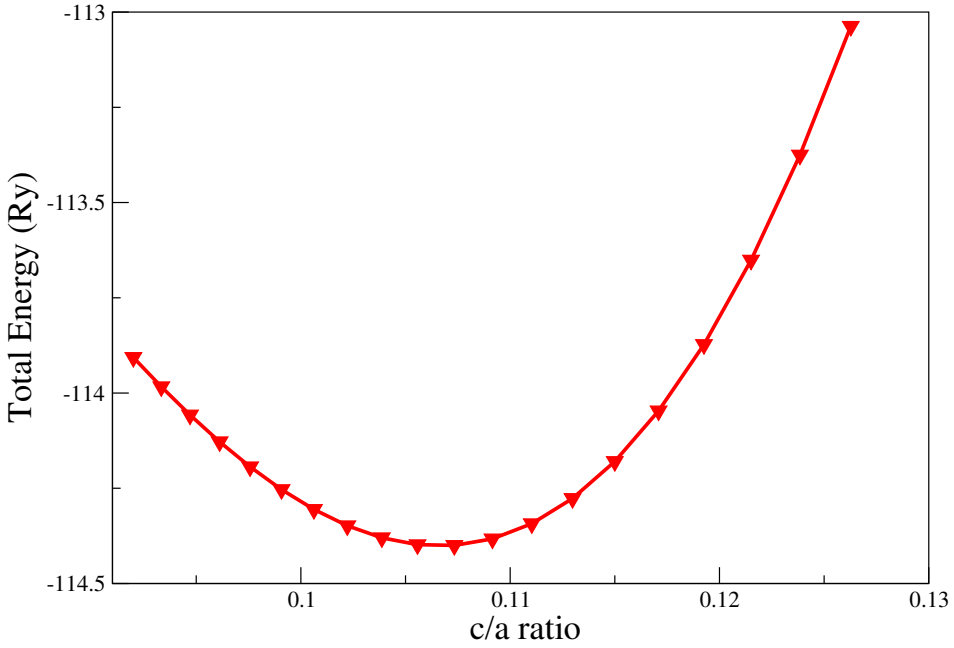

Figure A.3: Graph of total energy against the c/a ratio of MoS_2.

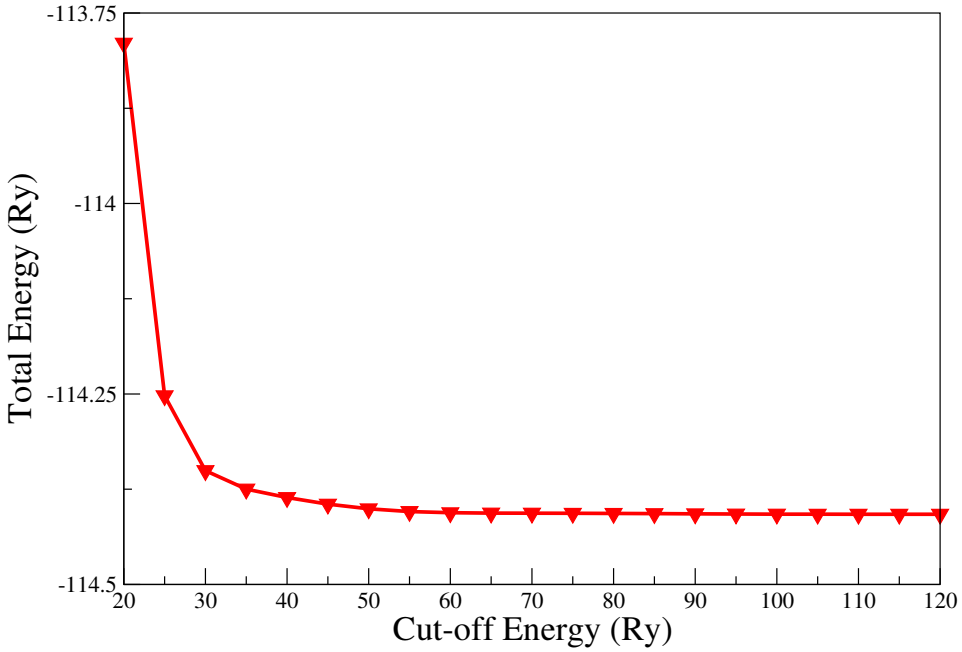

Figure A.4: Graph of total energy against cut-off energy of MoS_2.

A.2 Cyclic Voltammograms

The cyclic voltammograms for all the seven electrodes samples at various scan rates are shown in Figures A.5, A.6, A.7, A.8, A.9, A.10 and A.11.

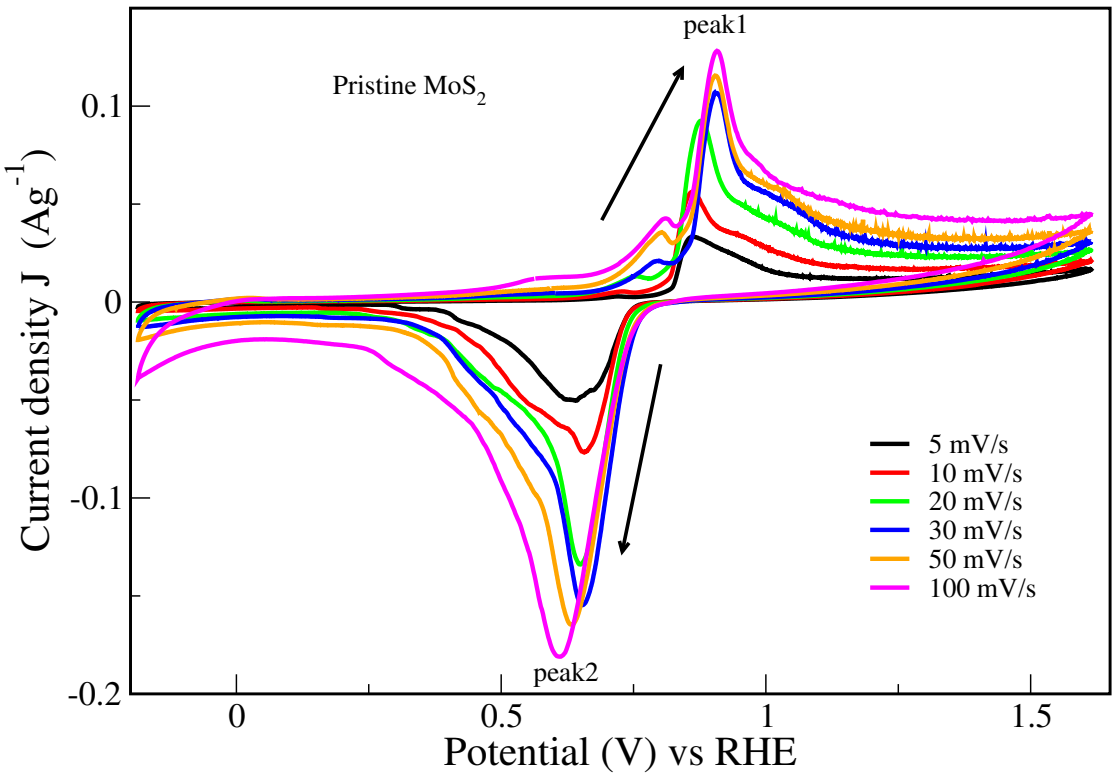

Figure A.5: Cyclic voltammograms for pristine MoS_2 electode at various scan rates.

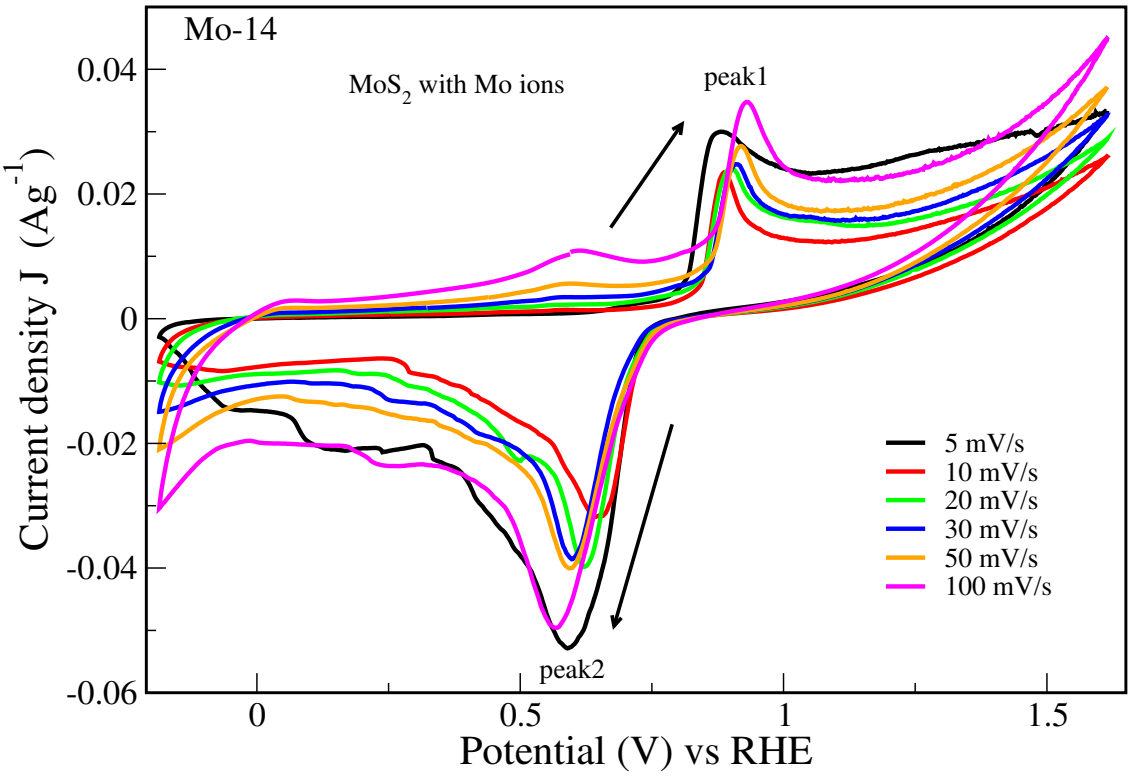

Figure A.6: Cyclic voltammograms for Mo-14 electrode at various scan rates.

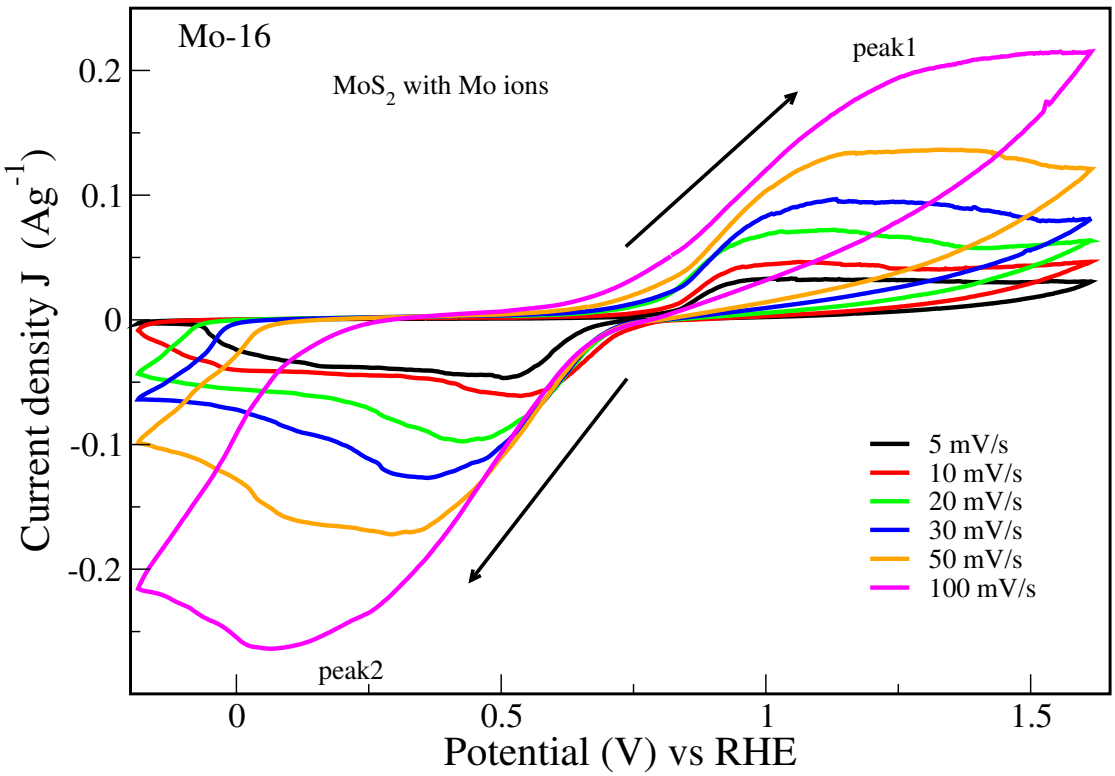

Figure A.7: Cyclic voltammograms for Mo-16 electrode at various scan rates.

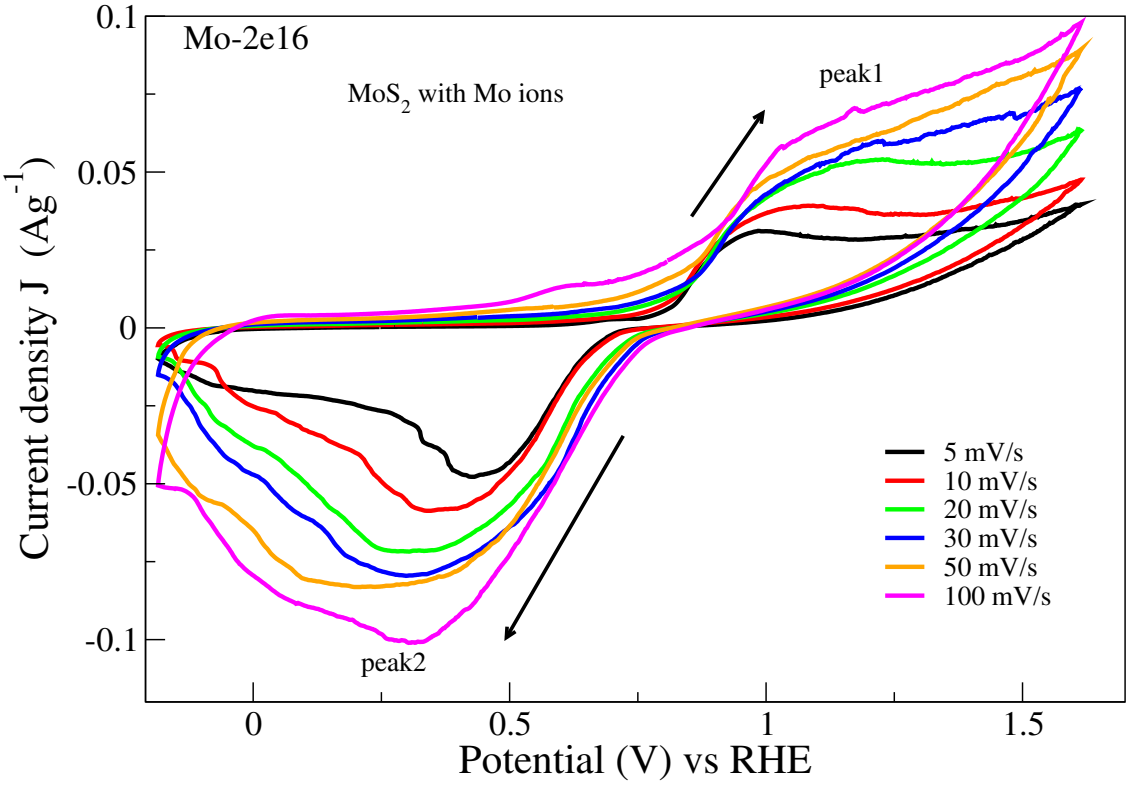

Figure A.8: Cyclic voltammograms for Mo-2e16 electrode at various scan rates.

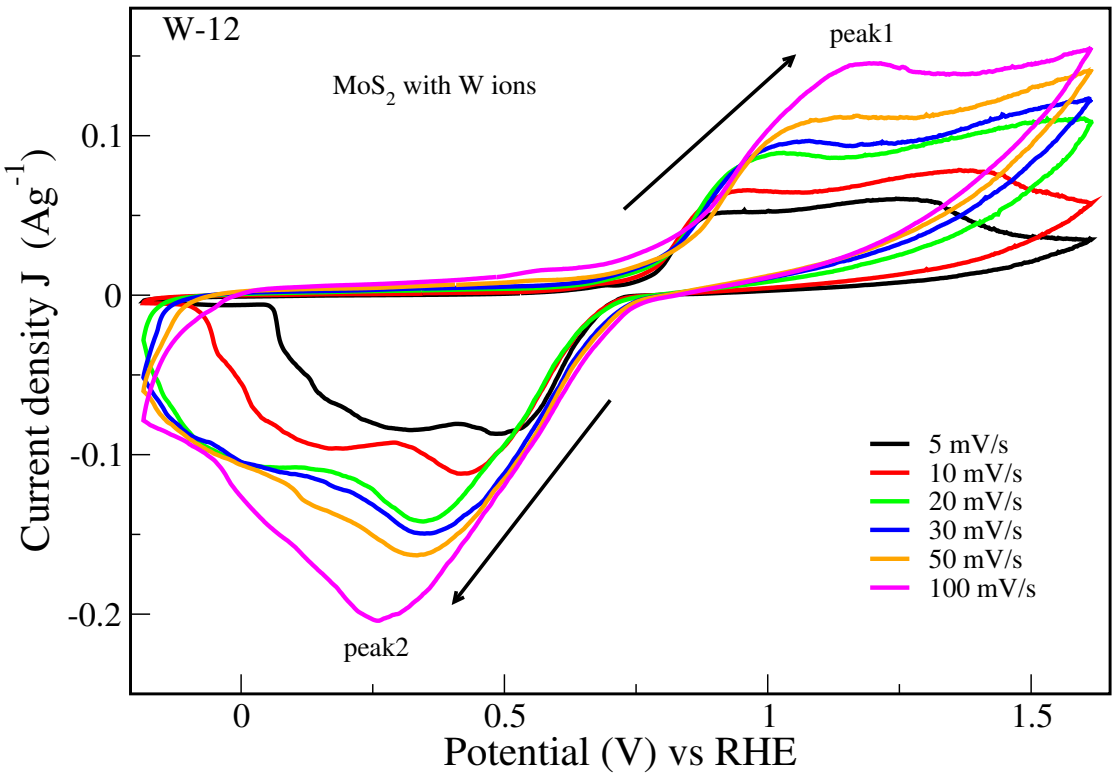

Figure A.9: Cyclic voltammograms for W-12 electrode at various scan rates.

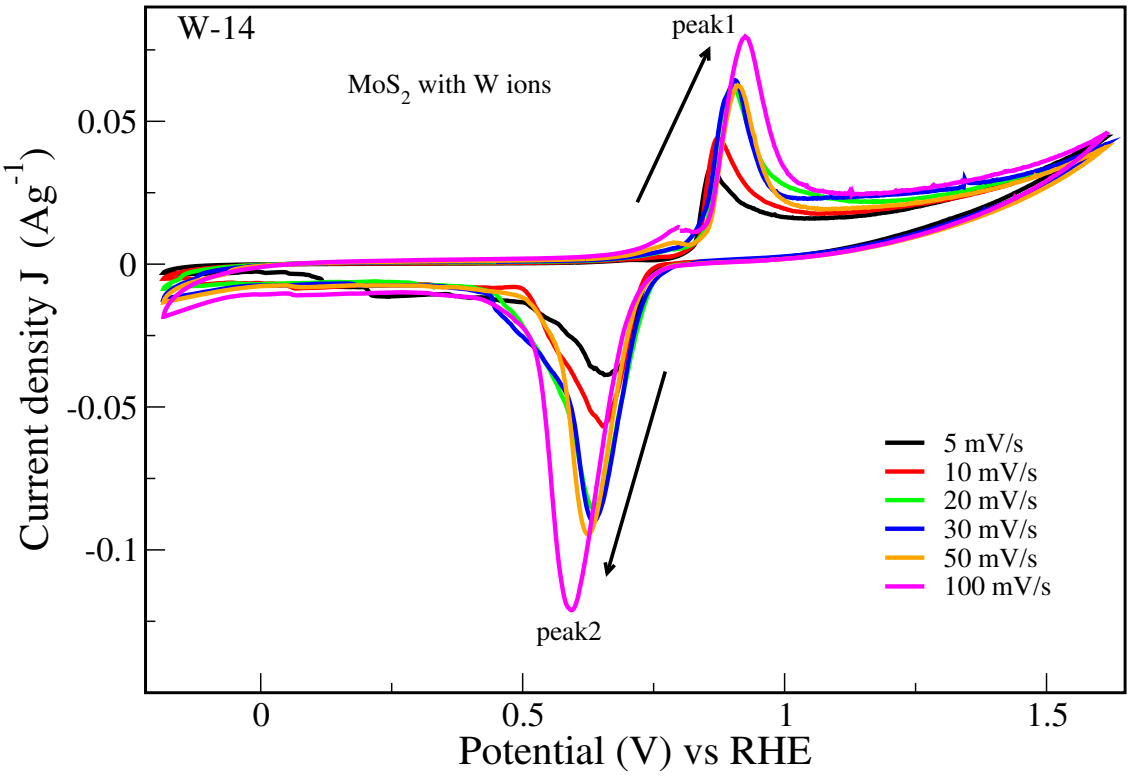

Figure A.10: Cyclic voltammograms for W-14 electrode at various scan rates.

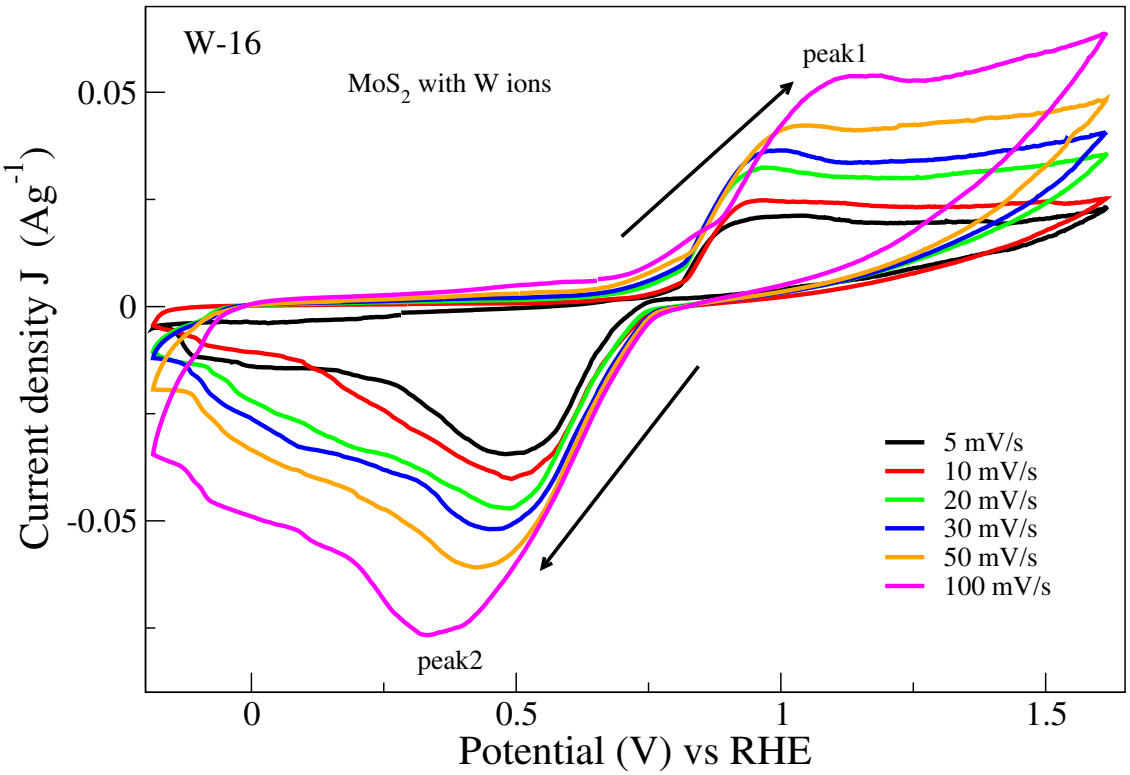

Figure A.11: Cyclic voltammograms for W-14 electrode at various scan rates.

APPENDIX B

CONFERENCES AND PUBLICATIONS

B.1 Publications

- P. V. Mwonga, R. Barik, S. R. Naidoo, A. Quandt and K. I. Ozoemena, Interrogating the effects of ion-implantation-induced defects on the energy storage properties of bulk molybdenum disulphide, *Physical Chemistry Chemical Physics*, (2018), **20**, 28232-28240, doi:10.1039/c8cp05384g.

- P. V. Mwonga, S. R. Naidoo, A. Quandt and K. I. Ozoemena, Tuning the bandgap of bulk molybdenum disulphide using defects, *South African Institute of Physics (SAIP)*, (2019) (Accepted), .

- P. V. Mwonga, S. R. Naidoo, A. Quandt and K. I. Ozoemena, Interrogating the effects of ion-implantation-induced defects on the energy storage properties of powdered molybdenum disulphide, *Physical Chemistry Chemical Physics*, (2019), (writing in progress).

B.2 Conferences

This work has been orally presented in the following conferences;

- Materials for Energy Research Group (MERG) Workshop 7^{th} to 9^{th} September 2015, held at SunWa River Lodge-Parys, in Free State, South Africa,

- Materials for Energy Research Group (MERG) Workshop 1^{st} to 3^{rd} November 2017, held at the Italian consular in Johannesburg, South Africa,

- 4^{th} International Symposium on Electrochemistry *"Pure and Applied Electrochemistry"*, 3^{rd} to 5^{th} April 2018, held at University of Johannesburg, South Africa,

- 63^{rd} South African Institute of Physics (SAIP) 24^{th} to 29^{th} June 2018, held at University of Free State, Bloemfontein, South Africa.

- Centre for High Performance Computing (CHPC), 2018 National Conference, 2^{nd} to 7^{th} December 2018, held at Century Conference Centre, Cape Town, South Africa.